

# **Near-Infrared Fluorescent Single-Chain Nanoparticles as Contrast Agents for Photoacoustic Imaging**

## **Dissertation**

zur Erlangung des Doktorgrades der Naturwissenschaften  
(Dr. rer. nat.)

der

Naturwissenschaftlichen Fakultät II  
Chemie, Physik und Mathematik

der Martin-Luther-Universität  
Halle-Wittenberg

vorgelegt von

Herrn Justus Friedrich Thümmeler (geb. Hoffmann)

Gutachter: Prof. Dr. Wolfgang H. Binder  
Prof. Dr. Brigitte Voit

Verteidigung: 16.04.2024

# Danksagung

Zuallererst möchte ich mich bei Prof. Dr. Wolfgang H. Binder bedanken für die Bereitstellung dieses spannenden Themas, all die intensiven Diskussionen über meine Ergebnisse und ganz allgemein dafür meinen Kindheitstraum Wissenschaftler zu werden zu ermöglichen.

Natürlich bedanke ich mich auch bei allen, die mich in meiner Zeit als Doktorand begleitet haben. Ohne meine Kooperationspartner, insbesondere Prof. Dr. Laufer und seiner Gruppe, Prof. Dr. Dariush Hinderberger, Dr. Andreas Kampe, Dr. Henrike Lucas und Dr. Franz-Josef Schmitt wäre es nicht möglich gewesen, all diese Ergebnisse zu produzieren und zu publizieren. Aus der AG Binder bedanke ich mich besonders bei Anke Hassi, die mich als Herz dieses Instituts bei allem Organisatorischen unterstützt hat, bei Julia Großert und Susanne Tanner für die Erfüllung all meiner Laborwünsche und auch bei allen anderen, mit denen ich in dieser Zeit zusammenarbeiten sowie mir ein Büro und Labor teilen durfte. Speziell mit Matthias Rohmer, Vico K. B. Adjedje, Kshitij S. Shinde und Philipp S. Hilgeroth konnte ich ein ums andere Mal den stressigen Laboralltag vergessen.

Dr. Dieder Ströhl und seinem Team danke ich für die Messung zahlreicher NMR Proben und die Erfüllung meiner ganzen Extrawünsche.

Bei Philipp S. Hilgeroth, Dr. Matthias Hoffmann und Dr. Franziska Dahmen bedanke ich mich für die detaillierten Korrekturen an dieser Doktorarbeit.

Zuletzt möchte ich mich meiner Familie und meinen Freunden dafür danken, dass sie mich während dieser Zeit stets unterstützt zu haben. Ganz besonders bedanke ich mich bei meiner Frau Sarah Luies Thümmler und Tochter Almira Luise Thümmler dafür, dass ihr, insofern schon geboren, immer für mich da gewesen seid und mich auch in schwierigen Phasen aufgefangen und aufgeheitert habt.

## Kurzdarstellung

Single-Chain Nanopartikel (SCNP) sind polymerbasierte Nanopartikel, die durch intramolekularen Kollaps und Vernetzung einzelner Polymerketten synthetisiert werden. Dieser Aufbau bietet die Möglichkeit proteinartige Strukturen zu imitieren und synthetisch herzustellen. Durch ihre chemische Flexibilität sind sie interessant für zahlreiche Anwendungsgebiete, insbesondere Katalyse und Drug-Delivery. Dabei bieten sie unter anderem die Möglichkeit, intern kompartimentierte Nanostrukturen auszubilden.

In dieser kumulativen Dissertation wurden wasserlösliche, Kern-Schale strukturierte SCNP synthetisiert und mit Radikal- und (nahinfraroten (NIR)) Fluoreszenzlabeln versehen. Die NIR fluoreszenten SCNP sollen als Kontrastmittel für pump-probe photoakustische (PA) Bildgebung genutzt werden können, welche eine neue biomedizinische Bildgebungsmethode ist, die eine hohe Auflösung erzielen kann.

Als Grundlage für diese SCNP wurden Poly(ethylenglycol)-methacrylat-basierte Polymere synthetisiert, die als Vorstufe für die SCNP dienten. Als Copolymere mit vernetzbaren Alkin- und/oder Azid-funktionalisierten Monomeren wurden sie durch Kupfer-katalysierte Azid-Alkin Clickreaktionen in Wasser oder THF auf zwei Wegen zu SCNP überführt: (I) das Polymer enthielt beide funktionelle Gruppen mit einem Überschuss an Aziden, um das SCNP nach der Vernetzung mit Alkin-funktionalisierten Labeln zu versehen; (II) das Polymer enthielt lediglich Azide, die durch externe, bivalent Alkin-funktionalisierte Crosslinker vernetzt wurden, die gleichzeitig auch als Label dienten.

Untersuchungen der thermoresponsiven Löslichkeit von Polymeren und SCNP in Wasser sowie spektroskopische Analysen mit Elektronenspinresonanz- und Fluoreszenzspektroskopie ergaben eine intern unterteilte Nanostruktur mit einem dichten, hydrophoben Kern und einer hydrophilen Schale. Der SCNP-Kern bildete dabei eine unpolare Verkapselung für die Fluoreszenzlabel, deren Fluoreszenzlebensdauer dadurch deutlich verlängert und die Fluoreszenzintensitäten erhöht wurden. Die hydrophile Schale ermöglichte zusätzlich eine gute Wasserlöslichkeit sowie eine hohe Biokompatibilität.

Die NIR-fluoreszenten SCNP konnten als Kontrastmittel für pump-probe PA Messungen verwendet werden. Ihr thermoresponsives Verhalten führte dabei, zusätzlich zu den bereits intensiven PA Signalen, zu einzigartigen Effekten, die durch die unterschiedlichen Thermoresponsivitäten von Kern und Schale erzeugt wurden und durch die pump-probe Anregungswärme ausgelöst werden konnten.

## Abstract

Single-chain nanoparticles (SCNPs) are polymeric nanoparticles that are produced by intramolecularly collapsing and crosslinking single polymer chains. Conceptually, they resemble and often mimic the structures of natural proteins. Their chemical flexibility and ability to form compartmentalized internal nanostructures make them perfect candidates for numerous applications, especially catalysis and drug delivery.

In this cumulative thesis, water soluble, core-shell structured SCNPs were synthesized and labelled with radical and (near infrared (NIR)) fluorescent labels. The NIR-fluorescent SCNPs were supposed to be suitable as contrast agents for pump-probe photoacoustic (PA) imaging, a novel strategy for biomedical imaging with high spatial resolution.

The synthetic approach was the synthesis of poly(ethylene glycol)-methacrylate-based precursor polymers, that were copolymerized with crosslinkable monomers bearing alkyne and/or azide moieties. Single-chain collapse was performed by copper catalyzed azide-alkyne click reaction in water or THF. Two main approaches were followed: (I) the precursor polymer contained both crosslinkable moieties with an excess of azides for subsequent labelling with alkyne-functionalized labels; (II) the precursor polymer contained only azides as functional units, that were crosslinked with external, bivalently alkyne-functionalized crosslinkers that also acted as labels.

Studies of the thermoresponsive solubility behavior of the precursor polymers and the SCNPs in water, as well as spectroscopic analyses using electron-paramagnetic-resonance and fluorescence spectroscopy revealed an internal compartmentalization of the SCNPs with a confined hydrophobic core and a hydrophilic shell. The hydrophobic core turned out to be a good environment for the fluorescent dyes, prolonging their fluorescence lifetime and increasing their fluorescence intensity, while the hydrophilic shell provided high water solubility as well as biocompatibility.

The NIR-fluorescent SCNPs could be used as contrast agents for pump-probe PA measurements. The thermoresponsive behavior of the SCNPs provided not only intense PA responses, but also unique effects, caused by the different thermoresponsivities of core and shell, that could be triggered by the heat that followed the pump-probe excitation.

# Table of Contents

1.	Introduction .....	1
1.1.	Types of Nanoparticles .....	1
1.1.1.	Inorganic and Carbon-based Nanoparticles .....	2
1.1.2.	Organic Nanoparticles .....	3
1.1.3.	Polymer Nanoparticles.....	4
1.2.	Single-Chain Nanoparticles (SCNPs) .....	9
1.3.	Synthetic Approaches and Collapse Methodologies to SCNPs .....	11
1.3.1.	Non-Covalent and Supramolecular Collapse Methodologies .....	14
1.3.2.	Covalent Collapse Methodologies .....	16
1.4.	Internal Substructures of SCNPs .....	19
1.4.1.	Thermodynamic Background.....	19
1.4.2.	Compartmentalized SCNPs.....	20
1.5.	Characterization of SCNPs .....	24
1.5.1.	Size and Shape Analysis .....	24
1.5.2.	Compartment Analysis.....	26
1.6.	Applications and Special Functionalities of SCNPs .....	27
1.6.1.	SCNPs as Enzyme Mimetic Catalysts .....	27
1.6.2.	SCNPs for Biomedical Applications .....	28
1.6.3.	Incorporation of Functional Units .....	30
1.6.4.	Stimuli-Responsive Behavior .....	31
2.	Aim of the Thesis .....	34
3.	Scientific Approach .....	35
4.	List of Publications .....	38

*[P1] Fluorescent and Water Dispersible Single-Chain Nanoparticles: Core-Shell Structured Compartmentation*

*[P2] Tuning the Internal Compartmentation of Single-Chain Nanoparticles as Fluorescent Contrast Agents*

*[P3] Thermoresponsive Swelling of Photoacoustic Single-Chain Nanoparticles*

5. Conclusion .....	63
5.1. Synthesis and Properties of Precursor Polymers and SCNPs.....	64
5.2. Spectroscopic Nanostructure Analysis .....	65
5.3. Photoacoustic Measurements.....	68
6. Syntheses .....	70
6.1. Fluorescent Dyes and Radical Labels .....	70
6.2. Chain Transfer Agent and Monomers.....	76
6.3. Polymers .....	78
6.4. Single-Chain Nanoparticles .....	80
7. List of Abbreviations.....	83
8. Literature .....	85
Curriculum Vitae.....	107
Eigenständigkeitserklärung .....	110
Appendix .....	111

# 1. Introduction

## 1.1. Types of Nanoparticles

Nanoparticles (NPs) are particles in the nanometer size range, usually below 100 nm. Countless synthetical possibilities as well as numerous applications have attracted the interest of many scientists all around the world.

Nanoparticles can be classified as:<sup>1, 2</sup>

- Inorganic NPs, e.g., gold NPs, Fe<sub>3</sub>O<sub>4</sub> NPs, silica NPs;
- Carbon-based NPs, e.g., graphene, carbon nanotubes, fullerenes;
- Organic NPs, e.g., micelles, liposomes, proteins; and
- Polymeric NPs, e.g., dendrimers, block copolymer micelles, single-chain NPs.

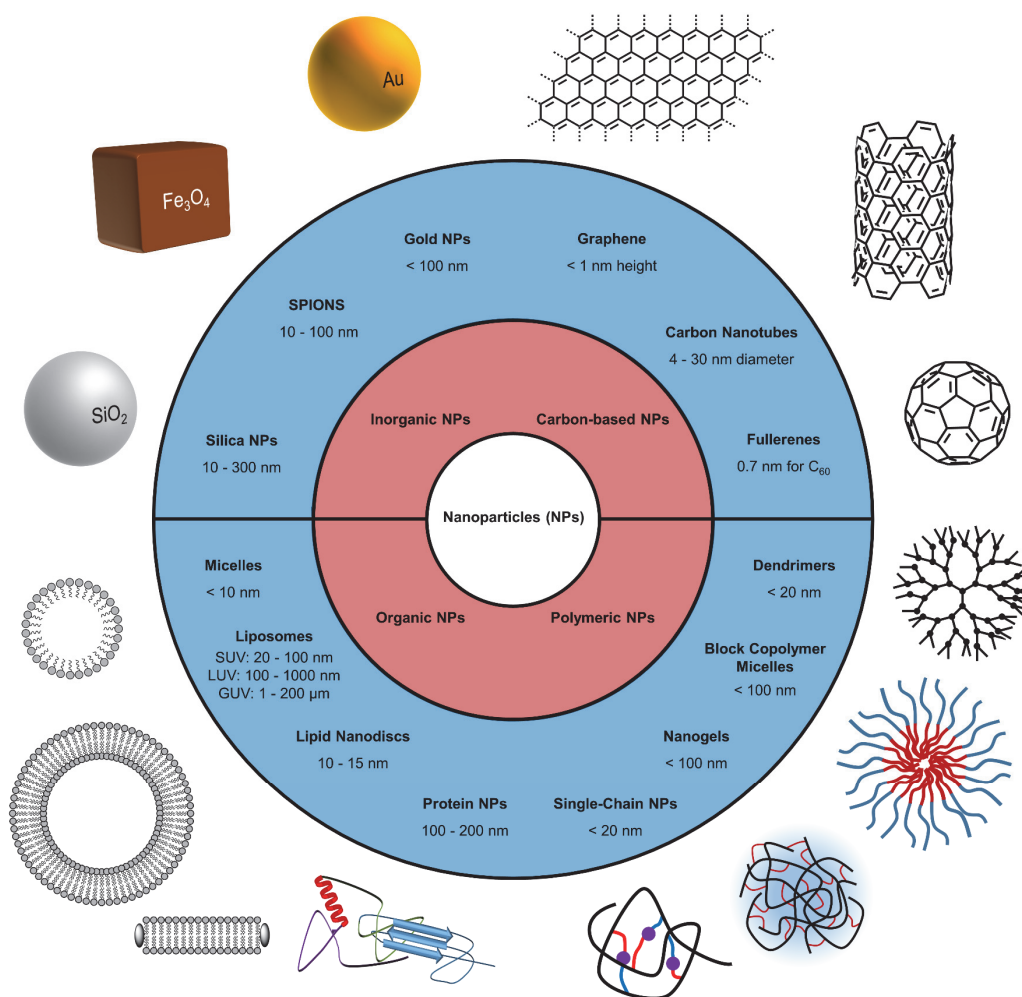


**Figure 1.** Classification into inorganic, carbon-based, organic, and polymeric nanoparticles, including their usual sizes and schematic illustrations of examples for each class.

### 1.1.1. Inorganic and Carbon-based Nanoparticles

Inorganic nanoparticles are made from inorganic materials, e.g., colloidal dispersions of the pure elements, alloys, or oxides. The earliest nanoparticles ever to be synthesized were gold nanoparticles. Since the 4<sup>th</sup> century, roman glass manufacturers – probably unknowingly – used gold nanoparticles to create red-dyed glass, e.g., in the Lycurgus Cup.<sup>3</sup> Gold as well as other metal nanoparticles get their colors from their small sizes (usually < 100 nm),<sup>4</sup> as, in such case, their electrons can interact with light *via* localized surface plasmon resonances. This means the electron clouds can resonate with incoming light and absorb it, which then excites enhanced movement of those electrons.<sup>5,6</sup> This movement results in the generation of heat that can be used in biomedical applications, i.e., photothermal therapy<sup>7,8</sup> or photoacoustic imaging.<sup>9,10</sup> Furthermore, gold NPs can be used as drug carriers by modifying their surface, e.g., by coordinating thiols that are bound to a drug.<sup>11</sup> Next to these biomedical applications, gold NPs can also be used as catalysts, e.g., in electrochemical reactions.<sup>12,13</sup> Using metal oxide nanoparticles instead of the pure metals can create their very own specific properties that are interesting for many different applications. Magnetite (Fe<sub>3</sub>O<sub>4</sub>) for example is a ferrimagnetic oxide of iron. If magnetite exists in the form of nanoparticles (10 – 100 nm),<sup>14</sup> it changes its magnetic behavior, becoming superparamagnetic iron oxide nanoparticles (SPIONs). Superparamagnetism is a specific type of ferri- and ferromagnetism of nanoparticles, in which there is no magnetic field dependent hysteresis of magnetization. This property makes SPIONs perfect candidates in theranostic (diagnostic and therapeutic) biomedical applications, as they can first act as contrast agents for magnetic resonance imaging, and eventually be used for magnetic fluid hypothermia.<sup>15,16</sup> As third example for inorganic nanoparticles, silica (SiO<sub>2</sub>) nanoparticles are particularly interesting because of their versatile internal and external morphology. Especially their ability to create extremely porous systems with adjustable pore sizes from 2 to 50 nm,<sup>17</sup> and therefore their high specific surface area, makes them perfect substances, e.g., for the absorption of pollutants or as carriers for catalysts, next to many other applications.<sup>18,19</sup> One of the smallest possible ways to create inorganic NPs is in the form of quantum dots: (semiconductor) NPs which are so small, the energies of their electrons are not continuous anymore and need to be described by quantum mechanical effects. Their discovery and description was awarded with the Nobel Prize 2023 for Ekimov, Brus, and Bawendi.<sup>20-22</sup>

Technically seen, nanostructured allotropes of elemental carbon, e.g., graphenes, fullerenes, or carbon nanotubes, can be counted as inorganic NPs as well. But because of their specific nanostructures (see **Figure 1**, upper right corner), they create their own class of NPs. As structural basis of all other nanostructured allotropes of carbon, graphenes are not particularly nanoparticles, but rather two-dimensional, single-layered carbon films with heights below

1 nm. The carbon atoms are arranged in an  $sp^2$ -hybridised, planar, hexagonal honeycomb lattice with delocalized  $\pi$ -systems.<sup>23</sup> Although mathematical descriptions of single layered planar structures indicate their thermodynamic instability, and therefore their theoretical non-existence,<sup>24</sup> Geim *et al.* were the first to isolate free, single-layered graphene in 2004,<sup>25</sup> probably stabilized by crumbling of the two-dimensional layers.<sup>26</sup> Because of the delocalized  $\pi$ -system over the complete structure graphene provides interesting properties, including high electrical<sup>23</sup> and thermal<sup>27</sup> conductivity, that makes it a promising candidate especially as substitute for silicon based materials. While the applications of graphene are mostly hypothetical and still under development, carbon nanotubes are already widely used, e.g., in batteries or polymer composites, also because of their high electrical<sup>28</sup> and thermal<sup>29</sup> conductivity, as well as their high tensile strength.<sup>30</sup> Just like graphene, carbon nanotubes are made out of hexagonally ordered carbon atoms with a delocalized  $\pi$ -system, but not in a flat two-dimensional system, rather rolled up into cylinders with diameters up to tens of nanometers.<sup>31</sup> Fullerenes are the third nanostructured allotrope of carbon. However, in their case, the nanostructure originates from six-, as well as five-membered rings, resulting in ball-like structures with high symmetries. Their first synthesis was accomplished accidentally by Kroto *et al.* in 1985,<sup>32</sup> who found a molecule out of exactly 60 carbon atoms and a diameter below 1 nm. Later, fullerenes were successfully isolated from natural sources as well.<sup>33</sup> Because of their ability to encapsulate small molecules in their cage-like structure, fullerenes find broad applications in biomedical applications, e.g., as carrier for contrast agents for different imaging methods.<sup>34</sup>

### 1.1.2. Organic Nanoparticles

Organic nanoparticles like micelles, liposomes, and lipid nanodiscs, as well as protein and polymer NPs use organic molecules as building blocks for their structures which usually self-assemble into nanostructured materials. Micelles and liposomes/vesicles are mostly spherical structures, that are formed from amphiphilic small molecules with hydrophilic heads and one or more hydrophobic tails. Micelles are formed above certain critical concentrations in water, at which the hydrophobic parts of the molecules will self-assemble into hydrophobic compartments that are shielded by the hydrophilic heads, which orientate themselves towards the surrounding water molecules. The hydrophobic compartments can be used to encapsulate non-polar substances like drugs. While the maximum sizes of micelles depend on the maximum expansion of the hydrophobic chains, and are usually sized below 10 nm,<sup>35</sup> the structures of liposomes can become relatively large in comparison. This is because the liposome building lipids self-assemble into lipid bilayers with varying dimensions and structures. Unilamellar liposomes or vesicles are spherical, hollow particles with a lipid bilayer shell and a water filled core. They can be classified into small unilamellar vesicles (SUV,

20 - 100 nm), large unilamellar vesicles (LUV, 100 - 1000 nm), and giant unilamellar vesicles (GUV, 1 - 200  $\mu\text{m}$ ).<sup>36</sup> While liposomes can also be used for drug delivery purposes, they are important scientific tools, mimicking the cell membranes of living tissues. By using artificial vesicles as model systems, interactions of e.g., drugs or proteins with natural cell membranes can be simulated and studied.<sup>37-40</sup> It is even possible to take small sheets of lipid bilayers and stabilize them with polymer belts to form lipid nanodiscs with sizes around 10 - 15 nm for the same purpose.<sup>41, 42</sup> Using biopolymers as platforms for the development of nanoparticles opens the door to efficient and safe materials that can be used for biomedical applications. Especially polysaccharides such as alginate or cellulose, and proteins like albumin or collagen can be altered to form nanoparticles.<sup>43</sup> Their sizes, usually between 100 and 200 nm, strongly depend on the preparation method and can also reach up to 1  $\mu\text{m}$ . Next to the possibility to physically adsorb or encapsulate drugs for their delivery,<sup>44</sup> protein and polysaccharide NPs naturally provide chemical groups including amines, carboxyls, or thiols that can be functionalized with drugs or tissue targeting moieties.<sup>45</sup> Their natural origin is the cause for their perfect suitability for biomedical applications, since that usually makes those NPs less toxic and increases their biocompatibility and biodegradability, in comparison to their synthetic counterparts.<sup>43</sup>

### 1.1.3. *Polymer Nanoparticles*

Ever since the 1950s, when living polymerizations were found to be the key to complex polymeric architectures such as block copolymers,<sup>46</sup> their structures and properties in bulk and solution were studied, eventually leading to their application as basis for nanoparticles. Just like the amphiphilic small molecules that build micelles and liposomes, polymers can be designed to have hydrophilic and hydrophobic regions. But because of their numerous possible architectures like blocks, grafts, stars, etc., the resulting nanostructures can become even more complex and versatile. Amphiphilic block copolymers with a hydrophilic and a hydrophobic block can form more than 20 different morphologies in water, e.g., micelles, rods, lamellae, vesicles, or even more complex structures such as hexagonally packed hollow hoops or large compound micelles, as depicted in **Figure 2**.<sup>47</sup>

In a typical procedure to form nanoparticle structures by self-assembling block copolymers by slowly exchanging a non-polar solvent with water, the first structures to be formed will be simple spherical micelles. Those structures consist of a spherical, hydrophobic core, surrounded by hydrophilic coronal chains. The radius of those polymer micelles cannot be broader than the longest hydrophobic chain in its planar all-trans conformation. Just like their small-molecule analoga, those micelles can be used to encapsulate hydrophobic drugs, (fluorescent) probes, or even larger entities like proteins.<sup>48-50</sup> To stabilize the micellar structure for example against solvent changes or influences from other external stimuli, they can be

crosslinked and, therefore, fixed in their conformation enabling a variety of other applications. The cores of polymer micelles can exemplarily be crosslinked by introducing cinnamoyl ester cores that can be photochemically dimerized, as first time reported by Liu *et al.*<sup>51</sup> Moreover, the hydrophilic shells of polymer micelles can be crosslinked, as reported by Wooley *et al.*<sup>52</sup> Similar to spherical micelles, micellar rods are formed from hydrophobic cores with hydrophilic coronas, however, here the core has a cylindrical shape instead of being spherical. While the radius of the cylindrical core is again limited by the maximum elongation of the longest polymer chain, its length can reach several micrometers.<sup>47</sup>

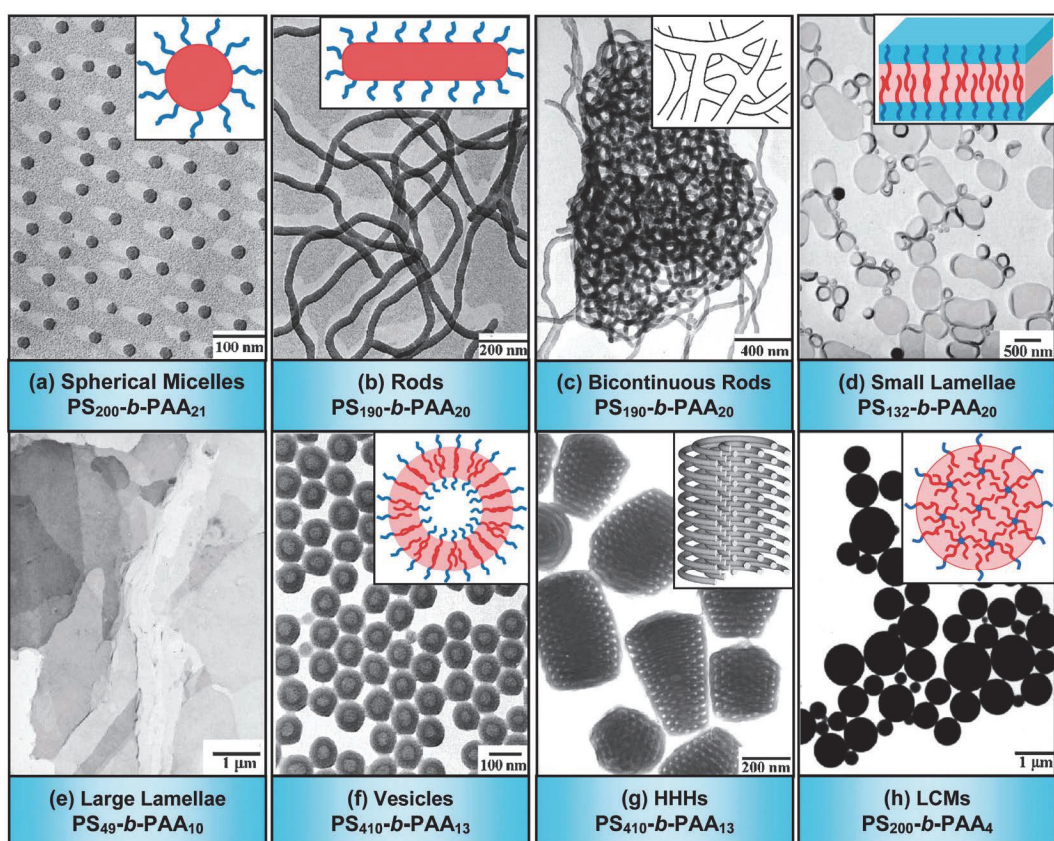


**Figure 2.** Schematic illustrations and TEM images of the morphologies from amphiphilic AB-type block copolymer systems. Red color represents the hydrophobic and blue the hydrophilic block. HHHs: hexagonally packed hollow hoops, LCMs: large compound micelles. Reprinted with permission from the Royal Society of Chemistry, copyright © 2012.<sup>47</sup>

Just as it is possible to form micellar structures from polymeric systems, block copolymers can be used to form liposome-like structures, often referred to as polyerosomes. Like liposomes, polyerosomes are hollow spheres with a hydrophilic interior being encapsulated by a hydrophobic wall, which in turn is covered by a hydrophilic corona. The tunable molecular weight and composition of the individual building blocks of polyerosomes enables various opportunities to tune their properties, for instance size, wall thickness, as well as permeability and mechanical properties.<sup>53-55</sup> Because polyerosomes provide both, a hydrophobic wall, as

well as a hydrophilic interior, they can be used to encapsulate hydrophilic and -phobic entities like drugs, nanoparticles, or proteins.<sup>56, 57</sup> This way they are excellent candidates for drug delivery applications.

Block copolymer nanoparticles can be prepared by various methods. The typically used method is the co-solvent method, in which the polymer is first dissolved in a solvent that dissolves all blocks. Then, a solvent that is a selective non-solvent for one block, usually water, is added until a critical water content results in the self-assembly of the now non-soluble blocks.<sup>47</sup> Among other additional methods like electroformation,<sup>58</sup> polymerization-induced self-assembly (PISA) is an emerging tool to overcome several challenges in the preparation of those nanoparticles, like high costs and low efficiencies.<sup>59</sup> Here, a water soluble precursor polymer is further polymerized with monomers whose respective polymer is hydrophobic. After reaching a critical chain length of this second block, the polymer chains will self-assemble into the respective nanostructures. Simply by arranging the polymerization conditions, the types of nanostructures can be tuned to result in micelles, polymerosomes, or others.<sup>60</sup> PISA also provides higher reproducibility, and enables preparations of nanoparticles at high concentrations up to 50 wt%, which makes it more applicable for commercial purposes.<sup>61</sup>

A completely different approach to polymeric nanoparticles was introduced 1978 by Vögtle *et al.*, who were the first to synthesize “cascade-like” structures, nowadays known as dendrimers.<sup>62</sup> Dendrimers are polymers with tree-like branched architectures and a spherical geometry as depicted in **Figure 3a**. Their unique structure results in monodisperse polymers/nanoparticles, with high symmetries, surface polyvalency, and internal cavernous structures.<sup>63, 64</sup> There are two main synthetical approaches to reach dendritic structures: the divergent, and the convergent path. In the divergent path, a multi-functional core creates the first generation of branches or “dendrons”, each providing two new functional units. Those functional units can react with the second generation of dendrons. In the convergent path, first the multifunctional dendrons are synthesized, which form the surface blocks. Those surface blocks are then step by step combined, forming the respective generations, that are eventually combined to the central core.<sup>65</sup> The divergent method has multiple disadvantages, such as incomplete growth of the branches, or various side reactions.<sup>64</sup> Those disadvantages can be overcome by using the convergent method, that ensures a better control over the structure, more efficient single reactions, and higher purities.<sup>66, 67</sup> However, the convergent method is not free of its own challenges, for instance difficult surface functionalization or problems of reaching high generation dendrimers.<sup>68</sup> Both synthetic methods are characterized by their exponential growth of molecular weight and number of functional groups on the surface as well as their roughly linear growth of diameter with every added generation of dendrons, exemplarily reaching 13.5 nm in the tenth generation.<sup>69</sup>

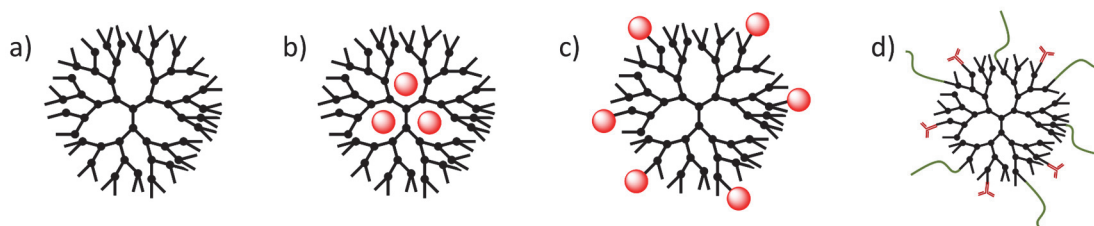


**Figure 3.** Schematic illustration of dendrimers: a) native, non-functionalized dendrimer, b) drug encapsulated in the cavities of a dendrimer, c) drug covalently bound to the surface functional groups, d) modification of the surface functional groups.

The applications of dendrimers arise from their unique structure which is compartmentalized into three substructures: the core at the center, which is the starting point of the dendron growth; the dendrons, which create hydrophobic empty cavities; and the terminal functional groups at the surface of the dendritic particles. This compartmentalized structure enables the application of dendrimers as carriers for catalytic sites, or templates for the synthesis of metal nanoparticles.<sup>70</sup> Especially the possibility to use the dendrimers as drug delivery systems has attracted the interest of many researchers. The hydrophobic and differently sized cavities that are surrounded by the hydrophilic surface, create a unimolecular micelle-like structure, in which hydrophobic drugs can be encapsulated, as depicted in **Figure 3b**.<sup>71</sup> Hydrophilic drugs can also be conjugated to dendrimers as drug vehicles. Here, the surface functional groups can be used to covalently bind those drugs, as depicted in **Figure 3c**, usually combined with a stimuli-responsive trigger, to eventually release the drug into the tissue of interest.<sup>72, 73</sup> The surface functional groups can further be used to conjugate other functionalities, as depicted in **Figure 3d**. Those functionalities can be either used to increase solubility and decrease toxicity, e.g., by adding poly(ethylene glycol), polysaccharides, or polypeptides;<sup>74, 75</sup> or they can be used to enhance tissue targeting. For this purpose, targeting moieties like antibodies, enzymes, or other targeting ligands can be covalently attached to the surface.<sup>63</sup>

One more possibility to achieve nanosized polymeric particles are nanogels, that are especially interesting for drug delivery purposes.<sup>76</sup> Nanogels are three-dimensional, physically or chemically crosslinked, hydrophilic or amphiphilic polymers in aqueous dispersions, and, therefore, they are swollen with water.<sup>77</sup> They are usually in the size range below 100 nm, but also larger systems with sizes of up to 1000 nm have been reported as nanogels.<sup>78</sup> The syntheses of nanogels are usually performed using reverse micelles, as depicted in **Figure 4**. Here, water soluble monomers are copolymerized with crosslinking monomers in inverse micelles that are dispersed in an organic solvent, in which the monomers are not soluble. Upon purification, removing the organic solvent and surfactants, water swollen nanogels are achieved.<sup>78</sup> Next to this main method, other techniques can be used as well, including

crosslinking of block copolymer micelles as mentioned above, precipitation polymerization,<sup>79</sup> or microtemplate lithography, which further is able to tune the shape of the nanogel.<sup>80</sup>

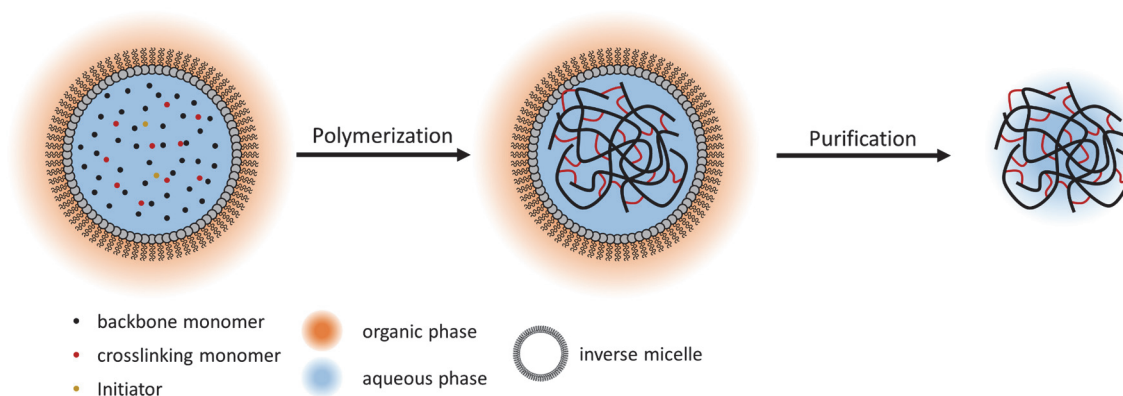


**Figure 4.** Synthesis of nanogels by copolymerizing water-soluble backbone monomers with crosslinking monomers in inverse micelles, resulting in a water swollen nanogel.

The applications of nanogels as drug delivery systems result from their tunable properties, allowing them to be adaptable to any type of drug, stimuli-responsibility, targeting method, or biocompatibility and -degradability. Already in the synthetical process, important aspects such as crosslinker density, backbone material, or the general synthetic procedure are crucial for properties like pore size, softness/deformability, or shape. The pore size is critical for the encapsulation of drugs as it determines which size of molecules can enter and/or leave the nanogel.<sup>81</sup> Moreover, the shape and viscoelastic behavior of nanogels are crucial for the intravascular circulation time, as spherical particles are easier effected by phagocytosis or mechanical retention.<sup>82-84</sup> Other aspects for the biomedical application, for example biocompatibility and -degradability, or stimuli-responsive behavior, are similarly applicable to other nanoparticle-based systems, and have already been discussed above, and will be further discussed in chapter 1.6..

## 1.2. Single-Chain Nanoparticles (SCNPs)

While every class of nanoparticles has its own specific and important field of application, polymer NPs are especially suitable for drug delivery.<sup>84-86</sup> Their potential to be widely modified chemically and (3D) structurally, their stimuli-responsive behavior,<sup>84</sup> and other properties like biocompatibility or the stealth effect<sup>87</sup> provides excellent suitability for biomedical applications. Among the numerous types of polymeric NPs that have been under development in the last decades, the relatively novel single-chain nanoparticles (SCNPs) have been proven to be of the most versatile and adaptable in view of catalysis<sup>88</sup> or drug delivery purposes.<sup>89</sup>

SCNPs are crosslinked, polymeric nanostructures that are formed from intramolecularly collapsed single polymer chains. Conceptually, they are a special, extremely small type of nanogels, but due to their unique architectures, synthesis methodologies, and properties, they create a completely new class of polymeric NPs. SCNPs are synthesized by single-chain collapse at very high dilutions to exclusively achieve intramolecular assembly of the individual chains, completely avoiding intermolecular interactions.<sup>90</sup> Subsequent internal crosslinking interactions, e.g., H-bonds, click-reactions, or metal complexation, can preserve the collapsed chains in these conformations.<sup>91</sup>

The shape and, therefore, also the functionality of SCNPs is mostly influenced by the architecture of the individual polymer chains (see **Figure 5**), the solvent that is used during the collapse reaction, and the solvophilicities of the individual monomer units. Using random copolymers without specific solvophilicities or interactions mostly results in random, sparse structures, while using amphiphilic polymers can yield compartmentalized SCNPs.<sup>92</sup> Adjusting a random copolymer in a way that most parts are solvophilic and the crosslinking parts are solvophobic, enables the synthesis of globular shaped and core-shell structures SCNPs (see **Figure 5a**).<sup>93-96</sup>

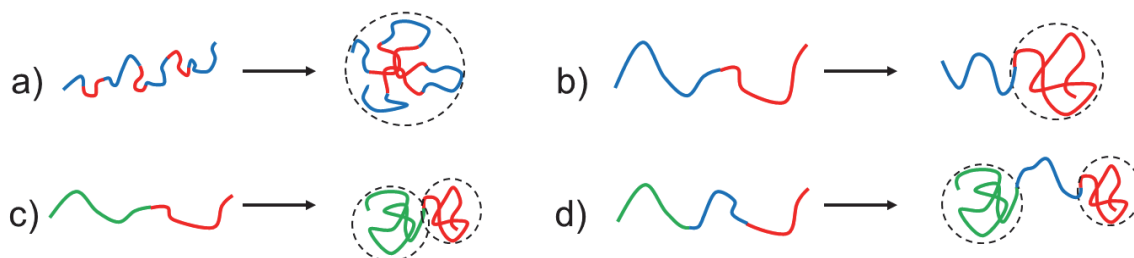


**Figure 5.** Examples of possible structures achieved by different single-chain nanoparticle synthesis approaches. a) A random copolymer collapsing into a globular or random shaped SCNP, block copolymers collapsing into b) a tadpole-shaped SCNP, c) a Janus SCNP, and d) a dumbbell-shaped SCNP. Blue: non-crosslinking polymer segments. Red and green: crosslinking polymer segments.

Using block copolymers enables the synthesis of SCNPs with multiple coiled structures. As depicted in **Figure 5b**, collapsing a block copolymer in which one block is non-reactive and solvophilic, and the other block is solvophobic and reactive, tadpole-shaped SCNPs can be synthesized<sup>97</sup> resembling the structure of surfactants. Because of their specific structure, these types of SCNPs are able to aggregate into micelle- or vesicle-like superparticles.<sup>98-100</sup> Block copolymers with two reactive blocks, are able to collapse into two-sided “Janus” SCNPs (see **Figure 5c**). While it is mostly effective to use differently crosslinking sites and solvophilicities for the individual blocks,<sup>101, 102</sup> recent studies show that also blocks with the same crosslinking functionality will collapse into Janus SCNPs because of the higher reactivity of spatial closer sites.<sup>103</sup> Adding a non-reactive spacer block in between the crosslinkable blocks also enables the formation of dumbbell-shaped SCNPs as depicted in **Figure 5d**.<sup>104-106</sup>

Though they do not represent actual nanoparticles, symbol shaped single-chain structures can be synthesized using the same strategies. The difference is, that single reactive groups are placed at specific spots along the polymer chain. This enables specific shapes that the polymer chain can be folded into, as depicted in **Figure 6**.<sup>107</sup> The loops that define the shape of those symbols resemble the loops that are – way more often – also present in SCNPs and define their shape and nanostructure.

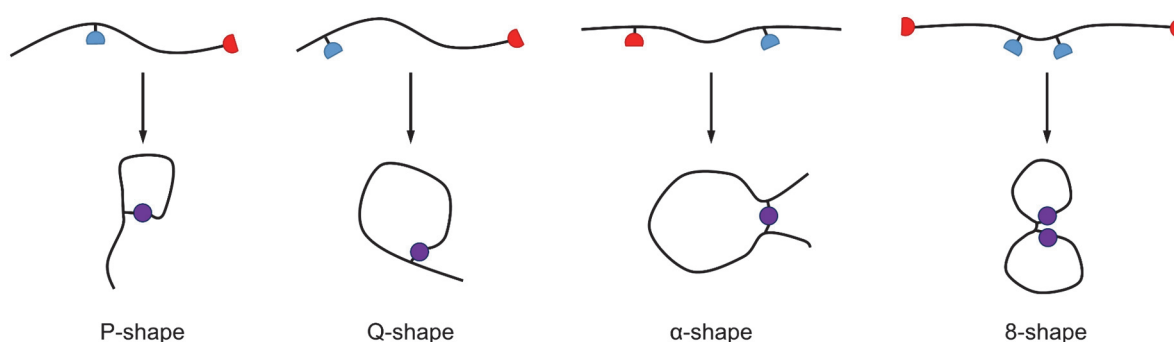


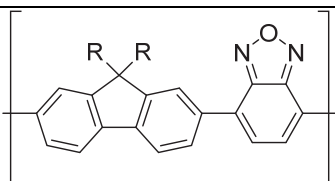
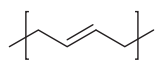
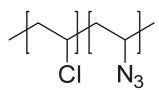
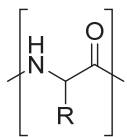
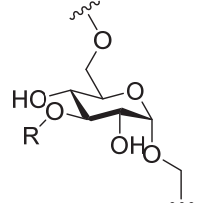
**Figure 6.** Symbol shaped single-chain structures synthesized by means of specifically placed reactive groups.

### 1.3. Synthetic Approaches and Collapse Methodologies to SCNPs

For the design of a polymer that is supposed to be formed into a SCNP, a well-made choice of backbone material is crucial, since it will be mainly responsible for the properties of the final SCNP, e.g., mechanical properties, solubility, biocompatibility, or stimuli-responsive behavior. A selection of possible backbone materials is shown in **Table 1**. The vast majority of reported SCNPs is based on (meth)acrylates, (meth)acrylamides, or styrene derivatives. Their ability to be functionalized with theoretically any suitable functionality at their side chains enables them to be widely applicable. Next to their functional versatility, they are also readily polymerized by numerous polymerization techniques, that can be chosen according to reactivities of functional groups, or the field of purpose. Mostly used are free<sup>108</sup> and controlled radical polymerizations (RP), such as atom transfer RP (ATRP),<sup>98, 109-113</sup> nitroxide mediated RP (NMP),<sup>114-116</sup> reversible-addition-fragmentation chain-transfer polymerization (RAFT),<sup>117-119</sup> Ru-catalyzed living RP (LRP),<sup>120</sup> and further other polymerization techniques, for instance anionic and cationic polymerization,<sup>97, 121</sup> or group transfer polymerization (GTP).<sup>122</sup>

**Table 1.** Examples of polymer backbones/materials that can be functionalized to enable subsequent single-chain collapses and crosslinks.

Backbone Material	Chemical Structure	Synthetic Procedure
Poly(meth)acrylates and acrylamides		free RP, ATRP, RAFT, Ru-catalyzed LRP, GTP
Polystyrene		ATRP, NMP, RAFT, anionic polymerization
Polycarbonate <sup>123</sup>		ROP of cyclic carbonates
Polyethers <sup>124-126</sup>		(Zwitterionic) ROP
Polynorbornenes <sup>95, 102, 127-132</sup>		ROMP
Polyesters <sup>142</sup>		Polycondensation

Backbone Material	Chemical Structure	Synthetic Procedure
Conjugated backbones <sup>133</sup>		Pd-catalyzed Suzuki polymerization
Polybutadiene <sup>134</sup>		Commercial polymer, variation of <i>cis</i> -content <i>via</i> irradiation
Modified polyvinyl chloride <sup>135</sup>		Commercial, recycled polymer, modified by S <sub>N</sub> 2 reaction
Polypeptides and proteins <sup>139-141, 143</sup>		Bacterial biosynthesis, ROP of NCAs, denaturation of natural proteins
Carbohydrates <sup>136-138</sup>		Bacterial biosynthesis, commercial product

In addition to those mainly used materials, other mostly application-specialized materials can be used. Ring opening polymerization (ROP) techniques are applicable to synthesize backbones from polycarbonates,<sup>123</sup> polyethers,<sup>124-126</sup> or polynorbornenes, using ring opening metathesis polymerization (ROMP).<sup>95, 102, 127-132</sup> It is even possible to synthesize conjugated aromatic backbones as basis for SCNPs by Pd-catalyzed Suzuki polymerizations.<sup>133</sup> Commercial polymers which are originally used in more technical applications can be modified to serve as basis for SCNPs. For instance, it is possible to irradiate polybutadiene to achieve a certain amount of *cis* double bonds.<sup>134</sup> Those double bonds can later on serve as ligands for Rh atoms, and therefore crosslink the polymer into a SCNPs. In a very recent approach, Pomposo *et al.* recycled polyvinyl chloride (PVC) to act as backbone for SCNPs.<sup>135</sup> They functionalized PVC *via* S<sub>N</sub>2 reactions with NaN<sub>3</sub>, so that the azide groups can be reacted with the Sondheimer diyne in a strain-promoted azide-alkyne cycloaddition (SPAAC).

Bioinspired SCNPs are especially interesting for biomedical applications because of their natural biocompatibility. Hence, it was tried to use biological materials such as polypeptides and carbohydrates as backbone materials. Both materials can be produced by biosynthesis,<sup>136-138</sup> and are usually further altered from their natural composition and structure to be applicable for SCNPs.<sup>139, 140</sup> Polypeptides can also be produced synthetically, by performing ROPs of *N*-carboxyanhydrides (NCAs).<sup>141</sup>

The most important aspect during the collapse and crosslink procedure of SCNPs is to prevent intermolecular interactions between individual polymer chains, since only intramolecular interactions will result in single-chain nanoparticles. To achieve that, different methods have been developed (see **Figure 7**) that all have in common that they need high dilutions in the range of  $< 1$  mg/mL for polymers, or  $10^{-6}$  M for reactive groups along the polymer chains.

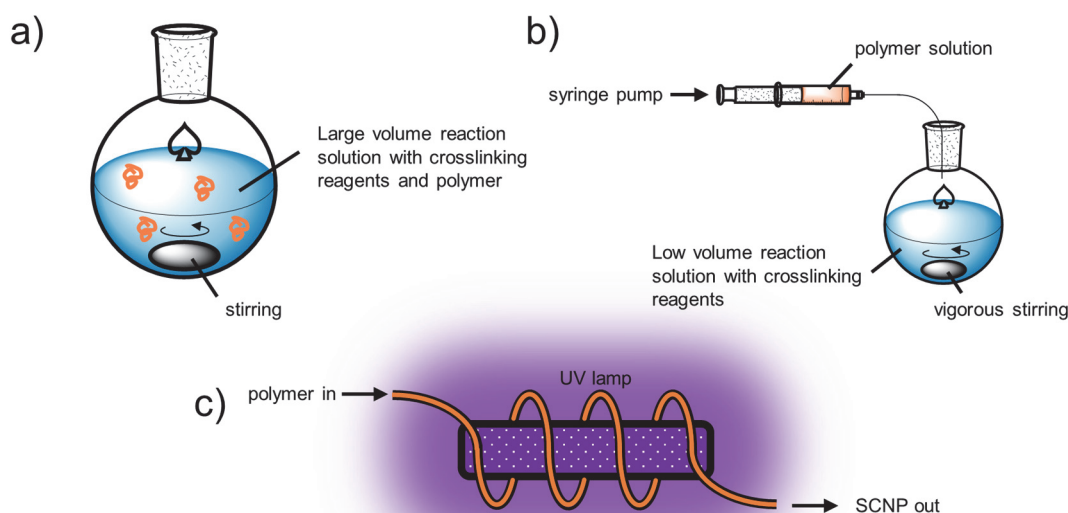
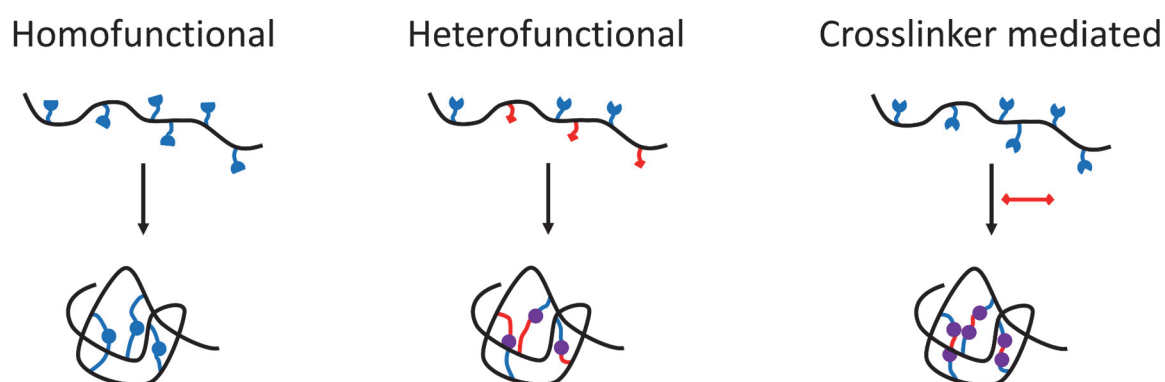


**Figure 7.** Schematic illustration of experimental procedures for the synthesis of SCNPs using a) a large volume reaction solution with a low concentration of polymer, b) the continuous-addition protocol, and c) a photochemical flow reactor.

Performing a SCNP synthesis by simply using high dilutions as depicted in **Figure 7a** either requires a very high solvent volume or a very low quantity of polymer. Because of that, this synthetic path is mostly used for SCNP systems that rely on non-covalent interactions like H-bonds or solvophobic interactions, that cannot be achieved by using the other techniques. For SCNP syntheses, wherein a covalent reaction needs to take place, the continuous-addition protocol, developed by Harth *et al.*,<sup>89, 114, 145, 146</sup> has been found to be the most efficient. Here, a concentrated polymer solution is slowly dropped into a solution with the reactants under vigorous stirring, as depicted in **Figure 7b**. The polymer solution droplet that is entering the reaction solution is reacted under highly diluted conditions, resulting in intramolecular crosslinks only. Since all reactive groups along the polymer chains of this droplet are completely consumed, the resulting SCNPs are now inert for the next droplets. Hence, the reactive groups of the next droplet will again react only intramolecularly under highly diluted conditions. Therefore, this synthetic method is much more convenient, allows SCNP syntheses under much higher final concentrations, and enables yields in the gram-scale.<sup>147</sup>

Another way to continuously synthesize larger quantities of SCNPs is the use of flow reactors. Since in such case the reaction is taking place along a tube through which a reaction solution is constantly flowing, those reactors allow larger scale syntheses. For example, a polymer that contains photodimerizing groups can be pushed through a tube that is wrapped around an ultraviolet (UV) lamp as depicted in **Figure 7c**. This way, SCNPs can be synthesized with shorter irradiation times and higher conversions than in a comparable reaction in a batch reactor, making this method more efficient.<sup>148</sup>

The approaches for the intramolecular crosslinking reactions can be categorized as homofunctional, where two equal pendent functionalities form a crosslink; heterofunctional, where two complementary functionalities are connected; or crosslinker mediated, where an external, bivalently functionalized molecule connects two functionalities of the polymer chain, as depicted in **Figure 8**.<sup>91, 145</sup> The crosslinks can be achieved either by enabling non-covalent interactions or by performing covalent reactions, as described in detail in the following.

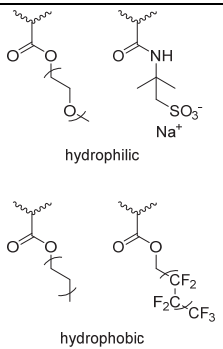
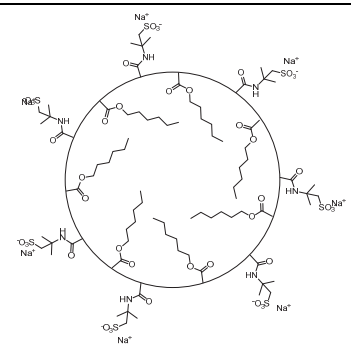
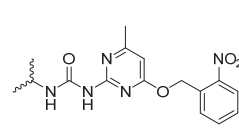
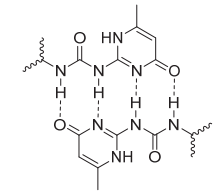
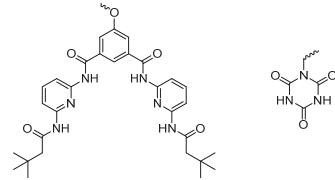
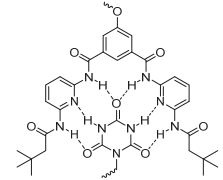
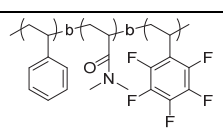
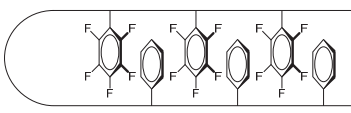
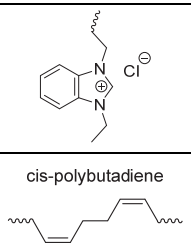
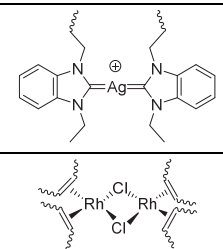


**Figure 8.** Crosslinking reaction categories: homofunctional, heterofunctional, crosslinker mediated crosslinking reaction.

### 1.3.1. Non-Covalent and Supramolecular Collapse Methodologies

It is possible to form stable SCNPs without any covalent crosslinking reaction. Examples of those non-covalent interactions are given in **Table 2**. Strong non-covalent or supramolecular interactions, including the formation of metal complexes, are necessary for a successful formation of SCNPs. Non-covalently crosslinked SCNPs are conceptually dynamic structures that can be formed and opened again, e.g., by adjusting solvent quality or by adding H-bond breaking substances. The simplest method for the formation of SCNPs is to use pure solvophilic-solvophobic, usually hydrophilic-hydrophobic, interactions by creating unimolecular micelles, that will be further described in chapter 1.4.2..

**Table 2.** Examples of non-covalent and supramolecular interactions that can be used as crosslinking methods for the formation of single-chain nanoparticles.

Crosslinking Method	Functional Groups	Crosslinked Groups
solvophilic-solvophobic interactions <sup>120, 149-156</sup>	 <p>hydrophilic</p> <p>hydrophobic</p>	
hydrogen bonds <sup>109, 127, 157-162</sup>		
chiral hydrogen bonds <sup>95, 111, 163-170</sup>		
$\pi$ -stacking <sup>128, 171</sup>		
metal complexation <sup>94, 131, 134, 172-179</sup>	 <p>cis-polybutadiene</p>	

Besides the relatively weak, purely solvophobic interactions of unimolecular micelles, supramolecular interactions such as hydrogen bonds are effective ways to form SCNPs, using ureidopyrimidinone<sup>109, 127, 157, 158, 160-162</sup> or Hamilton wedges with cyanuric acid derivatives.<sup>159</sup> Other hydrogen bonding moieties for an effective SCNPF formation are derivatives of the chiral benzene-1,3,5-tricarboxamide. These moieties do not only provide the possibility to create hydrogen bonds, but furthermore add a helical structure inside the SCNPF core, similar to

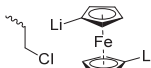
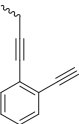
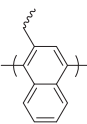
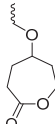
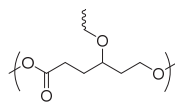
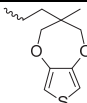
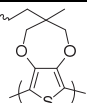
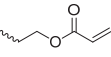
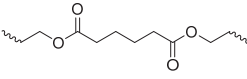
$\alpha$ -helices in proteins.<sup>95, 111, 163-170</sup>  $\beta$ -Hairpin-like single-chain structures can be formed using supramolecular quadrupole  $\pi$ -stacking interactions between electron-rich benzene moieties and electron deficient pentafluorobenzene moieties in an ABC-block copolymer with a polystyrene, and a poly(pentafluorostyrene) block, separated by a spacer block.<sup>171</sup>

The formation of metal complexes can be used for the crosslinking of a single polymer chain with the ligands covalently bound to the polymer chain, thereby utilizing the complexation of a metal ion.<sup>94, 131, 134, 172-178</sup> This interaction can also be used to incorporate a metal catalyst inside the SCNP to synthesize an enzyme analogue.<sup>130, 131, 176, 177, 180, 181</sup>

### 1.3.2. Covalent Collapse Methodologies

Using covalent crosslinking reactions enables the synthesis of SCNPs that cannot change their internal nanostructure, even if external properties like solvent quality are changed. Basically any reaction that is able to form covalent bonds can be used as a crosslinking reaction for SCNPs as shown in **Table 3**, such as simple organic reactions like nucleophilic substitutions,<sup>116</sup> or ester and amide formations.<sup>106, 137, 140, 182-185</sup> Also polymerizable groups such as vinyl groups<sup>121, 186</sup> or cyclic esters<sup>187, 188</sup> can be used for efficient crosslinking reactions.

**Table 3.** Examples of covalent interactions that can be used as crosslinking methods for the formation of single-chain nanoparticles.

Crosslinking Method	Functional Groups	Crosslinked Groups
nucleophilic substitution <sup>116</sup>		
azide decomposition <sup>126, 198</sup>		
radical polymerization <sup>121, 186</sup>		
Bergmann cyclization <sup>199</sup>		
ring opening polymerization <sup>187, 188</sup>		
oxidative polymerization <sup>112</sup>		
atom transfer radical coupling <sup>147</sup>		

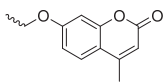
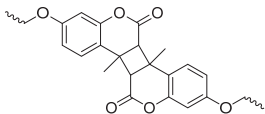
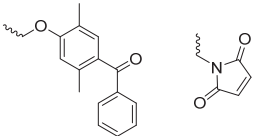
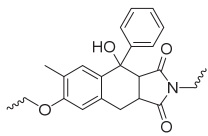
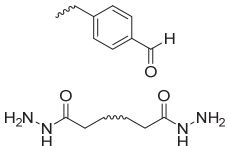
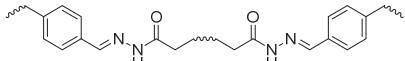
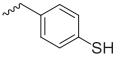
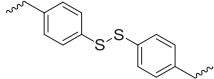
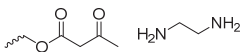
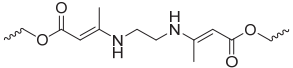
Crosslinking Method	Functional Groups	Crosslinked Groups
olefin metathesis <sup>97, 122, 123</sup>		
isocyanate crosslinking <sup>160</sup>		
amine quaternization <sup>100</sup>		
ester formation <sup>182</sup>		
amide formation <sup>106, 137, 140, 183-185</sup>		
Hantzsch ester formation <sup>200</sup>		
(thiol)-Michael addition <sup>136, 201, 202</sup>		
Glaser coupling <sup>106, 203</sup>		
thiol-yne click reaction <sup>124</sup>		
strain-promoted azide-alkyne cycloaddition <sup>135</sup>		
copper catalyzed azide-alkyne click reaction <sup>96, 107, 189-195</sup>		

Because of their high efficiency, click reactions, especially the copper catalyzed azide-alkyne click reaction (CuAAC),<sup>96, 107, 189-195</sup> that is also used in this thesis, became one of the most important methods for covalently crosslinking SCNPs.<sup>146</sup> Following the definitions of Meldal and Sharpless, who together with Bertozzi won the Nobel Prize 2022 for their developments in click chemistry, click reactions are reactions that have large free reaction enthalpies (> 50 kJ/mol), result in high yields, are selective, clean, orthogonal, and should be insensitive

to moisture and oxygen, just to name a few properties.<sup>196, 197</sup> Those properties make click reactions ideal reactions for the synthesis of SCNPs, since the crosslinking reactions should be effective, complete, fast, and highly selective. Only this way, solely intramolecular crosslinks can be accomplished, and defined internal nanostructures can be achieved, that are fundamental for the various applications of SCNPs.

The wide variety of possible covalent reactions also allows the incorporation of functionalities like responsiveness to external stimuli to change the structure of the SCNPs. This further enables the synthesis of covalently crosslinked SCNPs that can be dynamically opened and closed. As shown in **Table 4**, especially photodimerizations<sup>98, 101, 108, 132, 142, 148, 204-211</sup> and formations of disulfide bridges<sup>129, 212</sup> are methods that achieve responsiveness to light irradiation or pH-changes, respectively. Those dynamic covalent SCNPs are especially interesting for biomedical applications since their responsiveness can increase their drug delivery efficiency and biodegradability.<sup>186</sup>

**Table 4.** Examples of dynamic covalent interactions that can be used as crosslinking methods for the formation of single-chain nanoparticles.

Crosslinking Method	Functional Groups	Crosslinked Groups
photodimerizations <sup>98, 101, 108, 132, 142, 148, 204-211</sup>		
photoinduced Diels-Alder reaction <sup>213, 214</sup>		
acyl hydrazone formation <sup>117, 215, 216</sup>		
disulfide bridges <sup>129, 212</sup>		
enamine bonds <sup>217</sup>		

## 1.4. Internal Substructures of SCNPs

Conceptually, SCNPs are synthetical analogues to natural proteins. SCNPs can fold into compartmentalized structures during the single-chain collapse according to their solvophilicity, even with the possibility to form secondary structures.<sup>218</sup> Just like in their natural counterparts, the internal and external substructures of SCNPs provide the opportunity to incorporate functionalities such as catalytic sites,<sup>130, 156, 219</sup> pockets for the transport of drugs,<sup>137, 152, 153, 162, 202, 220</sup> or sites for the covalent encapsulation of contrast agents for biomedical imaging.<sup>136, 221</sup>

### 1.4.1. Thermodynamic Background

The substructures that arise during single-chain collapse are mainly influenced by the thermodynamic behavior of the individual polymer chains in solution. For a successful dissolution of a polymer in a solvent, the Gibbs energy of mixing  $G_{mix}$  must be reduced. The Gibbs-Helmholtz-equation for the mixing of a polymer and a solvent is

$$\Delta G_{mix} = \Delta H_{mix} - T\Delta S_{mix} \quad (1)$$

with the enthalpy of mixing  $\Delta H_{mix}$ , the entropy of mixing  $\Delta S_{mix}$ , and the temperature  $T$ . For a better description of the changes of entropy during mixing, Flory and Huggins developed a lattice model, in which every solvent molecule and every polymer segment or monomer unit fills one lattice point (see **Figure 9**).<sup>222, 223</sup>

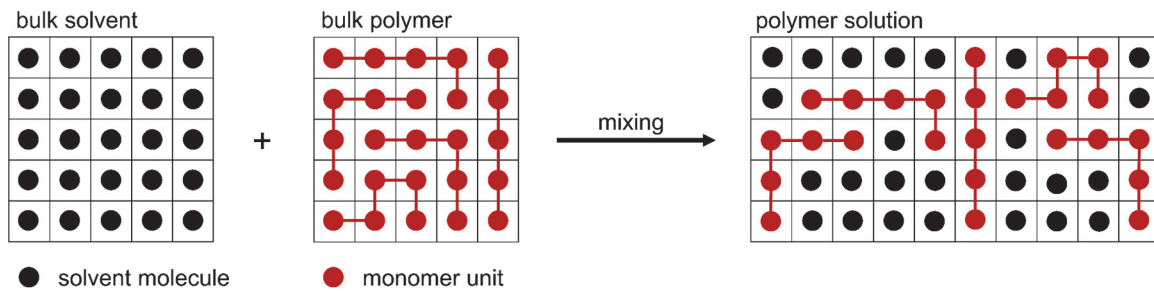


**Figure 9.** Lattice model for the solution of a polymer (red) in a solvent (black) according to the Flory-Huggins theory.

The Flory-Huggins theory, hence, considers all possible interactions between: (I) a polymer segment and the solvent; (II) a polymer segment of one chain with a polymer segment of another chain; and (III) two polymer segments of the same chain. Taking into account these interactions and their influence on  $\Delta H_{mix}$  and  $\Delta S_{mix}$ , equation (1) can be adapted to

$$\Delta G_{mix} = RT[n_s \ln \phi_s + n_p \ln \phi_p + n_s \phi_p \chi] \quad (2)$$

with the universal gas constant  $R$ , the number of moles of solvent and polymer  $n_s$  and  $n_p$ , the volume fraction of solvent and polymer  $\phi_s$  and  $\phi_p$ , and the mixing parameter  $\chi$ , which includes the entropic and enthalpic changes of the different types of interactions of polymer and solvent.

This relatively simple but helpful mathematical description quickly comes to its limitations, for example, when phase separating block copolymers are to be described. Here, the Hansen solubility parameters<sup>224</sup> can be included into the theory to achieve an optimized description of the behavior of the individual blocks and their segregation as a bulk system. A description of the segregation of those copolymers on the nanoscale still remains a major challenge. Russel, Nealey, and others have tried to find a modification of the Flory-Huggins theory to describe phase segregating block copolymers in confined systems, e.g., thin films between two surfaces whose distances are below the size of a segregated phase. They found that the phases of those systems showed major differences in their morphology in dependence on film thickness resulting, for example, in differently oriented lamellar or hexagonal morphologies.<sup>225-229</sup>

Strictly taken, the unmodified Flory-Huggins theory can only be used to look at the miscibility behavior of complete bulk systems, and not of single chains and their behavior in a solvent. Nevertheless, it still helps to understand the behavior of single random copolymer chains in solution and, therefore, the formation of substructures during single-chain collapse reactions. At very low concentrations, as they are used during SCNP synthesis, interactions of multiple polymer chains can be neglected. When an amphiphilic polymer is dissolved in a solvent which is good for all polymer segments, it should behave like an ideal chain with balanced polymer-polymer and polymer-solvent interactions. Here, a single-chain collapse reaction would result in a non-compartmentalized, sparse SCNP.<sup>92, 93</sup> Reducing the solvent quality for some segments of the polymer would reduce polymer-solvent interactions and increase polymer-polymer interactions for those segments, while the remaining segments would still be balanced between polymer-solvent and polymer-polymer interactions. Hence, the polymer-polymer interactions would cause the formation of compartmentalized substructures upon crosslinking of the single chain.<sup>230</sup>

#### 1.4.2. *Compartmentalized SCSs*

As mentioned above, the architecture and philicities of the precursor polymer as well as the polarity of the collapse solvent have a major influence on the final internal structure of the SCNP. The possibility to achieve controlled compartmentalized substructures of e.g., core-shell structured SCSs is one of the main features that SCSs provide for their applications in catalysis or drug delivery systems.<sup>231</sup>

Unimolecular micelles are micellar structures that are produced by folding amphiphilic single polymer chains without crosslinking interactions. Although they are not crosslinked, they can

arguably be counted as the simplest way to achieve compartmentalized SCNPs. They usually form core-shell-like structures in water with hydrophilic sidechains in the shell and hydrophobic sidechains in the core, as depicted in **Figure 10a**. The hydrophilicities in the shell can be achieved e.g., by using poly ethylene glycol (PEG)<sup>120, 152-154</sup> or ionic sidechains.<sup>149-151</sup> The core-building, hydrophobic parts can be introduced by using either aliphatic<sup>120, 149-151, 154</sup> or fluorinated sidechains.<sup>152, 153</sup> Unimolecular micelles can for instance be used as antimicrobial compounds<sup>154</sup> and are especially interesting for drug delivery systems. For these applications, drug cargos can be covalently bound and carried inside its hydrophobic core,<sup>149-151</sup> or encapsulated inside the hydrophobic core as controlled drug-release systems, similar to classical micellar structures.<sup>153</sup>

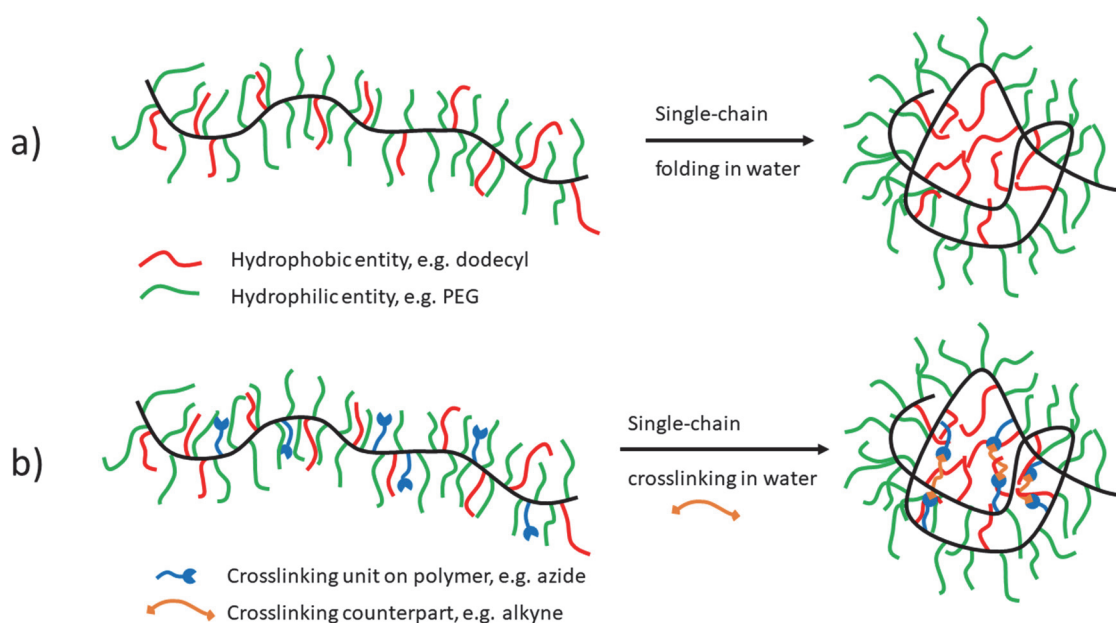


**Figure 10.** a) An amphiphilic random copolymer folding into a unimolecular micelle in water. b) An amphiphilic random copolymer with crosslinking units collapsing and crosslinking into a single-chain nanoparticle.

The synthesis of crosslinked, compartmentalized SCNPs is based on the same mechanism as the formation of unimolecular micelles but with an additional crosslinking reaction to retain the compartmentalized structure even after concentration or solvent changes. As depicted in **Figure 10b**, the philicities of the individual segments can, again, lead to the formation of core-shell structured SCNPs. Ideally, the crosslinking moieties are also solvophobic. This way, the crosslinking reactions will only take place in the core, resulting in stronger compartmentalized structures.<sup>95, 132, 232</sup> The crosslinking reactions can be either the formation of covalent bonds or strong non-covalent interactions, which are discussed in chapter 1.3..

As mentioned above, the solvents in which the collapse and crosslinking reactions take place have a major influence on the internal compartmentalized structures of the SCNPs. It is important to keep control over the solvent quality to achieve perfect control over the desired

structures. A solvent or solvent mixture that shows good quality for all segments of the precursor polymer, including the crosslinking units, will result in non-controlled, sparse SCNPs,<sup>95, 132</sup> while a solvent with a poor quality for all segments can result in multi-chain aggregation instead of the collapse of single chains.<sup>132</sup> Exemplary, Simon *et al.* showed that the single-chain collapse of a comb-copolymer with poly isobutylene (PIB) sidechains and anthracene crosslinking units resulted in differently structured particles, dependent on the solvent quality.<sup>132</sup> The photodimerization of the anthracene units in pure tetrahydrofuran (THF), a good solvent for both monomer units, resulted in low conversions and sparse SCNPs, while the same reaction in pure hexane, which is only a good solvent for the PIB units, resulted in multi-chain particles. Only a mixture of both solvents was able to yield high conversions and well-defined core-shell structured SCNPs.

Temperature control over the formation of compartmentalized structures can be achieved by using thermoresponsive segments in the precursor polymer chain, e.g., poly (oligo ethylene glycol) methacrylates (PEGMA) or poly *N*-isopropyl acrylamide (PNIPAM). These polymers show lower critical solution temperature (LCST) behavior in water, which means they become insoluble in water above the cloud point temperature  $T_{cp}$ . At temperatures well below  $T_{cp}$  of those segments, the SCNP synthesis will result in sparse non-compartmentalized SCNPs. At temperatures well above  $T_{cp}$ , core-shell structured SCNPs with a dense core will be obtained as depicted in **Figure 11**. Performing the SCNP synthesis at medium temperatures, the core-shell structure will still be obtained, but in a less dense state. Here, swelling of the core with water is possible, which leads to a certain thermoresponsivity of the core itself, which is bearing the thermoresponsive units of the precursor polymer.<sup>233</sup>

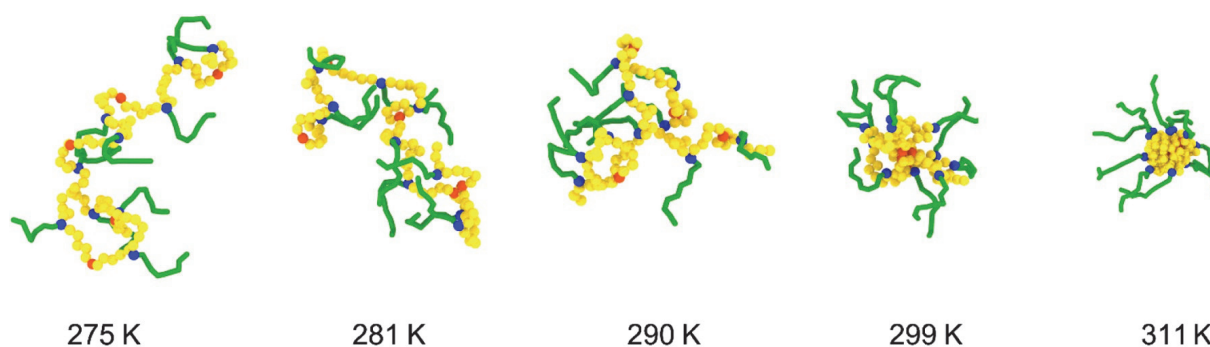


**Figure 11.** Simulated chain conformations of a thermoresponsive precursor polymer chain that will preserve these structures after SCNP crosslinking reactions at the indicated temperatures. Reprinted with permission from the Chinese Chemical Society, copyright © 2020 (open access).<sup>233</sup>

While the use of amphiphilic precursor polymers is the main approach to compartmentalized SCNPs, there are also other ways of generating segregated regions inside SCNPs. For example, liquid crystals create phases that are made from small molecules which behave like liquids but still form crystal-like ordered systems. Introducing such small molecules like

stilbenes or azobenzenes as side chains to the precursor polymer chain can result in a compartmentalized SCNP upon crosslinking. Inside the relatively unordered SCNPs, those groups will still be able to self-assemble and form ordered structures which segregate from the polymer backbone.<sup>208, 234</sup> Another widely discussed supramolecular motif to generate an internal compartment inside a SCNP is the benzene-1,3,5-tricarboxamide (BTA) group introduced by Meijer and Palmans. BTA molecules form supramolecular assemblies that build helical stacks with threefold intermolecular hydrogen bonds, resembling  $\alpha$ -helices of proteins. When BTA molecules are part of a precursor polymer that is dissolved in water, those groups will self-assemble inside the SCNP's interior, intramolecularly crosslink the polymer chain, segregate from other parts of the polymer, and mainly influence the overall shape of the resulting SCNP.<sup>95, 111, 163, 165, 168, 235</sup> This helical stacked structure can be used as platform for catalytic sites, enabling enzyme-like internal structures which drastically increase catalytic activities.<sup>164, 166, 167, 218, 236-240</sup> To gain external confinements like in Janus-shaped SCNPs, block copolymers can be used instead of random copolymers, as described in chapter 1.2.. Even if the same reactive groups are present in both blocks, the spatially closer groups in the respective blocks will rather react with themselves instead of those of the other block, independent from solvent effects, resulting in Janus-shaped SCNPs.<sup>103</sup>

## 1.5. Characterization of SCNPs

The external and internal characterization of SCNPs is challenging due to their extremely small sizes below 20 nm. Because of that, many different methodologies have been tried to use to describe their size, shape, and internal structure, including chromatography, microscopy, scattering techniques, and different types of spectroscopy.

### 1.5.1. Size and Shape Analysis

Collapsing linear precursor polymer chains into SCNPs is usually followed by size reductions that can be measured as hydrodynamic diameters  $d_h$ .<sup>145, 241</sup> While a non-crosslinked precursor chain is able to be straightened to its full size, the crosslinked SCNP is unable to change its conformation and is trapped in its collapsed position. Hence, its hydrodynamic radius is smaller than that of the precursor chain, as depicted in **Figure 12**. This change in  $d_h$  can be used as proof of a successful single-chain collapse with solely intramolecular crosslinks and the absence of intermolecular interactions, that would lead to increased values of  $d_h$ .

The most convenient and most widely used method for the proof of a successful single-chain collapse is gel permeation chromatography (GPC).<sup>241</sup> In said method, the separation is based on differences in the hydrodynamic diameter of the analytes, first eluting large species of a polymer mixture, followed by small species. GPC is usually used to determine molecular weights and their dispersity using external calibration standards, as different molecular weights will result in different  $d_h$ . Since differences of molecular weight before and after single-chain collapse and crosslink can usually be neglected, differences in the GPC curve can be addressed to changes of  $d_h$  with the SCNPs exhibiting higher retention times because of their smaller size compared to the precursor.

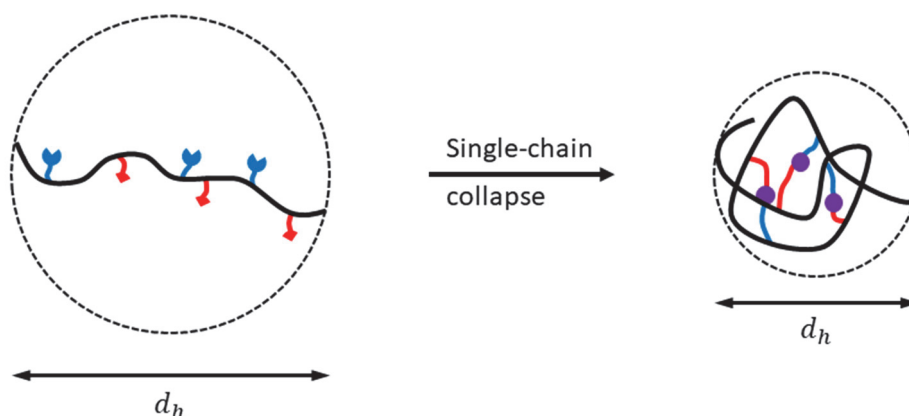


**Figure 12.** Schematic illustration of the reduction of the hydrodynamic diameter  $d_h$  upon single-chain collapse.

Two additional methods for the analysis of  $d_h$  of precursor polymer and SCNP are dynamic light scattering (DLS) and diffusion ordered nuclear magnetic resonance spectroscopy (DOSY-NMR). Both methods are based on the determination of the diffusion coefficient  $D$ , which can be calculated into the hydrodynamic diameter using the Stokes-Einstein equation

$$d_h = \frac{k_B \cdot T}{3 \cdot \pi \cdot \eta \cdot D} \quad (3)$$

with the Boltzmann constant  $k_B$ , temperature  $T$ , and the viscosity of the solvent  $\eta$ . Similar to the analysis *via* GPC, the SCNPs will show higher diffusion coefficients, and therefore smaller hydrodynamic diameter compared to the precursor polymers.

Although methods like GPC, DLS, and DOSY-NMR can give good information about the hydrodynamic diameter of a SCNP and its relative change after single-chain collapse, these methods usually lack information about the SCNP's shape, since  $d_h$  is defined as the diameter of a perfect hard sphere with the same diffusion properties as the SCNP, ignoring its actual shape. To get more detailed information about the shape, scattering techniques such as small angle X-ray or neutron scattering (SAXS, SANS), and static light scattering (SLS) are required. These methods do not only yield information about the dimensions of a SCNP in form of the radius of gyration  $r_G$ , but additionally about its shape, e.g., if the SCNP is sparse, globular, stick-like, or compartmentalized. To get these information, the shape factor can be calculated from the hydrodynamic radius and the radius of gyration.<sup>92, 95, 102, 103, 168, 232, 235, 242, 243</sup>

Besides size and shape characterization in solution *via* chromatographic and scattering techniques, microscopy methods like atomic force microscopy (AFM) and transmission electron microscopy (TEM) have been used to visualize and analyze SCNPs in the dry state. AFM is a universal method that is theoretically able to visualize any type of SCNP. Nevertheless, its exact interpretation and comparison to other techniques like DLS or DOSY-NMR can be challenging, since the SCNPs tend to lose their shape in the dry state. This, in addition to resolution issues due to the SCNP's size being below the width of the AFM cantilever tip, can lead to unreliable results.<sup>109, 127, 201</sup> TEM does not have these issues since generally its resolution is higher than that of AFM, resulting in more accurate results for SCNPs when compared to other techniques.<sup>100</sup> However, TEM is not universally applicable for all SCNP systems, which usually lack heavy atoms that are necessary for achieving good contrasts.

While the above are numerous techniques to measure the size of SCNPs and their precursor polymers, the exact values should still be interpreted with care, and should be seen as relative values.<sup>244</sup> As mentioned above, measuring the sizes of SCNPs can yield quite drastically different results when measurements are performed in different solvents (e.g., DLS, DOSY-NMR) or in the "dry" state (e.g., AFM, TEM) due to differences of shape, swelling

behavior, or solvation shells. Additionally, comparing, e.g., DLS and DOSY-NMR can be problematic because of different accuracies, that can lead to different values, as well as differences to theoretical values.<sup>244</sup> GPC can also have limited validity, in case the separation on the GPC column is not exclusively caused by entropic, but also enthalpic interactions, which are, for instance, possible on water-based GPC systems.<sup>241</sup>

### 1.5.2. Compartment Analysis

Analyzing the internal structure of SCNPs can be even more complex than the analysis of the exterior. Generally, the proof of a compartmentalization inside SCNPs or the formation of other types of substructures are proven indirectly by using spectroscopic techniques like nuclear magnetic resonance spectroscopy (NMR).

A first sign for a compartmentalized and confined structure using  $^1\text{H-NMR}$  spectroscopy is a differing half-width of different signals.<sup>120</sup> The half width of a signal can be used as a qualitative measure for the mobility of the respective chemical group, since freely moving groups will show a sharp half-width, while hindered movements will result in broad signals. Hence, the chemical groups that are in the core of a compartmentalized SCNP will appear broader than those in the less confined shell. More complex (2D-)NMR techniques, e.g., nuclear Overhauser effect spectroscopy (NOESY)<sup>103, 149, 171</sup> or  $T_2$ -relaxation<sup>245</sup> can give detailed information about the formation of compartments with specific chemical groups and their density inside the SCNP. Other spectroscopic methodologies that directly prove the formation of compartmentalized structures will be discussed in detail in the main part of this thesis (see chapters 4. and 5.).

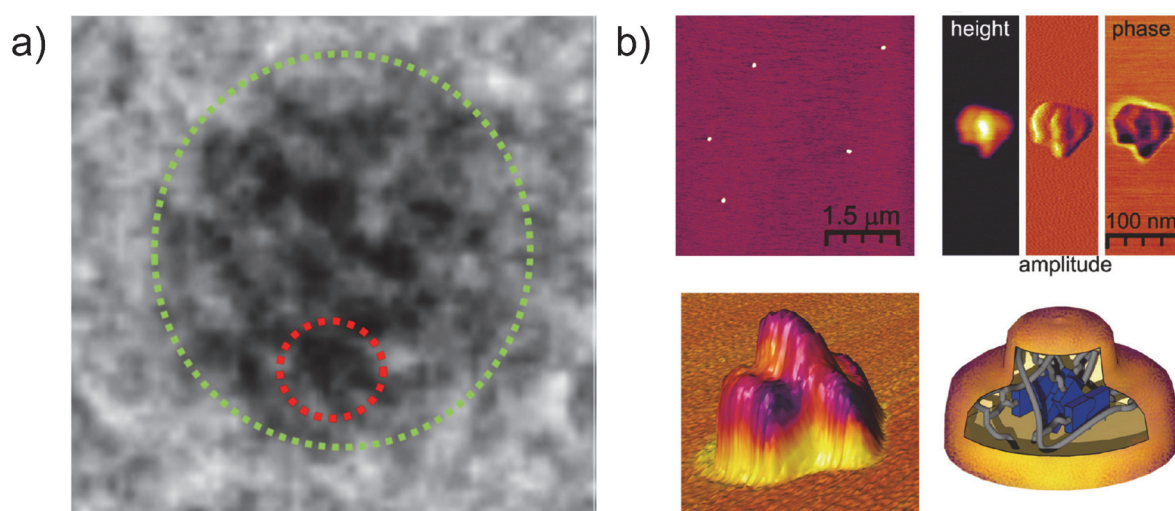


**Figure 13.** a) TEM image of local domains of a Cu-folded SCNP. Reprinted with permission from the American Chemical Society, copyright © 2018 (open access).<sup>246</sup> b) High resolution AFM image of a SCNP showing a dense core and a less dense shell. Reprinted and adapted with permission from the American Chemical Society, copyright © 2010.<sup>109</sup>

Although direct visualizations of those compartments using microscopic techniques are challenging due to insufficient resolutions, as discussed above, TEM or high-resolution AFM can be used, e.g., to prove the formation metal-based local domains inside an SCNP (see **Figure 13a**)<sup>180, 246</sup> or differently dense parts of the SCNPs (see **Figure 13b**),<sup>109</sup> respectively.

## 1.6. Applications and Special Functionalities of SCNPs

Single-chain nanoparticles have various applications that arise from their extremely small size, internal and external structure, and specific functionalities. As mentioned above, the nanostructures of SCNPs resemble – and are often inspired by – natural enzymes, as both systems are made out of single macromolecular chains that fold into nanoparticle-like structures with internal compartmentalizations. Thus, just like enzymes, SCNPs can be designed to act as catalysts with high catalytic activity and specificity.<sup>88</sup> Their enzyme-like structure is also an important factor for biomedical applications.<sup>89</sup> Next to these two main applications, SCNPs can also be used for detecting specific chemicals,<sup>123, 128, 247</sup> antifouling,<sup>141, 154</sup> catching of carbon nanotubes,<sup>108</sup> or as surfactants.<sup>99</sup>

### 1.6.1. SCNPs as Enzyme Mimetic Catalysts

When it comes to catalytical reactions, synthetical chemistry has still not reached the perfection that nature developed in its enzymes. Enzymatic reactions are usually superior in the matters of reaction speed, specificity, and activity under ambient conditions.<sup>248</sup> Inspired by those reactions, macrocyclic compounds, star or helical polymers, dendrimers, micelles, vesicles, or polymerosomes have been designed, trying to copy said reactions.<sup>88</sup> All these approaches tried to imitate the unique internal structure of enzymes. That is, enzymes provide specific local environments to which compounds can be bound and wherein they are reacted with each other. Those environments are characterized by hydrophobic, compartmentalized cavities which are stabilized by H-bonds, hydrophobic agglomerations, or disulfide bonds. Often also so-called cofactors are localized in those compartments, which additionally effect the catalytic activity.

SCNPs are conceptually synthetical analoga to enzymes. Just like them, SCNPs are collapsed/folded single polymer chains and are able to provide compartments with specific local properties, e.g., hydrophobic, confined environments, or the opportunity to bind catalytic sites.<sup>231</sup> It was found by electron-paramagnetic-resonance spectroscopy that especially the hydrophobic environments – or rather the retardation of water from those compartments – is crucial for their catalytic activity.<sup>167</sup> Similar to enzymes, catalytically active SCNPs are able to provide high selectivities for reactions by providing hydrophobic compartments and confined

spaces to which specific compounds can bind and react with each other, even with the possibility to bind cofactors.<sup>156, 177, 180, 238</sup> Both, organic as well as metal-complex catalysts can be incorporated into the hydrophobic compartments inside SCNPs that can catalyze e.g., the reduction of ketones,<sup>236, 249</sup> oxidation of alcohols,<sup>238</sup> aldol reactions,<sup>179, 237, 239</sup> Glaser couplings,<sup>135, 180</sup> Sonogashira and Suzuki couplings,<sup>176, 179, 250</sup> CuAAC,<sup>130, 131, 156</sup> phenol hydroxylations,<sup>177</sup> photocatalytic generations of singlet oxygen,<sup>219, 240</sup> benzoin condensations,<sup>178</sup> or intramolecular hydroaminations,<sup>214</sup> even in aqueous environments, in which some of those reactions are usually not possible. One advantage that SCNPs-based, enzyme-mimetic catalytic systems have over their natural analogs is their stimuli-responsive behavior. This enables the possibility to recycle the catalytic system several times while maintaining the catalytic activity.<sup>237, 251, 252</sup> Using biocompatible, catalytic SCNPs enables their use in biomedical applications. Their specific nanostructure can be tuned so that they can be introduced into living cells, where they can perform their catalytic reactions either alone or together with natural enzymes.<sup>131, 194, 240</sup> Hence, it is possible to specifically generate harmful molecules or other components inside of specific cells like tumor tissues, i.e., those cells can be killed specifically without harming healthy tissue.

### 1.6.2. SCNPs for Biomedical Applications

Next to their use as carriers of catalytic sites, the main field of interest in the research of SCNPs is in their application for biomedical purposes. Their internal compartmentalized structures are perfect environments for the encapsulation of drugs, or to covalently bind labels as imaging contrast agents. However, the design of SCNPs for biomedical applications can be quite complicated as they have to account several basic requirements:<sup>76</sup>

- water solubility;
- ability to carry and protect hydrophobic drugs;
- non-toxicity;
- biocompatibility / stability in biological media;
- biodegradability (will be discussed in chapter 1.6.4.); and
- tissue specificity.

To overcome the problem of water solubility, the precursor polymer needs to be designed in a way that the resulting SCNPs will have a polar shell, that is compatible with water. Usually PEG, sidechains are used to provide a proper water solubility,<sup>152, 153, 162, 170, 186, 253</sup> e.g., by using (oligo ethylene glycol) methacrylate (OEGMA) monomers as part of the precursor polymer. Furthermore quarternised amines,<sup>133</sup> alcohols,<sup>254, 255, 256, 257</sup> acrylic acid,<sup>221</sup> or sugar carbohydrate backbones<sup>136, 137, 258</sup> can be used.

PEG based shells do not only enable good water solubilities, they also provide the SCNP with low toxicity and good biocompatibility.<sup>154, 162, 170, 187, 240</sup> Next to PEG, also other precursor polymer designs which are based, e.g., on PNIPAM,<sup>247</sup> acrylic acid,<sup>221</sup> or carbohydrates<sup>136-138, 258</sup> can provide good biocompatibilities with cell viabilities of up to 10 mg/mL. Hence, otherwise toxic entities can be hidden in the cores of such SCNPs without harming any living tissue.

Biocompatibility and the stability of SCNPs in biological media is one further major issue in the design of biomedical SCNPs. Biological media are complex aqueous mixtures containing salts, glucose, amino acids, vitamins, and natural macromolecular assemblies like enzymes, all able to interact with, and alter the SCNP.<sup>170</sup> To overcome this issue, approaches to biocompatible SCNPs using natural materials like sugars were used as mentioned above, but also proteins and polypeptides have already been modified to be the basis of SCNPs with less harmful interactions with biological media.<sup>139, 140, 143</sup> To achieve the same biocompatibility and stability on synthetic SCNPs, the so-called “stealth effect” can be used, mostly found for PEG based systems.<sup>87</sup> Having PEG at the surface of a nanoparticle hinders other molecules from binding to that surface, e.g., proteins that are supposed to catch non-natural materials. Hence, the particle can move through the biological medium without any hindrance.

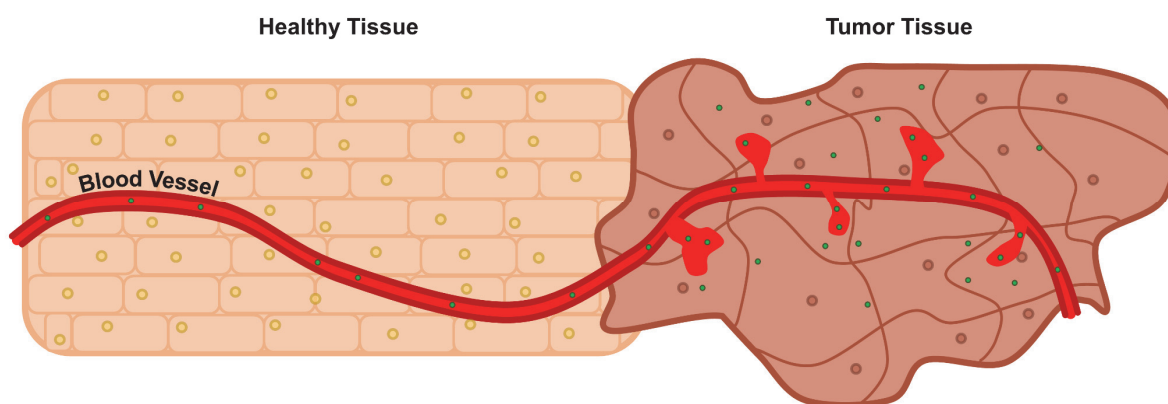


**Figure 14.** Schematic illustration of the enhanced permeation and retention effect, an indirect targeting method for tumor tissue using NPs. Green dots: NPs moving through blood vessels and being released into tumor tissue.

Tissue specificity, e.g., targeting tumor or inflamed tissue, can be achieved in two ways: either the SCNP gets distributed over all tissues statistically, but the SCNP’s functionality gets activated only in a specific tissue, e.g., by acting as a sensor for signaling molecules like nitric oxides;<sup>247</sup> or the SCNP is designed in a way, that it only targets a specific type of tissue. An indirect targeting method that applies to all types of nanoparticles is the enhanced permeation and retention effect.<sup>85</sup> This effect uses the leaky vasculature of tumors, accumulating nanoparticles only there, since the nanoparticles can easily leave the blood vessels through

the leaks and enter this tissue as illustrated in **Figure 14**. Furthermore, the chemical flexibility of SCNPs can be used to incorporate different functionalities that enable targeting of specific tissues or even specific compartments of a living cell. It is possible to bind tissue specific moieties such as antigens,<sup>137</sup> hormones,<sup>221</sup> or proteins<sup>133</sup> that only bind to specific tissue types. Targeting of specific cell types or cell compartments is also possible, for example by adding cell compartment specific moieties like Concanavalin A binding glucose,<sup>258</sup> by the formation of polyplexes,<sup>256</sup> or by adjusting the surface charge of the SCNPs.<sup>255, 257</sup>

### 1.6.3. Incorporation of Functional Units

To use SCNPs as catalysts or drug delivery systems, functional units like catalysts, labels for biomedical imaging, or drugs need to be incorporated into the internal compartments (see chapter 1.4.2.). This can be achieved in three general pathways, as depicted in **Figure 15**:

- (I) physically mixing a nonpolar small functional molecule within a compartmentalized SCNP;
- (II) binding the functional unit to the precursor polymer backbone or the SCNP either
  - a. during polymerization as monomer, or
  - b. after polymerization/single-chain collapse; and
- (III) using the functional unit as part of an external crosslinker.

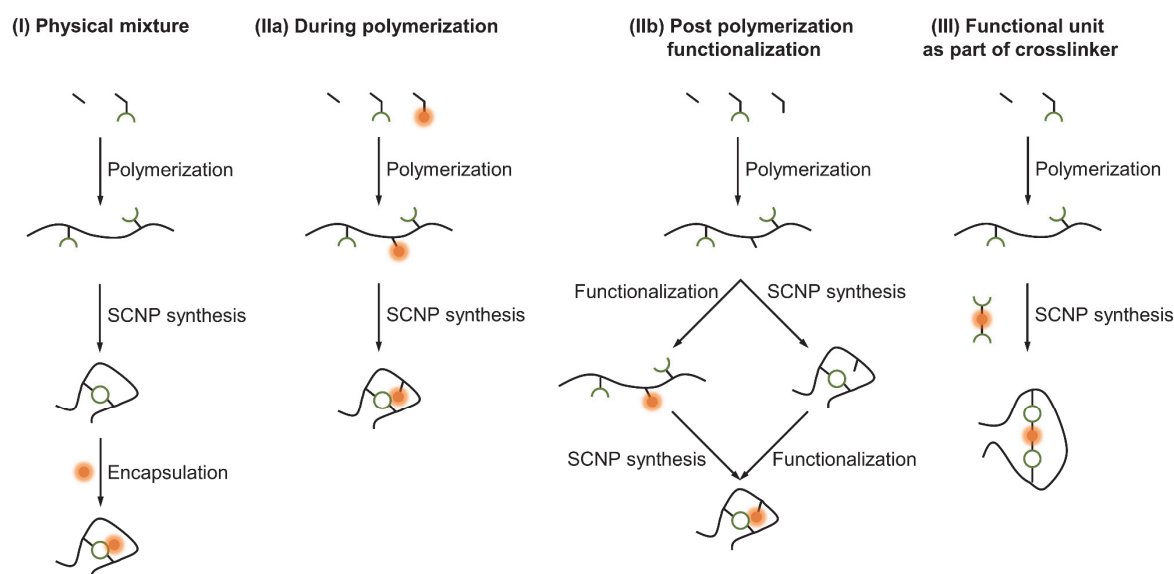


**Figure 15.** The three general pathways of incorporating a functional unit (orange circle) to a SCNP.

#### Pathway I:

When a functional small molecule is physically mixed with a compartmentalized SCNP that provides a non-polar core for a non-polar drug, the small molecule can dynamically enter and leave the SCNP. This procedure can be used as an efficient drug delivery and release system.

The SCNP will encapsulate the drug and deliver it to the tissue of interest. There, the drug will slowly be released and can operate without getting into contact with other tissues.<sup>153, 162, 186, 220, 256</sup> SCNPs can also be used as cofactors for transition metal catalysis by physically mixing a non-polar metal complex into the compartments of a SCNP, where it can operate as an enzyme-like catalyst.<sup>156</sup>

#### *Pathway II:*

To bind the functional unit to the precursor polymer chain, it can be added during the polymerization as the sidechain of a monomer.<sup>123, 185, 218, 236, 237, 240, 251</sup> Another way to achieve this covalent connection to the polymer is to functionalize either the precursor chain after the polymerization,<sup>151, 182, 214, 238</sup> or after single-chain collapse, e.g., by having reactive side chains that are able to react with different types of labels,<sup>136, 170, 195, 221, 257</sup> or ligands, that complexate metals.<sup>214, 218, 236, 238, 240, 253</sup>

#### *Pathway III:*

Functional units can also be added by using them as crosslinkers or parts of the crosslinkers for the single-chain collapse. Following this pathway, the units themselves are responsible for the formation of the SCNP and its compartmentalized, enzyme-like nanostructure. To use a functional unit as part of the crosslinker, it needs to be further functionalized bivalently with chemical groups that can react with the precursor polymer, e.g., by adding alkynes for CuAAC,<sup>194, 195</sup> phthalocyanine-forming units,<sup>259</sup> nucleophiles for  $S_N2$  and ring opening reactions,<sup>116, 219</sup> or benzene-1,3,5-tricarboxamides (BTAs) that will be part of a BTA-stack.<sup>239</sup> Catalytic metal complexes can be used as crosslinkers either by being part of the crosslinking unit as mentioned above, or the formation of the catalytic complex acts as the crosslinking reaction, by having the ligands at the precursor polymer chain and the metal center added externally.<sup>94, 130, 131, 134, 172-174, 176-180, 232, 250</sup>

#### *1.6.4. Stimuli-Responsive Behavior*

One main advantage for the various applications of SCNPs is the possibility of stimuli-responsive behavior. The chemical flexibility of SCNPs enables the incorporation of differently sensitive groups reacting to various external stimuli, e.g., changes of temperature, pH, or contact to specific chemicals.

The most widely used stimuli-response of SCNPs is thermoresponsivity, usually using LCST-behavior in water of specific (co-)polymer units in the precursor polymer. This LCST-behavior leads to insolubilities of the analogue SCNPs at increased temperatures, resulting in agglomeration, and, eventually, precipitation of the SCNPs. Usually, PEG<sup>96, 152, 153, 162, 215</sup> or PNIPAM<sup>192, 233</sup> sidechains are used to incorporate this responsivity. Thermoresponsive

behavior can be used as an efficient drug delivery mechanism for anticancer drugs, since tumor tissues are known to show higher temperatures than healthy tissue. Encapsulating this type of drug into a thermoresponsive SCNP, whose cloud point temperature  $T_{cp}$  is close to the temperature of a tumor, can therefore release the drug in this tumor more efficiently than in healthy tissue, as depicted in **Figure 16a**.<sup>153, 162</sup>

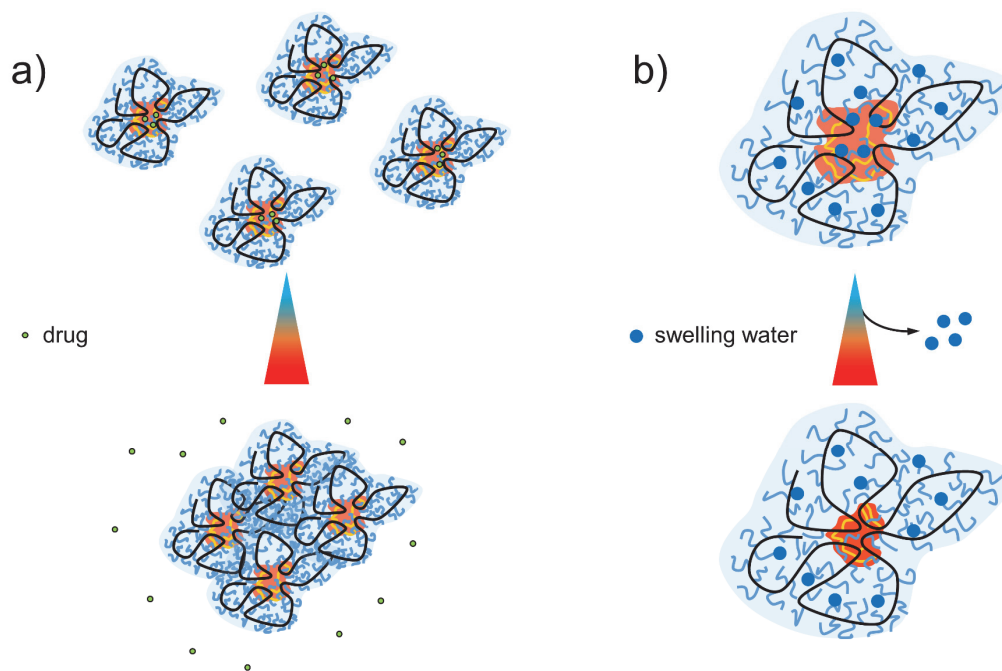


**Figure 16.** Schematic illustration of thermoresponsive SCNPs. a) Release of drugs, that were encapsulated into an LCST-type SCNP. b) Removal of swelling water from the core with a lower cloud point temperature than the outer shell, reducing its inner diameter.

Reversibly switching between hydrophilicity and -phobicity is also possible using other external stimuli, e.g., by using  $\text{CO}_2$ -sensitive units.<sup>251</sup> To do so,  $\text{CO}_2$  reactive sites like amidines can be incorporated into the precursor polymer chain. The inherently hydrophobic amidines can be converted into ionic moieties by bubbling the aqueous polymer suspension with  $\text{CO}_2$ . The resulting protonated amidines will subsequently become hydrophilic, dissolving the polymer into the aqueous phase, and eventually forming a SCNP. Bubbling that solution with  $\text{N}_2$  removes the  $\text{CO}_2$ . This converts the amidines back to the non-protonated, hydrophobic form, resulting in precipitation of the polymer. This enables an effective recycling of those SCNPs after using them in aqueous conditions, e.g., as catalysts.

Next to changes of the globular behavior of the complete SCNP, the internal nanostructure inside the SCNP can be influenced by external stimuli, e.g., by utilizing thermoresponsivity or light switchable units. To alter the internal nanostructure thermally, LCST-type core-shell structured SCNPs can be synthesized in which the core shows a lower  $T_{cp}$  than the outer shell. Dissolving this type of SCNP in water would lead to a certain degree of swelling with water in

the complete SCNP, including the core. Hence, an increase of temperature above  $T_{cp}$  of the core and below  $T_{cp}$  of the shell would release that swelling water from the core. Its diameter and polarity would therefore be reduced, and the core would become more dense, as depicted in **Figure 16b**.<sup>96, 233</sup> This behavior can have significant influence on e.g., fluorescent labels in the SCNP core. Those labels are usually sensitive to differences of surrounding polarities, as well as mobility and distances in between individual label molecules.

Contraction and expansion or other types of deformation of SCNPs can as well be accomplished by using *cis/trans* light-switchable azobenzene units. The *cis* and *trans* isomers have different end-to-end distances, resulting in expanded SCNPs if irradiated with the *trans*-wavelength, and contracted SCNP if irradiated with the *cis*-wavelength.<sup>182, 208</sup> This behavior enables a light-switchable mechanism to effectively open or close a SCNP, e.g., to enable small molecules to enter the SCNP or not.

Actively triggering the decomposition or transformation of SCNPs is a promising approach for their applications, e.g., by enabling a faster cleavage from the body after drug delivery, or as an effective removal of catalytic SCNPs after a successful reaction. To introduce this functionality into SCNPs, usually dynamic crosslinking methods are used, as described in chapter 1.3. The most commonly used dynamic crosslinking methods for an effective decomposition are pH-sensitive moieties or disulfide bonds. Lowering the pH of aqueous SCNP dispersions can trigger rearrangements of acylhydrazone bonds,<sup>117, 215</sup> or break enamine bonds,<sup>217</sup> as well as H-bonding U-DAP dimers.<sup>162</sup> Disulfide bonds can be reversibly formed and broken using redox interactions.<sup>129, 186</sup> The exact position of those disulfide bonds is crucial here, since the reduction of disulfides as crosslinkers will simply yield the precursor polymer, while SCNPs in which the disulfides are located in the polymer backbone will be broken into smaller entities.<sup>186</sup> In addition to these widely used methods, more specialized methods such as light induced reactions,<sup>142, 260</sup> self-immolative moieties,<sup>261</sup> hetero Diels-Alder reactions,<sup>262</sup> or voltage responsive crosslinking interactions<sup>263</sup> can be used.

## 2. Aim of the Thesis

The aim of this cumulative thesis is the synthesis and nanostructural analysis of water soluble, core-shell structured, and biocompatible single-chain nanoparticles, bearing highly fluorescent dye molecules.

These SCNPs are supposed to be suitable as contrast agents for pump-probe photoacoustic (PA) imaging, a new biomedical imaging method in which detectable acoustic signals are generated by the photoacoustic effect. The photoacoustic effect is a result of pulsed irradiation of chromophores, which give the excitation heat to the surrounding medium by internal conversion. The subsequent pulsating, thermal expansion of the surrounding medium creates a detectable acoustic wave.<sup>264, 265</sup> Pump-probe excitation is a more precise variation of the generation of those signals, in which the dye molecule is first excited with a light pulse of its absorption wavelength, and then its fluorescence is stimulated with a second light pulse of its fluorescence wavelength (see **Figure 17b**).<sup>266-268</sup> To use this excitation path, fluorescent dyes are required as contrast agents, which provide both, a high fluorescence quantum yield, as well as long fluorescence lifetimes.

Since aqueous media, as they are mainly present in biological media, usually quench fluorescence processes, and therefore prevent pump-probe excitation, fluorescent dye molecules need to be encapsulated in hydrophobic media that reduce their contact to water. For this thesis the dyes should be covalently incorporated into core-shell structured SCNPs, since they are able to provide the needed hydrophobic medium for the dye molecules in the core. Additionally, the chemical flexibility of SCNPs is able to provide desirable properties for their application as biomedical contrast agents, like sufficient water solubility, biocompatibility, and stimuli-responsive behavior.

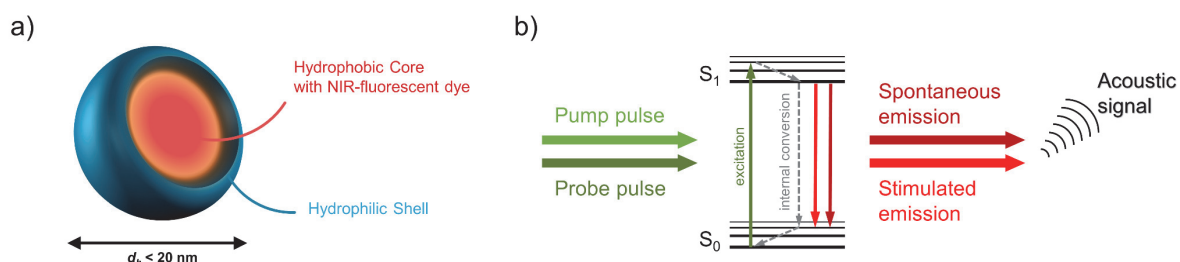
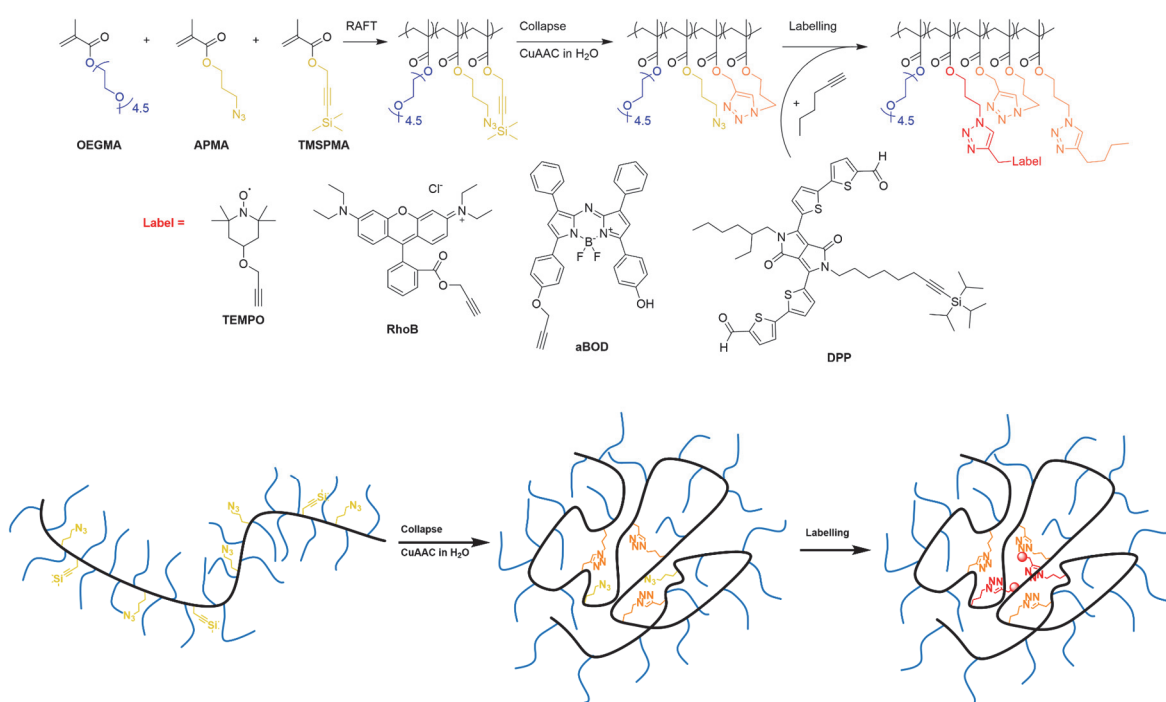


**Figure 17.** a) Schematic interpretation of a core-shell structured nanoparticle encapsulating NIR-fluorescent dyes. b) Jablonski diagram of the excitation and signal generation of pump-probe PA imaging.

### 3. Scientific Approach

The synthetical approach to achieve those core-shell structured SCNPs is to firstly synthesize amphiphilic precursor copolymers bearing hydrophilic monomers as well as hydrophobic monomers that act as crosslinkable units. Next to other candidates like polyoxazolines, PEGMA provides several advantages for a successful synthesis of the desired SCNPs, like a sufficient water solubility; and further for their application in biomedical systems, such as low toxicities, stimuli-responsive behavior, or the stealth effect, as discussed in chapters 1.6.2. and 1.6.4.. The polymerizations are performed using reversible-addition-fragmentation chain-transfer (RAFT) polymerization with cyanoisopropyl dithiobenzoate (CPDB) as chain transfer agent and azobisisobutyronitrile (AIBN) as initiator. The crosslinkable precursor polymers are collapsed into SCNPs and crosslinked by copper catalyzed azide-alkyne click reactions (CuAAC) in two different paths:

(I) *Internal crosslinking reaction*<sup>269, 270</sup> (**Scheme 1**)

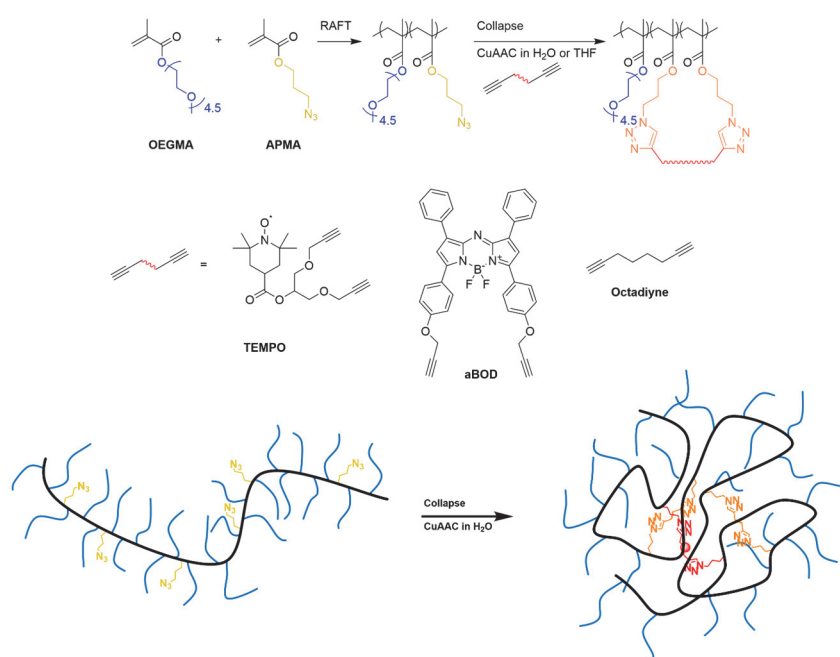


**Scheme 1.** Synthesis scheme for TEMPO- and dye-labelled SCNPs with a single-chain collapse by an internal crosslinking reaction.

For the internal crosslinking reaction, a random tri-copolymer is synthesized using the hydrophilic OEGMA monomer as main-monomer together with the hydrophobic crosslinking monomers azidopropyl methacrylate (APMA) and 3-trimethylsilylpropargyl methacrylate (TMSPPMA). An excess of APMA is used to label the resulting SCNPs with alkyne functionalized labels. By performing the collapse reaction in water using the continuous-addition protocol (see

chapter 1.3.), the polymer should precollapse into a core-shell structured unimolecular-micelle-like particle, since the hydrophilic PEG chains create a shell, and the hydrophobic crosslinking groups agglomerate in a core, which is the driving force in the core-shell structure formation. The subsequent CuAAC fixes the polymer in this conformation. Directly after the collapse reaction, the resulting SCNPs are labelled with different alkyne-functionalized labels: (2,2,6,6-tetramethylpiperidin-1-yl)oxyl (TEMPO), to analyze the internal nanostructure *via* continuous-wave electron-paramagnetic-resonance (CW-EPR) spectroscopy; Rhodamine B (RhoB), as a highly fluorescent dye in the visible light range; as well as different amounts of an aza-BODIPY (aBOD) and a diketopyrrolopyrrole (DPP) dye, as near-infrared fluorescent dyes, as they are applicable for actual biomedical applications because of deeper penetration depths of light of such wavelength into living tissue.<sup>271</sup> Finally, hexyne is added as a hydrophobic non-functionalized entity for full consumption of any unreacted azide moieties.

(II) *External crosslinking reaction*<sup>272</sup> (**Scheme 2**)



**Scheme 2.** Synthesis scheme for TEMPO- and aBOD-labelled SCNPs with a single-chain collapse by an external crosslinking reaction.

The second synthesis path is similar to the first one, but this time the precursor polymer is missing the alkyne functional units. Here the crosslinks are achieved by adding external crosslinkers, that bear two alkyne moieties each. In this approach, the driving force of the core-shell structure formation should be – similar to the first approach – the encapsulation of the hydrophobic crosslinking units. The crosslinkers are mixtures of different amounts of crosslinkers that also act as labels, together with octadiyne as a non-labelling crosslinker. Again, TEMPO is used to analyze the nanostructure of the SCNPs *via* CW-EPR spectroscopy,

and an aza-BODIPY dye is used as NIR-fluorescent dye. To show, if the collapse solvent actually has any influence on the SCNP's nanostructure, the collapse reactions are performed in water as well as in THF as a non-polar solvent.

After the successful synthesis of the polymers and SCNPs, their chemical integrity is analyzed using NMR- and ATR-IR-spectroscopy. Furthermore, the actual collapse of single polymer chains with solely intramolecular crosslinks is verified by proving decreases in their hydrodynamic diameter using GPC, DLS, and DOSY-NMR-spectroscopy, as described in chapter 1.5.1., together with their visualization by AFM.

To prove the formation of core-shell structured SCNPs, different types of measurements are performed, including investigations of their LCST behavior as well as spectroscopic analyses of the labels. A localization of the non-polar crosslinked groups inside the inner core of the SCNPs should have a major influence on the external polarity and solubility in water. In aqueous solutions, the precursor polymers should show lower polarities than the respective SCNPs, since their non-crosslinked hydrophobic groups can interact with water, in turn decreasing the overall water solubility. Contrary to that, the SCNPs should show higher polarities, since the contact of the hydrophobic groups is reduced by their location in the cores, in turn reducing their influence on the outer solubility. This effect is measurable by performing cloud-point measurements, since stronger influence of non-polar groups will lead to reductions of the cloud-point temperatures ( $T_{cp}$ ), whereas less influence of those groups will lead to increased  $T_{cp}$  values.<sup>273</sup> CW-EPR spectroscopy is a powerful tool to investigate the direct environment within a radius of  $\approx 1$  nm around a radical label, in this case TEMPO.<sup>274-276</sup> This provides the possibility of analyzing the exact location of the labels inside the SCNP, their number, their surrounding polarity, as well as their mobility. Similar investigations of the labels can be performed by decay-associated-fluorescence spectroscopy (DAS). This spectroscopic technique yields detailed information about fluorescence lifetimes, possible coupling behavior between individual dye molecules, and how they are influenced by their embedding inside a SCNP.

Finally, the photophysical behaviors of the dye-labelled SCNPs are investigated, next to DAS, with UV/VIS/NIR absorption and fluorescence spectroscopy. Together with investigations of the biocompatibility of the SCNPs, these measurements are the basis for their intended application as contrast agents for pump-probe PA measurements.

## 4. List of Publications

The results of this thesis are published in the following four publications. The three first-author publications [P1] - [P3] are reprinted as part of this cumulative thesis with the permissions from Wiley-VCH,<sup>269, 272</sup> and the Royal Society of Chemistry.<sup>270</sup>

### **[P1] Fluorescent and Water Dispersible Single-Chain Nanoparticles: Core-Shell Structured Compartmentation**

Justus F. Hoffmann, Andreas H. Roos, Franz-Josef Schmitt, Dariush Hinderberger, Wolfgang H. Binder\*

*Angew. Chem. Int. Ed.* **2021**, 60, 7820-7827. DOI: 10.1002/anie.202015179. Lit [269]

The conceptualization and writing of this publication were done by me. Furthermore, I performed the syntheses as well as chemical and structural characterization of all products, the size analyses, and the absorption and fluorescence measurements. Thermal analyses were conducted by me together with A. H. Roos. A. H. Roos and D. Hinderberger performed the CW-EPR spectroscopy and evaluated those data. F.-J. Schmitt performed and evaluated the decay associated spectra. All steps of this project were supervised by W. H. Binder. All authors were involved in the reviewing process of this publication.

### **[P2] Tuning the Internal Compartmentation of Single-Chain Nanoparticles as Fluorescent Contrast Agents**

Justus F. Hoffmann, Andreas H. Roos, Jana Krüger, Dariush Hinderberger, Franz-Josef Schmitt, Guo Tang, Farzin Ghane Golmohamadi, Jan Laufer, Wolfgang H. Binder\*

*Macromol. Rapid Commun.* **2023**, 44, 2200618. DOI: 10.1002/marc.202200618. Lit [272]

The conceptualization and writing of this publication were done by me. Furthermore, I performed the syntheses as well as the chemical and structural characterization of all products, the size and thermal analyses, and the absorption and fluorescence measurements. J. Krüger conducted the CW-EPR spectroscopy which data were evaluated by A. H. Roos and D. Hinderberger. F.-J. Schmitt performed and evaluated the decay associated spectra. G. Tang performed and evaluated the pump-probe PA measurements on a system that was developed by F. G. Golmohamadi, both supervised by J. Laufer. All steps of this project were supervised by W. H. Binder. All authors were involved in the reviewing process of this publication.

### **[P3] Thermoresponsive Swelling of Photoacoustic Single-Chain Nanoparticles**

Justus F. Hoffmann, Ramesh Maragani, Franz-Josef Schmitt, Guo Tang, Samira Mahmoudi Rahmanlou, Jan Laufer, Henrike Lucas, Karsten Mäder, Wolfgang H. Binder\*

*Chem. Commun.* **2023**, 59, 11373-11376. DOI: 10.1039/d3cc03851c. Lit [270]

The conceptualization and writing of this publication were done by me. Furthermore, I performed the syntheses as well as the chemical and structural characterization of all products, the size and thermal analyses, and the absorption and fluorescence measurements. The synthesis of the DPP dye was performed by Ramesh Maragani. F.-J. Schmitt performed and evaluated the decay associated spectra. G. Tang and S. M. Rahmanlou performed and evaluated the pump-probe PA measurements, both supervised by J. Laufer. H. Lucas performed and evaluated the cell viability assays under supervision of K. Mäder. All steps of this project were supervised by W. H. Binder. All authors were involved in the reviewing process of this publication.

### **[P4] Nanoscale structure and dynamics of thermoresponsive single-chain nanoparticles investigated by EPR spectroscopy<sup>1</sup>**

Andreas H. Roos, Justus F. Hoffmann, Wolfgang H. Binder, Dariush Hinderberger\*

*Soft Matter* **2021**, 17, 7032-7037, DOI: 10.1039/d1sm00582k. Lit [269]

The conceptualization and writing of this publication were done by A. H. Roos. He also performed all CW-EPR measurements as well as the simulation and evaluation of the spectra. The polymers and SCNPs, that were analyzed in this publication, were synthesized and characterized by me based on [P1]. All steps of this project were supervised by W. H. Binder and D. Hinderberger. All authors were involved in the reviewing process of this publication.

---

<sup>1</sup> [P4] will not be shown in this thesis, since I am not first author and it was already presented in A. H. Roos's PhD thesis ("Thermoresponsive Polymere – Einfluss von Variationen der chemischen Struktur in thermoresponsiven Polymeren auf ihr Solvatationsverhalten in Wasser" **2021**, Martin Luther University Halle-Wittenberg).

## Polymer Nanoparticles

## Fluorescent and Water Dispersible Single-Chain Nanoparticles: Core–Shell Structured Compartmentation

Justus F. Hoffmann, Andreas H. Roos, Franz-Josef Schmitt, Dariush Hinderberger, and Wolfgang H. Binder\*

**Abstract:** Single-chain nanoparticles (SCNPs) are highly versatile structures resembling proteins, able to function as catalysts or biomedical delivery systems. Based on their synthesis by single-chain collapse into nanoparticulate systems, their internal structure is complex, resulting in nanosized domains preformed during the crosslinking process. In this study we present proof of such nanocompartments within SCNPs via a combination of electron paramagnetic resonance (EPR) and fluorescence spectroscopy. A novel strategy to encapsulate labels within these water dispersible SCNPs with hydrodynamic radii of  $\approx 5$  nm is presented, based on amphiphilic polymers with additional covalently bound labels, attached via the copper catalyzed azide/alkyne “click” reaction (CuAAC). A detailed profile of the interior of the SCNPs and the labels’ microenvironment was obtained via electron paramagnetic resonance (EPR) experiments, followed by an assessment of their photophysical properties.

## Introduction

Among many nanosized carriers single chain nanoparticles (SCNPs) are the most versatile, both in molecular design, structural diversity and embedded functionalities.<sup>[1]</sup> Derived from single polymer chains by covalent or noncovalent crosslinking they directly link the vast synthetic space of controlled polymer synthesis with their function, embedding

chemical functionalities into the final SCNPs to allow applications of SCNPs in the areas of catalysis,<sup>[2]</sup> drug delivery<sup>[3]</sup> or imaging technologies<sup>[3b,4]</sup> such as photoacoustic imaging.<sup>[5]</sup> Crucial thereto is the placement of specific chemical functionalities within the SCNP, further stimulated by its nanosized dimension, excellent dispersion and internal compartmentation. The formation of nanosized compartments within such SCNPs has been intensely discussed,<sup>[1a,6]</sup> proposing their use as functional units to generate micro-environments for catalysis,<sup>[7]</sup> photophysics,<sup>[8]</sup> or subsequent embedding of chiral elements.<sup>[9]</sup> As the formation of SCNPs is based on the collapse of single polymer chains at low concentration via covalent or non-covalent intramolecular bonding interactions,<sup>[10]</sup> it “freezes-in” the conformational state of the polymer chain into the final, crosslinked SCNP.<sup>[11]</sup> However, dynamics of the polymer chains often is at least partially preserved depending on the degree of crosslinking and solvent effects during the crosslinking process.<sup>[6]</sup> Thus recently a strong solvent dependency on the final size of single-chain nanoparticles has been observed using comb-shaped polymers, bearing for example, polyisobutylene (PIB) sidechains with a direct correlation between solvent quality and the final SCNP size.<sup>[8b]</sup> Strong photophysical effects as for example an increasing rate of photoinduced dimerization has been observed within pre-folded SCNPs via an increase of quantum yields by the confinement-effects within the SCNP.<sup>[8b]</sup> Structural dynamics can lead to a modulation of the band structure of SCNPs and the excited states of bound dye molecules on the sub-ns timescale which determines the achieved fluorescence quantum yield and both, the absorption and fluorescence spectra of the dyes.<sup>[12]</sup>

Although the formation of nanosized compartments within the SCNPs has been often proposed and observed indirectly, a direct proof has not been accomplished as many of the used methodologies provide an only indirect measure of compartmentation. Thus monitoring the molecular dynamics of water molecules around SCNPs via Overhauser dynamic nuclear polarization (ODNP) hinted to supramolecular organized hydrophobic benzene-1,3,5-tricarboxamides (BTA) into chiral folds within the SCNP, resembling their self-assembly in solution.<sup>[13]</sup> Also the solution behavior of polymers within SCNPs has been shown to deviate from those of the respective uncrosslinked polymers due to confinement within nanosized compartments, leading to significant changes in their lower critical solution (LCST) behavior.<sup>[14]</sup>

We here probe the formation of compartments within synthetic SCNPs based on amphiphilic polymers, equipped with an active spin label, via continuous wave electron

[\*] J. F. Hoffmann, Prof. Dr. W. H. Binder  
Macromolecular Chemistry, Institute of Chemistry, Faculty of Natural Science II (Chemistry, Physics and Mathematics), Martin Luther University Halle-Wittenberg  
von-Danckelmann-Platz 4, 06120 Halle (Germany)  
E-mail: wolfgang.binder@chemie.uni-halle.de

A. H. Roos, Prof. Dr. D. Hinderberger  
Physical Chemistry, Institute of Chemistry, Faculty of Natural Science II (Chemistry, Physics and Mathematics), Martin Luther University Halle-Wittenberg  
von-Danckelmann-Platz 4, 06120 Halle (Germany)

Dr. F.-J. Schmitt  
Institute of Physics, Faculty of Natural Science II (Chemistry, Physics and Mathematics), Martin Luther University Halle-Wittenberg  
von-Danckelmann-Platz 3, 06120 Halle (Germany)

Supporting information and the ORCID identification number(s) for the author(s) of this article can be found under:  
<https://doi.org/10.1002/anie.202015179>.

© 2020 The Authors. Angewandte Chemie International Edition published by Wiley-VCH GmbH. This is an open access article under the terms of the Creative Commons Attribution License, which permits use, distribution and reproduction in any medium, provided the original work is properly cited.

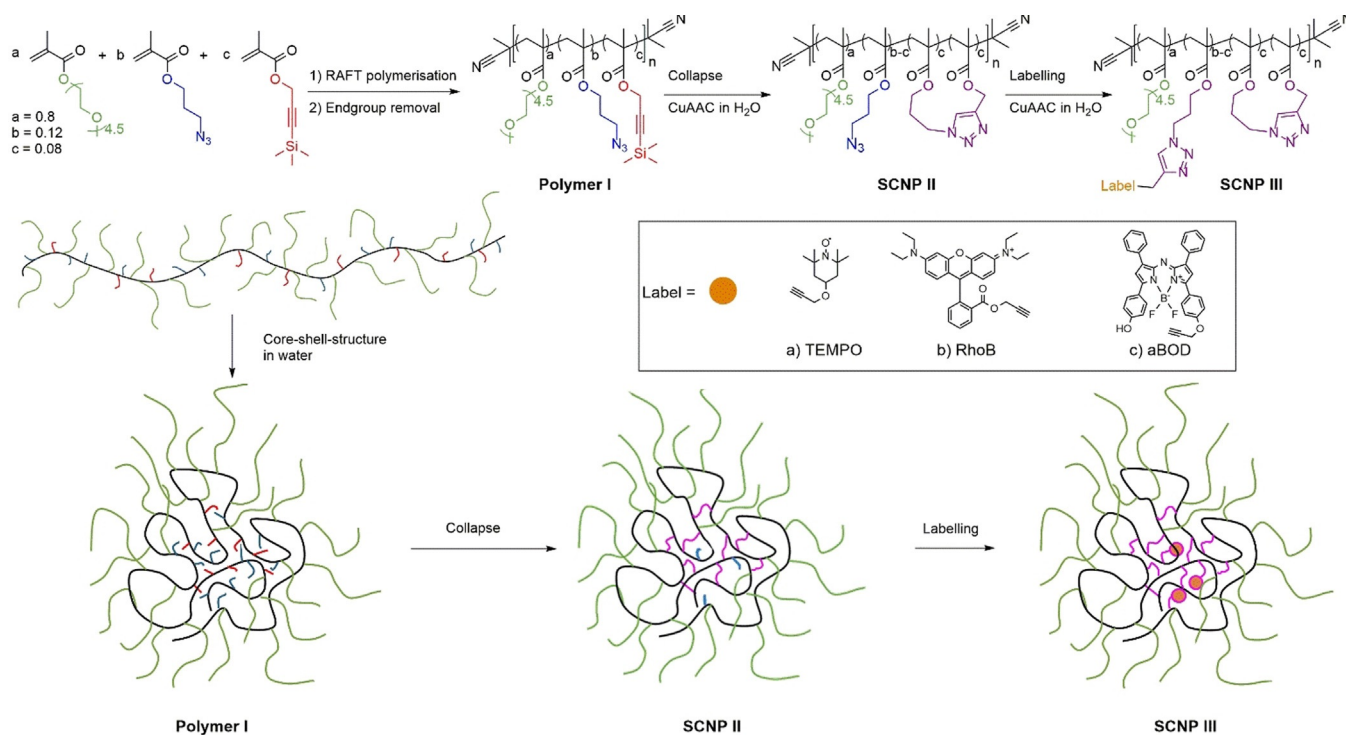
paramagnetic wave resonance (CW EPR), allowing to probe the internal compartments of the formed SCNPs. Additionally, fluorescent dyes, appropriate for use in pump-probe photoacoustic imaging<sup>[15]</sup> are embedded into small ( $r_h < 10$  nm) SCNPs to allow sufficient permeation for cell-incorporation.<sup>[16]</sup> Thus the SCNPs act as a barrier against defense mechanisms of the targeted tissues and stabilize the dye against external photobleaching. Important in our endeavor was the quest to position the dye within the hydrophobic core of the SCNP, as such its accessibility is reduced and thus a proposed protection effect of the SCNP could be expected to be most effective.

With the here reported single-chain nanoparticles one can therefore generate a scaffold for encoding the required different functionalities stimuli-response, for example, thermo- or pH-responsivity,<sup>[3c,17]</sup> and biocompatibility,<sup>[18]</sup> by using three types of monomers to adjust both, the required amphiphilic balance for the single-chain collapse, and the dye attachment.

## Results and Discussion

The required poly(poly(ethylene glycol) methacrylate) (PEGMA)-copolymer (**polymer I**) was synthesized by RAFT copolymerization of poly(ethylene glycol) methacrylate ( $M_n = 300$  Da,  $n = 4.5$ ), azidopropyl methacrylate, and 3-(trimethylsilyl)propargyl methacrylate in DMF, using AIBN as initiator and cyanoisopropyl dithiobenzoate (CPDB) as chain transfer agent (CTA), followed by the removal of the CTA using an excess of AIBN.<sup>[19]</sup> The CTA,<sup>[20]</sup> the mono-

mers,<sup>[21]</sup> and the dye labels<sup>[22]</sup> were synthesized according to literature with small adaptations (see Supporting Information). For the polymerization the molar fractions of the three monomers were set as 0.8, 0.12, and 0.08, respectively, to achieve an appropriate number of crosslinking groups<sup>[23]</sup> and to retain residual attachment sites for modification with the labels after the single-chain collapse (**polymer I**:  $M_n = 36.1$  kDa,  $PDI = 1.7$ ,  $DP = 129$ ). Furthermore, this composition allows to induce thermoresponsivity together with sufficient dispersibility and hydrophobic packaging of the labels. Final composition and structural integrity of the resulting polymer was proven by NMR-spectroscopy, allowing to adjust the desired functionalities along the polymer chain in relation to the initially used amounts of the three monomers (see Supporting Information, including the final copolymer-compositions). Subsequently, single-chain collapse of **polymer I** and labelling (see Scheme 1) was accomplished in a two-step/one-pot reaction, where the alkyne group was first deprotected by tetra butyl ammonium fluoride in water, followed by slow addition of the resulting polymer solution to an aqueous  $\text{CuSO}_4/\text{NaAsc}$  solution via a syringe pump to adjust low concentrations ( $c_{\text{polymer}} < 10^{-6}$  M) for the required single-chain folding. The amphiphilic polymer thus is adopting a preorganized nanoparticle by forming an intramolecular core-shell structure with the hydrophilic PEG sidechains in the shell and the reactive azide-groups in the core, resulting in sole intrachain crosslinking of the reactive groups to form **SCNP II** via CuAAC-reaction (see Scheme 1).<sup>[24]</sup> For further labelling of **SCNP II**, the catalyst was reactivated by adding additional sodium ascorbate and a label-alkyne solution in water (with the help of Kolliphor EL as detergent for the



**Scheme 1.** Synthesis of the precursor **polymer I** by RAFT polymerization followed by the formation of the unlabeled **SCNP II** and labelling to obtain the labelled **SCNP IIIa-c**.

2,2,6,6-tetramethylpiperidine oxide (TEMPO)-label and aza-BODIPY (aBOD)). This allows a reaction of the still present residual terminal azido moieties in the hydrophobic core to attach the two fluorescent dyes Rhodamine B (RhoB) and aBOD as a NIR-fluorescent dye. Especially aBOD is attractive as it displays a tumor targeting functionality via deprotonation, resulting in intramolecular charge transfer, and thereby suppression of fluorescence.<sup>[22d,25]</sup> The EPR-label 2,2,6,6-tetramethylpiperidine oxide (TEMPO) was attached for subsequent EPR investigations of the SCNP's inner core (see Scheme 1).

Progress of the crosslinking was followed by attenuated total reflection infrared (ATR-IR) spectroscopy (see Figure S1a and b) indicating a full disappearance of the alkyne band at 2178 cm<sup>-1</sup> in the **SCNP II**, and a partial and complete removal of the azide band at 2100 cm<sup>-1</sup> for **SCNP II** and the **SCNPs III**, respectively. The new bands of the triazole ring are overlapped by the bands of the polymer backbone and the PEG sidechains and therefore not visible in the spectrum. <sup>1</sup>H-NMR spectroscopy proves a complete reaction of the reactive groups under formation of triazole rings (see Figure S1d, removal of the TMS-protecting group at 0.2 ppm, absence of the alkyne proton at 2.6 ppm). A crosslinking density of  $\approx 9$  crosslinks per SCNP was roughly calculated from the stoichiometric ratios, leaving  $\approx 4$  remaining attachment sites per SCNP for the labels. The so obtained SCNPs are water dispersible and can be redispersed after freeze-drying.

Diffusion-ordered NMR spectroscopy (DOSY-NMR) and dynamic light scattering measurements of **polymer I** and **SCNP II** (see Figure 1 and Table 1) independently show a reduction of the hydrodynamic radius after the CuAAC from 5.2 nm to 4.2 nm. This proves the single-chain collapse in good agreement with literature, where a reduction of the hydrodynamic radius is an indication of a single-chain collapse.<sup>[26]</sup> Upon further labelling of the **SCNP II** yielding **SCNPs IIIa-c**, both methods show the trend of an increased

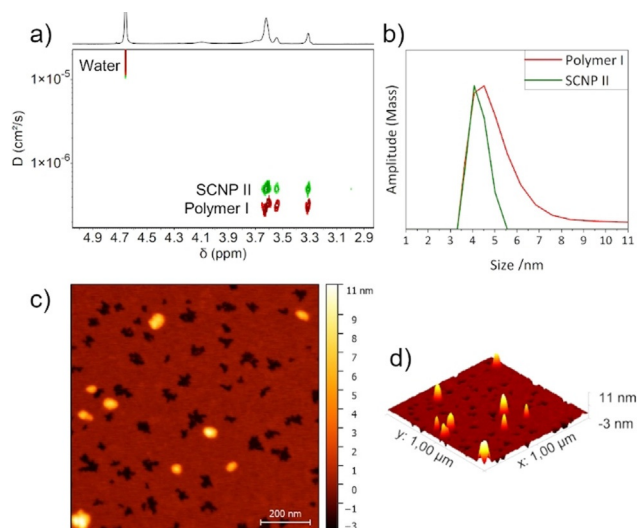


**Figure 1.** a) DOSY-NMR and b) DLS measurements of the precursor **polymer I** and the unlabelled **SCNP II** at concentrations of 1 mg mL<sup>-1</sup> in water and D<sub>2</sub>O, respectively. c) 2D and d) 3D AFM topography image of **SCNP IIIb** (1 × 1 μm).

**Table 1:** The hydrodynamic radii ( $r_h$ ) and cloud point temperatures ( $T_{cp}$ ) of the precursor **polymer I**, the unlabelled **SCNP II** and labelled **SCNPs IIIa-c**, bearing the different labels TEMPO (**IIIa**), RhoB (**IIIb**) and aBOD (**IIIc**).

	$D_{\text{DOSY}}^{[a]}$ [ $\times 10^{-7}$ cm <sup>2</sup> s <sup>-1</sup> ]	$r_{h,\text{DOSY}}^{[b]}$ [nm]	$r_{h,\text{DLS}}^{[c]}$ [nm]	$T_{cp}^{[d]}$ [°C]
Polymer I	3.3	5.3	5.2 ± 1.9	48
SCNP II	4.9	3.6	4.2 ± 0.4	54
SCNP IIIa (TEMPO)	3.4	5.2	4.9 ± 1.0	65
SCNP IIIb (RhoB)	3.4	5.2	4.5 ± 0.6	69
SCNP IIIc (aBOD)	3.7	4.7	4.6 ± 0.4	75

[a] Diffusion coefficient measured by DOSY-NMR in D<sub>2</sub>O. [b] Calculated using the Stokes–Einstein equation ( $r_h = (k_B T) / (6\pi\eta D)$ ) with  $D = D_{\text{DOSY}}$ ,  $\eta_{\text{D}_2\text{O}} = 1.25$  MPa s). [c] Measured by DLS in H<sub>2</sub>O. [d] Cloud point temperature measured by turbidimetry,  $T_{cp} = T$  at 96% transmittance (see Figure S3 b).

hydrodynamic radius of  $\approx 1.4$  nm (DOSY-NMR, see Table 1) and of  $\approx 0.5$  nm (DLS) indicating the successful attachment of the respective labels, which lead to an expansion of the measured volume, as the dye-labels are comparably large in dimension. Atomic force microscopy (AFM) further proved the formation of SCNPs with an average height of  $7.5 \pm 1.5$  nm (see Figure 1 c,d and Figure S2). This underscores the formation of distorted particles due to the surface/SCNP-interaction between the polar mica-surface and the hydrophilic PEG-shell, also indicative of the high responsivities of the SCNPs during adsorption, inline with previous observations.<sup>[27]</sup>

Size exclusion chromatography (SEC) measurements in water further prove the covalent attachment of the labels to the SCNPs via an overlap of the R.I. and UV/Vis track for the dye-labelled **SCNPs IIIb** and **IIIc** (see Figure S4 d and e). During single-chain collapse, the hydrophobic reactive groups (azide/alkyne) are proposed to be located in the inner core of the nanoparticles, hidden from the aqueous surroundings. We therefore observe a polarity shift in SEC, inline with an increased hydrophobic collapse ( $T_{cp}$ ) after the single-chain collapse and with further modification moving from the native **polymer I** ( $T_{cp} = 48^\circ\text{C}$ ) to **SCNP II** ( $T_{cp} = 54^\circ\text{C}$ ) to **SCNP IIIa-c** ( $T_{cp} = 65^\circ\text{C}$ ,  $69^\circ\text{C}$  and  $75^\circ\text{C}$ , respectively) (see Table 1 and Figure S3). It should be noted that this is the first observation of such a consequent increase of  $T_{cp}$ , initially only observed for noncrosslinked, dynamic random copolymers.<sup>[14]</sup> Additionally, this behavior explains the decrease of retention time in SEC moving from **polymer I** to **SCNP II**, with concomitantly increasing  $T_{cp}$ . Labelling **SCNP II** with the dyes to yield **SCNPs IIIa-c** leads to a further decrease of the retention time and a further increase of  $T_{cp}$ .

To achieve a deeper understanding of the microstructure and the distribution and location of the individual polymer and label segments within the SCNPs, CW EPR measurements were conducted. For the protective effect in SCNPs to be effective, the exact location (spatially and in chemical environments) of the labels within the SCNPs and the desired location within the hydrophobic core is crucial. Moreover, a rough quantification of the number of labels in one SCNP is needed. With the CW EPR spectra of the attached TEMPO label it is possible to specify the chemical environment of the

nanostructure surrounding the probe within a radius of  $\approx 1$  nm.<sup>[28]</sup> For comparison of the TEMPO-labelled **SCNP IIIa** with an equally labelled linear polymer, the TEMPO-labelled **polymer I'a** was synthesized analogously to **polymer I**, but without the alkyne moieties (see Supporting Information).

Upon covalently binding TEMPO as a label (Figure 2b) to **polymer I** yielding **polymer I'a**, a significant broadening of the EPR peaks is observed, caused by the hindered rotation of the label attached to the large polymer. This effect is even stronger in the TEMPO-labelled **SCNP IIIa**, indicating a reduction of the mobility of the label upon attachment to the SCNP. Figure 2a in comparison shows the CW EPR spectra of **polymer I** and **SCNP II** in water in pure physical

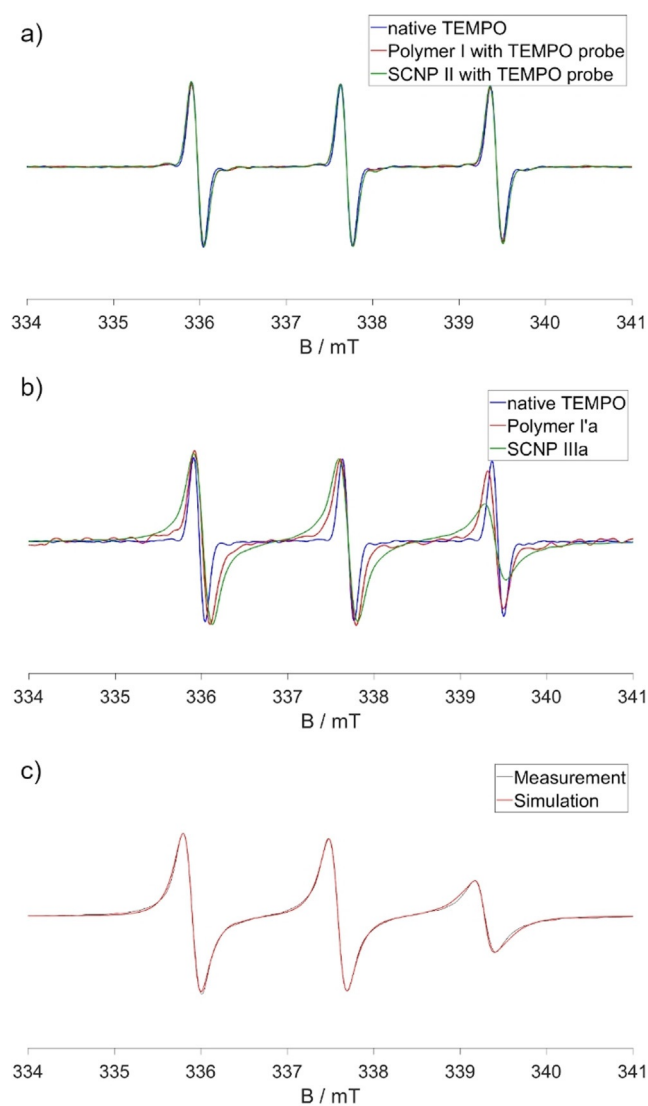


**Figure 2.** CW EPR spectra of a) native TEMPO, **polymer I** with a TEMPO probe, and **SCNP II** with a TEMPO probe; b) native TEMPO, **polymer I'a**, and **SCNP IIIa**; c) simulated spectrum of **SCNP IIIa**. The spectra were all normalized to the center peak. All measurements were conducted in water at 20°C. The concentrations of the polymers and SCNPs were  $1 \text{ mg mL}^{-1}$ . The concentrations of the TEMPO probes were  $100 \mu\text{M}$ .

mixtures with the free TEMPO probe. The three identical normalized spectra indicate free TEMPO in water, proving the absence of specific, mostly hydrophobic interactions of the amphiphilic TEMPO probe with the polymer and the SCNP, respectively, as we usually and regularly observe it with amphiphilic (LCST-type) polymers.<sup>[28a]</sup> Simulated spectra of the samples quantify the mobility reduction and the low polarity of the environment as expected for water-depleted, polymer-rich regions (see Figure 2c). For **SCNP IIIa**, but not for the respective polymers an exchange coupling of 6 MHz had to be included to the calculation, indicating high local concentrations and direct contact of two or more TEMPO labels with distances  $< 1$  nm. Even though a certain amount of TEMPO was probably deactivated by reduction during the labelling process because of sodium ascorbate present in the reaction mixture, the degree of labelling was approximated to be 1.3 active labels per particle (see Figure S10). This, together with our spectra, leads to the conclusion that the SCNPs bear one to two chemically attached active spin labels and even more EPR-inactive labels.

Concentration dependent measurements of **SCNP IIIa** in Figure 3a,b indicate that the label is hidden from the

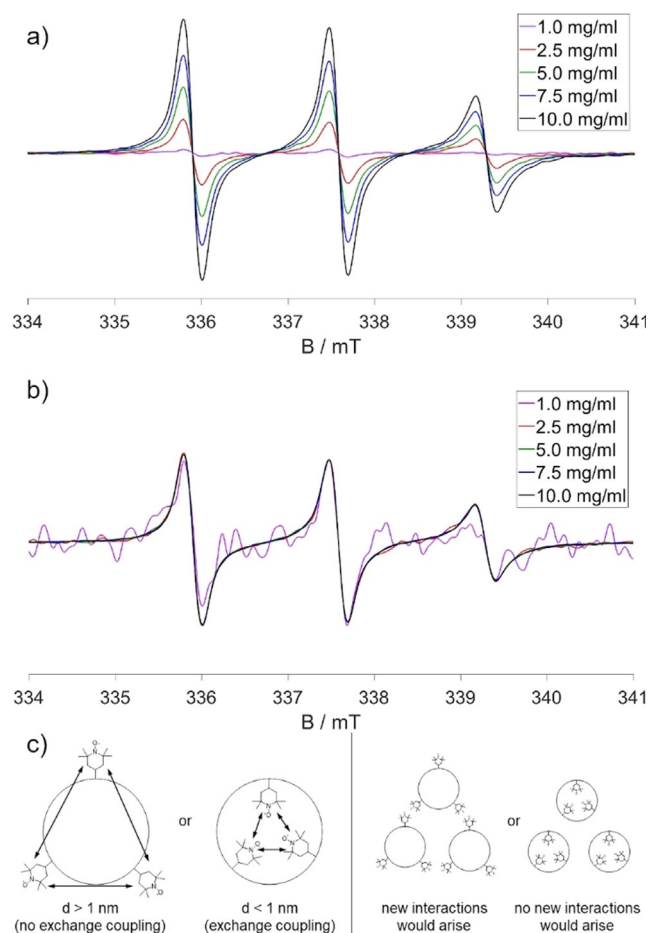


**Figure 3.** CW EPR spectra of **SCNP IIIa** at different concentrations: a) unnormalized, b) normalized to the center peak. All measurements were conducted in water at 20°C. c) Schematic depiction of the CW EPR results from the simulation (left side) and the concentration dependence (right side).

environment outside the nanoparticle as expected for the specific topology and compartmentation in the SCNPs. All normalized spectra show the same shape, apart from small differences in the signal-to-noise ratio. Even at high concentrations the surroundings of the labels remain the same. Thus, the label seems to be completely unaffected by external influences outside of the particle, even though collision or agglomerates with other particles at high concentrations might occur (see Figure 3c). Summing up the EPR results, the up to two active labels per nanoparticle are covalently bound in **SCNP IIIa** in a confined space surrounded by the non-polar polymer backbone, which is reflected in the lower hyperfine splitting of labels on SCNPs, in the nanoparticles core, altogether as a strong proof for the formation of such a compartment. External influences do not affect the label, indicating its embedding in the SCNP's core. Considering that TEMPO is more hydrophilic than the hydrophobic dyes embedded for optical applications, the SCNPs are therefore able to protect a photoactive label from photooxidation or other degradational processes.

The optical properties of dyes can be constructively tuned by binding to SCNPs.<sup>[12,29]</sup> Figure 4 and Table 2 show the absorption and fluorescence spectra and wavelengths of the RhoB and aBOD labelled SCNPs in water and aqueous phosphate buffer (pH 6.0), respectively, spectra of the free dyes can be seen in Figure S5. In comparison to free RhoB-alkyne, the RhoB-labelled **SCNP IIIb** shows a red shifted absorption at 559 nm and a blue shifted fluorescence at 582 nm (Stokes shift reduced to 23 nm). In the aBOD-labelled **SCNP IIIc**, resonances are blue shifted by 6 nm in comparison to the free aBOD dye in aqueous phosphate buffer, with a Stokes shift of 27 nm for the free aBOD dye and **SCNP IIIc**, respectively. In line with the results from EPR measurements, those shifts occur by a different solvation of the dyes in the particle's hydrophobic core, well separated from the sur-

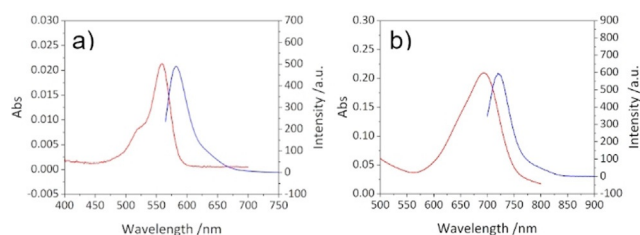


**Figure 4.** Absorption and fluorescence spectra of a) RhoB-labelled **SCNP IIIb** in water ( $c = 0.5 \text{ mg mL}^{-1}$ ,  $\lambda_{\text{Ex}} = 559 \text{ nm}$ , slit = 5 nm,  $V_{\text{detector}} = 600 \text{ V}$ ), and b) aBOD-labelled **SCNP IIIc** in aqueous phosphate buffer (pH 6.0),  $c = 0.5 \text{ mg mL}^{-1}$ ,  $\lambda_{\text{Ex}} = 694 \text{ nm}$ , slit = 5 nm,  $V_{\text{detector}} = 600 \text{ V}$ ).

**Table 2:** Absorption and fluorescence maxima of the fluorescent dyes and the dye-labelled SCNPs in water.

	RhoB-alkyne	SCNP IIIb	aBOD	SCNP IIIc
$\lambda_{\text{Abs}}$ [nm]	558	559	700	694
$\lambda_{\text{Fl}}$ [nm]	596	582	727	721
Stokes shift [nm]	38	23	27	27
$\text{p}K_{\text{a}}$	–	–	6.8	7.6

rounding bulk water phase, again indicative for the compartmented nanostructure of the SCNP.

The near neighborhood of two or more bound dye molecules leads to interactions and, dependent on their distance and orientation, possible excitonic coupling between the dyes which changes the fluorescence quantum yield, the wavelength maximum and FWHM of the fluorescence emission.<sup>[12]</sup> In addition internal relaxation processes on the sub-ns time scale and the interaction of the dye with the polymer at different sites and possible distributions of the molecular structure modulate the fluorescence emission and determine the fluorescence lifetime of excited states.<sup>[30]</sup> Time resolved fluorescence spectroscopy enables the analysis of sub-band structures, dynamics of interaction between excited states and the environment and possible heterogeneous decay channels resulting from excitonic coupling and/or compartmentation that contribute to the integral fluorescence spectrum. Just like in the EPR measurements we synthesized a linear aBOD-labelled polymer (**polymer Ic** see Supporting Information) to compare it to **SCNP IIIc** in view of their excitational behavior and heterogeneity.

Figure 5 reveals how an excited state heterogeneity that might either result from molecular coupling and/or a structural heterogeneity, possibly with subsequent relaxation dynamics after light absorption in the bound dyes, leads to a split of the formerly homogeneous excited singlet states of different molecules as indicated in Figure 5d. While the free aBOD quickly decays with a time constant of 110 ps in water due to quenching of the surrounding aqueous medium the fluorescence lifetime and fluorescence quantum yield significantly rises after binding the dye to a polymer or SCNP. For **polymer Ic** one can see a strong heterogeneity in the decay associated spectra (DAS, Figure 5b) with a spectral separation of two states with distinct different lifetimes of  $1.2 \pm 0.2 \text{ ns}$  (red curve, energetically lower level) and  $2.7 \pm 0.2 \text{ ns}$  (blue curve, energetically higher level) additionally to a fast decay component that is similar to the free dye (black curve,  $220 \pm 50 \text{ ps}$ ) with contributions from molecular interaction (see below). This is caused by a weak and dynamic compartmentation, as depicted in Figure 5e, with partially folded regions in which the dye molecules can have direct contact to each other and free unfolded regions without direct contact between dye molecules that can be quenched by the aqueous surrounding. This heterogeneity between the bound dye molecules also explains the strong inhomogeneous broadening of the absorption band in Figure S6. The absorption is therefore even broader as compared to **SCNP IIIc** because the elongated polymer has a larger degree of freedoms as compared to the SCNP. As the fluorescence maxima of all components in the DAS are similar the observed heterogeneity refers to structural differences rather than excitonic interaction of the different dye molecules.

For **SCNP IIIc** a stronger compartmentation can be observed from the DAS (Figure 5c). The decay components redistribute with distinct different maxima, indicating that absorbed light energy potentially is transferred between strongly coupled dye molecules. Slight spectral separation of the two states which were also observed in **polymer Ic** can be seen. The  $1.2 \pm 0.2 \text{ ns}$  component (red curve) seems to be

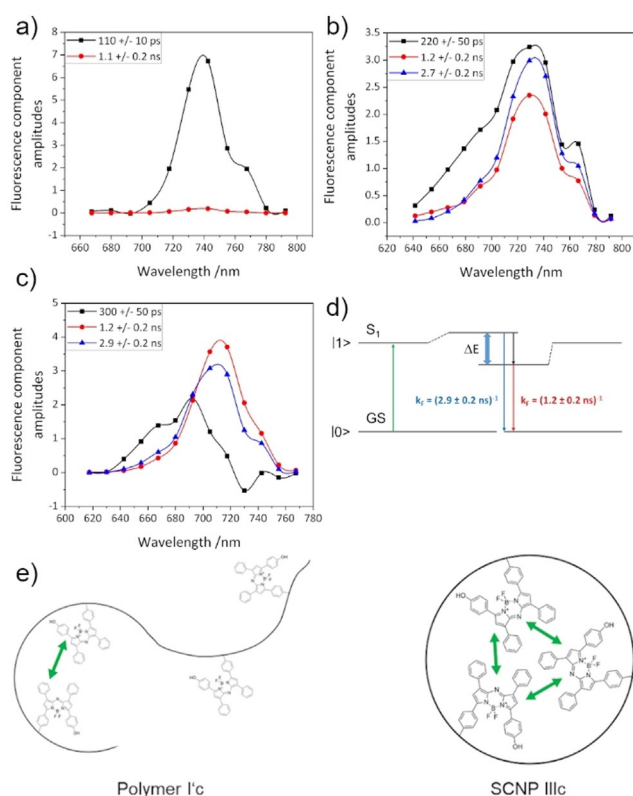


**Figure 5.** Decay associated spectra measured on a) aBOD in water ( $c = 25 \mu\text{M}$ ), b) **polymer I'c** in water ( $c = 0.1 \text{ mg mL}^{-1}$ , dye concentration ca.  $5\text{--}10 \mu\text{M}$ ) and c) **SCNP IIIc** in water ( $c = 0.1 \text{ mg mL}^{-1}$ , dye concentration ca.  $5\text{--}10 \mu\text{M}$ ) after fit with 3 exponential functions (excitation wavelength 632 nm, see SI for further information). d) Excitonic interaction in **SCNP IIIc** and resulting split of the  $S_1$  states and qualitative band structure due to excitonic splitting and/or interaction with the environment of the first excited singlet state ( $S_1$ ). The green arrow indicates the excitation from the ground state (GS) and the blue arrow fluorescence from the higher excitonic level with a time constant of 2.9 ns while fluorescence from the lower level decays with 1.2 ns. e) Schematic interpretation of the time resolved fluorescence spectroscopic data of **polymer I'c** (left side) and **SCNP IIIc** (right side).

emitted from the energetically lower level while the  $2.9 \pm 0.2 \text{ ns}$  component (blue curve) results from the energetically higher level. The fastest component slows down further as compared to **polymer I'c** and was measured  $300 \pm 50 \text{ ps}$  with strong spectral asymmetry and negative value at 730 nm which is typical for an excitonic relaxation from strongly blue shifted states with an emission around 700 nm to the observed fluorescence maximum around 720–730 nm.

The possible band structure in the material is described schematically in Figure 5d. The decay associated spectra in Figure 5c indicate that excitation from the ground state (GS) is followed by radiative decay from the higher state with a time constant of 2.9 ns while fluorescence from the lower state decays with 1.2 ns. Light absorption and relaxation of the exciton induce a complex dynamic into the surrounding polymer and SCNP environment that might cause an apparent relaxation time of about 300 ps possibly accompanied by rearrangements of different compartments or molecular dynamics/conformation changes of the polymer.<sup>[30]</sup>

The spectroscopic properties are strongly determined by the exact localization of the states at the binding sites of the aBOD molecules in **SCNP IIIc**. Specific configuration for the bound molecules by specific molecular design of the binding sites in the SCNP would allow for the creation of highly individual optical properties of the coupled aBOD dyes and allow for the fine tuning of color and fluorescence yield lifetime of the bound molecules.

The location of the aBOD dye in the SCNP's core also affects its  $pK_a$  and thereby its pH-responding functionality. As depicted in Table 2 and Figure S7 the fluorescence of the label is strongly changed by the pH value of the solvent, with a  $pK_a$  of 6.8 for the free aBOD and 7.6 for **SCNP IIIc**. Changing the pH of the **SCNP IIIc** dispersion from 6.0 to 8.6 strongly decreases its fluorescence, by 92%. The pH-responsivity has no strong influence on the fluorescence lifetime (see Figure S8 and S9). The lifetimes in both, the free aBOD dye and **SCNP IIIc**, stay nearly unchanged over the whole pH range, prospective for a proper tumor tissue targeting. These data are in compliance with the overall fluorescence yield shown in Figure S7 with stronger amplitude reduction observed for **SCNP IIIc** (see Figure S9, Figure S7d) as compared to aBOD in solution (Figure S8, Figure S7b).

## Conclusion

In summary we could observe the formation of internal compartments within single chain nanoparticles (SCNP's) via EPR- and fluorescence spectroscopic methods. The SCNPs are synthesized by using a clickable PEGMA based copolymer synthesized by RAFT polymerization, followed by an intramolecular CuAAC within its hydrophobic core. DLS and DOSY-NMR measurements proved single-chain collapse with hydrodynamic radii of 4–5 nm. The water dispersible SCNPs all displayed a  $T_{cp}$  higher than that of the free chain of the native **polymer I**, indicative for the formation of core-shell structured nanoparticles with the hydrophilic PEG chains in the shell and the hydrophobic groups with the embedded labels located inside the core. The inherent dynamics of the SCNPs allows for a medium-responsive nanostructure as indicated by their thermoresponsivities, and the formation of contacts between two or more labels in one SCNP. Definite proof of this compartmented model consisting of a core-shell structure was accomplished via EPR measurements, proving the presence of at least two covalently attached labels within a confined space with distances below 1 nm, surrounded by the non-polar polymer backbone and shielded from outer influences by the particle's shell. Based on the quite unique combination of thermal, EPR and photophysical measurements we could prove the nanocompartmented structure of such SCNPs, consisting of the hydrophobic labels embedded within the corresponding hydrophobic compartments, with the short PEG-chains generating the outer shell. Coupling between dye molecules and the local environment strongly influences their optical properties giving rise to a strategy that allows for specific molecular design of the optical properties. Due to the so enabled shielding of the fluorescent dyes inside the SCNPs,

the fluorescent SCNPs **IIIb** and **IIIc** prospect their application as contrasting agents in photoacoustic imaging, still maintaining their targeting properties uninfluenced by their encapsulation in the SCNPs.

### Acknowledgements

WHB acknowledges funding from the DFG (Deutsche Forschungsgemeinschaft) project BI1337/14-1, the SFB TRR 102, TP A03 Project ID 189853844, the TP B2 in the DFG-GRK 2670. We thank Matthias Hoffmann for the AFM measurements. Open access funding enabled and organized by Projekt DEAL.

### Conflict of interest

The authors declare no conflict of interest.

**Keywords:** amphiphiles · decay associated spectra · EPR spectroscopy · fluorescence spectroscopy · nanostructures · single-chain nanoparticles

- [1] a) E. Verde-Sesto, A. Arbe, A. J. Moreno, D. Cangialosi, A. Alegría, J. Colmenero, J. A. Pomposo, *Mater. Horiz.* **2020**, *7*, 2292–2313; b) J. A. Pomposo, *Single-Chain Polymer Nanoparticles: Synthesis Characterization, Simulations, and Applications*, Wiley-VCH, Weinheim, **2017**.
- [2] a) J. Chen, K. Li, J. S. L. Shon, S. C. Zimmerman, *J. Am. Chem. Soc.* **2020**, *142*, 4565–4569; b) J. Chen, J. Wang, Y. Bai, K. Li, E. S. Garcia, A. L. Ferguson, S. C. Zimmerman, *J. Am. Chem. Soc.* **2018**, *140*, 13695–13702; c) Y. Liu, T. Pauloehrl, S. I. Presolski, L. Albertazzi, A. R. Palmans, E. W. Meijer, *J. Am. Chem. Soc.* **2015**, *137*, 13096–13105; d) J. Rubio-Cervilla, E. Gonzalez, J. A. Pomposo, *Nanomaterials* **2017**, *7*, 341–360.
- [3] a) A. P. P. Kröger, N. M. Hamelmann, A. Juan, S. Lindhoud, J. M. J. Paulusse, *ACS Appl. Mater. Interfaces* **2018**, *10*, 30946–30951; b) A. P. P. Kröger, J. M. J. Paulusse, *J. Controlled Release* **2018**, *286*, 326–347; c) C.-C. Cheng, D.-J. Lee, Z.-S. Liao, J.-J. Huang, *Polym. Chem.* **2016**, *7*, 6164–6169.
- [4] a) J. Steinkoenig, H. Rothfuss, A. Lauer, B. T. Tuten, C. Barner-Kowollik, *J. Am. Chem. Soc.* **2017**, *139*, 51–54; b) C. T. Adkins, J. N. Dobish, S. Brown, E. Harth, *ACS Macro Lett.* **2013**, *2*, 710–714; c) Y. Bai, H. Xing, G. A. Vincil, J. Lee, E. J. Henderson, Y. Lu, N. G. Lemcoff, S. C. Zimmerman, *Chem. Sci.* **2014**, *5*, 2862–2868.
- [5] K. Li, B. Liu, *Chem. Soc. Rev.* **2014**, *43*, 6570–6597.
- [6] a) F. Lo Verso, J. A. Pomposo, J. Colmenero, A. J. Moreno, *Soft Matter* **2015**, *11*, 1369–1375; b) P.-B. Irma, I. Asenjo-Sanz, A. Arbe, A. J. Moreno, F. L. Verso, J. Colmenero, J. A. Pomposo, *Macromolecules* **2014**, *47*, 8270–8280.
- [7] a) M. Artar, E. R. J. Souren, T. Terashima, E. W. Meijer, A. R. A. Palmans, *ACS Macro Lett.* **2015**, *4*, 1099–1103; b) H. Rothfuss, N. D. Knofel, P. W. Roesky, C. Barner-Kowollik, *J. Am. Chem. Soc.* **2018**, *140*, 5875–5881; c) M. Artar, T. Terashima, M. Sawamoto, E. W. Meijer, A. R. A. Palmans, *J. Polym. Sci. Part A* **2014**, *52*, 12–20; d) D. Xiang, B. Jiang, F. Liang, L. Yan, Z. Yang, *Macromolecules* **2020**, *53*, 1063–1069; e) Z. Cui, L. Huang, Y. Ding, X. Zhu, X. Lu, Y. Cai, *ACS Macro Lett.* **2018**, *7*, 572–575.
- [8] a) C. H. Liu, L. D. Dugas, J. I. Bowman, T. Chidanguro, R. F. Storey, Y. C. Simon, *Polym. Chem.* **2020**, *11*, 292–297; b) H. Frisch, J. P. Menzel, F. R. Bloesser, D. E. Marschner, K. Mund-singer, C. Barner-Kowollik, *J. Am. Chem. Soc.* **2018**, *140*, 9551–9557.
- [9] G. M. ter Huurne, M. A. J. Gillissen, A. R. A. Palmans, I. K. Voets, E. W. Meijer, *Macromolecules* **2015**, *48*, 3949–3956.
- [10] M. Gonzalez-Burgos, A. Latorre-Sanchez, J. A. Pomposo, *Chem. Soc. Rev.* **2015**, *44*, 6122–6142.
- [11] H. Frisch, F. R. Bloesser, C. Barner-Kowollik, *Angew. Chem. Int. Ed.* **2019**, *58*, 3604–3609; *Angew. Chem.* **2019**, *131*, 3642–3648.
- [12] G. Renger, J. Pieper, C. Theiss, I. Trostmann, H. Paulsen, T. Renger, H. J. Eichler, F. J. Schmitt, *J. Plant Physiol.* **2011**, *168*, 1462–1472.
- [13] P. J. M. Stals, C. Y. Cheng, L. v. Beek, A. C. Wauters, A. R. A. Palmans, S. Han, E. W. Meijer, *Chem. Sci.* **2016**, *7*, 2011–2015.
- [14] T. Terashima, T. Sugita, K. Fukae, M. Sawamoto, *Macromolecules* **2014**, *47*, 589–600.
- [15] J. Märk, A. Wagener, E. Zhang, J. Laufer, *Sci. Rep.* **2017**, *7*, 40496.
- [16] A. B. Benito, M. K. Aiertza, M. Marradi, L. Gil-Iceta, T. S. Zahavi, B. Szczupak, M. Jimenez-Gonzalez, T. Reese, E. Scanziani, L. Passoni, M. Matteoli, M. D. Maglie, A. Orenstein, M. Oron-Herman, G. Kostenich, L. Buzhansky, E. Gazit, H. J. Grande, V. Gomez-Vallejo, J. Llop, I. Loinaz, *Biomacromolecules* **2016**, *17*, 3213–3221.
- [17] D. E. Whitaker, C. S. Mahon, D. A. Fulton, *Angew. Chem. Int. Ed.* **2013**, *52*, 956–959; *Angew. Chem.* **2013**, *125*, 990–993.
- [18] E. H. H. Wong, S. J. Lam, E. Nam, G. G. Qiao, *ACS Macro Lett.* **2014**, *3*, 524–528.
- [19] Y. Tsuru, M. Kohri, T. Taniguchi, K. Kishikawa, T. Karatsu, M. Hayashi, *J. Colloid Interface Sci.* **2019**, *547*, 318–329.
- [20] S. H. Thang, B. Y. K. Chong, R. T. A. Mayadunne, G. Moad, E. Rizzardo, *Tetrahedron Lett.* **1999**, *40*, 2435–2438.
- [21] a) B. S. Sumerlin, N. V. Tsarevsky, G. Louche, R. Y. Lee, K. Matyjaszewski, *Macromolecules* **2005**, *38*, 7540–7545; b) V. Ladmiraal, G. Mantovani, G. J. Clarkson, S. Cauet, J. L. Irwin, D. M. Haddleton, *J. Am. Chem. Soc.* **2006**, *128*, 4823–4830.
- [22] a) X. Wang, J. Huang, L. Chen, Y. Liu, G. Wang, *Macromolecules* **2014**, *47*, 7812–7822; b) R. H. Staff, J. Willersinn, A. Musyanovich, K. Landfester, D. Crespy, *Polym. Chem.* **2014**, *5*, 4097–4104; c) X. Chen, Q. Wu, L. Henschke, G. Weber, T. Weil, *Dyes Pigm.* **2012**, *94*, 296–303; d) J. Murtagh, D. O. Frimannsson, D. F. O'Shea, *Org. Lett.* **2009**, *11*, 5386–5389; e) P. Wang, H. Pu, J. Ge, M. Jin, H. Pan, Z. Chang, D. Wan, *Mater. Lett.* **2014**, *132*, 102–105.
- [23] N. Ormategui, I. García, D. Padro, G. Cabañero, H. J. Grande, I. Loinaz, *Soft Matter* **2012**, *8*, 734–740.
- [24] a) W. H. Binder, R. Sachsenhofer, *Macromol. Rapid Commun.* **2008**, *29*, 952–981; b) S. Neumann, M. Biewend, S. Rana, W. H. Binder, *Macromol. Rapid Commun.* **2020**, *41*, 1900359.
- [25] X. Liu, B. Chen, X. Li, L. Zhang, Y. Xu, Z. Liu, Z. Cheng, X. Zhu, *Nanoscale* **2015**, *7*, 16399–16416.
- [26] E. Blasco, B. T. Tuten, H. Frisch, A. Lederer, C. Barner-Kowollik, *Polym. Chem.* **2017**, *8*, 5845–5851.
- [27] a) C.-C. Cheng, F.-C. Chang, H.-C. Yen, D.-J. Lee, C.-W. Chiu, Z. Xin, *ACS Macro Lett.* **2015**, *4*, 1184–1188; b) A. P. P. Kröger, R. J. E. A. Boonen, J. M. J. Paulusse, *Polymer* **2017**, *120*, 119–128.
- [28] a) D. Kurzbach, M. J. Junk, D. Hinderberger, *Macromol. Rapid Commun.* **2013**, *34*, 119–134; b) J. Hunold, T. Wolf, F. R. Wurm, D. Hinderberger, *Chem. Commun.* **2019**, *55*, 3414–3417; c) M. J. N. Junk, W. Li, A. D. Schlüter, G. Wegner, H. W. Spiess, A. Zhang, D. Hinderberger, *Macromol. Chem. Phys.* **2011**, *212*, 1229–1235.
- [29] F. Collette, T. Renger, M. S. a. Busch, *J. Phys. Chem. B* **2014**, *118*, 11109–11119.

[30] a) F.-J. Schmitt, I. Trostmann, C. Theiss, J. Pieper, T. Renger, J. Fuesers, E. Hubrich, H. Paulsen, H. J. Eichler, G. Renger, *J. Phys. Chem. B* **2008**, *112*, 13951–13961; b) D. Buhrke, F. V. Escobar, L. Sauthof, S. Wilkening, N. Herder, N. N. Tavraz, M.

Willoweit, A. Keidel, T. Utesch, M.-A. Mroginski, F.-J. Schmitt, P. Hildebrandt, T. Friedrich, *Sci. Rep.* **2016**, *6*.

Manuscript received: November 13, 2020  
Revised manuscript received: December 13, 2020  
Accepted manuscript online: December 29, 2020  
Version of record online: February 25, 2021

2023  
02

# [M]acro- [M]olecular

## Rapid Communications

### PHOTOACOUSTIC IMAGING

In article 2200618 by Wolfgang H. Binder and co-workers, NIR fluorescent aza-BODIPY molecules are encapsulated in the hydrophobic core of a compartmented single-chain nanoparticle, in turn generating an efficient photoacoustic signal in water by pump-probe excitation.

# Tuning the Internal Compartmentation of Single-Chain Nanoparticles as Fluorescent Contrast Agents

Justus F. Thümmeler, Andreas H. Roos, Jana Krüger, Dariush Hinderberger, Franz-Josef Schmitt, Guo Tang, Farzin Ghane Golmohamadi, Jan Laufer, and Wolfgang H. Binder\*

Controlling the internal structures of single-chain nanoparticles (SCNPs) is an important factor for their targeted chemical design and synthesis, especially in view of nanosized compartments presenting different local environments as a main feature to control functionality. We here design SCNPs bearing near-infrared fluorescent dyes embedded in hydrophobic compartments for use as contrast agents in pump–probe photoacoustic (PA) imaging, displaying improved properties by the location of the dye in the hydrophobic particle core. Compartment formation is controlled via single-chain collapse and subsequent crosslinking of an amphiphilic polymer using external crosslinkers in reaction media of adjustable polarity. Different SCNPs with hydrodynamic diameters of 6–12 nm bearing adjustable label densities are synthesized. It is found that the specific conditions for single-chain collapse have a major impact on the formation of the desired core–shell structure, in turn adjusting the internal nanocompartments together with the formation of excitonic dye couples, which in turn increase their fluorescence lifetime and PA signal generation. SCNPs with the dye molecules accumulate at the core also show a nonlinear PA response as a function of pulse energy—a property that can be exploited as a contrast mechanism in molecular PA tomography.

## 1. Introduction

Single-chain nanoparticles (SCNPs) are nanostructured, enzyme-like particles that are made of a single polymer chain collapsed and intramolecularly crosslinked either covalently or non-covalently. The countless possibilities of chemical functionalities, synthetic routes, and unique nanostructures enable their use in modern research, like (enzyme like) catalysis,<sup>[1]</sup> antifouling,<sup>[2]</sup> or biomedical applications.<sup>[3]</sup> Their internal structures allow the embedding of functional units like fluorescent dyes in specific regions inside these particles.<sup>[4]</sup> Choice of the polymer backbone embeds biocompatibility<sup>[5]</sup> or degradability,<sup>[6]</sup> changes in the polymer's architecture<sup>[7]</sup> and the use of crosslinkers for specific covalent or non-covalent collapse reaction types<sup>[8]</sup> as well as the collapse medium are main factors to reach compartments inside a SCNP.<sup>[9]</sup>

There are only few reports on a precise control of nanosized compartments inside SCNPs, as they are dynamic entities

before and even during the crosslinking process. The formation of compartmented SCNPs<sup>[7a]</sup> using grafted tri-block copolymers of ABC and ACB type as precursors has been described, displaying differential miscibilities where block A and C are compatible with each other, but block B is compatible with neither. Collapse into SCNPs was accomplished by core crosslinking via photodimerization of cinnamic acid side chains, in turn proving the formation of discrete A, B, and C domains inside the SCNPs. It was shown that the correct choice of both, the surrounding medium of collapse and the crosslinker have a major influence on the SCNP's shape, highlighting the importance of precollapsing the precursor polymer in a poor solvent before the actual crosslinking reaction to yield more globular shaped particles.<sup>[10]</sup> Both, pre-collapsing and the use of long crosslinkers cause long-range crosslink loops that result in more compact and globular nanoparticles. A similar behavior was found via photocrosslinking a purely hydrophobic polymer either in THF, in hexane, or mixtures of both, resulting in differently dense particles with variable crosslink densities, thus proving the compartmentation of the precursor polymer already in the collapse medium.<sup>[11]</sup>

In our previous work<sup>[12]</sup> we have demonstrated the formation of compartmented core–shell structured SCNPs by single-chain

J. F. Thümmeler, W. H. Binder  
 Macromolecular Chemistry, Institute of Chemistry, Faculty of Natural Science II (Chemistry, Physics and Mathematics)  
 Martin Luther University Halle-Wittenberg  
 von-Danckelmann-Platz 4, D-06120 Halle, Germany  
 E-mail: wolfgang.binder@chemie.uni-halle.de

A. H. Roos, J. Krüger, D. Hinderberger  
 Physical Chemistry, Institute of Chemistry, Faculty of Natural Science II (Chemistry, Physics and Mathematics)  
 Martin Luther University Halle-Wittenberg  
 von-Danckelmann-Platz 4, D-06120 Halle, Germany

F.-J. Schmitt, G. Tang, F. G. Golmohamadi, J. Laufer  
 Institute of Physics, Faculty of Natural Science II (Chemistry, Physics and Mathematics)  
 Martin Luther University Halle-Wittenberg  
 von-Danckelmann-Platz 3, D-06120 Halle, Germany

 The ORCID identification number(s) for the author(s) of this article can be found under <https://doi.org/10.1002/marc.202200618>

© 2022 The Authors. Macromolecular Rapid Communications published by Wiley-VCH GmbH. This is an open access article under the terms of the Creative Commons Attribution-NonCommercial-NoDerivs License, which permits use and distribution in any medium, provided the original work is properly cited, the use is non-commercial and no modifications or adaptations are made.

DOI: 10.1002/marc.202200618

collapse of an amphiphilic polymer in an aqueous crosslinking medium. The hydrophobic crosslinking groups were located at the particle core with a size of 1-2 nm while the hydrophilic PEG side chains formed a water-soluble shell. By covalently binding either a fluorescent or a radical label to unreacted crosslinking sites, we were able to prove their location at the core via fluorescence and electron-paramagnetic-resonance spectroscopy.<sup>[12a]</sup> The hydrophobic core was still swollen with water molecules, depleted by increasing the temperature.<sup>[12b]</sup> Different properties of the individual compartments could be proven since the core and shell displayed largely different cloud point temperatures.

In this study, we demonstrate the controlled formation of different nanosized compartments in amphiphilic single-chain nanoparticles by collapsing in different reaction media to specifically embed and protect a fluorescent dye for application in photoacoustic (PA) measurements. The embedding into such compartments is expected to result in enhanced photophysical properties in aqueous solution, such as significantly enlarged fluorescence lifetimes, as the dye molecules are then located in the nonpolar, nanosized compartments able to form excitonic couples, undisturbed by the aqueous surrounding. Furthermore, the embedding into such SCNPs with hydrodynamic diameters of  $\approx 10$  nm should be advantageous for the dye's biodistribution and for tissue specific targeting, making the labeled SCNPs good candidates as contrast agents for biomedical applications. We are using the copper catalyzed azide/alkyne click reaction (CuAAC) in either water or in THF using external bivalent crosslinkers for single-chain collapse to effect the formation of compartments. Several spectroscopic methods are used, such as continuous wave electron-paramagnetic-resonance (CW EPR) spectroscopy, standard and time resolved fluorescence spectroscopy, and photoacoustic (PA) pump-probe spectroscopy, a method that exploits long lived excited states in fluorophores.<sup>[13]</sup> The near-infrared fluorescent dye aza-BODIPY is exploited as a crosslinker due to its optical properties being strongly dependent on the local environment,<sup>[12a]</sup> thus paving the way toward a targeted design of dye-encapsulating SCNP contrast agents for optical and PA imaging.

## 2. Results and Discussion

### 2.1. Polymer and Single-Chain Nanoparticle Synthesis

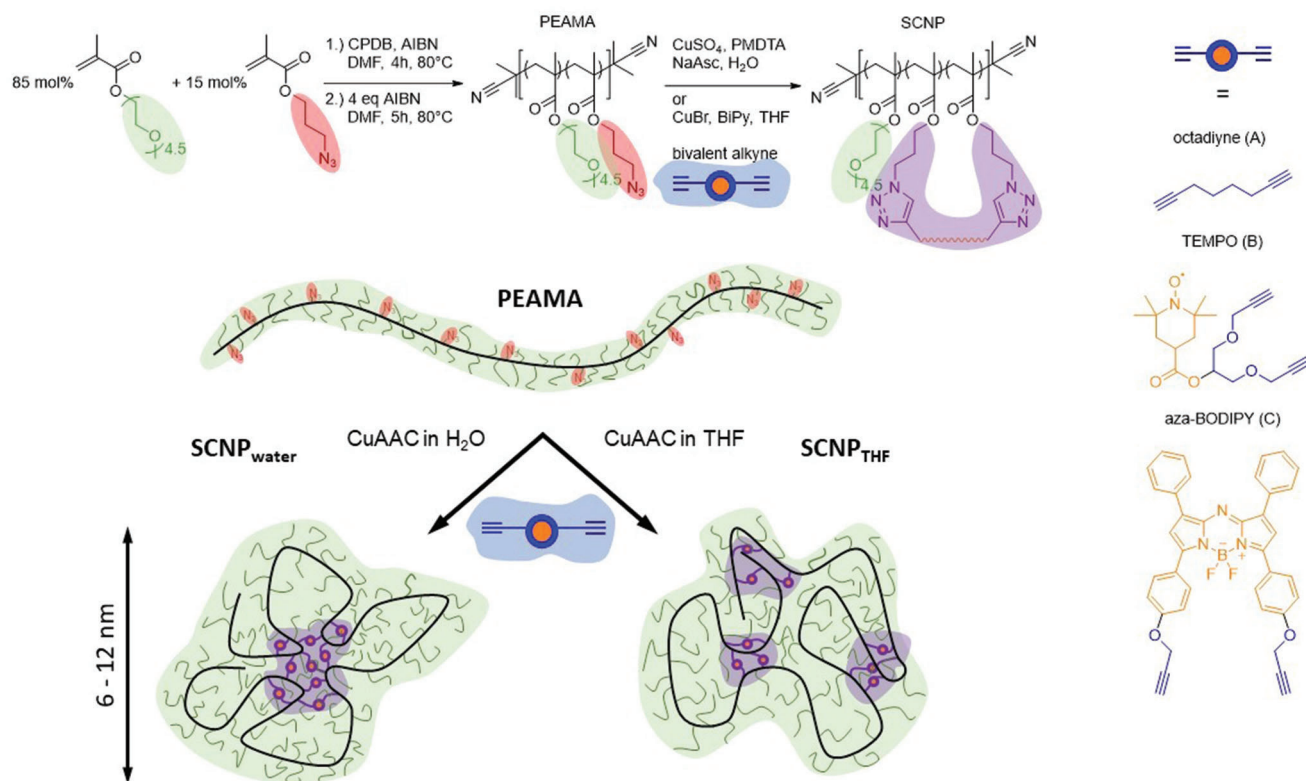
The first step in the design of compartmented SCNPs is the chemical synthesis of the polymeric precursor bearing the desired amphiphilicity, coupled to the inherently present crosslinking sites to stabilize the initially formed compartments. We here relied on RAFT-polymerization of a set of hydrophobic and hydrophilic monomers, reaching a sufficiently high molecular weight ( $> 30$  kDa), coupled to the desired amphiphilic properties. The monomers, the chain transfer agent (CTA), and the crosslinking labels were synthesized according to literature with small adaptations (see Supporting Information).<sup>[14]</sup> The amphiphilic azide containing precursor polymer was synthesized by RAFT copolymerization of poly(ethylene glycol)<sub>n</sub> methacrylate ( $M_n$  (PEG) = 198 Da,  $n = 4.5$ , 85 mol%) and 3-azidopropyl methacrylate (15 mol%) in DMF using cyanoisopropyl dithiobenzoate (CPDB) as CTA and azobisisobutyronitrile (AIBN) as initiator. The CTA end group of the resulting polymer was removed

using an excess of AIBN. Subsequently the polymer was purified by dialysis in THF (10 kDa cutoff) to obtain poly[(poly(ethylene glycol) methacrylate)-co-(3-azidopropyl methacrylate)] (PEAMA,  $M_n = 34.6$  kDa,  $PDI = 1.4$ ,  $DP = 129$ ). The reached degree of polymerization of 129 and an azide content of 15 mol% allows an average of 19-20 crosslinking sites and thus 9-10 bivalent crosslinkers per collapsed polymer, prospectively embedding up to this number of label molecules, dependent on the ratio of the labeled crosslinker.

Single-chain collapse was accomplished in water and THF by CuAAC of pendant azide groups along the polymer chain together with external bis-alkynes as crosslinkers. This allows a fast and complete reaction of the crosslinkers in both reaction media, coupled to a complete removal of the Cu-salts after crosslinking.<sup>[15]</sup> Both, the precursor polymer and the crosslinker were dissolved in THF and added slowly either to a vigorously stirred aqueous solution containing CuSO<sub>4</sub>, sodium ascorbate (NaAsc), and *N,N,N',N''*-pentamethyldiethylenetriamine (PMDTA) to achieve SCNPs with a compartmented core-shell structure; or to a vigorously stirred THF solution containing CuBr and 2,2'-bipyridine, to achieve SCNPs with a differently compartmented structure. The polymer-crosslinker solution was added via a syringe pump (10 mgmL<sup>-1</sup>, 20 mL, 1 mLh<sup>-1</sup>) ensuring low concentrations of reactive groups during the whole reaction time to prevent interchain crosslinking. As crosslinkers octadiyne (A), and the alkyne functionalized derivatives of 2,2,6,6-tetramethylpiperidinyloxy (TEMPO, B) or aza-BODIPY (C) were used as depicted in **Scheme 1**. To further achieve different label densities in the resulting SCNPs, different molar mixtures of octadiyne with aza-BODIPY or TEMPO were used during the collapse reaction, either with the pure crosslinker, or mixtures with 50 mol% octadiyne/50 mol% label, and with 75 mol% octadiyne/25 mol% label (see **Table 1**). The samples are named as SCNP<sub>[collapse medium]</sub>A<sub>[mol% octadiyne]</sub>B/C<sub>[mol% TEMPO or aza-BODIPY]</sub>. Intense purification was done by extraction, column chromatography, and dialysis with different solvents (10 kDa cutoff, see Supporting Information for further details) to remove potentially unreacted label and residues of the copper catalysts. Complete reaction of all azides on the polymer side chains was followed by attenuated total reflection infrared (ATR-IR) spectroscopy, demonstrating the complete removal of the azide band at 2100 cm<sup>-1</sup> under all reaction conditions as can be seen in Figure S1 (Supporting Information).

### 2.2. Single-Chain Nanoparticle Characterization

Diffusion-ordered NMR spectroscopy (DOSY-NMR) in D<sub>2</sub>O, dynamic light scattering (DLS) in water, and size exclusion chromatography (SEC) in THF independently proved the formation of single-chain nanoparticles by showing reductions of the hydrodynamic diameters  $D_h$  for all SCNPs after the collapse reaction, compared to the precursor polymer PEAMA (see **Table 1**, **Figure 1b**, and **Figures S2 and S4**, Supporting Information). DLS measurements of aza-BODIPY labeled SCNPs were not possible due to absorption of the laser of the instrument (see Supporting Information). DOSY-NMR experiments showed size reductions of 4-53% for all SCNPs compared to the precursor polymer PEAMA as seen in **Figure 1b**. For the initial PEAMA a



**Scheme 1.** RAFT polymerization of the precursor polymer PEAMA followed by single-chain collapse into labeled and unlabeled SCNPs in different reaction media and with different crosslinkers. All reaction conditions yielded SCNPs with hydrodynamic diameters of 6–12 nm. Collapse in different media resulted in the formation of different nanocompartments with the polar PEG chains (green) in the shell (green) and the non-polar crosslinking groups (azide—red, alkyne—blue, reacted crosslinkers—violet, labels—orange) in the compartmented crosslinked cores (violet).

**Table 1.** Data of the synthesized SCNPs and their precursor polymer PEAMA: label type, number of label molecules per SCNP, hydrodynamic diameter  $D_h$  as measured by DLS and DOSY-NMR, cloud point temperatures  $T_{cp}$  as measured by turbidimetry, and the average height in AFM topographies of the precursor polymer PEAMA and the resulting SCNPs.

Sample name	Label	Labels per particle <sup>a)</sup>	$D_{h, DLS}^{b,c)}$ [nm]	$D_{h, DOSY}^{d)}$ [nm]	$T_{cp}^{e)}$ [°C]	AFM height [nm]
PEAMA	–	–	$10.4 \pm 1.8$	$12.6 \pm 0.11$	57.9	$21.5 \pm 1.7^f)$
SCNP <sub>water</sub> A <sub>100</sub>	–	0	$7.4 \pm 1.3$	$7.8 \pm 0.05$	65.2	$6.3 \pm 0.5$
SCNP <sub>THF</sub> A <sub>100</sub>	–	0	$7.2 \pm 1.1$	$5.8 \pm 0.03$	66.2	$4.2 \pm 0.5$
SCNP <sub>water</sub> B <sub>100</sub>	TEMPO	9–10	$8.9 \pm 1.7$	$7.7 \pm 0.13$	61.2	$5.8 \pm 0.4$
SCNP <sub>THF</sub> B <sub>100</sub>	TEMPO	9–10	$8.2 \pm 1.5$	$6.3 \pm 0.01$	62.9	$1.7 \pm 0.7$
SCNP <sub>water</sub> A <sub>50</sub> B <sub>50</sub>	TEMPO	4–5	$9.1 \pm 0.9$	$10.1 \pm 0.06$	60.7	$8.6 \pm 0.9$
SCNP <sub>THF</sub> A <sub>50</sub> B <sub>50</sub>	TEMPO	4–5	$9.4 \pm 1.1$	$11.3 \pm 0.05$	65.5	$1.3 \pm 0.1$
SCNP <sub>water</sub> A <sub>75</sub> B <sub>25</sub>	TEMPO	2–3	$8.6 \pm 1.5$	$11.6 \pm 0.02$	59.5	$5.8 \pm 0.4$
SCNP <sub>THF</sub> A <sub>75</sub> B <sub>25</sub>	TEMPO	2–3	$9.8 \pm 1.5$	$12.1 \pm 0.15$	71.5	$3.5 \pm 0.5$
SCNP <sub>water</sub> C <sub>100</sub>	aza-BODIPY	9–10	–	$9.7 \pm 0.17$	59.5	$5.4 \pm 0.1$
SCNP <sub>THF</sub> C <sub>100</sub>	aza-BODIPY	9–10	–	$10.6 \pm 0.10$	67.5	$5.5 \pm 0.2$
SCNP <sub>water</sub> A <sub>50</sub> C <sub>50</sub>	aza-BODIPY	4–5	–	$9.4 \pm 0.03$	57.4	$3.6 \pm 0.4$
SCNP <sub>THF</sub> A <sub>50</sub> C <sub>50</sub>	aza-BODIPY	4–5	–	$7.4 \pm 0.05$	70.4	$4.9 \pm 0.1$
SCNP <sub>water</sub> A <sub>75</sub> C <sub>25</sub>	aza-BODIPY	2–3	–	$9.4 \pm 0.04$	62.5	$3.2 \pm 0.4$
SCNP <sub>THF</sub> A <sub>75</sub> C <sub>25</sub>	aza-BODIPY	2–3	–	$7.2 \pm 0.12$	67.8	$3.2 \pm 0.1$

<sup>a)</sup> Calculated from the initial mol% of azide monomer during polymerization, the  $M_n$  of the precursor polymer PEAMA, and the mol% of labeled crosslinker during the collapse reaction. <sup>b)</sup> Measured by DLS in H<sub>2</sub>O at 1 mg mL<sup>-1</sup>. <sup>c)</sup> DLS measurements for aza-BODIPY labeled SCNPs were not possible due to absorption of the irradiation wavelength of the scattering laser. <sup>d)</sup> Measured by DOSY-NMR in D<sub>2</sub>O at 1 mg mL<sup>-1</sup>, calculated using the Stokes–Einstein equation ( $D_h = (k_B \cdot T) / (3 \cdot \pi \cdot \eta \cdot D)$ ) with the diffusion coefficient  $D$ ,  $\eta_{D2O} = 1.25$  mPa s). <sup>e)</sup> Cloud point temperature measured by turbidimetry at concentrations of 1 mg mL<sup>-1</sup>,  $T_{cp} = T$  at 50% transmittance. <sup>f)</sup> Larger size for PEAMA caused by agglomeration of multiple polymer chains, no single chains were detectable.

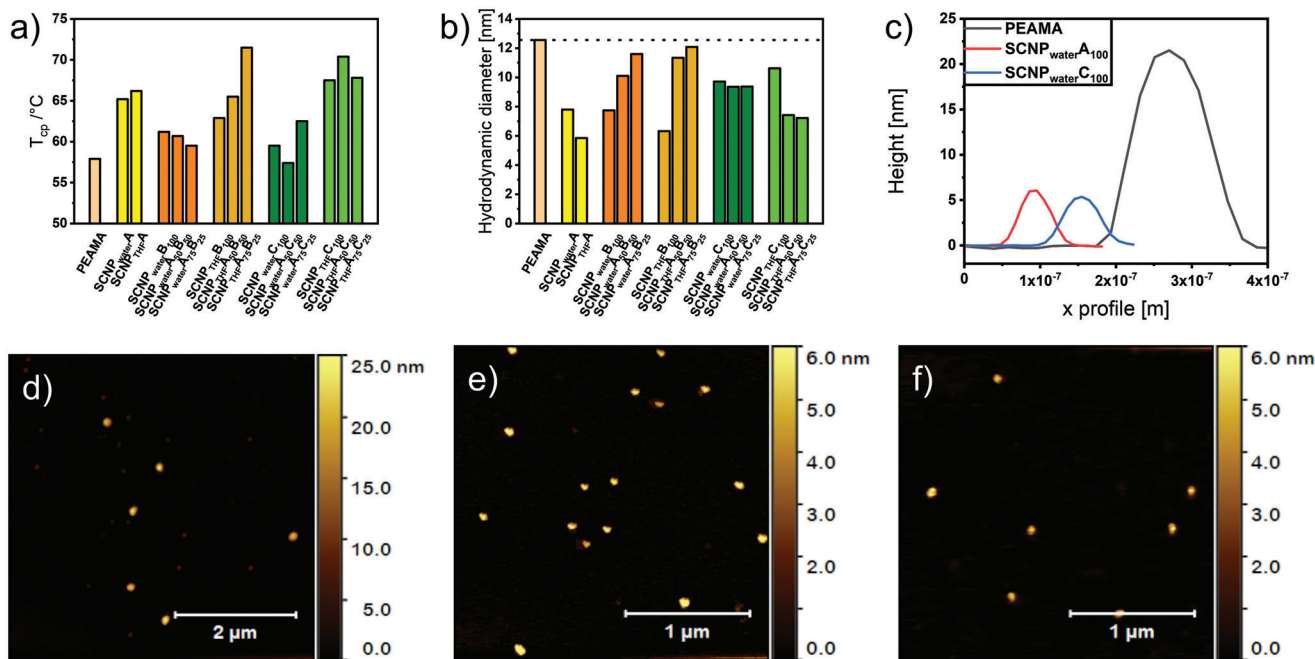


**Figure 1.** a) Cloud point temperatures  $T_{cp}$  of the precursor polymer PEAMA and the SCNPs. Complete turbidimetry measurements are shown in Figure S5, Supporting Information. b) Hydrodynamic diameter of PEAMA and the SCNPs as determined by DOSY-NMR. c) Average profiles of the precursor polymer PEAMA,  $SCNP_{water A_{100}}$ , and  $SCNP_{water C_{100}}$ , as extracted from AFM topographies. d–f) AFM topographies of PEAMA,  $SCNP_{water A_{100}}$ , and  $SCNP_{water C_{100}}$ , respectively. AFM topographies of all SCNPs are shown in Figure S6, Supporting Information.

hydrodynamic diameter of 12.6 nm was measured. The strongest size reduction was found for  $SCNP_{THF A_{100}}$  with a hydrodynamic diameter of 5.8 nm. DOSY-NMR also revealed that the size reduction is dependent on the crosslinker mixture. Adding B and octadiyne as crosslinkers during the collapse is leading to an increased hydrodynamic diameter from 7.7 nm for  $SCNP_{water B_{100}}$  and 6.3 nm for  $SCNP_{THF B_{100}}$  to 11.6 nm for  $SCNP_{water A_{75} B_{25}}$  and 12.1 nm for  $SCNP_{THF A_{75} B_{25}}$ , respectively. We attribute this effect either to long range crosslink reactions being less effective for the crosslinker mixtures, or to a less effective pre-collapsing behavior when octadiyne and B are mixed during the collapse.<sup>[10]</sup> This effect is not present for the aza-BODIPY dye C showing that the long-range crosslink and pre-collapsing behavior of C is less effected when mixed with octadiyne.

In contrast to SEC measurements in THF, SEC measurements in water show an exact opposite behavior of the peak shifts for the labeled SCNPs as seen in Figure S3 (Supporting Information). As reported earlier,<sup>[12a]</sup> this behavior is caused by changes of the polarity of the polymer in response to the surrounding solvent. As after single-chain collapse the nonpolar crosslinking groups are in reduced contact with the aqueous solvation shell, the now increased polarity of the particle shell leads to a partially enthalpic, and therefore not only size but also polarity driven separation on the aqueous SEC column, an effect already described by Barner-Kowollik et al.<sup>[16]</sup> The formation of those compartments of different polarity is also evident in the LCST-behavior of the precursor polymer and the therefrom derived SCNPs in Figure 1a and Figure S5 (Supporting Information): collapsing the polymer into SCNPs always leads to higher cloud point temperatures, caused by the formation of hydrophobic compartments within the SCNPs,

with the crosslinking groups located in these compartments, expectedly surrounded by the hydrophilic PEG side chains, thus increasing the SCNP's solubility in water. A second effect in the  $T_{cp}$  measurements is the difference caused by the choice of the collapse medium. SCNPs collapsed in THF always tend to display higher  $T_{cp}$  values than those collapsed in water. This effect can be attributed to the formation of more open structures when the collapse is performed in THF, in turn increasing the SCNP's solubility and thus its  $T_{cp}$ . In contrast, single-chain collapse in water leads to the formation of denser structures with lower water permeability. Together with the results from SEC, this is a first indication of the formation of different compartments inside the SCNPs depending on the surrounding medium during single-chain collapse.

As electron microscopy (TEM) did not yield interpretable pictures, we further proved the formation of distinct single-chain nanoparticles by atomic force microscopy (AFM) topographies as seen in Figure 1c–f and Figure S6 (Supporting Information). The average height of the precursor polymer PEAMA on the mica surface was found to be 21.5 nm (Figure 1d) showing agglomerations of multiple polymer chains on the surface, with single polymer chains not detectable. The AFM topography images of  $SCNP_{water A_{100}}$  and  $SCNP_{water C_{100}}$  in Figure 1e,f show single particles on the mica surface with average heights of 6.3 and 5.4 nm, respectively. Although all average heights of the SCNPs found by AFM (see Figure S6, Supporting Information for all topographies) are smaller than the hydrodynamic diameters measured by DLS and DOSY-NMR, the values are fitting well since SCNPs tend to lose their spherical shape on the mica surface and therefore display smaller sizes.<sup>[17]</sup> Additionally, AFM measures the heights

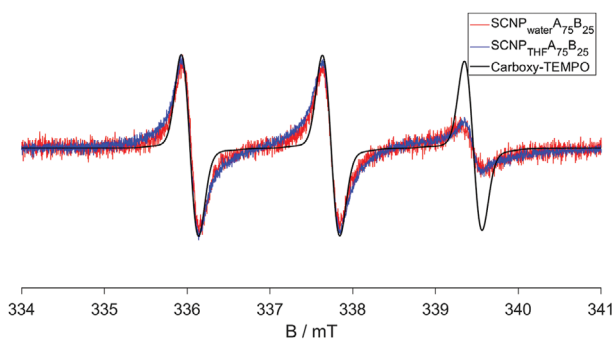


**Figure 2.** EPR-spectra of  $\text{SCNP}_{\text{water}}\text{A}_{75}\text{B}_{25}$  and  $\text{SCNP}_{\text{THF}}\text{A}_{75}\text{B}_{25}$  measured in water at 20 °C with a concentration of 10  $\text{mgmL}^{-1}$  in water, and of carboxy-TEMPO measured in water at 20 °C with a concentration of 1 mM in water. The spectra were normalized to the center peak.

of the particles without their solvation shell leading to apparently smaller values.

### 2.3. Internal Structure Analysis of Differently Collapsed SCNPs by EPR Spectroscopy

Labeling SCNPs with TEMPO (B) enabled to probe location, distribution, and movement of the labeled crosslinkers inside the SCNPs via electron-paramagnetic-resonance (EPR) spectroscopy. When compared to the EPR spectra of the non-bound nitroxide radical, strong changes in the spectra of the nitroxide labeled SCNPs prove the formation of differently compartmented structures, dependent on the collapse media and the crosslinker mixtures that were used as shown in **Figure 2**. Simulations of the measured spectra (see Figures S7 and S8, and Table S1, Supporting Information) revealed the presence of up to three label species per SCNP, additionally proving the formation of compartments. For all labeled SCNPs Heisenberg coupling was found with exchange coupling constants of 2.5–3.0 MHz, with higher values for those SCNPs synthesized in water (see Table S1, Supporting Information): an important effect, as Heisenberg coupling only occurs, when two or more labels get closer than 1 nm, thus proving that the labels are concentrated into specific compartments rather than being homogeneously distributed along the SCNP.<sup>[12]</sup> The  $\tau$  values in species 1 (see Table S1, Supporting Information), which represent the rotational mobility of the TEMPO labels, were measured to be higher for those SCNPs that were synthesized in water, hence showing a stronger reduction in mobility for those labels. As proposed from the results from the  $T_{\text{cp}}$  measurements, this is a further proof of the formation of denser compartments for these SCNPs and therefore of less dense compartments for those SCNPs synthesized in THF. Simulations of the spectrum of  $\text{SCNP}_{\text{water}}\text{B}_{100}$  revealed the presence of a third species without Heisenberg coupling. This indicates a position of these label molecules outside the compartments with a distance of more than 1 nm from other labels. In addition, lower  $\tau$  values indicate a much faster movement. Hence, this label species is located on the outer shell of the particles where its movement is less strong hindered. This proves that a collapse in water without a second, unlabeled crosslinker results in a reduced compartmentation and a less pronounced effective core-shell structure.

### 2.4. Influence of Different Compartmentations on Photophysical Properties of Fluorescent SCNPs

The effect of the compartmentation of the SCNPs on the optical and thermomechanical properties of the dye aza-BODIPY (C) as crosslinker is important for their envisaged application as contrast agent in fluorescence and PA imaging, as high extinction coefficients, high fluorescence quantum yields, and long fluorescence lifetimes are advantageous for the desired pump-probe excitation.<sup>[18]</sup> The absorption and fluorescence spectra of non-bound aza-BODIPY in water are shown in Figures S9 and S10 (Supporting Information). Since the dye itself is not soluble in water, it was kept in aqueous solution with the surfactant Kolliphor EL (see Supporting Information). The absorption spectrum shows a maximum at 695 nm with Lambert–Beer behavior over the entire concentration range (see Figure S9b, Supporting Information). The fluorescence spectra in Figure S10 (Supporting Information) with a maximum at 720 nm lose their linear behavior at concentrations higher than  $8 \times 10^{-6}$  M. The effects of high concentrations on the fluorescence intensity and the wavelength maximum are shown in Figure S10b,c (Supporting Information).

Covalently binding the aza-BODIPY dye to the nanoparticles significantly changes its optical behavior as seen in **Figure 3a,b**. In the absorption spectra of water collapsed SCNPs in Figure 3a the shoulder at 647 nm shows an increased intensity compared to the non-bound dye, independently from the aza-BODIPY load inside the particle. Additionally there is a new absorption band for  $\text{SCNP}_{\text{water}}\text{A}_{50}\text{C}_{50}$  at 765 nm. The absorption spectra of the THF collapsed SCNPs in Figure 3b show a markedly different behavior with an absorption band at 647 nm that increases with increasing aza-BODIPY content per particle, caused by the formation of different types of compartments inside the SCNPs depending on the collapse medium and the ratio between aza-BODIPY and octadiyne during the crosslink reaction.

The internal structure of the SCNPs and the dye content has a significant effect on the fluorescence intensity and thus their usefulness for pump-probe excitation. When collapsed in THF, the incorporation of the aza-BODIPY molecules to the SCNP leads to a decreased fluorescence intensity (see Figure 3b) which is reduced further with increasing aza-BODIPY load inside the particle by fluorescence quenching indicative of a rather polar environment of the dye molecules with direct contact to water for this type of SCNPs. By contrast, water-collapsed SCNPs form a core-shell structure where the aza-BODIPY molecules are located in the non-polar core of the particle due to their hydrophobicity. The fluorescence spectra of the co-crosslinked SCNPs that were collapsed in water support this hypothesis by showing a significant increase in intensity. Additionally,  $\text{SCNP}_{\text{water}}\text{A}_{75}\text{C}_{25}$  shows a fluorescence intensity that is only 25% lower than that of  $\text{SCNP}_{\text{water}}\text{A}_{50}\text{C}_{50}$  even though the dye concentration is 50% lower indicating a more effective formation of the non-polar core. When aza-BODIPY is solely used as crosslinker during the collapse reaction, the formation of a core-shell structure is less effective, inline with EPR measurements. This increases the polarity of the surrounding medium of the individual dye molecules in the SCNP, yielding lower fluorescence intensities (see **Scheme 2**).

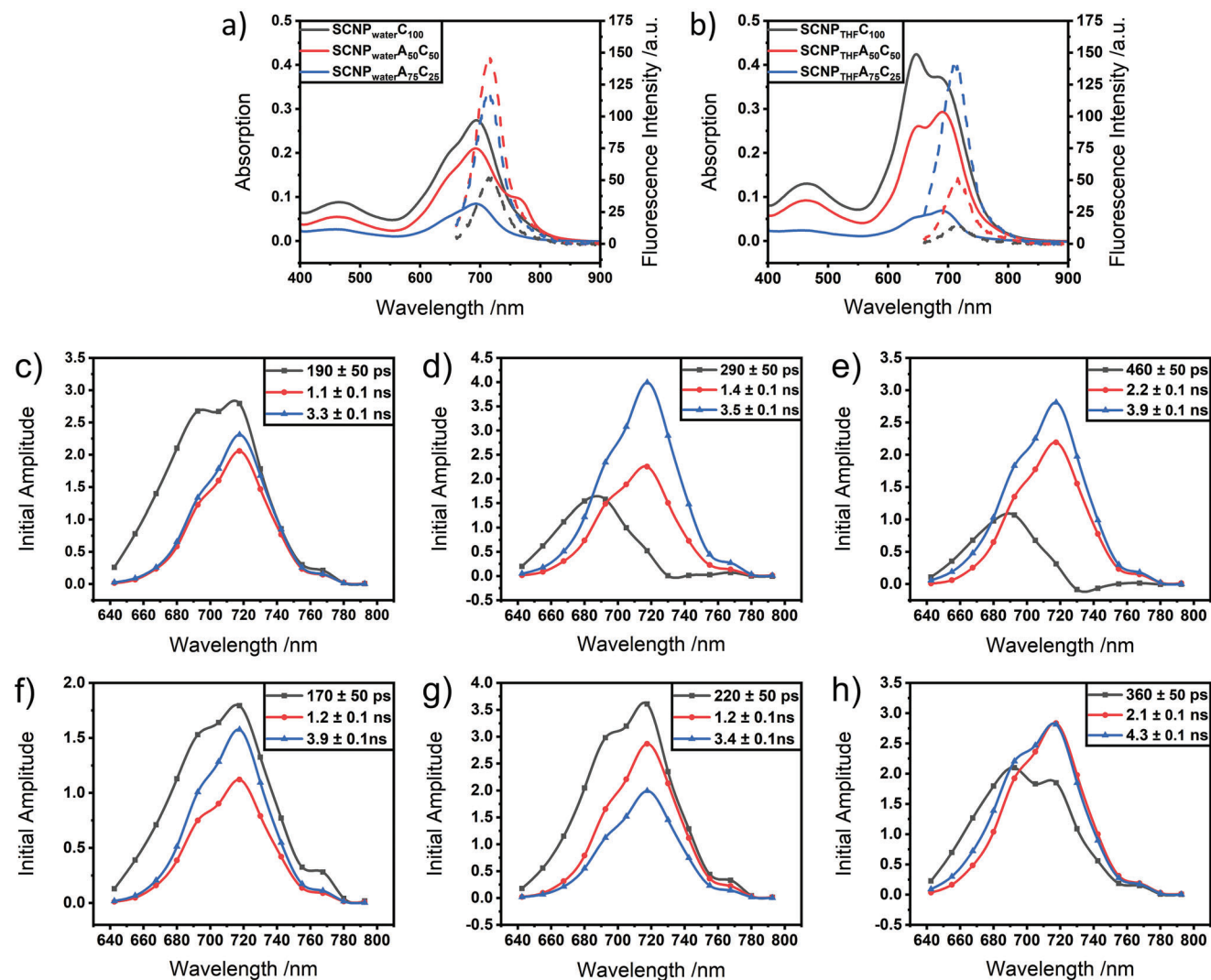


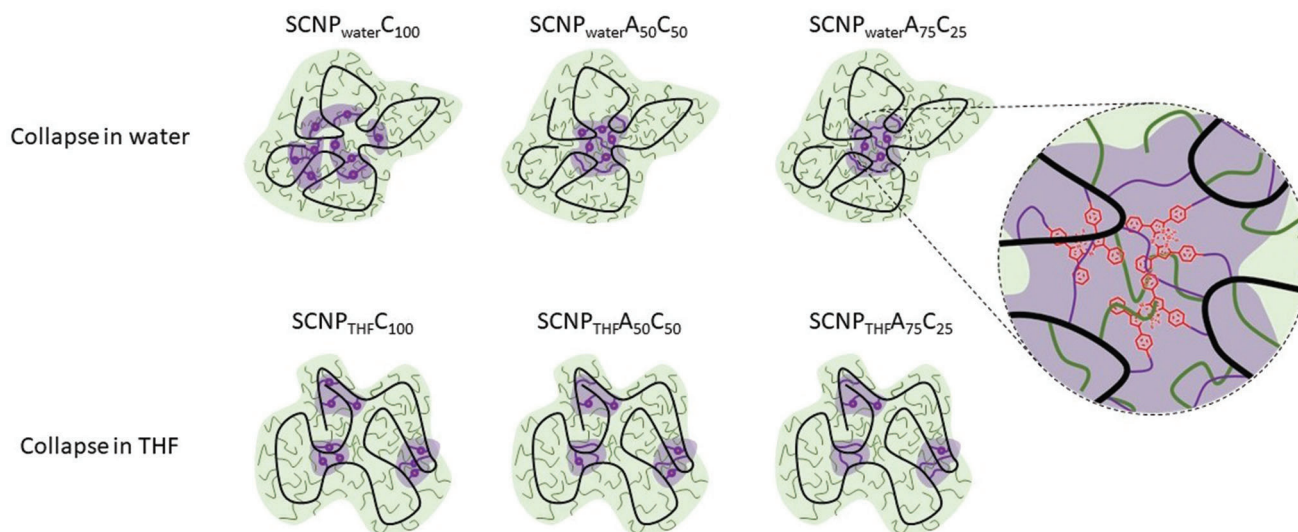
**Figure 3.** Absorption (solid line) and fluorescence (dashed line) spectra of a) water-collapsed and b) THF-collapsed aza-BODIPY labeled SCNPs at concentrations of  $0.1 \text{ mg mL}^{-1}$  in water.  $\lambda_{\text{ex}} = 650 \text{ nm}$ , slit = 5 nm,  $V_{\text{detector}} = 600 \text{ V}$ . Decay associated spectra of c)  $\text{SCNP}_{\text{water}}\text{C}_{100}$ , d)  $\text{SCNP}_{\text{water}}\text{A}_{50}\text{C}_{50}$ , e)  $\text{SCNP}_{\text{water}}\text{A}_{75}\text{C}_{25}$ , f)  $\text{SCNP}_{\text{THF}}\text{C}_{100}$ , g)  $\text{SCNP}_{\text{THF}}\text{A}_{50}\text{C}_{50}$ , h)  $\text{SCNP}_{\text{THF}}\text{A}_{75}\text{C}_{25}$  at concentrations of  $0.1 \text{ mg mL}^{-1}$  in water.

To further check for the exact location of the fluorescent labels inside the SCNP's compartments and how this influences the optical properties of aza-BODIPY including its fluorescence lifetime, decay-associated spectra (DAS)<sup>[19]</sup> were measured. DAS of the free dye are shown in Figure S11 (Supporting Information). In aqueous solution, aza-BODIPY exhibits a fast decay of 260 ps, as a polar solvation, especially with water, quenches the first excited singlet state.<sup>[12a]</sup> However, the surfactant Kolliphor EL reduces the environments polarity resulting in additional slow decay components (red and blue curves in Figure S11, Supporting Information, respectively).

The decay associated spectra for aza-BODIPY labeled SCNPs in Figure 3c–h also represent three fluorescence components. While all THF-collapsed SCNPs and  $\text{SCNP}_{\text{water}}\text{C}_{100}$  show a dominant short-lived component, two water-synthesized SCNPs, i.e.,  $\text{SCNP}_{\text{water}}\text{A}_{50}\text{C}_{50}$  and  $\text{SCNP}_{\text{water}}\text{A}_{75}\text{C}_{25}$ , show dominant long-lived lifetimes ranging from 2.1 to 4.3 ns (Figure 3d,e). In addition, the lifetime of the fast component is gradually increas-

ing as the number of aza-BODIPY molecules per SCNP is reduced. For  $\text{SCNP}_{\text{water}}\text{C}_{100}$ , for example, the lifetime of 190 ns indicates that a large fraction of the aza-BODIPY molecules is located in a polar environment. This situation is different for  $\text{SCNP}_{\text{water}}\text{A}_{75}\text{C}_{25}$  where the time constant increases to 460 ps. This would suggest that here the dye molecules are encapsulated in the core of the particle and therefore shielded from the quenching effects of water. For SCNPs collapsed in THF, the fraction of aza-BODIPY in a polar environment is proportional to the aza-BODIPY content.

In the water-collapsed and co-crosslinked SCNPs, an additional heterogeneity in the fast-lived component is observed as evidenced by a maximum at 690 nm and a minimum (negative amplitude) at 730 nm (Figure 3d,e, black curves). Direct contact between individual dye molecules is leading to the formation of excitonic couples,<sup>[12a]</sup> inline with the Heisenberg exchange found in the EPR measurements, an important effect since it increases fluorescence lifetimes and intensities.



**Scheme 2.** Schematic interpretation of the spatial distribution of aza-BODIPY inside the nanoparticles depending on the collapse medium and the amount of label crosslinker. Collapse in different media resulted in the formation of different nanocompartments with the polar PEG chains (green) in the shell (green) and the non-polar crosslinking groups (violet, aza-BODIPY—red) in the compartmented crosslinked cores (violet).

The overall picture of the compartments formed by collapse and crosslinking in different media is schematically shown in Scheme 2. Thus collapse in either water or in THF resulted in the formation of different nanosized compartments inside the SCNPs, with the polar PEG chains (green) in the shell (green) and the non-polar crosslinking groups (violet, aza-BODIPY—red) in the compartmented crosslinked cores (violet). It must be noted that—as expected—collapse in water leads to the formation of core-shell structured SCNPs, although there is an influence of the molar ratio of the labeled crosslinker on the final structure. Collapse in THF leads to a more open structure, where the dyes are located in several smaller compartments inside a looser and rather hydrophilic core.

### 2.5. Application of Compartmented Fluorescent SCNPs as Contrast Agents for Photoacoustic Measurements

The compartmented structure and specific composition of the SCNPs also resulted in marked differences in the amplitude and time-course of photoacoustic (PA) signals. PA waves are generated by the absorption of short excitation pulses (several ns duration) by absorbing chromophores. The optical energy is converted to heat and initial pressure which relaxes by emitting a broadband ultrasound wave. Using an ultrasound transducer, time-resolved signals are acquired. Under conditions of thermal and stress confinement and for simple geometries, such as cuvettes, the time-course of the signals can be assumed to represent the axial distribution of the absorbed optical energy along the excitation beam. PA signals generated using pump-probe excitation, i.e., using excitation pulses at different wavelengths and time delays, allow information on the dynamics of absorption and relaxation from excited states in fluorophores to be obtained.<sup>[18,20]</sup> Here, we apply this method to investigate the correlation between the structure and composition of the SCNPs, their optical properties as represented by the decay associated spectra, and PA data.

Details of the experimental setup and the methods are given in the Supporting Information. PA signals were measured at room temperature in aqueous SCNP solutions with a concentration of  $1 \text{ mg mL}^{-1}$  using pump and probe wavelengths that coincided with the wavelengths of peak absorption and fluorescence ( $\lambda_{\text{probe}} = 690 \text{ nm}$ ,  $\lambda_{\text{probe}} = 730 \text{ nm}$ ). **Figure 4a–c** shows time-resolved PA signals acquired using pump-probe time delays of 0, 5, and 10 ns. The signal amplitudes are normalized with respect to SCNP absorption at the pump and probe wavelengths. Each graph shows two sets of PA signals measured in solutions of water-collapsed (solid lines) or THF-collapsed (dashed lines) SCNPs with identical dye load. Since the time-course of the PA signals corresponds to the absorbed energy distribution along the axis of the excitation beam, qualitative comparisons of the absorption and relaxation dynamics between the different SCNPs can be made. In **Figure 4a–c**, the boundaries of the sample volume within the cuvette are indicated by dashed lines. The early arriving signal around  $0.6\text{--}1.0 \mu\text{s}$  corresponds to the PA wave from the back of the cuvette, while the signal at  $4.4 \mu\text{s}$  originates from the illuminated side. Marked differences in the shape of the signals measured in water- and THF-collapsed SCNPs are observed. In **Figure 4a,b**, the signal amplitude generated adjacent to the illuminated window (between  $3.0$  and  $4.4 \mu\text{s}$ ) is lower in water-collapsed SCNPs than in those collapsed in THF. This difference is likely due to the more dominant slow decay component in water-collapsed SCNPs (see **Figure 3**), which results in ground state depopulation in regions of high fluence. This, in turn, reduces the absorbed energy density, and hence PA signal amplitude generated in the sample volume adjacent to the illuminated window. THF-collapsed particles, by comparison, exhibit predominately fast relaxations (see **Figure 3**), which prevents ground state depopulation and results in a larger PA signal amplitude near the source. The time-course of these signals also approaches the typical exponential shape expected of absorbers with short lifetimes. Although the signals acquired in SCNPs with minimal dye load, i.e.,  $\text{SCNP}_{\text{water A75 C25}}$  and  $\text{SCNP}_{\text{THF A75 C25}}$ , show

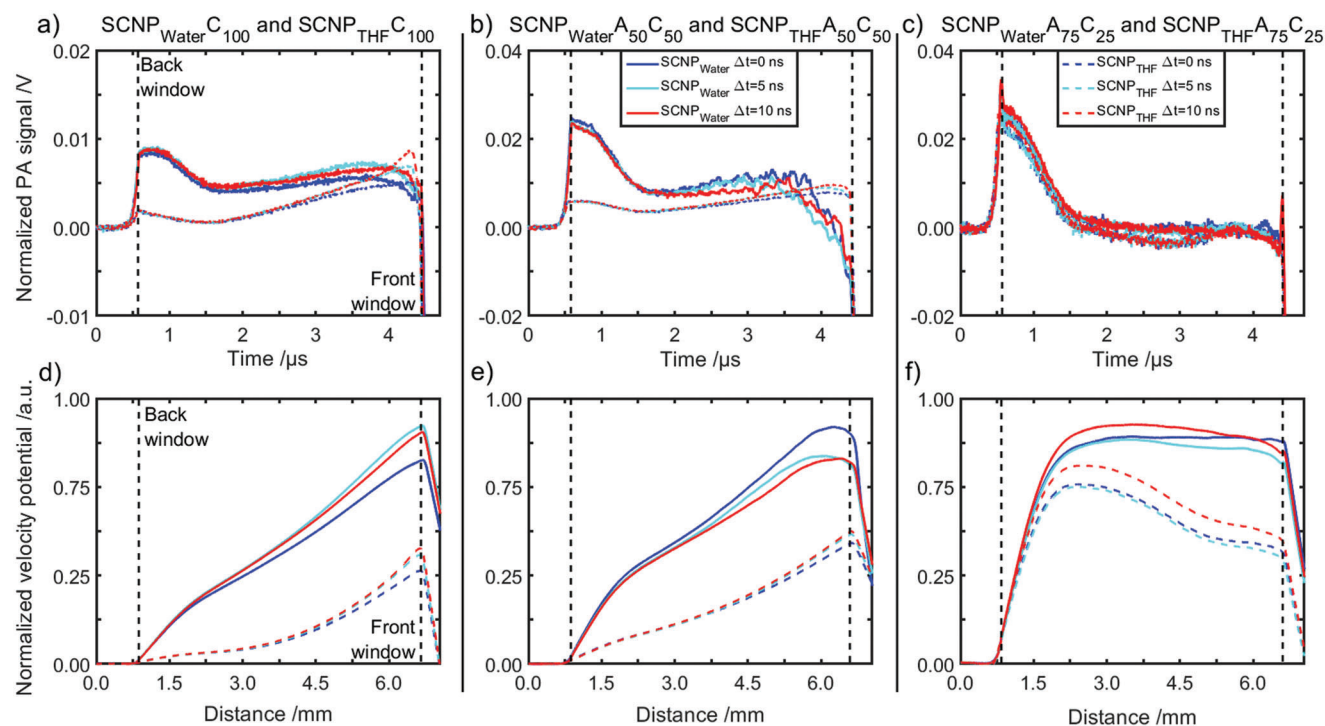


**Figure 4.** a–c) Absorption normalized PA pump–probe signals measured in aza-BODIPY labeled SCNPs and d–f) the corresponding velocity potential at time delays of 0 ns (blue), 5 ns (cyan), and 10 ns (red). The concentration of SCNPs was  $1 \text{ mg mL}^{-1}$ , and the pump and probe fluences were  $\Phi_{\text{pump}} = 8.0 \text{ mJ cm}^{-2}$  and  $\Phi_{\text{probe}} = 13.4 \text{ mJ cm}^{-2}$ . The solid lines show the PA signals and velocity potentials measured in water-collapsed SCNPs, while the dashed lines show the data acquired in THF-collapsed SCNPs. The vertical dashed lines indicate the location of the cuvette windows.

similar features (Figure 4c), they are not easily discerned due to low signal-to-noise ratios (SNR).

To improve SNR and to obtain a qualitative measure of the total initial pressure that was generated in the SCNPs solutions, the velocity potential was calculated by time-integrating the PA signals. The velocity potential is shown in Figure 4d–f as a function of depth assuming the speed of sound in water. The peak values of the velocity potentials suggest that the total initial pressure is larger in water-collapsed SCNPs compared to those collapsed in THF. This may be explained by differences in the Grüneisen parameter that are a consequence of the compartmentation in the different SCNPs. In THF collapsed particles, the dye molecules are distributed randomly across the particles and are therefore likely to be quenched by water. In water-collapsed SCNPs, by contrast, the dye molecules accumulate at the core surrounded by the polymer. Since the polymer is expected to exhibit a larger Grüneisen parameter than water, the PA signal and the velocity potential is larger in water-collapsed SCNPs. The pump–probe time delay was also found to modulate the PA signal in ways that appear to be dependent upon the particle structure and composition. In most SCNPs, the change in the PA signal near the cuvette was modest and increased with time delay. Only the water-collapsed particles with low dye load, i.e.,  $\text{SCNP}_{\text{water}}\text{A}_{50}\text{C}_{50}$  and  $\text{SCNP}_{\text{water}}\text{A}_{75}\text{C}_{25}$ , exhibited the behavior expected of fluorophores,<sup>[18]</sup> i.e., an increase in signal amplitude and velocity potential was observed for a time delay of 0 ns compared to 5 ns and 10 ns (Figure 4b,c,e,f). This observation can again be explained by the dominant long-lived excited states of these particles (Figure 3) as compared to the other SC-

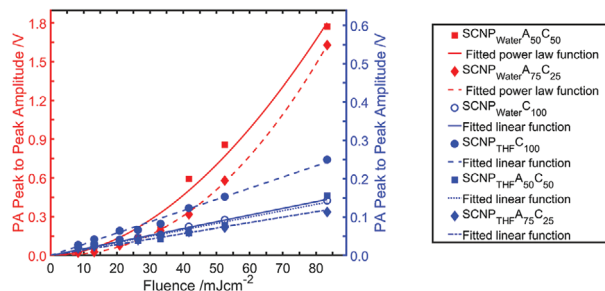


**Figure 5.** The absorption normalized PA signal amplitude measured in aza-BODIPY labeled SCNPs as a function of the incident fluence. A linear dependence was observed in THF-collapsed particles and water-collapsed particles with a high dye load, i.e.,  $\text{SCNP}_{\text{water}}\text{C}_{100}$ , as illustrated by linear regressions (blue symbols and lines). Water-collapsed SCNPs ( $\text{SCNP}_{\text{water}}\text{A}_{50}\text{C}_{50}$ ,  $\text{SCNP}_{\text{water}}\text{A}_{75}\text{C}_{25}$ ) with a dye load of up to 50% exhibit a nonlinear fluence dependence (red symbols) which was found to agree with a quadratic fit function (red lines). The SCNPs concentrations were  $1 \text{ mg mL}^{-1}$  in water.

NPs. Since the pump-probe induced change in signal amplitude is the contrast mechanism in molecular PA imaging applications,  $\text{SCNP}_{\text{water}}\text{A}_{50}\text{C}_{50}$  would appear to possess the most advantageous properties.

**Figure 5** shows the fluence dependence of the PA signal amplitude measured in the SCNPs solutions for a pump–probe time delay of 0 ns. The fluence was set using ND filters and ranged from 8.5 to 85.3  $\text{mJ cm}^{-2}$ .  $\text{SCNP}_{\text{water}}\text{C}_{100}$  and the SCNPs collapsed in THF show a linear increase in signal with modest

signal amplitudes. By contrast, two of the SCNPs collapsed in water (SCNP<sub>water</sub>A<sub>50</sub>C<sub>50</sub>, SCNP<sub>water</sub>A<sub>75</sub>C<sub>25</sub>) show a strong nonlinear fluence dependence with signal amplitudes up to two orders of magnitude greater than that of equivalent THF-collapsed SCNPs. The origin of this nonlinearity is unclear. Possible explanations may include a heat-induced change in the thermomechanical properties, such as the Grüneisen parameter, due to the strong spatial confinement of the dye molecules, or interactions between molecules in an excited state. An immediate benefit of the nonlinear fluence dependence arises in in vivo applications of the particles where it can be exploited as a contrast mechanism.<sup>[21]</sup>

### 3. Conclusion

In summary, we were able to generate dye-loaded, compartmented single-chain nanoparticles by collapse in reaction media of different polarity. Using differently labeled crosslinkers we could analyze the influence of the crosslinker and the collapse medium on the nanosized compartmentation of the individual particles and how these can be used to tune the optical properties for applications in fluorescence tomography and photoacoustic measurements. Collapsing the PEGMA copolymer with azide side chains using copper catalyzed azide-alkyne click reactions in water resulted in the formation of core-shell structured particles with the hydrophobic groups in the core and the hydrophilic PEG side chains in the shell. Collapse in THF resulted in looser compartmented particles in which the hydrophobic groups were located in multiple smaller compartments distributed over the whole particle. The formation of those compartments was followed by using water based SEC and  $T_{cp}$  measurements individually showing changes in the water solubility of the SCNPs and therefore their polarity. One proof of the formation of the compartmented structures was accomplished by EPR spectroscopy after introducing a TEMPO label as crosslinker. Simulations of the measured spectra revealed large Heisenberg exchange coupling with high  $\tau$  values for all SCNPs, demonstrating close contact for the labels with distances in the sub-nanometer range. Collapsing the TEMPO labeled SCNPs in water resulted in higher  $\tau$  values, revealing a denser encapsulation of the labels at the core. Labeling the SCNPs with the fluorescent dye aza-BODIPY as a crosslinker enabled an independent validation of these compartmented structures using optical methods. Depending on the degree of compartmentation, SCNPs showed differences in the absorption and fluorescence spectra. New absorption bands and strong differences in fluorescence intensities were observed depending on the collapse medium and dye load. In the core-shell structured particles, excitonic couples and non-polar environments for the dye molecules were generated, yielding increased fluorescence lifetimes and intensities. The compartments are advantageous for PA measurements, which showed that water-collapsed SCNPs with comparatively low dye loads possess advantageous properties compared to THF-collapsed particles. Most importantly increased signal generation efficiency, susceptibility to contrast mechanisms based on pump-probe excitation, and a non-linear fluence dependence of the signal amplitude were observed, which can be exploited as a contrast mechanism.

The concept described in this paper therefore paves the way toward precise engineering of nanosized contrast agents for imaging technologies, where the tuning of photophysical and thermomechanical properties is required. Applications in biomedical fluorescence and PA imaging are particularly attractive, as SCNPs may offer new contrast mechanisms, which could include the multiplexed detection of contrast agents based on differences in the lifetime and nonlinearity, and the use of SCNPs as biosensors.

### 4. Experimental Section

Detailed information on the materials, all methods, and syntheses are given in the Supporting Information.

### Supporting Information

Supporting Information is available from the Wiley Online Library or from the author.

### Acknowledgements

The authors thank the DFG-Graduate College GRK 2670 (German research foundation-project D43649874, TP B2, RTG 2670) for financial support (WHB, JFT). J.L. acknowledges funding by the DFG via project grant LA3273/7-1. D.H. acknowledges funding by TP A2 (DH) in the GRK 2670. Open Access funding enabled and organized by Projekt DEAL.

### Conflict of Interest

The authors declare no conflict of interest.

### Data Availability Statement

The data that support the findings of this study are available in the supplementary material of this article.

### Keywords

decay-associated spectra, EPR spectroscopy, fluorescence spectroscopy, nanocompartments, photoacoustic imaging, single-chain nanoparticles

Received: July 13, 2022  
Revised: August 5, 2022  
Published online: August 27, 2022

- [1] a) Y. Bai, X. Feng, H. Xing, Y. Xu, B. K. Kim, N. Baig, T. Zhou, A. A. Gewirth, Y. Lu, E. Oldfield, S. C. Zimmerman, *J. Am. Chem. Soc.* **2016**, *138*, 11077; b) Y. Liu, S. Pujals, P. J. M. Stals, T. Paulöhr, S. I. Presolski, E. W. Meijer, L. Albertazzi, A. R. A. Palmans, *J. Am. Chem. Soc.* **2018**, *140*, 3423; c) H. Rothfuss, N. D. Knofel, P. W. Roesky, C. Barner-Kowollik, *J. Am. Chem. Soc.* **2018**, *140*, 5875; d) S. Garmendia, S. B. Lawrenson, M. C. Arno, R. K. O'reilly, D. Taton, A. P. Dove, *Macromol. Rapid Commun.* **2019**, *40*, 1900071; e) T. Terashima, T. Mes, T. F. A. De Greef, M. A. J. Gillissen, P. Besenius, A. R. A. Palmans, E. W. Meijer, *J. Am. Chem. Soc.* **2011**, *133*, 4742; f) A. Sanchez-Sanchez, A. Arbe, J. Kohlbrecher, J. Colmenero, J. A. Pomposo, *Macromol. Rapid Commun.* **2015**, *36*, 1592.

- [2] X. Tian, R. Xue, F. Yang, L. Yin, S. Luan, H. Tang, *Biomacromolecules* **2021**, *22*, 4306.
- [3] a) N. M. Hamelmann, J.-W. D. Paats, J. M. J. Paulusse, *ACS Macro Lett.* **2021**, *10*, 1443; b) L. Deng, L. Albertazzi, A. R. A. Palmans, *Biomacromolecules* **2021**, *23*, 326; c) A. P. P. Kroger, M. I. Komil, N. M. Hamelmann, A. Juan, M. H. Stenzel, J. M. J. Paulusse, *ACS Macro Lett.* **2019**, *8*, 95; d) A. P. P. Kroger, N. M. Hamelmann, A. Juan, S. Lindhoud, J. M. J. Paulusse, *ACS Appl. Mater. Interfaces* **2018**, *10*, 30946.
- [4] S. Liu, J. Rong, R. Liu, J. S. Lindsey, *ACS Appl. Polym. Mater.* **2021**, *3*, 1767.
- [5] a) R. Gracia, M. Marradi, U. Cossío, A. Benito, A. Pérez-San Vicente, V. Gómez-Vallejo, H.-J. Grande, J. Llop, I. Loinaz, *J. Mater. Chem. B* **2017**, *5*, 1143; b) Y. Koda, T. Terashima, M. Sawamoto, H. D. Maynard, *Polym. Chem.* **2015**, *6*, 240.
- [6] J. T. Offenloch, J. Willenbacher, P. Tzvetkova, C. Heiler, H. Mutlu, C. Barner-Kowollik, *Chem. Commun.* **2017**, *53*, 775.
- [7] a) J. Nam, S. Kwon, Y.-G. Yu, H.-B. Seo, J.-S. Lee, W. B. Lee, Y. Kim, M. Seo, *Macromolecules* **2021**, *54*, 8829; b) K. Watanabe, N. Kaizawa, B. J. Ree, T. Yamamoto, K. Tajima, T. Isono, T. Satoh, *Angew. Chem., Int. Ed.* **2021**, *60*, 18122; c) Y. M. S. Nomura, T. Ikeda, M. Seki, M. Kamachi, *Macromolecules* **1995**, *28*, 2874; d) J. Rubio-Cervilla, H. Frisch, C. Barner-Kowollik, J. A. Pomposo, *Macromol. Rapid Commun.* **2019**, *40*, 1800491.
- [8] a) T. S. Fischer, D. Schulze-Sunninghausen, B. Luy, O. Altintas, C. Barner-Kowollik, *Angew. Chem., Int. Ed.* **2016**, *55*, 11276; b) T. Terashima, T. Sugita, K. Fukae, M. Sawamoto, *Macromolecules* **2014**, *47*, 589.
- [9] a) E. Verde-Sesto, A. Arbe, A. J. Moreno, D. Cangialosi, A. Alegrá-A, J. Colmenero, J. A. Pomposo, *Mater. Horiz.* **2020**, *7*, 2292; b) K. Watanabe, R. Tanaka, K. Takada, M.-J. Kim, J.-S. Lee, K. Tajima, T. Isono, T. Satoh, *Polym. Chem.* **2016**, *7*, 4782.
- [10] S. Liao, L. Wei, L. A. Abriata, F. Stellacci, *Macromolecules* **2021**, *54*, 11459.
- [11] C. H. Liu, L. D. Dugas, J. I. Bowman, T. Chidanguro, R. F. Storey, Y. C. Simon, *Polym. Chem.* **2020**, *11*, 292.
- [12] a) J. F. Hoffmann, A. H. Roos, F. J. Schmitt, D. Hinderberger, W. H. Binder, *Angew. Chem., Int. Ed.* **2021**, *60*, 7820; b) A. H. Roos, J. F. Hoffmann, W. H. Binder, D. Hinderberger, *Soft Matter* **2021**, *17*, 7032.
- [13] J. Weber, P. C. Beard, S. E. Bohndiek, *Nat. Methods* **2016**, *13*, 639.
- [14] a) M. Abellan-Flos, M. Tanc, C. T. Supuran, S. P. Vincent, *J. Enzyme Inhib. Med. Chem.* **2016**, *31*, 946; b) S. H. Thang, B. Y. K. Chong, R. T. A. Mayadunne, G. Moad, E. Rizzardo, *Tetrahedron Lett.* **1999**, *40*, 2435; c) B. S. Sumerlin, N. V. Tsarevsky, G. Louche, R. Y. Lee, K. Matyjaszewski, *Macromolecules* **2005**, *38*, 7540; d) J. Murtagh, D. O. Frimannsson, D. F. O'Shea, *Org. Lett.* **2009**, *11*, 5386; e) D. Wu, D. F. O'Shea, *Tetrahedron Lett.* **2017**, *58*, 4468.
- [15] a) W. H. Binder, R. Sachsenhofer, *Macromol. Rapid Commun.* **2007**, *28*, 15; b) W. H. Binder, R. Sachsenhofer, *Macromol. Rapid Commun.* **2008**, *29*, 952.
- [16] J. Engelke, J. Brandt, C. Barner-Kowollik, A. Lederer, *Polym. Chem.* **2019**, *10*, 3410.
- [17] a) A. P. P. Kröger, R. J. E. A. Boonen, J. M. J. Paulusse, *Polymer* **2017**, *120*, 119; b) E. B. Berda, E. J. Foster, E. W. Meijer, *Macromolecules* **2010**, *43*, 1430.
- [18] J. Märk, F.-J. Schmitt, C. Theiss, H. Dortay, T. Friedrich, J. Laufer, *Biomed. Opt. Express* **2015**, *6*, 2522.
- [19] F.-J. Schmitt, E. G. Maksimov, H. Suedmeyer, V. Jeyasangar, C. Theiss, V. Z. Paschenko, H. J. Eichler, G. Renger, *Photonics Nanostruct. - Fundam. Appl.* **2011**, *9*, 190.
- [20] a) J. Märk, F.-J. Schmitt, J. Laufer, *J. Opt.* **2016**, *18*, 54009; b) J. Märk, A. Wagener, E. Zhang, J. Laufer, *Sci. Rep.* **2017**, *7*, 40496; c) F. G. Golmohamadi, A. Mehmood, F.-J. Schmitt, J. Laufer, *Proc. SPIE* **2021**, *11923*, 119230F.
- [21] S. Schrof, G. Pang, J. Buchmann, J. Laufer, *J. Imaging* **2018**, *4*, 146.



## Thermoresponsive swelling of photoacoustic single-chain nanoparticles†

Cite this: *Chem. Commun.*, 2023, 59, 11373

Received 9th August 2023,  
Accepted 23rd August 2023

DOI: 10.1039/d3cc03851c

rsc.li/chemcomm

Justus F. Thümmeler,<sup>a</sup> Ramesh Maragani,<sup>a</sup> Franz-Josef Schmitt,<sup>b</sup> Guo Tang,<sup>b</sup> Samira Mahmoudi Rahmanlou,<sup>b</sup> Jan Laufer,<sup>b</sup> Henrike Lucas,<sup>c</sup> Karsten Mäder<sup>c</sup> and Wolfgang H. Binder<sup>\*a</sup>

**NIR-fluorescent LCST-type single-chain nanoparticles (SCNPs) change their photophysical behaviour upon heating, caused by depletion of water from the swollen SCNP interiors. This thermoresponsive effect leads to a fluctuating photoacoustic (PA) signal which can be used as a contrast mechanism for PA imaging.**

In recent years, modern concepts for biomedical imaging have been developed that can supplement classical methods like X-ray imaging, MRI, or PET scans, with special interest in fluorescence and (pump–probe) photoacoustic (PA) imaging due to their high spatial resolution.<sup>1–3</sup> New classes of near-infrared (NIR) fluorescent contrast agents are required to enable a precise and unique detection with high contrast in living tissue.<sup>4–6</sup> Exogenous contrast agents include molecular absorbers, such as fluorescent and non-fluorescent dyes, nanoparticles, as well as genetically engineered compounds, such as absorbing proteins or membrane vesicles.<sup>2,7–9</sup>

Encapsulating NIR fluorescent dyes in single-chain nanoparticles (SCNPs) is a promising method in the design of such contrast agents to achieve unique contrast mechanisms.<sup>10</sup> A SCNP is a synthetic polymer nanoparticle made from an isolated, collapsed, and crosslinked single polymer chain. Enzyme-like, compartmentalized nanostructures of different philicities can be produced by using amphiphilic precursor polymers for single-chain crosslinking.<sup>11–13</sup> Inside these structures, small molecules like catalysts,<sup>14–16</sup> drugs,<sup>17–20</sup> or (fluorescent) dyes<sup>21–25</sup> can be encapsulated, by binding either

non-covalently like in a unimolecular micelle, or covalently directly to the SCNP.

We herein design NIR-fluorescent SCNPs for PA-measurements based on transitions from open to compact structures, exploiting the thermoresponsive nature of the polymer subjected to single-chain collapse. Conceptually, the incorporation of fluorescent dyes into the hydrophobic core of amphiphilic lower-critical-solution-temperature (LCST)-responsive SCNPs can induce changes in their fluorescence behaviour, in turn leading to non-linear PA-responses.<sup>26,27</sup> Previously, dynamic and responsive entities such as thermoresponsivity,<sup>28,29</sup> disulfide bridges,<sup>30,31</sup> self immolative motives,<sup>32</sup> or switchable entities like CO<sub>2</sub>-responsive amidine derivatives<sup>33</sup> have been used to dynamically change volume and structure of SCNPs.

We here demonstrate NIR-fluorescent SCNPs whose thermoresponsive behaviour triggers swelling and deswelling with water, influencing fluorescent dyes inside the SCNPs core. We developed core–shell structured SCNPs bearing red – NIR-fluorescent dyes (diketopyrrolopyrrole (DPP) and aza-BODIPY (aBOD)) with different dye loads. Upon heating, the inhomogeneous interior of the SCNP leads to a local incompatibility with water, occurring at lower temperatures than the outer, macroscopic cloud point temperature ( $T_{cp}$ ). Consequently, heating the swollen SCNP causes deswelling by depletion of water from its interior, and reduces its inner polarity and particle diameter.<sup>28,29</sup> This has a significant influence on the photoacoustic properties of the embedded fluorescent dyes, which can be used as pump–probe PA contrast agents. The underlying process of PA signal generation is based on the generation of heat upon pump–probe excitation. The fluorescent SCNPs therefore provide an in-built contrast mechanism based on their thermoresponsive behaviour.

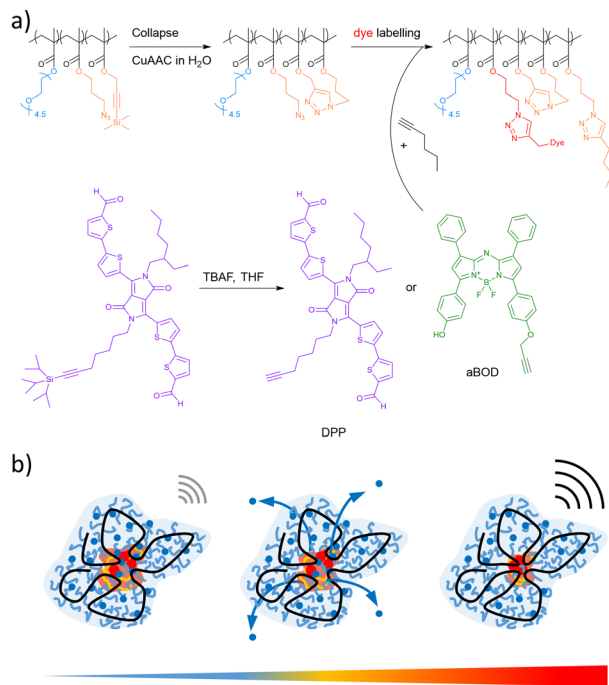
The precursor polymer used for the SCNP synthesis was prepared by reversible-addition–fragmentation chain-transfer (RAFT) polymerization using 80 mol% oligo(ethylene glycol) methacrylate ( $M_n = 300$  Da,  $DP = 4.5$ ), 12 mol% azidopropyl methacrylate, and 8 mol% 3-(trimethylsilyl)propargyl methacrylate, yielding the crosslinkable PEATMA ( $M_n = 33.6$  kDa,  $D = 1.9$ ).

<sup>a</sup> Institute of Chemistry, Faculty of Natural Sciences II, Martin Luther University Halle-Wittenberg, von-Danckelmann-Platz 4, Halle D-06120, Germany.  
E-mail: wolfgang.binder@chemie.uni-halle.de

<sup>b</sup> Institute of Physics, Faculty of Natural Sciences II, Martin Luther University Halle-Wittenberg, von-Danckelmann-Platz 3, Halle D-06120, Germany

<sup>c</sup> Institute of Pharmacy, Faculty of Natural Sciences I, Martin Luther University Halle-Wittenberg, Kurt-Mothes-Str. 3, Halle D-06120, Germany

† Electronic supplementary information (ESI) available. See DOI: <https://doi.org/10.1039/d3cc03851c>



**Scheme 1** (a) SCNP collapse with subsequent dye labelling by CuAAC in water. (b) Single-chain collapse yielded the formation of core-shell structured SCNPs with the fluorescent dyes in the hydrophobic core. The heat following PA excitation contracts the SCNPs interior, followed by an *in situ* enhanced PA response after each pulse.

A degree of polymerization of  $\sim 122$  enabled a sufficient number of crosslinking units in a single polymer chain ( $\approx 15$  azides,  $\approx 10$  alkynes), with an excess of five azides for subsequent labelling. Single-chain collapse with subsequent labelling was performed as a one-pot reaction *via* copper-catalysed azide-alkyne click reaction (CuAAC), as depicted in Scheme 1. After collapse the SCNPs were directly labelled with either a high or a low amount of dye molecules: first a solution of the dye (aBOD or DPP) in THF was added to the reaction solution, followed by a solution of hexyne in THF to achieve the full consumption of all the remaining azide groups. Statistical dye loads of 1 and 5 dye molecules per SCNP were achieved (sample names: SCNP\_[dye]\_[dye load]).

Proof of a full conversion and of a successful single-chain collapse are depicted in Fig. 1 and Fig. S2–S4 (ESI<sup>†</sup>), and Table 1. ATR-IR-spectra in Fig. 1a showed a complete removal of the azide vibrational band at  $2100\text{ cm}^{-1}$  for all SCNPs. Degrees of compaction of 34–59%, as calculated from the apparent peak molecular weights from GPC measurements, proved the single-chain collapse (see Table 1).

For application in living organisms, toxicity of the SCNPs was tested using cell viability assays on NHDF cells. Over the complete concentration range, good viabilities could be observed (see Fig. 1b and Fig. S5, ESI<sup>†</sup>). The seemingly lower viabilities of SCNP\_aBOD\_1 are probably caused by an absorption and emission overlap of aBOD with resazurin, that was used to count the living cells.

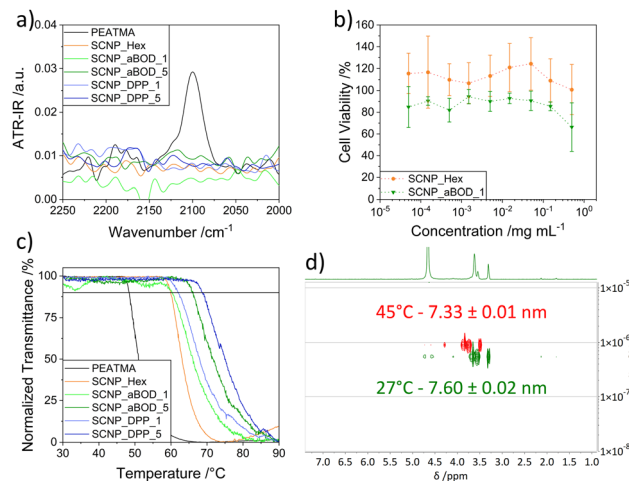


**Fig. 1** (a) ATR-IR spectra of the precursor polymer PEATMA and the SCNPs showing the removal of the azide vibrational band after SCNP collapse. (b) 96 h cell viability assay of SCNP\_Hex and SCNP\_aBOD\_1 on NHDF cells. (c) Turbidimetry measurements of PEATMA and the SCNPs at  $1\text{ mg mL}^{-1}$  in water. (d) DOSY-NMR spectra of SCNP\_aBOD\_5 in D<sub>2</sub>O, measured at 27 °C (green) and 45 °C (red).

**Table 1** Summarized data of the precursor polymer PEATMA and the SCNPs: apparent peak molecular weight  $M_p^{\text{app}}$  of the RAFT-synthesized polymer PEATMA and the non-labelled and labelled SCNPs, degree of compaction  $G$  after single-chain collapse, hydrodynamic diameter  $D_h$ , and cloud point temperatures  $T_{\text{cp}}$

Sample	$M_p^{\text{app}}$ /kDA	$G^b/\%$	$D_h^c/\text{nm}$	$T_{\text{cp}}^d/^\circ\text{C}$
PEATMA	43.8	—	$11.2 \pm 0.8$	48.8
SCNP_Hex	29.1	34	$6.59 \pm 0.01$	59.9
SCNP_aBOD_1	26.4	40	$9.2 \pm 0.3$	60.3
SCNP_aBOD_5	28.2	36	$7.60 \pm 0.02$	66.0
SCNP_DPP_1	23.5	46	$9.92 \pm 0.06$	62.2
SCNP_DPP_5	18.0	59	$5.3 \pm 0.3$	68.8

<sup>a</sup> Measured by GPC in THF. <sup>b</sup> Calculated with  $G = 100 \cdot (M_{p,\text{PEATMA}} - M_{p,\text{SCNP}}) / M_{p,\text{PEATMA}}$ . <sup>c</sup> Measured by DOSY-NMR in D<sub>2</sub>O at  $1\text{ mg mL}^{-1}$ , calculated using eqn (S1) and (S2). <sup>d</sup> Measured by turbidimetry at concentrations of  $1\text{ mg mL}^{-1}$ ,  $T_{\text{cp}} = T$  at 90% transmittance, see Fig. 1c.

We were able to tune the LCST-behaviour of the polymer by choosing the philicities of the crosslinker groups and the PEG sidechains resulting in higher cloud point temperatures ( $T_{\text{cp}}$ ).

Collapsing PEATMA into the non-labelled SCNP\_Hex increased its  $T_{\text{cp}}$  from 48.8 °C to 59.9 °C, as depicted in Fig. 1c and Table 1. Labelling the SCNPs with the dye molecules caused higher  $T_{\text{cp}}$  values the more dye labels were included, with the highest at 68.8 °C observed for SCNP\_DPP\_5. The first increase of  $T_{\text{cp}}$  after the single-chain collapse can be ascribed to the formation of a core-shell structure that reduced the influence of the non-polar crosslinking groups on the overall solubility behaviour, as reported earlier.<sup>26</sup> An additional increase of  $T_{\text{cp}}$  upon labelling with dyes is attributed to the bulkiness of the dye molecules, as they enlarged the pores inside the SCNP.

The cores of the SCNPs showed a different LCST-behaviour in comparison to their outer shells. Because of their higher

hydrophobicity, the incompatibility to water occurred already at temperatures below  $T_{cp}$ , as measured by reduced hydrodynamic diameters ( $D_h$ ) at increased temperatures in DOSY-NMR-spectroscopy. Thus,  $D_h$  of SCNP\_aBOD\_5 was reduced by 0.27 nm from 7.60 nm to 7.33 nm upon heating from 27 °C to 45 °C, as depicted in Fig. 1d, taking into account viscosity changes of  $D_2O$  at higher temperatures.<sup>34</sup>

This thermoresponsive deswelling had a significant influence on the photophysical properties of the encapsulated fluorescent dyes by enabling changes of dye agglomeration and of the fluorescence quenching effect of water, as visible in Fig. 2. Fig. 2a and b display the absorption and fluorescence behaviour of the SCNPs at room temperature. As expected, high dye loads inside the SCNPs led to increased absorptions. Contrary thereto, fluorescence intensities were reduced with high dye loads due to the coupling of multiple dye molecules and increased swelling with water. This caused an almost complete quenching of the fluorescence of both DPP labelled SCNPs, especially at high dye load (blue dashed curves in Fig. 2b). The aBOD labelled SCNPs showed high fluorescence intensities that, together with the absorption, can be tuned by adjusting the temperature, as depicted in Fig. 2c and d (the complete spectra can be seen in Fig. S7–S9, ESI†). Increasing the temperature led to higher absorption maxima, caused by denser encapsulation by the SCNP and by depletion of water, both resulting in changed polarities. Comparison to aBOD in Kolliphor EL (KolEL) micelles proved that this effect clearly originates from the SCNPs, as the dye without the SCNP shell showed reduced absorption maxima at higher temperatures. Fluorescence intensities of the aBOD labelled SCNPs were firstly increased by up to 5.8% upon heating, caused by reduced polarities around the dyes upon deswelling of water. Further increasing the temperature led to reduced intensities, caused by dye aggregation upon compaction of the SCNP core and

subsequent fluorescence quenching.<sup>35,36</sup> Fluorescence spectra were found to be stable in complex biological media, as depicted in Fig. S10 (ESI†).

Temperature dependent decay associated fluorescence spectra (DAS) supported this hypothesis. As reported earlier,<sup>26</sup> the aBOD-labelled SCNPs showed a three-component exponential decay with a slow ( $\sim 3.5$  ns, blue triangles), a medium ( $\sim 2$  ns, red circles), and a fast ( $\sim 500$  ps, black squares) decaying component (see Fig. 3a and Fig. S11, and S12, ESI†). As depicted in Fig. 3b, the relative contributions of the three individual components changed as a response to heating. Upon heating, the initial assumption of deswelling of water was supported by the increase of the medium decaying component. The slow decaying component decreased significantly, while the fast decaying component increased with rising temperature up to 50 °C due to quenching induced by closer contact of individual dye molecules. Due to the close contact of the coupled molecules, the excited states relax along the fastest channels in the ensemble, leading to an acceleration of the time constants at higher temperatures.<sup>37</sup>

Measurements of the photoacoustic (PA) signal amplitude of SCNP\_aBOD\_5 and an aqueous solution of aBOD support the hypothesis that thermally induced swelling and deswelling of water caused changes in the photophysical and thermomechanical properties of the SCNPs. Fig. 3c shows the PA signal as a function of the number of excitation pulses. While the amplitude of aBOD in water showed an almost unchanged signal, the embedding into SCNP\_aBOD\_5 resulted in substantial changes. The underlying mechanism for this signal is illustrated in Fig. 3d. While the first pump-probe excitation yielded a weak signal, the resulting excitation heat caused

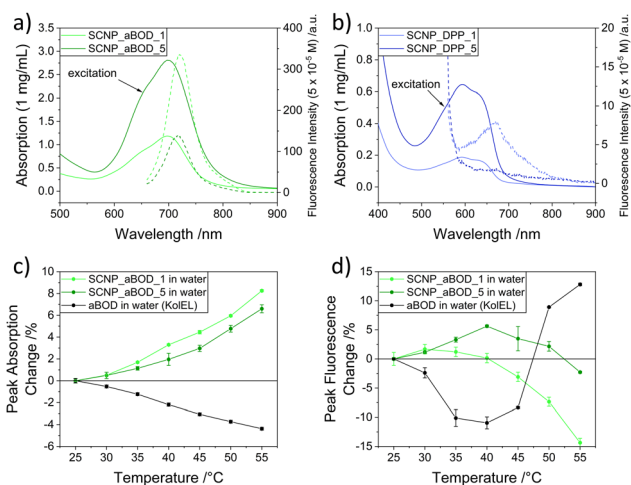


**Fig. 2** Absorption spectra (solid lines) at concentrations of 1 mg(SCNP) mL<sup>-1</sup> in water and fluorescence spectra (dashed lines) at concentrations of 5 × 10<sup>-5</sup> mol(dye) mL<sup>-1</sup> in water of (a) aBOD-, and (b) DPP-labelled SCNPs. Relative changes of (c) absorption, and (d) fluorescence peak intensities of SCNP\_aBOD\_1, SCNP\_aBOD\_5, and aBOD in water.

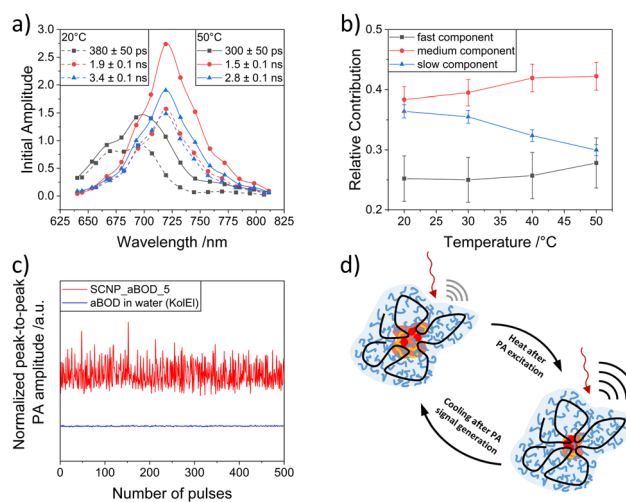


**Fig. 3** (a) Decay associated fluorescence spectra of SCNP\_aBOD\_1.0 at 20 °C (dashed lines) and 50 °C (solid lines). (b) Temperature dependent relative contributions of all fluorescent components of SCNP\_aBOD\_1. (c) Amplitude of PA signals generated in SCNP\_aBOD\_5.0 (red line) and aBOD in water (blue line) as a function of number of pump-probe excitation pulses. The amplitude is normalised with respect to pulse energy and absorption. (d) Schematic illustration of the thermoresponsive self-tuning behaviour of the SCNPs upon PA excitation.

deswelling of water from the SCNP. The so changed photo-physical properties resulted in a larger PA signal upon next excitation. Because the SCNP is able to cool down between two excitation pulses, water will swell back into the nanoparticle, again changing the photophysical properties. While this fluctuating PA signal seems uncontrollable so far, it displays a unique behaviour, that can be used as a contrast mechanism in addition to other contributions, like those from pump–probe excitation,<sup>3</sup> dye–dye interactions,<sup>27,38,39</sup> or pH-sensitivity.<sup>26</sup>

In summary, two sets of core–shell structured single-chain nanoparticles (SCNPs) were synthesized, bearing different amounts of either an aza-BODIPY (aBOD), or a diketopyrrolopyrrole (DPP) fluorescent dye. Such thermoresponsive SCNPs yielded a unique photoacoustic (PA)-response due to the PA-induced swelling and deswelling of the SCNPs. By tuning the LCST-behaviour of the SCNPs, their core displayed lower collapse temperatures in comparison to the outer shell, in turn removing water from the core upon heating. The so modified polarity and density around the embedded dyes changed their photophysical properties. This effect is a contrast mechanism for PA imaging, since the thermoresponsive behaviour creates a fluctuating signal that distinguishes the SCNPs from the background noise, an effect that is not achievable by conventional dye solutions. Further tuning of this thermoresponsive behaviour of the SCNPs and the so enhanced pump–probe excitation is currently probed for improved PA-imaging.

We thank the project TP B02 within the DFG Graduate College GRK 2670/TP 02, and the DFG project LA3273/8-1 for financial support.

## Conflicts of interest

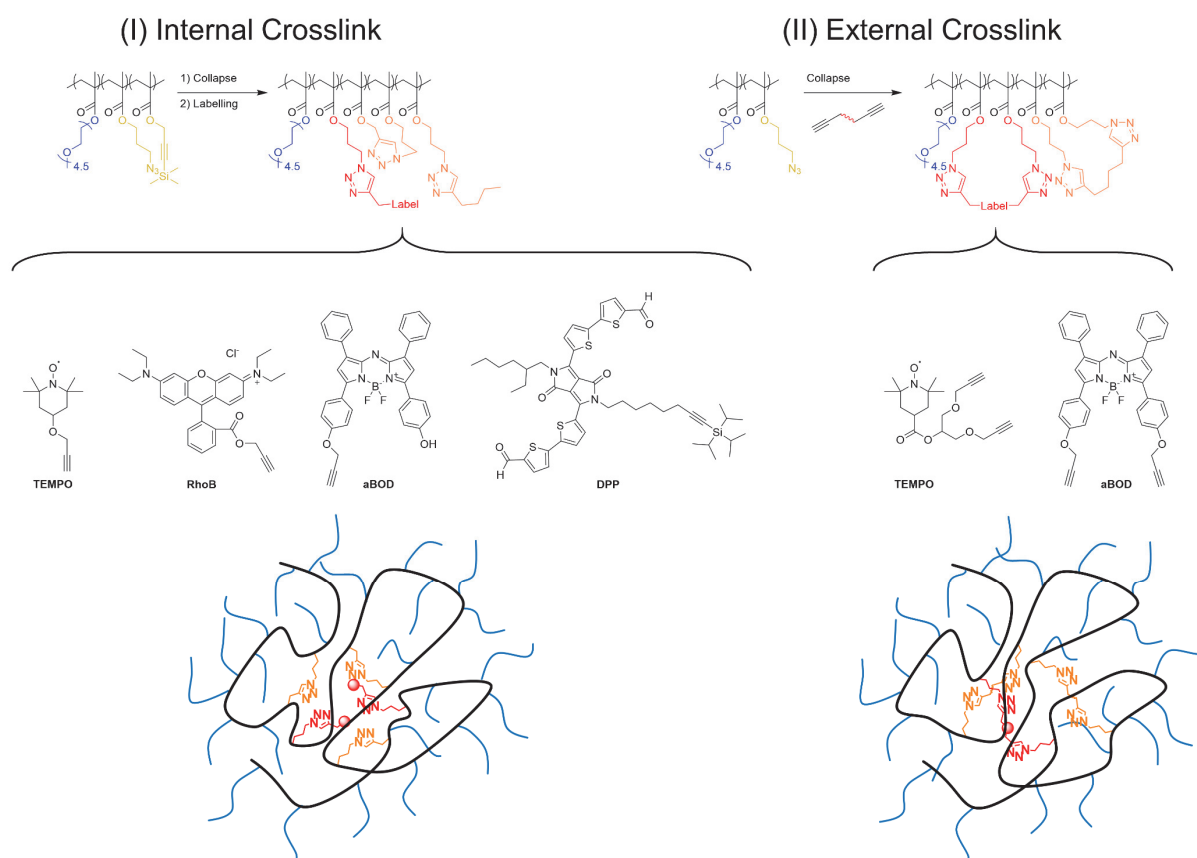
There are no conflicts to declare.

## References

- 1 K. Li and B. Liu, *Chem. Soc. Rev.*, 2014, **43**, 6570–6597.
- 2 J. Weber, P. C. Beard and S. E. Bohndiek, *Nat. Methods*, 2016, **13**, 639–650.
- 3 J. Märk, A. Wagener, E. Zhang and J. Laufer, *Sci. Rep.*, 2017, **7**, 40496.
- 4 Q. Li, S. Li, S. He, W. Chen, P. Cheng, Y. Zhang, Q. Miao and K. Pu, *Angew. Chem., Int. Ed.*, 2020.
- 5 N. Toriumi, N. Asano, T. Ikeno, A. Muranaka, K. Hanaoka, Y. Urano and M. Uchiyama, *Angew. Chem., Int. Ed.*, 2019, **58**, 7788–7791.
- 6 X. Li, E. Y. Park, Y. Kang, N. Kwon, M. Yang, S. Lee, W. J. Kim, C. Kim and J. Yoon, *Angew. Chem., Int. Ed.*, 2020.
- 7 N. Liu, K. Mishra, A. C. Stiel, V. Gujrati and V. Ntziachristos, *Adv. Drug Delivery Rev.*, 2022, **189**, 114506.
- 8 H. J. Knox and J. Chan, *Acc. Chem. Res.*, 2018, **51**, 2897–2905.
- 9 J. Chan, *Photoacoustic Probes for In Vivo Imaging*, Elsevier, Cambridge, United States, 2021.
- 10 A. P. P. Kroger and J. M. J. Paulusse, *J. Controlled Release*, 2018, **286**, 326–347.
- 11 E. Verde-Sesto, A. Arbe, A. J. Moreno, D. Cangialosi, A. Alegria, J. Colmenero and J. A. Pomposo, *Mater. Horiz.*, 2020, **7**, 2292–2313.
- 12 K. Watanabe, N. Kaizawa, B. J. Ree, T. Yamamoto, K. Tajima, T. Isono and T. Satoh, *Angew. Chem., Int. Ed.*, 2021, **60**, 18122–18128.
- 13 J. Nam, S. Kwon, Y.-G. Yu, H.-B. Seo, J.-S. Lee, W. B. Lee, Y. Kim and M. Seo, *Macromolecules*, 2021, **54**, 8829–8838.
- 14 T. M. Xiong, E. Garcia, J. Chen, L. Zhu, A. Alzona and S. C. Zimmerman, *Chem. Commun.*, 2022, **58**, 985–988.
- 15 S. Garmendia, S. B. Lawrenson, M. C. Arno, R. K. O'Reilly, D. Taton and A. P. Dove, *Macromol. Rapid Commun.*, 2019, **40**, e1900071.
- 16 Y. Bai, X. Feng, H. Xing, Y. Xu, B. K. Kim, N. Baig, T. Zhou, A. A. Gewirth, Y. Lu, E. Oldfield and S. C. Zimmerman, *J. Am. Chem. Soc.*, 2016, **138**, 11077–11080.
- 17 N. M. Hamelmann, S. Uijtewaal, S. D. Hujaya and J. M. J. Paulusse, *Biomacromolecules*, 2022, **23**, 5036–5042.
- 18 A. P. P. Kröger, N. M. Hamelmann, A. Juan, S. Lindhoud and J. M. J. Paulusse, *ACS Appl. Mater. Interfaces*, 2018, **10**, 30946–30951.
- 19 R. Gracia, M. Marradi, U. Cossío, A. Benito, A. Pérez-San Vicente, V. Gómez-Vallejo, H. J. Grande, J. Llop and I. Loinaz, *J. Mater. Chem. B*, 2017, **5**, 1143–1147.
- 20 C.-C. Cheng, D.-J. Lee, Z.-S. Liao and J.-J. Huang, *Polym. Chem.*, 2016, **7**, 6164–6169.
- 21 L. Deng, L. Albertazzi and A. R. A. Palmans, *Biomacromolecules*, 2022, **23**, 326–338.
- 22 P. H. Maag, F. Feist, H. Frisch, P. W. Roesky and C. Barner-Kowollik, *Macromolecules*, 2022, **55**, 9918–9924.
- 23 R. Liu and J. S. Lindsey, *ACS Macro Lett.*, 2019, **8**, 79–83.
- 24 R. Liu, S. Liu, G. Hu and J. S. Lindsey, *New J. Chem.*, 2020, **44**, 21293–21308.
- 25 S. Liu, J. Rong, R. Liu and J. S. Lindsey, *ACS Appl. Polym. Mater.*, 2021, **3**, 1767–1776.
- 26 J. F. Hoffmann, A. H. Roos, F. J. Schmitt, D. Hinderberger and W. H. Binder, *Angew. Chem., Int. Ed.*, 2021, **60**, 7820–7827.
- 27 J. F. Hoffmann, A. H. Roos, J. Kruger, D. Hinderberger, F. J. Schmitt, G. Tang, F. G. Golmohamadi, J. Laufer and W. H. Binder, *Macromol. Rapid Commun.*, 2023, **44**, 2200618.
- 28 H. Zhang, L. Zhang, J. You, N. Zhang, L. Yu, H. Zhao, H.-J. Qian and Z.-Y. Lu, *CCS Chem.*, 2021, **3**, 2143–2154.
- 29 A. H. Roos, J. F. Hoffmann, W. H. Binder and D. Hinderberger, *Soft Matter*, 2021, **17**, 7032–7037.
- 30 P. Malo de Molina, T. P. Le, A. Iturrospe, U. Gasser, A. Arbe, J. Colmenero and J. A. Pomposo, *ACS Omega*, 2022, **7**, 42163–42169.
- 31 Y. Gao, V. I. Bohmer, D. Zhou, T. Zhao, W. Wang and J. M. Paulusse, *J. Controlled Release*, 2016, **244**, 375–383.
- 32 J. T. Offenloch, J. Willenbacher, P. Tzvetkova, C. Heiler, H. Mutlu and C. Barner-Kowollik, *Chem. Commun.*, 2017, **53**, 775–778.
- 33 S. Liu, M. Tang, J. Pang, J. Hu, W. Chen, J. Cheng, Z. Liu, H. Zhao and R. Tan, *ACS Sustainable Chem. Eng.*, 2022, **10**, 11760–11772.
- 34 F. J. Millero, R. Dexter and E. Hoff, *J. Chem. Eng. Data*, 1971, **16**, 85–87.
- 35 E. Sebastian, A. M. Philip, A. Benny and M. Hariharan, *Angew. Chem., Int. Ed.*, 2018, **57**, 15696–15701.
- 36 S. Ma, S. Du, G. Pan, S. Dai, B. Xu and W. Tian, *Aggregate*, 2021, **2**, e96.
- 37 P. H. Lambrev, F. J. Schmitt, S. Kussin, M. Schoengen, Z. Varkonyi, H. J. Eichler, G. Garab and G. Renger, *Biochim. Biophys. Acta*, 2011, **1807**, 1022–1031.
- 38 M. Shakiba, K. K. Ng, E. Huynh, H. Chan, D. M. Charron, J. Chen, N. Muhanna, F. S. Foster, B. C. Wilson and G. Zheng, *Nanoscale*, 2016, **8**, 12618–12625.
- 39 C. Avigo, D. Cassano, C. Kusmic, V. Voliani and L. Menichetti, *J. Phys. Chem. C*, 2017, **121**, 6955–6961.

## 5. Conclusion

According to the scope of this cumulative thesis, core-shell structured single-chain nanoparticles (SCNPs) have been synthesized following two different collapse procedures, both using CuAAC: (I) internal crosslinking reactions with azides and alkynes both located on the polymer chain, with an excess of azides for subsequent labelling; and (II) external crosslinking reactions with the azides on the polymer chain and the alkynes on external crosslinkers, that also acted as labels (see **Scheme 3**). The SCNPs were labelled with radical and fluorescent labels, which enabled their nanostructural characterization by CW-EPR spectroscopy and DAS. The fluorescent dye labelled SCNPs revealed novel and unique contrast mechanisms in pump-probe photoacoustic (PA) measurements, that are interesting for PA imaging *in vivo*.



**Scheme 3.** Chemical structures of the Polymers and SCNPs that were synthesized by internal and external single-chain collapse by CuAAC, together and their labels, as well as the schematic interpretation of their respective nanostructures.

## 5.1. Synthesis and Properties of Precursor Polymers and SCNPs

RAFT syntheses of the precursor polymers yielded precisely tuned monomer compositions as well as high molecular weights, which were necessary for the later single-chain collapse reactions. For the internal crosslinking reactions (pathway I in **Scheme 3**) polymers with 80 mol% OEGMA were synthesized. The crosslinking monomers made up the remaining 20 mol% of the final polymer with 12 mol% of APMA and 8 mol% of TMSPMA. Molecular weights of  $M_n = 36.1$  kDa (DP = 129) and 33.6 kDa (DP = 122) with polydispersities of  $\mathcal{D} = 1.7 - 1.9$  were reached, as determined by GPC measurements. The degrees of polymerization and monomer compositions enabled sufficient reactive groups in the single polymer chains ( $\approx 15$  azides and  $\approx 10$  alkynes) for crosslinking densities of  $\approx 10$  crosslinks per SCNP. The remaining 5 azides could be used for labelling the SCNPs with up to 5 labels. The polymerization of the polymer which was used for the external crosslink reactions (pathway II in **Scheme 3**) was performed using 85 mol% OEGMA and 15 mol% APMA, resulting in a molecular weight of  $M_n = 34.6$  kDa (DP = 129). The  $\approx 20$  crosslinking sites enabled crosslinking densities of  $\approx 10$  crosslinkers per SCNP.

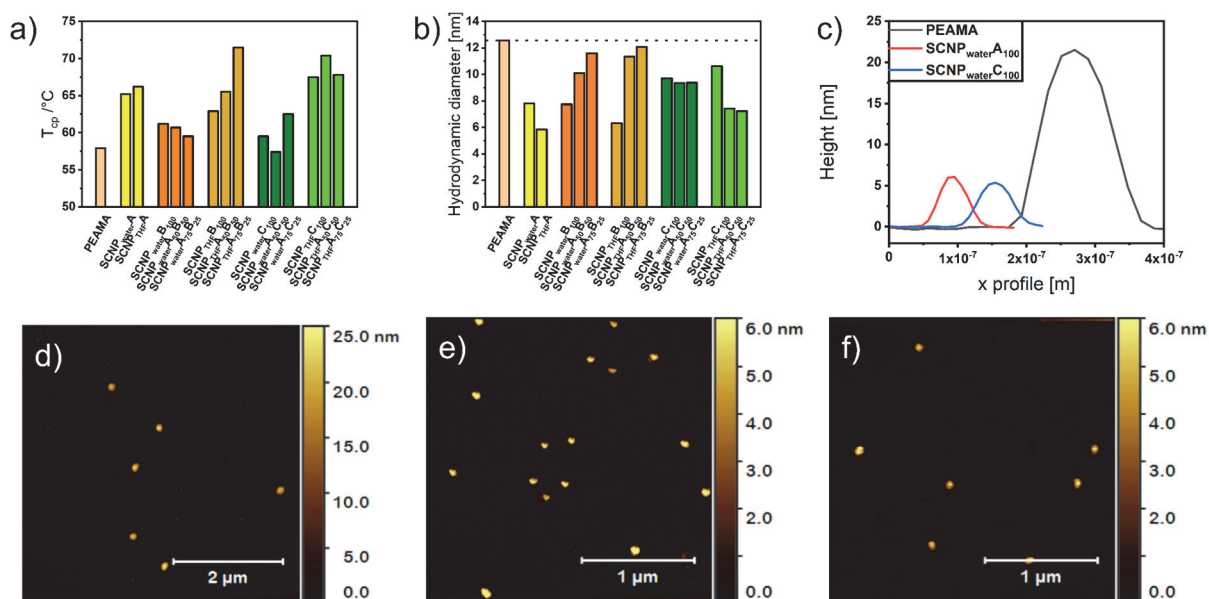


**Figure 18.** Selected results for the precursor polymer PEAMA and the resulting SCNPs (pathway II in **Scheme 3**), that were collapsed in either water or THF: a) turbidimetry measurements, b) hydrodynamic diameter calculated from DOSY-NMR measurements, c) averaged height profiles as determined from the AFM topologies of d) PEAMA, e) water-collapsed, non-labeled SCNP<sub>waterA100</sub>, f) water-collapsed, aBOD labeled SCNP<sub>waterC100</sub>. Reprinted with permission from Wiley-VCH, copyright © 2022 (open access).<sup>272</sup>

Collapsing and crosslinking the precursor polymers *via* CuAAC resulted in solely intramolecularly crosslinked SCNPs, regardless the synthetic pathway, or the collapse solvent. The hydrodynamic diameter of the SCNPs were found to be 5.3 - 12.1 nm depending on the

synthetic pathway, type of label, number of labels inside the SCNPs, and collapse solvent. AFM images (see **Figure 18c-f**) further proved the formation of distinct, ultra-small nanoparticles. The precursor polymer showed agglomerations of multiple chains and heights above 20 nm. Contrary to that, the SCNPs were found to be separated from each other, resulting in heights below 10 nm. This size range makes the here presented SCNPs perfect candidates for indirect tumor targeting by using the enhanced permeation and retention effect. Cell viability assays on NHDF cells further proved the suitability of the SCNPs for their intended use in biomedical applications by showing low toxicities for the non-labeled and the labeled SCNPs over a broad concentration range.

Turbidimetry measurements revealed that all SCNPs exhibited higher cloud point temperatures than their non-crosslinked precursor polymers. This was already a first sign of the formation of compartmented structures inside the SCNPs, where the non-polar parts of the polymers were hidden inside internal compartments, and hence contributed less to the overall polarity. Differences between the SCNPs that were synthesized in water and those that were synthesized in THF could also be seen in the turbidimetry measurements (see **Figure 18a**). Here, the THF-collapsed SCNPs all showed higher collapse temperatures than their analogous water-collapsed SCNPs, caused by the formation of rather sparse SCNPs if the collapse was performed in THF, while the water-collapsed SCNPs build compartmentalized core-shell structures.

## 5.2. Spectroscopic Nanostructure Analysis

The internal collapse reactions in water resulted in the formation of clearly core-shell structured SCNPs. To prove and analyze the formation of these structures, spectroscopic analyses were performed using CW-EPR-spectroscopy as well as DAS. For these measurements it was necessary to specifically label the internal compartments with the respective radical and fluorescence sensors. Following pathway I of **Scheme 3** enabled direct labelling of the SCNPs with different labels by using the excess of azides on the polymer chains. After finishing the collapse reaction, all the unreacted azides were located in the hydrophobic core. Hence, the likewise hydrophobic labels were able to diffuse into the core, react with the azides, and stay in this compartment. Performing the single-chain collapse reaction with external crosslinkers, that also acted as labels (pathway II of **Scheme 3**), enabled an elegant way to perform both reactions – crosslinking and labelling – at the same time.

CW-EPR spectroscopy proved the formation of confined cores inside the SCNPs in which the TEMPO-labels were encapsulated. As depicted in **Figure 19a** and **b**, Heisenberg exchange coupling had to be included in the simulations of the spectra. This effect occurs, when the distance between two or more radical labels is below 1 nm, indicating high local concentrations

of labels. This proved the agglomeration of the labels in a confined area of the SCNPs. Furthermore, concentration dependent measurements revealed that the labels were located inside the SCNP's core, and not on its surface, as shown in **Figure 19c** and **d**. If the labels were located in the outer shell, collisions of individual SCNPs at high concentrations would have led to at least minor changes of the shapes of the spectra, which were however found to be concentration independent.

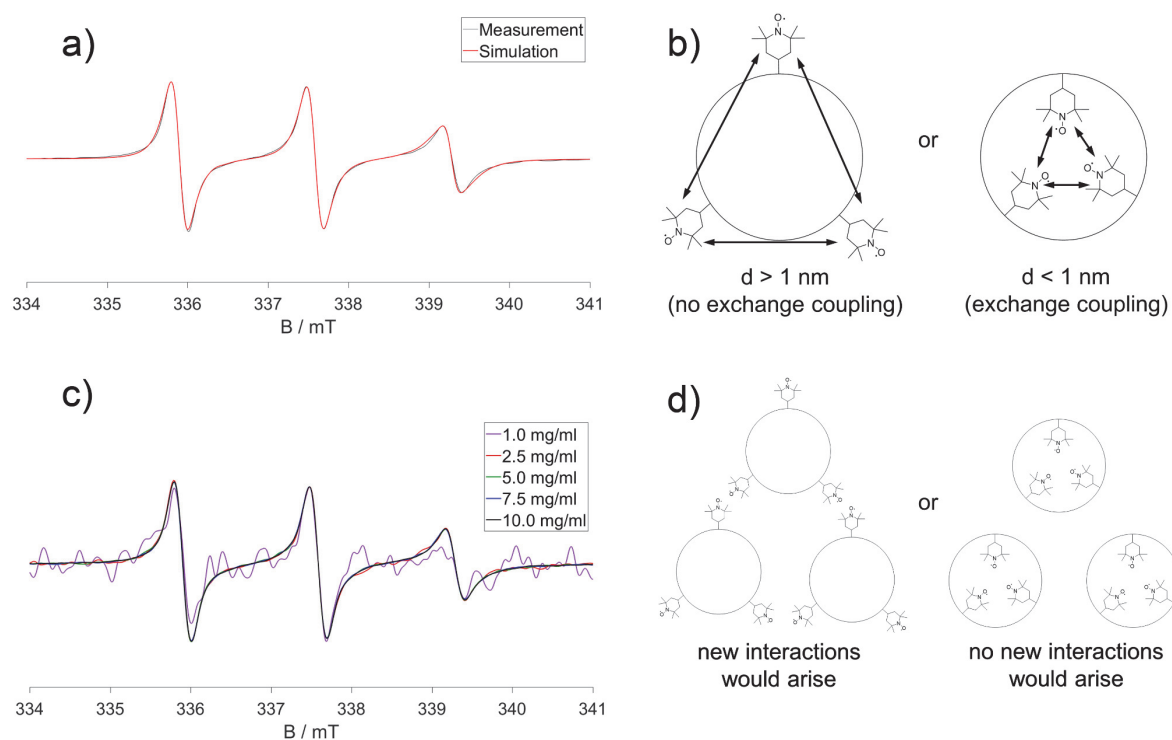


**Figure 19.** Results of the CW-EPR spectroscopic analysis of the SCNPs. a) The spectra revealed Heisenberg exchange coupling of individual TEMPO labels, that needed to be included to the spectral simulation for a perfect fit. b) Schematic interpretation of the Heisenberg exchange coupling. c) Concentration independent shape of the spectra proving the location of the labels inside the SCNPs, and not on their surface, as depicted in d). Reprinted and adapted with permission from Wiley-VCH, copyright © 2020 (open access).<sup>269</sup>

Decay associated fluorescence spectra (DAS) confirmed the results of the CW-EPR spectra by showing comparable effects, as shown in **Figure 20**. The non-bound dye aBOD in water fluoresced in a single exponential decay with a short fluorescence lifetime. Covalently binding it to a linear polymer created two additional decays with fluorescence lifetimes in the ns-range by enabling the formation of polymer regions, that could form hydrophobic environments with less contact of aBOD to the fluorescence quenching water. Binding the dye to the SCNP reduced the quenching effect of water even further, again prolonging the fluorescence lifetimes of all decays, and reducing the contribution of the fast decay. Hence, the surrounding environment of the dye molecules is even more hydrophobic, i.e., even less influenced by

water. In addition to that, the SCNP-bound aBOD molecules showed the formation of excitonic couples. Similar to the Heisenberg exchange in the CW-EPR spectra, those couples only occur, when two or more dye molecules get into direct contact with each other, again proving the formation of confined structures inside the SCNPs with high local label concentrations.

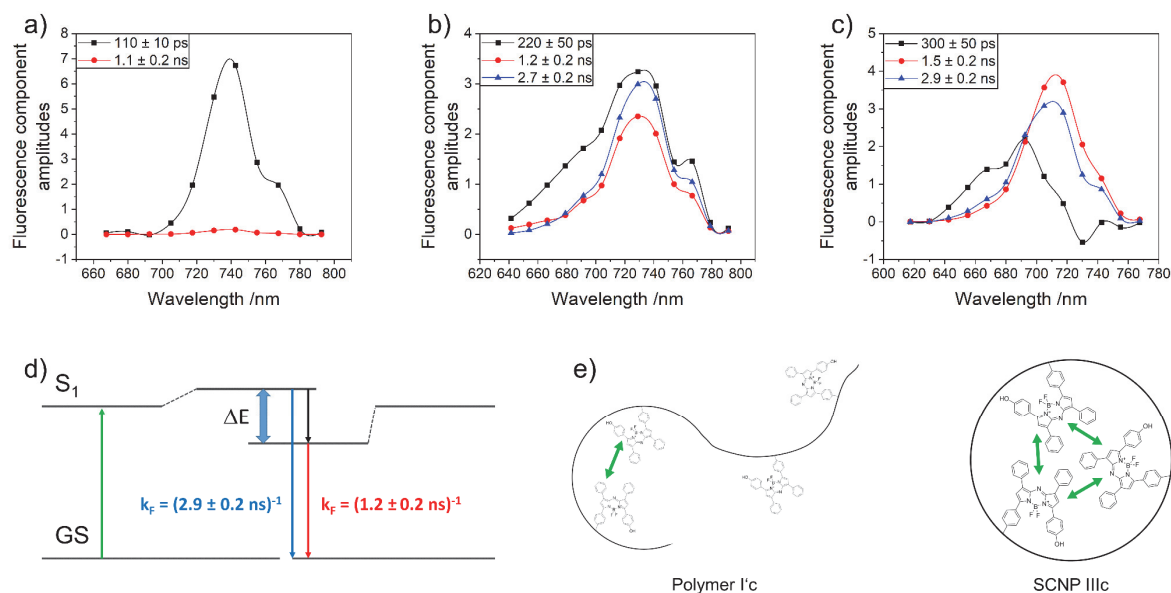
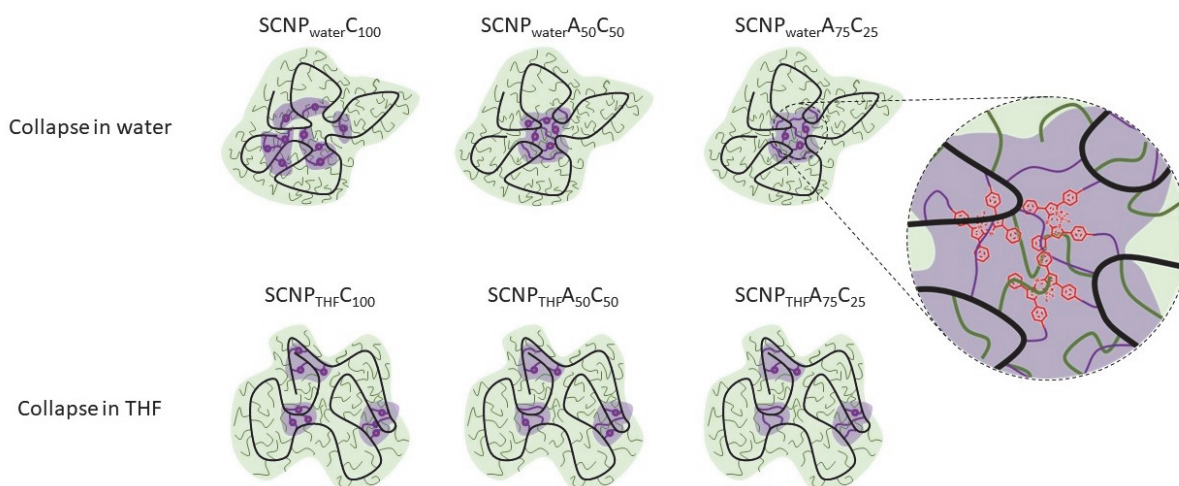


**Figure 20.** Decay associated fluorescence spectra of a) aBOD in water (KoleI), b) the aBOD labelled linear polymer, and c) the aBOD labelled SCNP. d) Jablonsky diagram of the excitonic coupling of multiple aBOD molecules. e) Schematic interpretation of the nanostructure of the aBOD labelled linear polymer and SCNP. Reprinted and adapted with permission from Wiley-VCH, copyright © 2020 (open access).<sup>269</sup>

Varying the collapse conditions in pathway II of **Scheme 3** proved that the solvent as well as the bulkiness and mobility of the crosslinkers have a major influence on the resulting nanostructure, as shown in **Scheme 4**. Choosing the non-polar THF as solvent for the collapse reaction resulted in open, sparse SCNPs with no defined internal structure, since there was no driving force for its formation. This driving force was achieved by changing the collapse solvent to water. Here, the crosslinkers and azide-modified monomer units of the polymer agglomerated into a hydrophobic core, resulting in a defined core-shell structure. Nevertheless, this core-shell structure was only able to form, when a mixture of the labelling crosslinkers and the flexible and less bulky octadiyne was used. Using only the labelling crosslinkers again resulted in open and sparse SCNPs because less long-range crosslinking reactions were possible. This observation was proven by DAS measurements. The fluorescent labels in the SCNPs which did not form a core-shell structure were distributed all over the SCNPs, hence, were unable to form excitonic couples. Therefore, the DAS of those SCNPs resembled that of the open polymer chain in **Figure 20b**, while the DAS of the SCNPs which formed the core-shell structure showed excitonic coupling.



**Scheme 4.** Schematic interpretation of the internal nanostructure of externally crosslinked SCNPs depending on variations of the collapse solvent as well as the crosslinker ability to perform long-range crosslinks. Reprinted with permission from Wiley-VCH, copyright © 2022 (open access).<sup>272</sup>

### 5.3. Photoacoustic Measurements

Combining the spectroscopic results, the formation of core-shell structured SCNPs has been proven, containing confined and hydrophobic cores that encapsulated the labels. This property of the SCNPs made them perfect candidates for their intended application as contrast agent carriers for pump-probe PA measurements, as they ensure water solubility, low toxicity, thermoresponsive behavior, and a hydrophobic environment around the fluorescent dyes, which therefore showed strong fluorescence intensities and long fluorescence lifetimes.

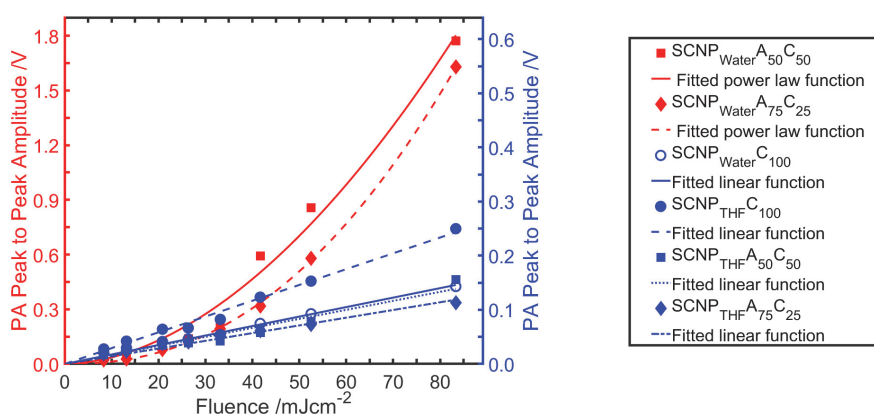


**Figure 21.** Absorption normalized PA signal amplitudes, revealing a non-linear fluence dependence of the PA response. Reprinted with permission from Wiley-VCH, copyright © 2022 (open access).<sup>272</sup>

Besides the general possibility to create intense PA responses, the aBOD-labelled SCNPs showed effects, that could be interesting contrast mechanisms, in addition to the already

contrasting pump-probe excitation. The SCNPs that were synthesized with an external crosslinker, as long as a core-shell structure was formed, have shown a non-linear PA amplitude response, as depicted in **Figure 21**. Analysis of the intramolecular crosslinked SCNPs has shown that each excitation pulse created a different PA amplitude, as depicted in **Figure 22**. This was caused by the thermally triggered compaction of the core, in which the dye molecules were located. This led to changed photophysical properties after each excitation of the dye molecules, resulting in changes of the PA signal generation. Both effects are promising contrasting mechanisms for actual biomedical PA imaging since both are unique for the here presented SCNPs and distinguish them from any biological material which could disturb the imaging procedure.

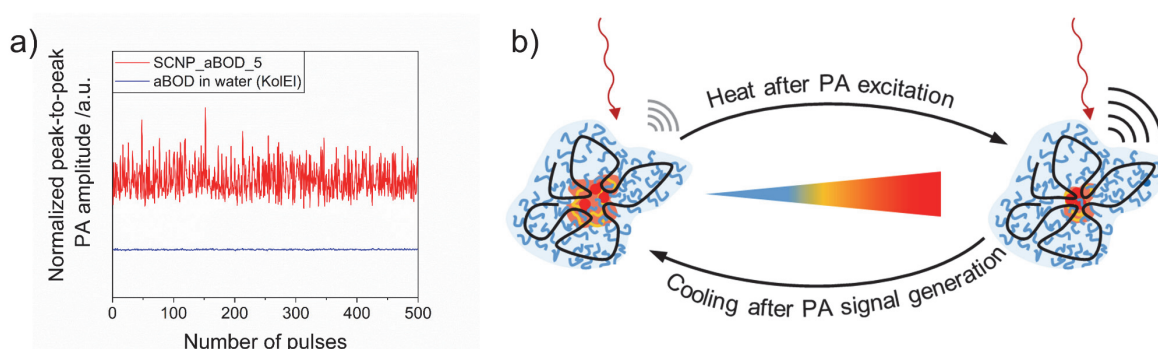


**Figure 22.** a) Fluctuating PA signal of the thermoresponsive SCNPs. b) Schematic interpretation of the thermoresponsive behavior. Reprinted and adapted with permission from the Royal Society of Chemistry, copyright © 2023.<sup>270</sup>

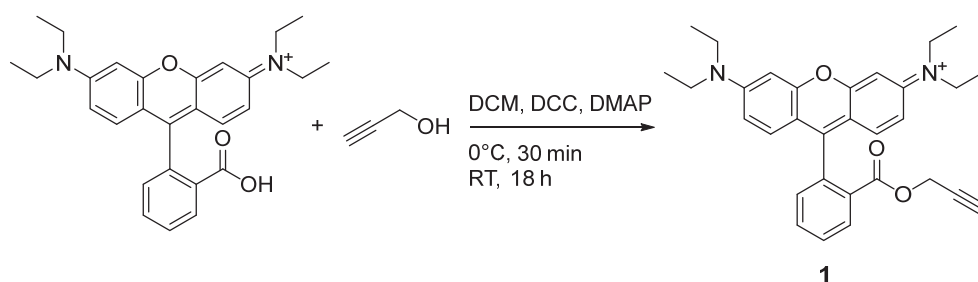
Summarizing the main results of this thesis leads to the conclusion, that the here presented synthetical approaches are capable of resulting in defined core-shell structured SCNPs, which – using various physicochemical analyses – were revealed to be excellent candidates for their intended application as contrast-agent-encapsulating systems for pump-probe PA imaging. The straight forward combination of using amphiphilic PEGMA-based copolymers with hydrophobic crosslinking units together with the effectiveness of CuAAC in water is capable of being used as platform for various applications, simply by using an alkyne-modified functionality of interest.

## 6. Syntheses

The following descriptions of the synthetical procedures have been taken and adapted from the main publications of this thesis [P1] - [P3] with the permissions from Wiley-VCH,<sup>269, 272</sup> and the Royal Society of Chemistry.<sup>270</sup>

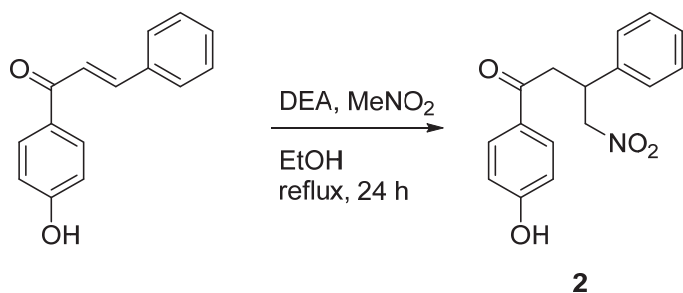
### 6.1. Fluorescent Dyes and Radical Labels

#### Synthesis of Rhodamine B propargyl ester **1**



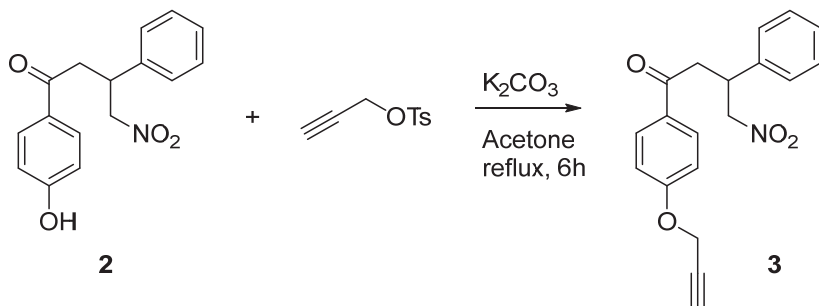
Rhodamine B (1 mmol, 146 mg), dicyclohexylcarbodiimid (1.1 mmol, 226.96 mg) and propargyl alcohol (1.1 mmol, 61.67 mg, 63.5  $\mu$ L) were dissolved in dry DCM (5 mL) in a Schlenk tube under nitrogen atmosphere. The tube was wrapped in aluminum foil and put into an ice bath. 4-(Dimethylamino)-pyridine (0.2 mmol, 24.43 mg) was added. The reaction mixture was stirred at 0°C for 30 min and at room temperature over night. The colorless precipitate was removed by filtration and washed with DCM. The DCM was removed in vacuum. The crude product was dissolved in ACN, filtered and dried under vacuum. The product was purified by column chromatography (methanol:chloroform 1:5,  $R_f = 0.4$ ) to get the product as a golden powder. Yield: 40%. <sup>1</sup>H-NMR (CDCl<sub>3</sub>, 500 MHz,  $\delta$  in ppm): 8.31 (1H, m,  $H_{Ar}$ ), 7.84 (1H, m,  $H_{Ar}$ ), 7.75 (1H, m,  $H_{Ar}$ ), 7.35 (1H, m,  $H_{Ar}$ ), 7.06 (2H, m,  $H_{Ar}$ ), 6.91 (2H, m,  $H_{Ar}$ ), 6.86 (2H, m,  $H_{Ar}$ ), 4.61 (2H, d,  $J^4 = 2.4$  Hz, OCH<sub>2</sub>), 3.63 (8H, q,  $J^3 = 7.2$  Hz, N-CH<sub>2</sub>CH<sub>3</sub>), 2.45 (1H, t,  $J^4 = 2.4$  Hz,  $\equiv$ CH), 1.33 (12H, t,  $J^3 = 7.2$  Hz, CH<sub>3</sub>).

### Synthesis of 1-(4-hydroxyphenyl)-4-nitro-3-phenylbutan-1-one **2**



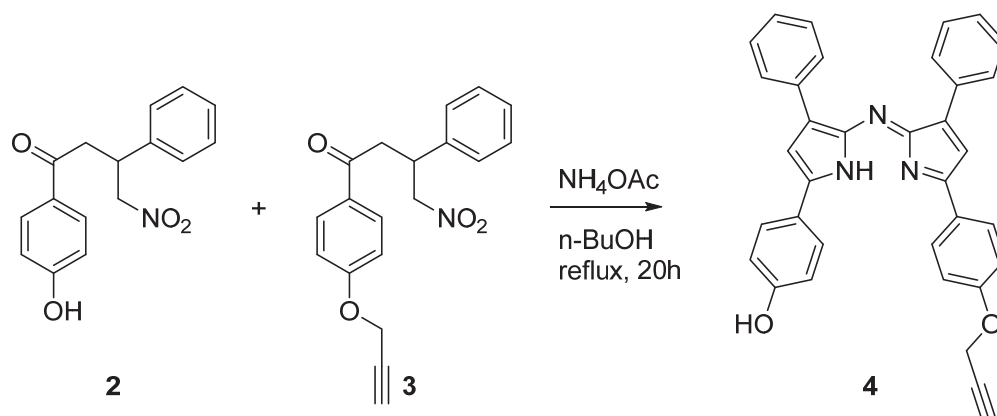
*p*-Hydroxychalcone (14.7 mmol, 3g) was dissolved in ethanol (20 mL). The solution was heated to reflux (90°C oil bath temperature). Diethylamine (66.75 mmol, 4.88 g, 6.9 mL) and nitromethane (147 mmol, 8.15 g, 7.2 mL) were added dropwise and the reaction solution was stirred under reflux for 18 h. The solution was poured in 100 mL 1 M HCl and the product extracted with ethyl acetate. The crude product was purified by column chromatography (methanol:DCM 1:10,  $R_f = 0.47$ ). Yield: 92%. <sup>1</sup>H-NMR (CDCl<sub>3</sub>, 400 MHz,  $\delta$  in ppm): 7.85 (2H, m,  $H_{Ar}$ ), 7.33 (2H, m,  $H_{Ar}$ ), 7.27 (3H, m,  $H_{Ar}$ ), 6.86 (2H, m,  $H_{Ar}$ ), 5.74 (1H, s (broad), -OH), 4.88-4.64 (2H, m, NO<sub>2</sub>-CH<sub>2</sub>), 4.21 (1H, m, Ph-CH), 3.39 (2H, m, O=C-CH<sub>2</sub>).

### Synthesis of 4-nitro-3-phenyl-1-(4-(prop-2-yn-1-yloxy)phenyl)butan-1-one **3**



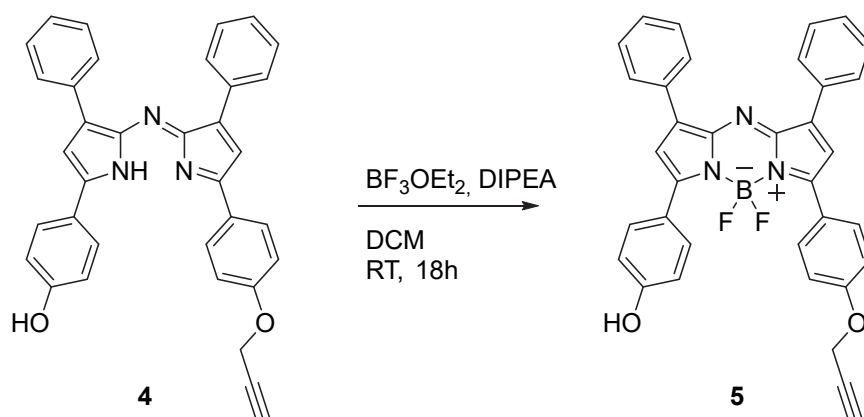
**2** (5 mmol, 1.43g) was dissolved in acetone (30 mL). K<sub>2</sub>CO<sub>3</sub> (15 mmol, 2.07 g) was added and the dispersion was heated to 70°C (reflux). After 1 h propargyl tosylate (7.5 mmol, 1.58 g, 1.28 mL) was dissolved in 5 mL acetone and added to the reaction mixture. After 6 h it was cooled to room temperature, filtrated and the acetone was removed under reduced pressure. The crude product was dissolved in ethyl acetate and washed with water. The organic phase was dried with Na<sub>2</sub>SO<sub>4</sub> and removed under reduced pressure. The product was purified by column chromatography (ethyl acetate:hexane 1:3,  $R_f = 0.25$ ). Yield: 55%. <sup>1</sup>H-NMR (CDCl<sub>3</sub>, 400 MHz,  $\delta$  in ppm): 7.91 (2H, m,  $H_{Ar}$ ), 7.33 (2H, m,  $H_{Ar}$ ), 7.27 (3H, m,  $H_{Ar}$ ), 7.01 (2H, m,  $H_{Ar}$ ), 5.74 (1H, s (broad), OH), 4.86-4-65 (2H, m, NO<sub>2</sub>-CH<sub>2</sub>), 4.75 (2H, d,  $J^d = 2.4$  Hz,  $\equiv$ C-CH<sub>2</sub>), 4.21 (1H, m, Ph-CH), 3.40 (2H, m, O=C-CH<sub>2</sub>), 2.55 (1H, t,  $J^t = 2.4$  Hz,  $\equiv$ CH).

Synthesis of [5-(4-Hydroxyphenyl)-3-phenyl-1H-pyrrol-2-yl]-[4-prop-2-yn-1-yloxyphenyl]-3-phenylpyrrol-2-ylidene]amine **4**



**2** (2.16 mmol, 618 mg), **3** (2.16 mmol, 700 mg) and ammonium acetate (150 mmol, 11.6 g) in  $n\text{-BuOH}$  (50 mL) were heated under reflux (130°C oil bath) for 20 h. The reaction mixture was cooled in an ice bath and filtrated. The isolated solid was washed with cold  $n\text{-BuOH}$  and dried under vacuum. The product was purified by column chromatography ( $\text{CHCl}_3$ :methanol 20:1,  $R_f = 0.51$ ). Yield: 7%.  $^1\text{H-NMR}$  ( $\text{CDCl}_3$ , 500 MHz,  $\delta$  in ppm): 8.05 (4H, m,  $H_{Ar}$ ), 7.93 – 7.82 (4H, m,  $H_{Ar}$ ), 7.42 (4H, m,  $H_{Ar}$ ), 7.35 (2H, m,  $H_{Ar}$ ), 7.13 (4H, m,  $H_{Ar}$ ), 6.99 (2, m,  $H_{Ar}$ ), 4.80 (2H, d,  $J^4 = 2.3$  Hz,  $\equiv\text{C-CH}_2$ ), 2.59 (1H, t,  $J^4 = 2.3$  Hz,  $\equiv\text{CH}$ ).

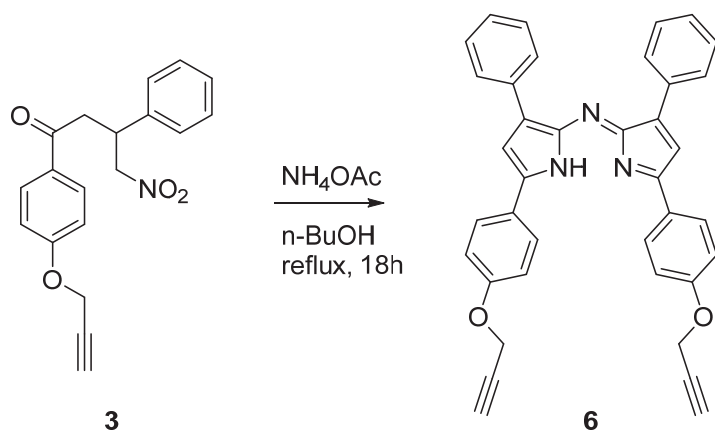
Synthesis of the  $\text{BF}_2$ -chelate of [5-(4-Hydroxyphenyl)-3-phenyl-1H-pyrrol-2-yl]-[4-prop-2-yn-1-yloxyphenyl]-3-phenylpyrrol-2-ylidene]amine **5**



**4** (0.15 mmol, 80 mg) was dissolved in dry DCM (20 mL). DIPEA (1.8 mmol, 233 mg, 306  $\mu\text{L}$ ) was added. The solution was stirred for 10 min at room temperature before being cooled to 0°C.  $\text{BF}_3\text{OEt}_2$  (2.7 mmol, 383 mg, 333  $\mu\text{L}$ ) was added. The resulting solution was stirred at 0°C for 30 min and then at room temperature for 18 h. The product solution was diluted with ethyl acetate, washed with  $\text{NH}_4\text{Cl}$ -solution, brine, and water, dried with  $\text{Na}_2\text{SO}_4$ , and the solvent was removed under reduced pressure. The crude product was purified by column

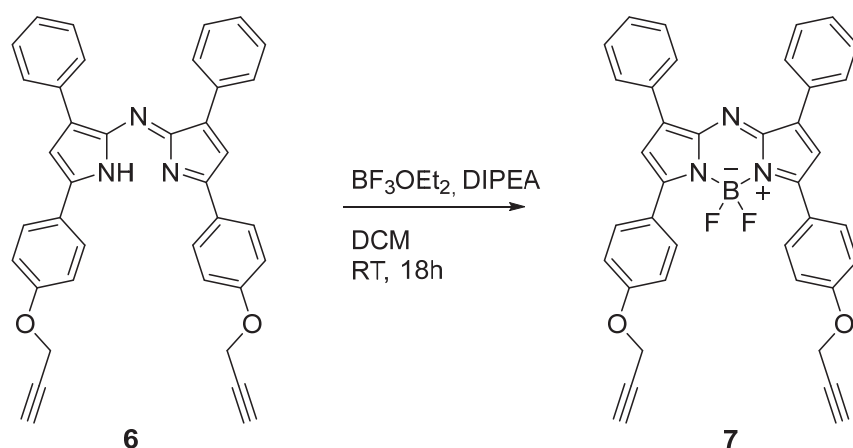
chromatography (ethyl acetate:hexane 1:1,  $R_f = 0.38$ ) to get the product as a red solid. Yield: 91%.  $^1\text{H-NMR}$  ( $\text{CDCl}_3$ , 500 MHz,  $\delta$  in ppm): 8.13 - 8.02 (8H, m,  $H_{Ar}$ ), 7.50 - 7.40 (6H, m,  $H_{Ar}$ ), 7.13 - 7.06 (2H, m,  $H_{Ar}$ ), 7.04 (2H, m,  $H_{Ar}$ ), 6.96 - 6.92 (2H, m,  $H_{Ar}$ ), 4.78 (2H, d,  $J^4 = 2.4$  Hz,  $\equiv\text{C-CH}_2$ ), 2.58 (1H, t,  $J^4 = 2.4$  Hz,  $\equiv\text{CH}$ ).

**Synthesis of [5-(4-prop-2-yn-1-yloxyphenyl)-3-phenyl-1H-pyrrol-2-yl]-[5-(4-prop-2-yn-1-yloxyphenyl)-3-phenylpyrrol-2-ylidene]amine 6**



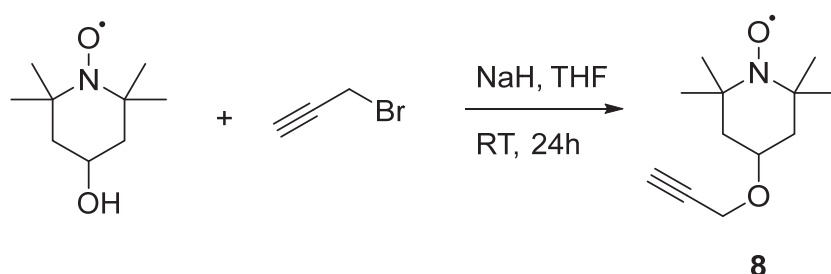
**3** (2.23 mmol, 722 mg) and ammonium acetate (78.1 mmol, 6 g) in *n*-BuOH (25 mL) were heated under reflux (130°C oil bath) for 20 h. The reaction was cooled to room temperature and filtrated. The isolated solid was washed with cold *n*-BuOH and dried under vacuum. The product was used without further purification. Yield: 51%.  $^1\text{H-NMR}$  ( $\text{CDCl}_3$ , 500 MHz,  $\delta$  in ppm): 8.06 (4H, m,  $H_{Ar}$ ), 7.92 (4H, m,  $H_{Ar}$ ), 7.42 (2H, m,  $H_{Ar}$ ), 7.35 (2H, m,  $H_{Ar}$ ), 7.14 (6H, m,  $H_{Ar}$ ), 5.36 (1H, s (broad), NH), 4.81 (4H, d,  $J^4 = 2.3$  Hz,  $\equiv\text{C-CH}_2$ ), 2.59 (2H, t,  $J^4 = 2.3$  Hz,  $\equiv\text{CH}$ ).

**Synthesis of the  $\text{BF}_2$ -chelate of [5-(4-prop-2-yn-1-yloxyphenyl)-3-phenyl-1H-pyrrol-2-yl]-[5-(4-prop-2-yn-1-yloxyphenyl)-3-phenylpyrrol-2-ylidene]amine 7**



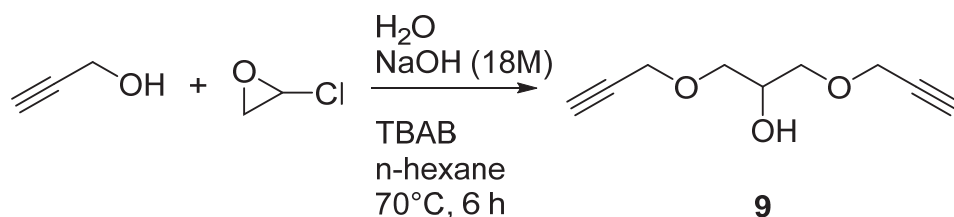
**6** (0.2 mmol, 113.5 mg) was dissolved in dry DCM (50 mL). DIPEA (2.4 mmol, 310.2 mg, 408  $\mu$ L) was added. The solution was stirred for 10 min at room temperature before being cooled to 0°C.  $\text{BF}_3\text{OEt}_2$  (3.6 mmol, 510.9 mg, 44  $\mu$ L) was added. The resulting solution was stirred at 0°C for 30 min and then at room temperature for 18 h. The product solution was washed with  $\text{NH}_4\text{Cl}$ -solution, brine, and water, dried with  $\text{Na}_2\text{SO}_4$  and the solvent was removed under reduced pressure. The crude product was purified by column chromatography (DCM:hexane 3:1,  $R_f = 0.54$ ) to get the product as a red solid. Yield: 77%.  $^1\text{H-NMR}$  ( $\text{CDCl}_3$ , 500 MHz,  $\delta$  in ppm): 8.09 (4H, m,  $H_{Ar}$ ), 8.06 (4H, m,  $H_{Ar}$ ), 7.49-7.38 (6H, m,  $H_{Ar}$ ), 7.09 (4H, m,  $H_{Ar}$ ), 7.03 (2H, m,  $H_{Ar}$ ), 4.76 (4H, d,  $J^4 = 2.4$  Hz,  $\equiv\text{C-CH}_2$ ), 2.57 (2H, t,  $J^4 = 2.4$  Hz,  $\equiv\text{CH}$ ).

#### Synthesis of TEMPO propargyl ether **8**



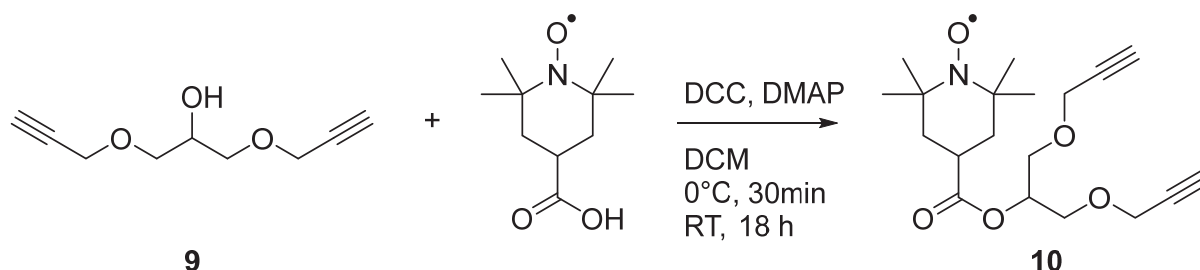
Sodium hydride (60% suspension in mineral oil, 10 mmol, 400 mg) was placed in a Schlenk flask under nitrogen atmosphere and 20 mL of dry THF were added. A solution of *p*-hydroxy-TEMPO (8.71 mmol, 1.5 g) in 5 mL of dry THF was added slowly to the stirring suspension at 0°C. After stirring for 30 min at 0°C propargyl bromide (80% solution in toluene, 11 mmol, 1.0 mL) was added dropwise. The solution was stirred at room temperature for one day and then poured into 150 mL of ice water. The product was extracted with ethyl acetate. The combined organic phases were again washed with water and brine, dried over  $\text{Na}_2\text{SO}_4$ , filtered and evaporated under vacuum. The residue was purified by column chromatography (ethyl acetate:hexane 1:2,  $R_f = 0.45$ ) to get the product as an orange powder. Yield: 71%.  $^1\text{H-NMR}$  ( $\text{CDCl}_3$ , 400 MHz,  $\delta$  in ppm): 4.11 (s, 2H,  $\text{OCH}_2$ ), 2.46 (s, 1H,  $\equiv\text{CH}$ ) (due to paramagnetic broadening of the nitroxide radical not all signals were observable).

Synthesis of 1,3-bis(2-propyn-1-yloxy)-2-propanol **9**



Tetrabutylammonium bromide (0.4 mmol, 128.85 mg) was given to an 18 M solution of NaOH in water (5 mL). n-Hexane (5 mL) was added and the resulting biphasic mixture was heated to  $70^\circ\text{C}$  under vigorous stirring. Propargyl alcohol (20 mmol, 1.12 g, 1.18 mL) was added. After 10 minutes epichlorohydrin (8 mmol, 740 mg, 630  $\mu\text{L}$ ) was added and the reaction solution was stirred for 6 h at  $70^\circ\text{C}$ . The resulting solution was poured into 100 mL cold water and neutralized with HCl. The product was extracted with ethyl acetate. The combined organic phases were dried with  $\text{Na}_2\text{SO}_4$  and evaporated under vacuum. The product was purified by column chromatography (ethyl acetate:hexane 1:1,  $R_f = 0.45$ ). Yield: 53%.  $^1\text{H-NMR}$  ( $\text{CDCl}_3$ , 400 MHz,  $\delta$  in ppm): 4.19 (4H, m,  $\equiv\text{C-CH}_2$ ), 4.00 (1H, m, HO-CH), 3.59 (4H, m, O- $\text{CH}_2$ -CH), 2.44 (2H, m,  $\equiv\text{CH}$ )

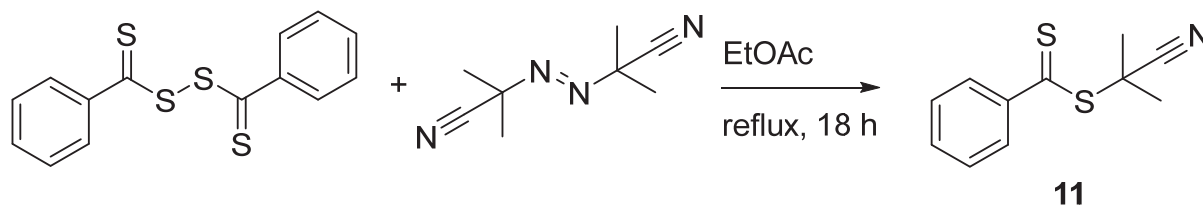
Synthesis of 1,3-bis(prop-2-yn-1-yloxy)propan-2-yl TEMPO-4-carboxylate **10**



Under  $\text{N}_2$ -atmosphere carboxy-TEMPO (1 mmol, 200.26 mg), N, N'-dicyclohexylcarbodiimide (DCC, 1.1 mmol, 227 mg) and **1** (1.1 mmol, 185 mg, 174.7  $\mu\text{L}$ ) were dissolved in DCM (10 mL) and placed in an ice bath. 4-dimethylaminopyridine (DMAP, 0.2 mmol, 24.4 mg) was added and stirred for 30 min at  $0^\circ\text{C}$ . The reaction solution was stirred for further 18 h at room temperature. The precipitate was filtered and the DCM was removed under reduced pressure. The crude product was purified by column chromatography (DMC:methanol 100:1,  $R_f = 0.65$ ). Yield: 56%.  $^1\text{H-NMR}$  ( $\text{CDCl}_3$ , 500 MHz,  $\delta$  in ppm, because of the nitroxyl radical some peaks do not appear in the spectrum and all other peaks are broadened): 5.32 (1H, COOCH), 4.26 (4H,  $\equiv\text{C-CH}_2$ ), 3.80 (4H, O- $\text{CH}_2$ ), 2.49 (2H,  $\equiv\text{CH}$ ). ESI-TOF:  $m/z$  calculated for  $\text{C}_{18}\text{H}_{26}\text{NO}_5^- + \text{Na}^+$  [M + H $^+$ ] = 373.1860, found 373.1857.

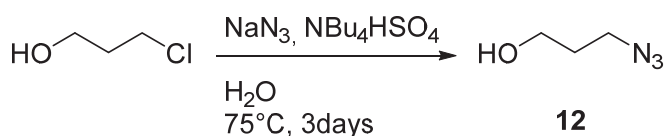
## 6.2. Chain Transfer Agent and Monomers

### Synthesis of Cyanoisopropyl dithiobenzoate **11** (CPDB)



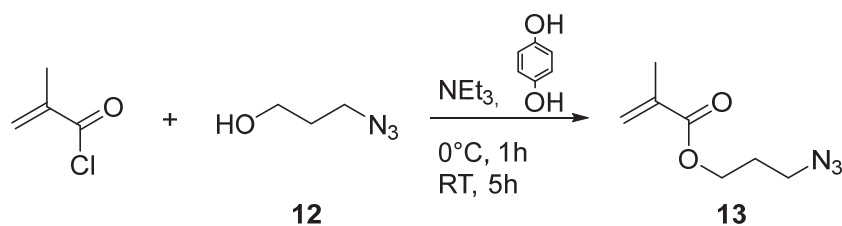
Bis(thiobenzoyl) disulfide (0.8 mmol, 245.2 mg) and AIBN (1.2 mmol, 197.1 mg) were dissolved in 10 mL ethyl acetate. The solution was degassed by five freeze-pump-thaw cycles and stirred under reflux for 18 h. The crude product was dried under vacuum and purified by column chromatography (hexane:ethyl acetate 10:1,  $R_f = 0.27$ ) to get the product as a red oil. Yield: 56%.  $^1\text{H-NMR}$  ( $\text{CDCl}_3$ , 400 MHz,  $\delta$  in ppm): 7.92 (2H, m, *o*- $H_{Ar}$ ), 7.56 (1H, m, *p*- $H_{Ar}$ ), 7.39 (2H, m, *m*- $H_{Ar}$ ), 1.94 (6H, s,  $\text{CH}_3$ ).

### Synthesis of 3-Azido-1-propanol **12**



3-Chloro-1-propanol (23.5 mmol, 2.2 g, 2 mL) was added dropwise to a solution of sodium azide (48 mmol, 3.13 g) and tetrabutylammonium hydrogen sulphate (0.2 mmol, 70 mg) in 50 mL water at room temperature. The resulting solution was heated to  $75^\circ\text{C}$ . After stirring for three days the product was extracted with DCM. The combined organic phases were dried with  $\text{Na}_2\text{SO}_4$  and the solvent was evaporated under vacuum to get the product as a colorless liquid. Yield: 85%.  $^1\text{H-NMR}$  ( $\text{CDCl}_3$ , 400 MHz,  $\delta$  in ppm): 3.71 (2H, t,  $J^3 = 6.0$  Hz,  $\text{HO-CH}_2$ ), 3.42 (2H, t,  $J^3 = 6.6$  Hz,  $\text{CH}_2\text{-N}_3$ ), 2.21 (1H, s,  $\text{OH}$ ), 1.80 (2H, tt,  $J^3 = 6.6, 6.0$  Hz,  $\text{CH}_2\text{CH}_2\text{CH}_2$ ).

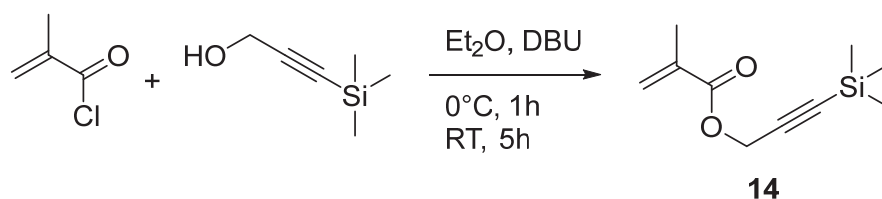
### Synthesis of 3-Azidopropyl methacrylate **13** (APMA)



**12** (19.3 mmol, 1.95 g, 1.8 mL), triethylamine (28.7 mmol, 2.9 g, 4 ml) and hydroquinone (10  $\mu\text{mol}$ , 1 mg) were dissolved in 25 mL of dry DCM and placed in an ice bath. Methacryloyl

chloride (28.7 mmol, 3 g, 2.8 mL) in 5 mL of dry DCM was added dropwise. The resulting solution was stirred at 0°C for 1 h and at room temperature for additional 5 h. The white precipitate was removed by filtration and the product solution was washed with water, saturated sodium bicarbonate solution and brine. The organic phase was dried with Na<sub>2</sub>SO<sub>4</sub> and the solvent was removed under vacuum. The product was purified by column chromatography (hexane:diethyl ether 2:1, *R<sub>f</sub>* = 0.46) to get the product as a pale-yellow liquid. The product was stored with hydroquinone as stabilizer. Yield: 25%. <sup>1</sup>H-NMR (CDCl<sub>3</sub>, 500 MHz, δ in ppm): 6.11 (1H, dq, *J*<sup>2</sup> = 2.0 Hz, *J*<sup>4</sup> = 1.0 Hz, =CH), 5.58 (1H, dq, *J*<sup>2</sup> = 2.0 Hz, *J*<sup>4</sup> = 1.6 Hz, =CH), 4.24 (2H, t, *J*<sup>3</sup> = 6.2 Hz, COO-CH<sub>2</sub>), 3.42 (2H, t, *J*<sup>3</sup> = 6.7 Hz, CH<sub>2</sub>-N<sub>3</sub>), 1.96 (2H, tt, *J*<sup>3</sup> = 6.7, 6.2 Hz, CH<sub>2</sub>CH<sub>2</sub>CH<sub>2</sub>), 1.95 (3H, dd, *J*<sup>4</sup> = 1.6, 1.0 Hz, CH<sub>3</sub>).

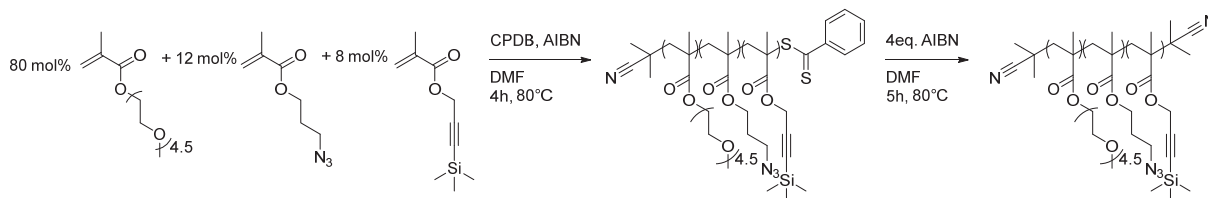
#### Synthesis of 3-(Trimethylsilyl)propargyl methacrylate **14** (TMSPMA)



3-(Trimethylsilyl)propargyl alcohol (15.58 mmol, 2.0 g, 2.15 mL) and 1,8-diazabicyclo[5.4.0]undec-7-ene (DBU) (18.7 mmol, 1.42 g, 1.4 mL) were dissolved in 20 mL of dry diethyl ether and cooled to 0°C. Methacryloyl chloride (18.7 mmol, 1.95 g, 1.8 mL) in 10 mL of dry diethyl ether was added dropwise. The resulting solution was stirred at 0°C for 1 h and at room temperature for additional 5 h. The yellow precipitate was removed by filtration and the product solution was washed with water and brine. The organic phase was dried with Na<sub>2</sub>SO<sub>4</sub> and the solvent was removed under vacuum. The product was purified by column chromatography (hexane:diethyl ether 20:1, *R<sub>f</sub>* = 0.19) to get the product as colorless liquid. Yield: 30%. <sup>1</sup>H-NMR (CDCl<sub>3</sub>, 400 MHz, δ in ppm): 6.17 (1H, dq, *J*<sup>2</sup> = 2.2 Hz, *J*<sup>4</sup> = 1.0 Hz, =CH), 5.61 (1H, dq, *J*<sup>2</sup> = 2.2 Hz, *J*<sup>4</sup> = 1.6 Hz, =CH), 4.76 (2H, s, OCH<sub>2</sub>), 1.96 (3H, dd, *J*<sup>4</sup> = 1.6, 1.0 Hz, CH<sub>3</sub>), 0.18 (9H, s, Si(CH<sub>3</sub>)<sub>3</sub>).

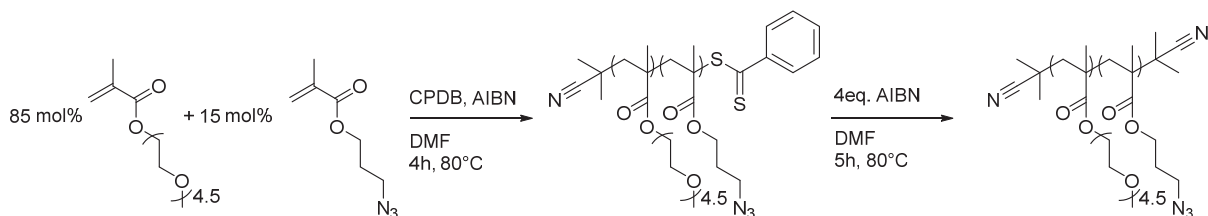
### 6.3. Polymers

#### Synthesis of Poly[(oligo(ethylene glycol) methyl ether methacrylate)-co-(3-azidopropyl methacrylate)-co-(3-(trimethylsilyl)propargyl methacrylate)] (PEATMA)



Oligo(ethylene glycol) methyl ether methacrylate ( $M_n = 300$  Da) (11.52 mmol, 3.46 g), APMA (1.73 mmol, 292 mg, 273  $\mu$ L), and TMSPMA (1.15 mmol, 226 mg, 243  $\mu$ L) were dissolved in 2.8 mL dry DMF in a Schlenk tube. 2 mL of a stock solution of AIBN (4.8 mM, 9.6  $\mu$ mol) and CPDB (24 mM, 48  $\mu$ mol). The resulting mixture was degassed by five freeze-pump-thaw cycles and stirred at 80°C for 3 h. The product was precipitated in cold hexane:diethyl ether (2:1) as a pink polymer. To remove the CTA-endgroup, the polymer was dissolved in 20 mL DMF, AIBN (152  $\mu$ mol, 25 mg) was added, and the solution was degassed by bubbling with  $N_2$ . The solution was stirred at 70°C for 18 h. The solvent was removed under reduced pressure. The resulting yellow polymer was purified by dialysis in THF. The highly viscous product was stored in THF at 5°C to prevent auto-crosslinking. Yield: 54%. GPC (THF):  $M_n = 36.1$  kDa,  $D = 1.7$ .  $^1H$ -NMR ( $CDCl_3$ , 500 MHz,  $\delta$  in ppm): 4.66-4.55 ( $CH_2\equiv Si(CH_3)_3$ ), 4.25-3.90 ( $COOCH_2$ ), 3.82-3.49 ( $OCH_2CH_2O$ ), 3.48-3.43 ( $N_3CH_2$ ), 3.39 ( $OCH_3$ ), 2.07-1.72 ( $CH_2$ ), 1.12-0.77 ( $CH_3$ ), 0.20 ( $Si(CH_3)_3$ ). IR (KBr): 2178  $cm^{-1}$  ( $\tilde{\nu}_{alkyne}$ ), 2100  $cm^{-1}$  ( $\tilde{\nu}_{N_3}$ ).

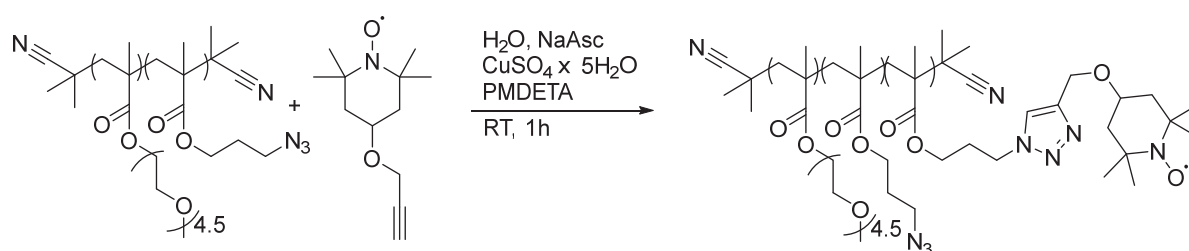
#### Synthesis of Poly[(oligo(ethylene glycol) methyl ether methacrylate)-co-(3-azidopropyl methacrylate)] (PEAMA)



Oligo(ethylene glycol) methyl ether methacrylate ( $M_n = 300$  Da) (12.243 mmol, 3.672 g) and **8** (2.16 mmol, 365.4 mg, 341.52  $\mu$ L) were dissolved in 2 mL dry DMF in a Schlenk tube. 2 mL of a stock solution of CPDB (24 mM, 48  $\mu$ mol) and AIBN (4.8 mM, 9.6  $\mu$ mol) were added to the solution. The resulting mixture was degassed by five freeze-pump-thaw cycles and stirred at 80°C for 4 h. The product was precipitated in cold hexane:diethyl ether (2:1) as a pink polymer. To remove the RAFT-endgroup, the polymer was dissolved in DMF (15 mL), AIBN (4 eq.) was

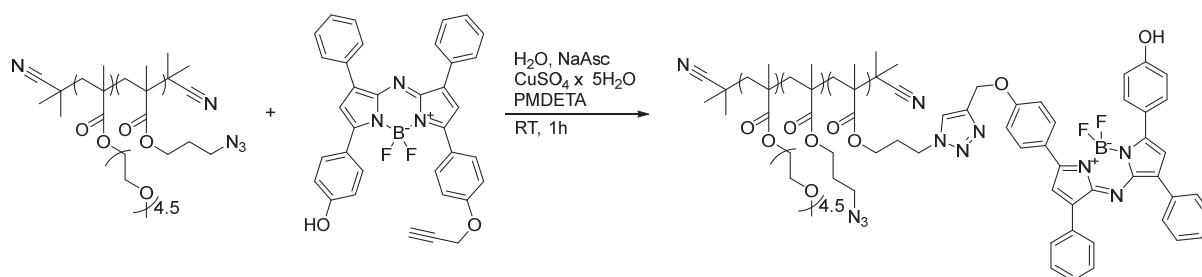
added and the was solution degassed by bubbling with  $N_2$ . The solution was stirred at  $80^\circ C$  for 5 h. The product was again precipitated in cold hexane:diethyl ether (2:1). The resulting yellow, highly viscous polymer was purified by dialysis in THF. Yield: 72%. GPC (THF):  $M_n = 34.6$  kDa,  $D = 1.4$ , DP = 123.  $^1H$ -NMR ( $CDCl_3$ , 500 MHz,  $\delta$  in ppm): 4.25-3.90 ( $COOCH_2$ ), 3.82-3.47 ( $OCH_2CH_2O$ ), 3.48-3.40 ( $N_3CH_2$ ), 3.37 ( $OCH_3$ ), 2.07-1.67 ( $CH_2$ ), 1.09-0.77 ( $CH_3$ ). IR (KBr):  $2100\text{ cm}^{-1}$  ( $\tilde{\nu}_{N_3}$ ).

*Synthesis of Poly[(poly(ethylene glycol) methyl ether methacrylate)-co-(3-azidopropyl methacrylate)-co-(TEMPO-labelled methacrylate)]*



PEAMA (50 mg, 25  $\mu\text{mol}$  of  $N_3$ ), **8** (12.5  $\mu\text{mol}$ , 2.62 mg) and sodium ascorbate (37.5  $\mu\text{mol}$ , 7.4 mg) were dissolved in a mixture of 10 ml THF and 20 mL degassed  $H_2O$ . A solution of  $CuSO_4 \times 5 H_2O$  (7.5  $\mu\text{mol}$ , 1.9 mg) and PMDETA (15  $\mu\text{mol}$ , 2.6 mg, 3.13  $\mu\text{L}$ ) in 5 ml degassed  $H_2O$  was added and the resulting mixture was stirred at room temperature. After 1 h, the product was extracted with DCM, dried with  $Na_2SO_4$  and the solvent was removed under vacuum. The product was cleaned by dialysis in THF to get an orange polymer. Yield: 80%.  $^1H$ -NMR ( $CDCl_3$ , 500 MHz,  $\delta$  in ppm): 5.10 (triazole-CH), 4.25-3.90 ( $COOCH_2$ ), 3.82-3.47 ( $OCH_2CH_2O$ ), 3.48-3.40 ( $N_3CH_2$ ), 3.37 ( $OCH_3$ ), 2.07-1.67 ( $CH_2$ ), 1.09-0.77 ( $CH_3$ ).

*Synthesis of Poly[(poly(ethylene glycol) methyl ether methacrylate)-co-(3-azidopropyl methacrylate)-co-(aBOD-labelled methacrylate)]*

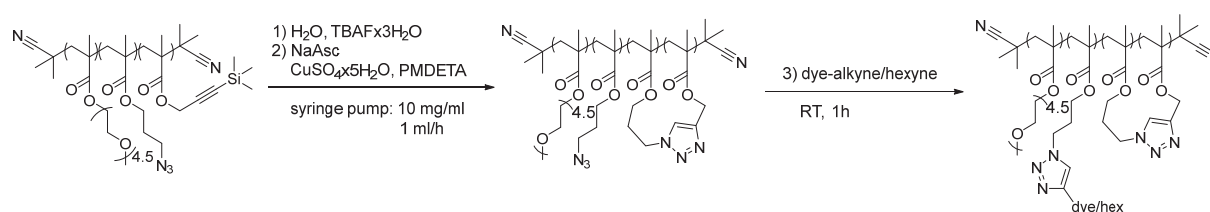


PEAMA (50 mg, 25  $\mu\text{mol}$  of  $N_3$ ), **7** (12.5  $\mu\text{mol}$ , 7.09 mg) and sodium ascorbate (37.5  $\mu\text{mol}$ , 7.4 mg) were dissolved in a mixture of 10 mL THF and 10 mL degassed  $H_2O$ . A solution of  $CuSO_4 \times 5 H_2O$  (7.5  $\mu\text{mol}$ , 1.9 mg) and PMDETA (15  $\mu\text{mol}$ , 2.6 mg, 3.13  $\mu\text{L}$ ) in 5 mL degassed

H<sub>2</sub>O was added and the resulting mixture was stirred at room temperature. After 1 h, the product was extracted with DCM, dried with Na<sub>2</sub>SO<sub>4</sub> and the solvent was removed under vacuum. The product was cleaned by dialysis in THF to get a green polymer. Yield: 64%. <sup>1</sup>H-NMR (CDCl<sub>3</sub>, 500 MHz, δ in ppm): 8.03 (*H<sub>Ar</sub>*), 7.41 (*H<sub>Ar</sub>*), 7.05 (*H<sub>Ar</sub>*), 6.95 (*H<sub>Ar</sub>*), 5.26 (triazole-CH), 4.49 (triazole-CH<sub>2</sub>-O), 4.25-3.90 (COOCH<sub>2</sub>), 3.87-3.47 (OCH<sub>2</sub>CH<sub>2</sub>O), 3.47-3.41 (N<sub>3</sub>CH<sub>2</sub>), 3.38 (OCH<sub>3</sub>), 2.11-1.59 (CH<sub>2</sub>), 1.14-0.67 (CH<sub>3</sub>).

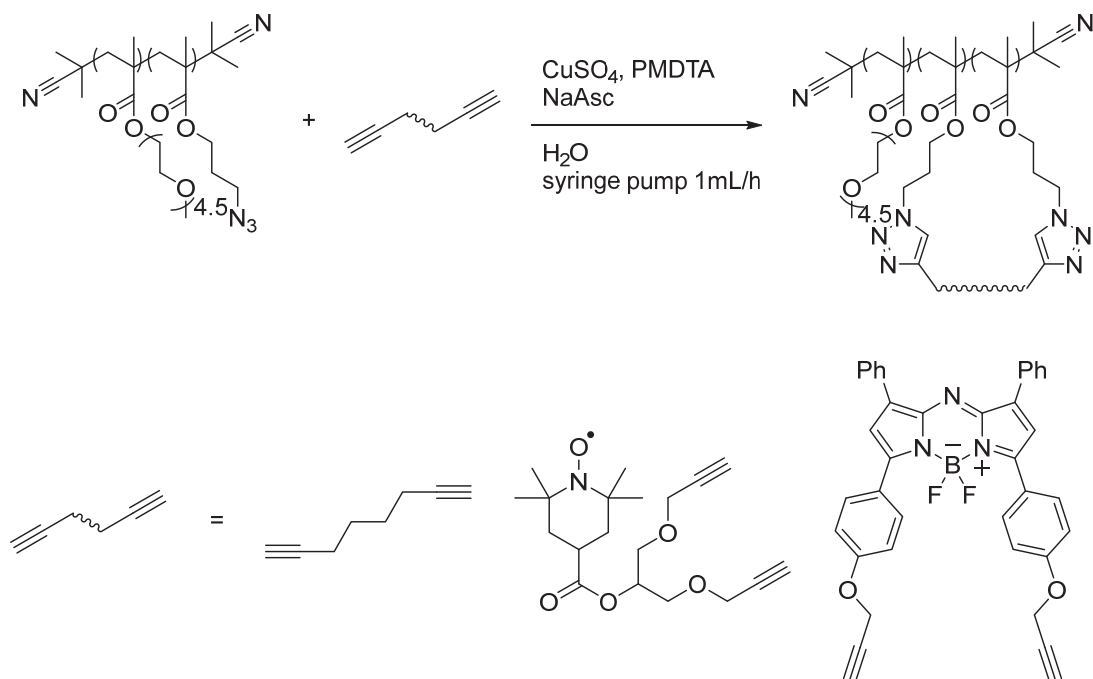
## 6.4. Single-Chain Nanoparticles

*General procedure for the internal single-chain collapse using PEATMA*



PEATMA (100 mg,  $4.35 \times 10^{-5}$  mol N<sub>3</sub>,  $2.90 \times 10^{-5}$  mol alkyne) was dissolved in 9 mL deionized water. A solution of TBAF x 3H<sub>2</sub>O ( $3.48 \times 10^{-5}$  mol, 11 mg, 1.2 eq.) in 1 mL deionized water was added. The solution was put into a syringe pump (0.5 mL/h) and added to a solution of sodium ascorbate (7.5 mmol, 1.5 g), CuSO<sub>4</sub> x 5 H<sub>2</sub>O (0.5 mmol, 125 mg), and PMDTA (1 mmol, 173 mg, 209 μL) in 100 mL degassed water. After 20 h the solution was stirred for one additional hour. For labelling, a solution of the corresponding label (**1**, **5**, or **8**) in 5 mL THF followed by a solution of hexyne in 5 mL THF were added (for complete consumption of N<sub>3</sub> in the incompletely labelled SCNPs), with 30 min stirring after each addition. For the purification it is important to keep the product wet, since the redissolution of dried samples is difficult. The product (and THF) was extracted with DCM. The DCM was reduced under vacuum to get a solution in THF. This solution was passed over a silica column to remove remaining copper impurities. The resulting solution was purified by dialysis going from THF with 1 mL PMDTA to a mixture of water/THF (1:1) and in the end to pure THF. The product was dried under vacuum. Yield: 50%.

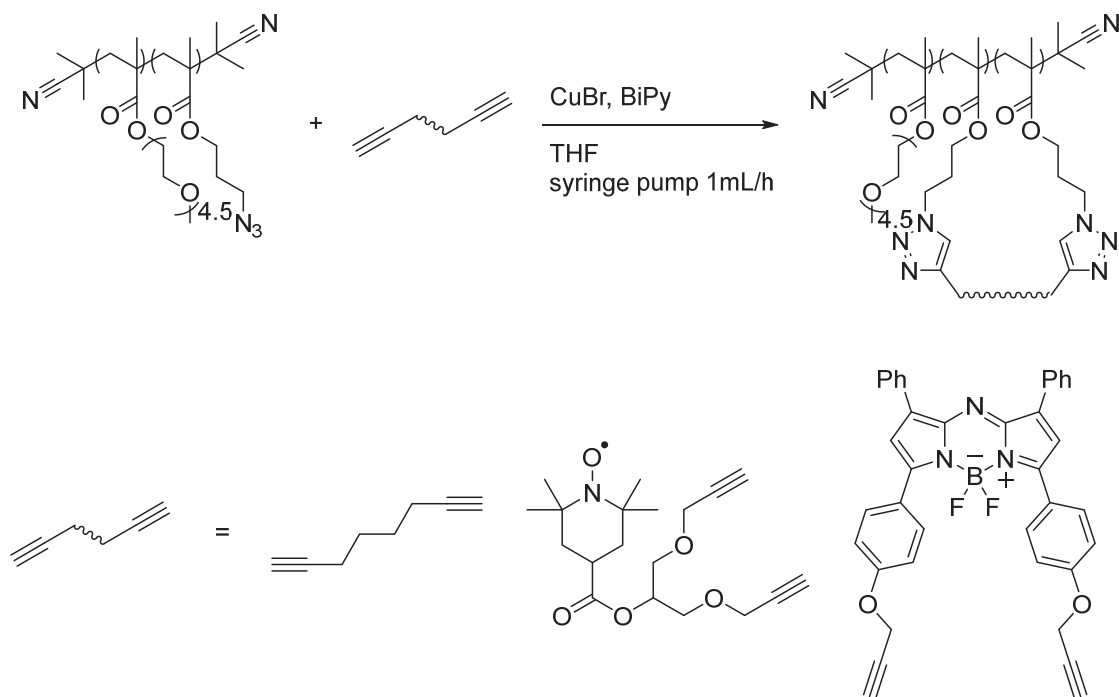
*General procedure for the single-chain collapse in water using external crosslinker*



PEAMA (200 mg,  $1.07 \times 10^{-4}$  mol N<sub>3</sub>) and crosslinker (octadiyne, **7**, **10**, or mixtures of octadiyne and **7** or **10**,  $\Sigma 5.35 \times 10^{-5}$  mol, 0.5 eq. to N<sub>3</sub>) were dissolved in 20 mL THF. The solution was put into a syringe pump (1 mL/h) and added to a solution of sodium ascorbate (7.5 mol, 1.5 g), CuSO<sub>4</sub> x 5 H<sub>2</sub>O (0.5 mmol, 125 mg), and PMDTA (1 mmol, 173 mg, 209  $\mu$ L) in 120 mL degassed H<sub>2</sub>O. After 20 h the solution was stirred for one additional hour. For the purification it is important to keep the product wet since the redissolution of dried samples is difficult. The product (and THF) was extracted with DCM. The DCM was reduced under vacuum to get a solution in THF. This solution was passed over a silica column to remove remaining copper impurities. The resulting solution was purified by dialysis going from THF with 1 mL PMDTA to a mixture of water/THF (1:1) and in the end to pure THF. The product was dried under vacuum. Yield: 50%.

Since TEMPO gets deactivated by sodium ascorbate, it needed to be reactivated. Therefore after the finished addition of the polymer/crosslinker solution, first sodium ascorbate ( $2.5 \times 10^{-4}$  mol, 50 mg) in 5 mL water and then H<sub>2</sub>O<sub>2</sub> (30wt% in H<sub>2</sub>O, 5  $\mu$ L) in 5 mL water were added. The remaining procedure was followed as described above.

General procedure for the single chain collapse in THF



PEAMA (200 mg,  $1.07 \times 10^{-4}$  mol  $N_3$ ) and crosslinker (octadiyne, TEMPO, aza-BODIPY, or mixtures of octadiyne and TEMPO / aza-BODIPY,  $\Sigma 5.35 \times 10^{-5}$  mol, 0.5 eq. to  $N_3$ ) were dissolved in 20 mL THF. The solution was put into a syringe pump (1 mL/h) and added to a solution of CuBr (0.5 mmol, 71.1 mg) and 2,2' bipyridine (1 mmol, 173 mg, 209  $\mu$ L) in 100 mL THF. After 20 h the solution was stirred for one additional hour. 50 mL water were added and the solution was stirred for 30 minutes. For the purification it is important to keep the product wet since the redissolution of dried samples is difficult. THF was removed under reduced pressure to get an aqueous solution. The product was extracted with DCM. THF was added and the DCM was reduced under vacuum to get a solution in THF. This solution was passed over a silica column to remove remaining copper impurities. The resulting solution was purified by dialysis going from THF with 1 mL PMDTA to a mixture of water/THF (1:1) and in the end to pure THF. The product was dried under vacuum. Yield: 60%.

## 7. List of Abbreviations

AFM	atomic force microscopy
ATRP	atom transfer radical polymerization
BTA	benzene-1,3,5-tricarboxamide
CuAAC	copper catalyzed azide-alkyne click reaction
DAS	decay-associated-fluorescence spectroscopy
DLS	dynamic light scattering
DOSY-NMR	diffusion ordered nuclear magnetic resonance spectroscopy
CW-EPR	continuous-wave electron-paramagnetic-resonance
GPC	gel permeation chromatography
GTP	group transfer polymerization
LCST	lower critical solution temperature
LRP	living radical polymerization
NCA	<i>N</i> -carboxyanhydride
NMP	nitroxide mediated radical polymerization
NMR	nuclear magnetic resonance spectroscopy
NOESY	nuclear Overhauser effect spectroscopy
NP	nanoparticle
OEGMA	(oligo ethylene glycol) methacrylate
PA	photoacoustic
PEG	poly ethylene glycol
PEGMA	poly (oligo ethylene glycol) methacrylate
PIB	poly isobutylene
PISA	polymerization-induced self-assembly
PNIPAM	poly <i>N</i> -isopropyl acrylamide
PVC	polyvinyl chloride
RAFT	reversible-addition-fragmentation chain-transfer polymerization
RhoB	Rhodamine B
ROMP	ring opening metathesis polymerization
ROP	ring opening polymerization
RP	radical polymerization
SANS	small angle neutron scattering
SAXS	small angle X-ray scattering
SCNP	single-chain nanoparticle
SLS	static light scattering
SPAAC	strain-promoted azide-alkyne cycloaddition

SPION	superparamagnetic iron oxide nanoparticle
TEM	transmission electron microscopy
TEMPO	(2,2,6,6-tetramethylpiperidin-1-yl)oxyl
THF	tetrahydrofuran
UV	ultraviolet

## 8. Literature

- (1) Altammar, K. A. A review on nanoparticles: characteristics, synthesis, applications, and challenges. *Front. Microbiol.* **2023**, *14*, 1155622. DOI: <https://doi.org/10.3389/fmicb.2023.1155622>
- (2) Ealias, A. M.; P, S. M. A review on the classification, characterisation, synthesis of nanoparticles and their application. *IOP Conf. Ser.: Mater. Sci. Eng.* **2017**, *263*, 032019. DOI: <https://doi.org/10.1088/1757-899X/263/3/032019>
- (3) Freestone, I.; Meeks, N.; Sax, M.; Higgitt, C. The Lycurgus Cup - A Roman nanotechnology. *Gold Bulletin* **2007**, *40* (4), 270-277. DOI: <https://doi.org/10.1007/Bf0321559>
- (4) Abdelhalim, M. A. K.; Mady, M. M.; Ghannam, M. M. Physical Properties of Different Gold Nanoparticles: Ultraviolet-Visible and Fluorescence Measurements. *J. Nanomed. Nanotechol.* **2012**, *03* (04). DOI: <https://doi.org/10.4172/2157-7439.1000135>
- (5) Kelly, K. L.; Coronado, E.; Zhao, L. L.; Schatz, G. C. The optical properties of metal nanoparticles: The influence of size, shape, and dielectric environment. *J. Phys. Chem. B* **2003**, *107* (3), 668-677. DOI: <https://doi.org/10.1021/jp026731y>
- (6) Link, S.; El-Sayed, M. A. Size and temperature dependence of the plasmon absorption of colloidal gold nanoparticles. *J. Phys. Chem. B* **1999**, *103* (21), 4212-4217. DOI: <https://doi.org/10.1021/jp984796o>
- (7) Liao, S.; Yue, W.; Cai, S.; Tang, Q.; Lu, W.; Huang, L.; Qi, T.; Liao, J. Improvement of Gold Nanorods in Photothermal Therapy: Recent Progress and Perspective. *Front. Pharmacol.* **2021**, *12*, 664123. DOI: <https://doi.org/10.3389/fphar.2021.664123>
- (8) Vines, J. B.; Yoon, J. H.; Ryu, N. E.; Lim, D. J.; Park, H. Gold Nanoparticles for Photothermal Cancer Therapy. *Front. Chem.* **2019**, *7*, 167. DOI: <https://doi.org/10.3389/fchem.2019.00167>
- (9) Pang, G. A.; Haisch, C.; Laufer, J. Quenching of nonlinear photoacoustic signal generation in gold nanoparticles through coating. *Nanoscale Adv.* **2020**, *2* (7), 2699-2704. DOI: <https://doi.org/10.1039/d0na00205d>
- (10) Schrof, S.; Pang, G. A.; Buchmann, J.; Laufer, J. Exploiting Nonlinear Photoacoustic Signal Generation in Gold Nanospheres for Selective Detection in Serial 3D PA Tomography. *J. Imaging* **2018**, *4* (12). DOI: <https://doi.org/10.3390/jimaging4120146>
- (11) Han, G.; Ghosh, P.; Rotello, V. M. Functionalized gold nanoparticles for drug delivery. *Nanomedicine* **2007**, *2* (1), 113-123. DOI: <https://doi.org/10.2217/17435889.2.1.113>
- (12) Dieterich, E.; Kinkelin, S. J.; Bron, M. Comparative Study of the Synthesis of sub-10 nm Carbon-Supported Gold Nanoparticles and their Suitability for Methanol Electrooxidation in Alkaline Media. *ChemNanoMat* **2022**, *8* (6). DOI: <https://doi.org/10.1002/cnma.202200098>
- (13) Dieterich, E.; Kinkelin, S. J.; Steimecke, M.; Bron, M. Quantifying the removal of stabilizing thiolates from gold nanoparticles on different carbon supports and the effect on their electrochemical properties. *Nanoscale Adv.* **2022**, *4* (23), 5154-5163. DOI: <https://doi.org/10.1039/d2na00561a>

- (14) Yang, Q.; Li, Y.; Zhao, X.; Zhang, J.; Cheng, X.; Zhu, N. Recent advances of superparamagnetic iron oxide nanoparticles and its applications in neuroscience under external magnetic field. *Applied Nanoscience* **2023**, *13* (8), 5489-5500. DOI: <https://doi.org/10.1007/s13204-023-02803-8>
- (15) Ho, D.; Sun, X.; Sun, S. Monodisperse magnetic nanoparticles for theranostic applications. *Acc. Chem. Res.* **2011**, *44* (10), 875-882. DOI: <https://doi.org/10.1021/ar200090c>
- (16) Mahdavi, M.; Ahmad, M. B.; Haron, M. J.; Namvar, F.; Nadi, B.; Rahman, M. Z.; Amin, J. Synthesis, surface modification and characterisation of biocompatible magnetic iron oxide nanoparticles for biomedical applications. *Molecules* **2013**, *18* (7), 7533-7548. DOI: <https://doi.org/10.3390/molecules18077533>
- (17) Manzano, M.; Vallet-Regí, M. Mesoporous Silica Nanoparticles for Drug Delivery. *Adv Funct Mater* **2019**, *30* (2). DOI: <https://doi.org/10.1002/adfm.201902634>
- (18) Croissant, J. G.; Butler, K. S.; Zink, J. I.; Brinker, C. J. Synthetic amorphous silica nanoparticles: toxicity, biomedical and environmental implications. *Nat Rev Mater* **2020**, *5* (12), 886-909. DOI: <https://doi.org/10.1038/s41578-020-0230-0>
- (19) Li, H.; Chen, X.; Shen, D.; Wu, F.; Pleixats, R.; Pan, J. Functionalized silica nanoparticles: classification, synthetic approaches and recent advances in adsorption applications. *Nanoscale* **2021**, *13* (38), 15998-16016. DOI: <https://doi.org/10.1039/d1nr04048k>
- (20) Ekimov, A. I.; Onushcheko, A. Quantum size effect in three-dimensional microscopic semiconductor crystals. *JETP Lett.* **1981**, *34* (6), 345-349.
- (21) Rossetti, R.; Brus, L. Electron-hole recombination emission as a probe of surface chemistry in aqueous cadmium sulfide colloids. *J Phys Chem-Us* **1982**, *86* (23), 4470-4472. DOI: <https://doi.org/10.1021/j100220a003>
- (22) Murray, C. B.; Norris, D. J.; Bawendi, M. G. Synthesis and Characterization of Nearly Monodisperse CdE (E = S, Se, Te) Semiconductor Nanocrystallites. *J. Am. Chem. Soc.* **1993**, *115*, 8706-8715. DOI: <https://doi.org/10.1021/ja00072a025>
- (23) Geim, A. K.; Novoselov, K. S. The rise of graphene. *Nat. Mater.* **2007**, *6* (3), 183-191. DOI: <https://doi.org/10.1038/nmat1849>
- (24) Mermin, N. D. Crystalline Order in Two Dimensions. *Physical Review* **1968**, *176* (1), 250-254. DOI: <https://doi.org/10.1103/PhysRev.176.250>
- (25) Novoselov, K. S.; Geim, A. K.; Morozov, S. V.; Jiang, D.; Zhang, Y.; Dubonos, S. V.; Grigorieva, I. V.; Firsov, A. A. Electric field effect in atomically thin carbon films. *Science* **2004**, *306* (5696), 666-669. DOI: <https://doi.org/10.1126/science.1102896>
- (26) Meyer, J. C.; Geim, A. K.; Katsnelson, M. I.; Novoselov, K. S.; Booth, T. J.; Roth, S. The structure of suspended graphene sheets. *Nature* **2007**, *446* (7131), 60-63. DOI: <https://doi.org/10.1038/nature05545>
- (27) Balandin, A. A.; Ghosh, S.; Bao, W.; Calizo, I.; Teweldebrhan, D.; Miao, F.; Lau, C. N. Superior thermal conductivity of single-layer graphene. *Nano Lett.* **2008**, *8* (3), 902-907. DOI: <https://doi.org/10.1021/nl0731872>

- (28) Tans, S. J.; Devoret, M. H.; Dai, H. J.; Thess, A.; Smalley, R. E.; Geerligs, L. J.; Dekker, C. Individual single-wall carbon nanotubes as quantum wires. *Nature* **1997**, *386* (6624), 474-477. DOI: <https://doi.org/10.1038/386474a0>
- (29) Berber, S.; Kwon, Y. K.; Tomanek, D. Unusually high thermal conductivity of carbon nanotubes. *Phys. Rev. Lett.* **2000**, *84* (20), 4613-4616. DOI: <https://doi.org/10.1103/PhysRevLett.84.4613>
- (30) Yu, M. F.; Lourie, O.; Dyer, M. J.; Moloni, K.; Kelly, T. F.; Ruoff, R. S. Strength and breaking mechanism of multiwalled carbon nanotubes under tensile load. *Science* **2000**, *287* (5453), 637-640. DOI: <https://doi.org/10.1126/science.287.5453.637>
- (31) Iijima, S. Helical Microtubules of Graphitic Carbon. *Nature* **1991**, *354* (6348), 56-58. DOI: <https://doi.org/10.1038/354056a0>
- (32) Kroto, H. W.; Heath, J. R.; O'Brien, S. C.; Curl, R. F.; Smalley, R. E. C<sub>60</sub>: Buckminsterfullerene. *Nature* **1985**, *318*, 162-163. DOI: <https://doi.org/10.1038/318162a0>
- (33) Buseck, P. R.; Tsipursky, S. J.; Hettich, R. Fullerenes from the geological environment. *Science* **1992**, *257* (5067), 215-217. DOI: <https://doi.org/10.1126/science.257.5067.215>
- (34) Lalwani, G.; Sitharaman, B. Multifunctional Fullerene- and Metallofullerene-Based Nanobiomaterials. *Nano LIFE* **2013**, *03* (03). DOI: <https://doi.org/10.1142/s1793984413420038>
- (35) Oliver, R. C.; Lipfert, J.; Fox, D. A.; Lo, R. H.; Doniach, S.; Columbus, L. Dependence of micelle size and shape on detergent alkyl chain length and head group. *PLoS One* **2013**, *8* (5), e62488. DOI: <https://doi.org/10.1371/journal.pone.0062488>
- (36) Rideau, E.; Dimova, R.; Schwille, P.; Wurm, F. R.; Landfester, K. Liposomes and polymersomes: a comparative review towards cell mimicking. *Chem. Soc. Rev.* **2018**, *47* (23), 8572-8610. DOI: <https://doi.org/10.1039/c8cs00162f>
- (37) Andrade, S.; Ramalho, M. J.; Loureiro, J. A.; Pereira, M. C. Liposomes as biomembrane models: Biophysical techniques for drug-membrane interaction studies. *Journal of Molecular Liquids* **2021**, *334*. DOI: <https://doi.org/10.1016/j.molliq.2021.116141>
- (38) Sen, N.; Haupt, C.; Hause, G.; Bacia, K.; Binder, W. H. Inhibition of the Fibrillation of Amyloid Abeta(1-40) by Hybrid-Lipid-Polymer Vesicles. *Macromol. Biosci.* **2023**, *23* (5), e2200522. DOI: <https://doi.org/10.1002/mabi.202200522>
- (39) Grimmer, M.; Bacia, K. Giant Endoplasmic Reticulum vesicles (GERVs), a novel model membrane tool. *Sci. Rep.* **2020**, *10* (1), 3100. DOI: <https://doi.org/10.1038/s41598-020-59700-1>
- (40) Auerswald, J.; Ebenhan, J.; Schwieger, C.; Scrima, A.; Meister, A.; Bacia, K. Measuring protein insertion areas in lipid monolayers by fluorescence correlation spectroscopy. *Biophys. J.* **2021**, *120* (8), 1333-1342. DOI: <https://doi.org/10.1016/j.bpj.2021.02.011>
- (41) Hoffmann, M.; Eisermann, J.; Schoffmann, F. A.; Das, M.; Vargas, C.; Keller, S.; Hinderberger, D. Influence of different polymer belts on lipid properties in nanodiscs characterized by CW EPR spectroscopy. *BBA - Biomembranes* **2021**, *1863* (10), 183681. DOI: <https://doi.org/10.1016/j.bbamem.2021.183681>

- (42) Hoffmann, M.; Haselberger, D.; Hofmann, T.; Muller, L.; Janson, K.; Meister, A.; Das, M.; Vargas, C.; Keller, S.; Kastritis, P. L.; Schmidt, C.; Hinderberger, D. Nanoscale Model System for the Human Myelin Sheath. *Biomacromolecules* **2021**, *22* (9), 3901-3912. DOI: <https://doi.org/10.1021/acs.biomac.1c00714>
- (43) Verma, M. L.; Dhanya, B. S.; Sukriti; Rani, V.; Thakur, M.; Jeslin, J.; Kushwaha, R. Carbohydrate and protein based biopolymeric nanoparticles: Current status and biotechnological applications. *Int. J. Biol. Macromol.* **2020**, *154*, 390-412. DOI: <https://doi.org/10.1016/j.ijbiomac.2020.03.105>
- (44) Sripriyalakshmi, S.; Jose, P.; Ravindran, A.; Anjali, C. H. Recent trends in drug delivery system using protein nanoparticles. *Cell. Biochem. Biophys.* **2014**, *70* (1), 17-26. DOI: <https://doi.org/10.1007/s12013-014-9896-5>
- (45) Tarhini, M.; Greige-Gerges, H.; Elaissari, A. Protein-based nanoparticles: From preparation to encapsulation of active molecules. *Int. J. Pharm.* **2017**, *522* (1-2), 172-197. DOI: <https://doi.org/10.1016/j.ijpharm.2017.01.067>
- (46) Ruzette, A. V.; Leibler, L. Block copolymers in tomorrow's plastics. *Nat. Mater.* **2005**, *4* (1), 19-31. DOI: <https://doi.org/10.1038/nmat1295>
- (47) Mai, Y.; Eisenberg, A. Self-assembly of block copolymers. *Chem. Soc. Rev.* **2012**, *41* (18), 5969-5985. DOI: <https://doi.org/10.1039/c2cs35115c>
- (48) Kabanov, A. V.; Batrakova, E. V.; Alakhov, V. Y. Pluronic® block copolymers as novel polymer therapeutics for drug and gene delivery. *J. Control. Release* **2002**, *82* (2-3), 189-212. DOI: [https://doi.org/10.1016/S0168-3659\(02\)00009-3](https://doi.org/10.1016/S0168-3659(02)00009-3)
- (49) Harada, A.; Kataoka, K. Supramolecular assemblies of block copolymers in aqueous media as nanocontainers relevant to biological applications. *Prog Polym Sci* **2006**, *31* (11), 949-982. DOI: <https://doi.org/10.1016/j.progpolymsci.2006.09.004>
- (50) Maysinger, D.; Lovric, J.; Eisenberg, A.; Savic, R. Fate of micelles and quantum dots in cells. *Eur. J. Pharm. Biopharm.* **2007**, *65* (3), 270-281. DOI: <https://doi.org/10.1016/j.ejpb.2006.08.011>
- (51) Henselwood, F.; Liu, G. J. Water-soluble nanospheres of poly(2-cinnamoyl ethyl methacrylate)-block-poly(acrylic acid). *Macromolecules* **1997**, *30* (3), 488-493. DOI: <https://doi.org/10.1021/ma961401v>
- (52) Thurmond, K. B.; Kowalewski, T.; Wooley, K. L. Water-soluble knedel-like structures: The preparation of shell-cross-linked small particles. *J. Am. Chem. Soc.* **1996**, *118* (30), 7239-7240. DOI: <https://doi.org/10.1021/ja961299h>
- (53) Bermudez, H.; Brannan, A. K.; Hammer, D. A.; Bates, F. S.; Discher, D. E. Molecular weight dependence of polymersome membrane structure, elasticity, and stability. *Macromolecules* **2002**, *35* (21), 8203-8208. DOI: <https://doi.org/10.1021/ma020669I>
- (54) Discher, D. E.; Eisenberg, A. Polymer vesicles. *Science* **2002**, *297* (5583), 967-973. DOI: <https://doi.org/10.1126/science.1074972>
- (55) Discher, B. M.; Won, Y. Y.; Ege, D. S.; Lee, J. C. M.; Bates, F. S.; Discher, D. E.; Hammer, D. A. Polymersomes: Tough vesicles made from diblock copolymers. *Science* **1999**, *284* (5417), 1143-1146. DOI: <https://doi.org/10.1126/science.284.5417.1143>

- (56) Tanner, P.; Baumann, P.; Enea, R.; Onaca, O.; Palivan, C.; Meier, W. Polymeric vesicles: from drug carriers to nanoreactors and artificial organelles. *Acc. Chem. Res.* **2011**, *44* (10), 1039-1049. DOI: <https://doi.org/10.1021/ar200036k>
- (57) Mai, Y.; Eisenberg, A. Controlled Incorporation of Particles into the Central Portion of Vesicle Walls. *J. Am. Chem. Soc.* **2010**, *132* (29), 10078-10084. DOI: <https://doi.org/10.1021/ja1024063>
- (58) Menger, F. M.; Angelova, M. I. Giant vesicles: Imitating the cytological processes of cell membranes. *Acc. Chem. Res.* **1998**, *31* (12), 789-797. DOI: <https://doi.org/10.1021/ar970103v>
- (59) Penfold, N. J. W.; Yeow, J.; Boyer, C.; Armes, S. P. Emerging Trends in Polymerization-Induced Self-Assembly. *ACS Macro Lett.* **2019**, *8* (8), 1029-1054. DOI: <https://doi.org/10.1021/acsmacrolett.9b00464>
- (60) Qiu, L.; Han, X.; Xing, C.; Glebe, U. Polymerization-Induced Self-Assembly: An Emerging Tool for Generating Polymer-Based Biohybrid Nanostructures. *Small* **2023**, *19* (18), e2207457. DOI: <https://doi.org/10.1002/smll.202207457>
- (61) Zhao, Z. Z.; Lei, S. J.; Zeng, M.; Huo, M. Recent progress in polymerization-induced self-assembly: From the perspective of driving forces. *Aggregate* **2023**. DOI: <https://doi.org/10.1002/agt2.418>
- (62) Buhleier, E.; Wehner, W.; Vögtle, F. Cascade-Chain-Like and Nonskid-Chain-Like Syntheses of Molecular Cavity Topologies. *Synthesis* **1978**, *2*, 155-158. DOI: <https://doi.org/10.1055/s-1978-24702>
- (63) Wang, J.; Li, B.; Qiu, L.; Qiao, X.; Yang, H. Dendrimer-based drug delivery systems: history, challenges, and latest developments. *J. Biol. Eng.* **2022**, *16* (1), 18. DOI: <https://doi.org/10.1186/s13036-022-00298-5>
- (64) Nikzamir, M.; Hanifehpour, Y.; Akbarzadeh, A.; Panahi, Y. Applications of Dendrimers in Nanomedicine and Drug Delivery: A Review. *J. Inorg. Organomet. Polym.* **2021**, *31* (6), 2246-2261. DOI: <https://doi.org/10.1007/s10904-021-01925-2>
- (65) Ambekar, R. S.; Choudhary, M.; Kandasubramanian, B. Recent advances in dendrimer-based nanopatform for cancer treatment: A review. *European Polymer Journal* **2020**, *126*. DOI: <https://doi.org/10.1016/j.eurpolymj.2020.109546>
- (66) Grayson, S. M.; Fréchet, J. M. J. Convergent dendrons and dendrimers:: from synthesis to applications. *Chem. Rev.* **2001**, *101* (12), 3819-3867. DOI: <https://doi.org/10.1021/cr990116h>
- (67) Tomalia, D. A.; Fréchet, J. M. J. Discovery of dendrimers and dendritic polymers:: A brief historical perspective. *J Polym Sci Pol Chem* **2002**, *40* (16), 2719-2728. DOI: <https://doi.org/10.1002/pola.10301>
- (68) Kawaguchi, T.; Walker, K. L.; Wilkins, C. L.; Moore, J. S. Double Exponential Dendrimer Growth. *J. Am. Chem. Soc.* **1995**, *117* (8), 2159-2165. DOI: <https://doi.org/10.1021/ja00113a005>
- (69) Scott, R. W.; Wilson, O. M.; Crooks, R. M. Synthesis, characterization, and applications of dendrimer-encapsulated nanoparticles. *J. Phys. Chem. B* **2005**, *109* (2), 692-704. DOI: <https://doi.org/10.1021/jp0469665>

- (70) Yamamoto, K.; Imaoka, T.; Tanabe, M.; Kambe, T. New Horizon of Nanoparticle and Cluster Catalysis with Dendrimers. *Chem. Rev.* **2020**, *120* (2), 1397-1437. DOI: <https://doi.org/10.1021/acs.chemrev.9b00188>
- (71) Menjoge, A. R.; Kannan, R. M.; Tomalia, D. A. Dendrimer-based drug and imaging conjugates: design considerations for nanomedical applications. *Drug Discov. Today* **2010**, *15* (5-6), 171-185. DOI: <https://doi.org/10.1016/j.drudis.2010.01.009>
- (72) Kurtoglu, Y. E.; Mishra, M. K.; Kannan, S.; Kannan, R. M. Drug release characteristics of PAMAM dendrimer-drug conjugates with different linkers. *Int. J. Pharm.* **2010**, *384* (1-2), 189-194. DOI: <https://doi.org/10.1016/j.ijpharm.2009.10.017>
- (73) Wang, G.; Zhou, Z.; Zhao, Z.; Li, Q.; Wu, Y.; Yan, S.; Shen, Y.; Huang, P. Enzyme-Triggered Transcytosis of Dendrimer-Drug Conjugate for Deep Penetration into Pancreatic Tumors. *ACS Nano* **2020**, *14* (4), 4890-4904. DOI: <https://doi.org/10.1021/acsnano.0c00974>
- (74) Liu, J.; Gray, W. D.; Davis, M. E.; Luo, Y. Peptide- and saccharide-conjugated dendrimers for targeted drug delivery: a concise review. *Interface Focus* **2012**, *2* (3), 307-324. DOI: <https://doi.org/10.1098/rsfs.2012.0009>
- (75) Yang, H.; Morris, J. J.; Lopina, S. T. Polyethylene glycol-polyamidoamine dendritic micelle as solubility enhancer and the effect of the length of polyethylene glycol arms on the solubility of pyrene in water. *J. Colloid Interface Sci.* **2004**, *273* (1), 148-154. DOI: <https://doi.org/10.1016/j.jcis.2003.12.023>
- (76) Li, Y.; Maciel, D.; Rodrigues, J.; Shi, X.; Tomas, H. Biodegradable Polymer Nanogels for Drug/Nucleic Acid Delivery. *Chem. Rev.* **2015**, *115* (16), 8564-8608. DOI: <https://doi.org/10.1021/cr500131f>
- (77) Kabanov, A. V.; Vinogradov, S. V. Nanogels as pharmaceutical carriers: finite networks of infinite capabilities. *Angew. Chem. Int. Ed.* **2009**, *48* (30), 5418-5429. DOI: <https://doi.org/10.1002/anie.200900441>
- (78) Neamtu, I.; Rusu, A. G.; Diaconu, A.; Nita, L. E.; Chiriac, A. P. Basic concepts and recent advances in nanogels as carriers for medical applications. *Drug Deliv.* **2017**, *24* (1), 539-557. DOI: <https://doi.org/10.1080/10717544.2016.1276232>
- (79) Li, C.; Obireddy, S. R.; Lai, W. F. Preparation and use of nanogels as carriers of drugs. *Drug Deliv.* **2021**, *28* (1), 1594-1602. DOI: <https://doi.org/10.1080/10717544.2021.1955042>
- (80) Oh, J. K.; Drumright, R.; Siegwart, D. J.; Matyjaszewski, K. The development of microgels/nanogels for drug delivery applications. *Prog Polym Sci* **2008**, *33* (4), 448-477. DOI: <https://doi.org/10.1016/j.progpolymsci.2008.01.002>
- (81) Sharma, A.; Garg, T.; Aman, A.; Panchal, K.; Sharma, R.; Kumar, S.; Markandeywar, T. Nanogel--an advanced drug delivery tool: Current and future. *Artif. Cells Nanomed. Biotechnol.* **2016**, *44* (1), 165-177. DOI: <https://doi.org/10.3109/21691401.2014.930745>
- (82) Euliss, L. E.; DuPont, J. A.; Gratton, S.; DeSimone, J. Imparting size, shape, and composition control of materials for nanomedicine. *Chem. Soc. Rev.* **2006**, *35* (11), 1095-1104. DOI: <https://doi.org/10.1039/b600913c>

- (83) Geng, Y.; Dalhaimer, P.; Cai, S.; Tsai, R.; Tewari, M.; Minko, T.; Discher, D. E. Shape effects of filaments versus spherical particles in flow and drug delivery. *Nat. Nanotechnol.* **2007**, *2* (4), 249-255. DOI: <https://doi.org/10.1038/nnano.2007.70>
- (84) Petros, R. A.; DeSimone, J. M. Strategies in the design of nanoparticles for therapeutic applications. *Nat. Rev. Drug Discov.* **2010**, *9* (8), 615-627. DOI: <https://doi.org/10.1038/nrd2591>
- (85) Mitchell, M. J.; Billingsley, M. M.; Haley, R. M.; Wechsler, M. E.; Peppas, N. A.; Langer, R. Engineering precision nanoparticles for drug delivery. *Nat. Rev. Drug Discov.* **2021**, *20* (2), 101-124. DOI: <https://doi.org/10.1038/s41573-020-0090-8>
- (86) Stark, W. J. Nanoparticles in biological systems. *Angew. Chem. Int. Ed.* **2011**, *50* (6), 1242-1258. DOI: <https://doi.org/10.1002/anie.200906684>
- (87) Butcher, N. J.; Mortimer, G. M.; Minchin, R. F. Drug delivery: Unravelling the stealth effect. *Nat. Nanotechnol.* **2016**, *11* (4), 310-311. DOI: <https://doi.org/10.1038/nnano.2016.6>
- (88) Rubio-Cervilla, J.; Gonzalez, E.; Pomposo, J. A. Advances in Single-Chain Nanoparticles for Catalysis Applications. *Nanomaterials* **2017**, *7* (10), 341-360. DOI: <https://doi.org/10.3390/nano7100341>
- (89) Kröger, A. P. P.; Paulusse, J. M. J. Single-chain polymer nanoparticles in controlled drug delivery and targeted imaging. *J. Control. Release* **2018**, *286*, 326-347. DOI: <https://doi.org/10.1016/j.jconrel.2018.07.041>
- (90) Lyon, C. K.; Prasher, A.; Hanlon, A. M.; Tuten, B. T.; Tooley, C. A.; Frank, P. G.; Berda, E. B. A brief user's guide to single-chain nanoparticles. *Polym. Chem.* **2015**, *6* (2), 181-197. DOI: <https://doi.org/10.1039/c4py01217h>
- (91) Mavila, S.; Eivgi, O.; Berkovich, I.; Lemcoff, N. G. Intramolecular Cross-Linking Methodologies for the Synthesis of Polymer Nanoparticles. *Chem. Rev.* **2016**, *116* (3), 878-961. DOI: <https://doi.org/10.1021/acs.chemrev.5b00290>
- (92) Pomposo, J. A.; Perez-Baena, I.; Lo Verso, F.; Moreno, A. J.; Arbe, A.; Colmenero, J. How Far Are Single-Chain Polymer Nanoparticles in Solution from the Globular State? *ACS Macro Lett.* **2014**, *3* (8), 767-772. DOI: <https://doi.org/10.1021/mz500354q>
- (93) Lo Verso, F.; Pomposo, J. A.; Colmenero, J.; Moreno, A. J. Simulation guided design of globular single-chain nanoparticles by tuning the solvent quality. *Soft Matter* **2015**, *11* (7), 1369-1375. DOI: <https://doi.org/10.1039/c4sm02475c>
- (94) Sanchez-Sanchez, A.; Arbe, A.; Kohlbrecher, J.; Colmenero, J.; Pomposo, J. A. Efficient Synthesis of Single-Chain Globules Mimicking the Morphology and Polymerase Activity of Metalloenzymes. *Macromol. Rapid Commun.* **2015**, *36* (17), 1592-1597. DOI: <https://doi.org/10.1002/marc.201500252>
- (95) ter Huurne, G. M.; Gillissen, M. A. J.; Palmans, A. R. A.; Voets, I. K.; Meijer, E. W. The Coil-to-Globule Transition of Single-Chain Polymeric Nanoparticles with a Chiral Internal Secondary Structure. *Macromolecules* **2015**, *48* (12), 3949-3956. DOI: <https://doi.org/10.1021/acs.macromol.5b00604>

- (96) Roos, A. H.; Hoffmann, J. F.; Binder, W. H.; Hinderberger, D. Nanoscale structure and dynamics of thermoresponsive single-chain nanoparticles investigated by EPR spectroscopy. *Soft Matter* **2021**, *17* (29), 7032-7037. DOI: <https://doi.org/10.1039/d1sm00582k>
- (97) Watanabe, K.; Katsuhara, S.; Mamiya, H.; Yamamoto, T.; Tajima, K.; Isono, T.; Satoh, T. Downsizing feature of microphase-separated structures via intramolecular crosslinking of block copolymers. *Chem. Sci.* **2019**, *10* (11), 3330-3339. DOI: <https://doi.org/10.1039/c8sc05016c>
- (98) Zhou, F.; Xie, M.; Chen, D. Structure and Ultrasonic Sensitivity of the Superparticles Formed by Self-Assembly of Single Chain Janus Nanoparticles. *Macromolecules* **2013**, *47* (1), 365-372. DOI: <https://doi.org/10.1021/ma401589z>
- (99) Xu, F.; Fang, Z.; Yang, D.; Gao, Y.; Li, H.; Chen, D. Water in oil emulsion stabilized by tadpole-like single chain polymer nanoparticles and its application in biphasic reaction. *ACS Appl. Mater. Interfaces* **2014**, *6* (9), 6717-6723. DOI: <https://doi.org/10.1021/am500427e>
- (100) Wen, J.; Yuan, L.; Yang, Y.; Liu, L.; Zhao, H. Self-Assembly of Monotethered Single-Chain Nanoparticle Shape Amphiphiles. *ACS Macro Lett.* **2013**, *2* (2), 100-106. DOI: <https://doi.org/10.1021/mz300636x>
- (101) Ji, X.; Zhang, Y.; Zhao, H. Amphiphilic Janus Twin Single-Chain Nanoparticles. *Chemistry* **2018**, *24* (12), 3005-3012. DOI: <https://doi.org/10.1002/chem.201705487>
- (102) Nam, J.; Kwon, S.; Yu, Y. G.; Seo, H. B.; Lee, J. S.; Lee, W. B.; Kim, Y.; Seo, M. Folding of Sequence-Controlled Graft Copolymers to Subdomain-Defined Single-Chain Nanoparticles. *Macromolecules* **2021**, *54* (18), 8829-8838. DOI: <https://doi.org/10.1021/acs.macromol.1c01674>
- (103) Watanabe, K.; Kaizawa, N.; Ree, B. J.; Yamamoto, T.; Tajima, K.; Isono, T.; Satoh, T. One-Shot Intra-block Cross-Linking of Linear Diblock Copolymer to Realize Janus-Shaped Single-Chain Nanoparticles. *Angew. Chem. Int. Ed.* **2021**, *60* (33), 18122-18128. DOI: <https://doi.org/10.1002/anie.202103969>
- (104) Cui, Z.; Huang, L.; Ding, Y.; Zhu, X.; Lu, X.; Cai, Y. Compartmentalization and Unidirectional Cross-Domain Molecule Shuttling of Organometallic Single-Chain Nanoparticles. *ACS Macro Lett.* **2018**, *7* (5), 572-575. DOI: <https://doi.org/10.1021/acsmacrolett.8b00199>
- (105) Cui, Z. G.; Cao, H.; Ding, Y.; Gao, P.; Lu, X. H.; Cai, Y. L. Compartmentalization of an ABC triblock copolymer single-chain nanoparticle coordination-driven orthogonal self-assembly. *Polym. Chem.* **2017**, *8* (24), 3755-3763. DOI: <https://doi.org/10.1039/c7py00582b>
- (106) Roy, R. K.; Lutz, J. F. Compartmentalization of single polymer chains by stepwise intramolecular cross-linking of sequence-controlled macromolecules. *J. Am. Chem. Soc.* **2014**, *136* (37), 12888-12891. DOI: <https://doi.org/10.1021/ja507889x>
- (107) Schmidt, B. V.; Fechner, N.; Falkenhagen, J.; Lutz, J. F. Controlled folding of synthetic polymer chains through the formation of positionable covalent bridges. *Nat. Chem.* **2011**, *3* (3), 234-238. DOI: <https://doi.org/10.1038/nchem.964>

- (108) Bilgi, M.; Balta, D. K.; Temel, B. A.; Temel, G. Single-Chain Folding Nanoparticles as Carbon Nanotube Catchers. *J Polym Sci Pol Chem* **2018**, *56* (24), 2709-2714. DOI: <https://doi.org/10.1002/pola.29245>
- (109) Berda, E. B.; Foster, E. J.; Meijer, E. W. Toward Controlling Folding in Synthetic Polymers: Fabricating and Characterizing Supramolecular Single-Chain Nanoparticles. *Macromolecules* **2010**, *43* (3), 1430-1437. DOI: <https://doi.org/10.1021/ma902393h>
- (110) Hosono, N.; Kushner, A. M.; Chung, J.; Palmans, A. R.; Guan, Z.; Meijer, E. W. Forced unfolding of single-chain polymeric nanoparticles. *J. Am. Chem. Soc.* **2015**, *137* (21), 6880-6888. DOI: <https://doi.org/10.1021/jacs.5b02967>
- (111) Hosono, N.; Gillissen, M. A.; Li, Y.; Sheiko, S. S.; Palmans, A. R.; Meijer, E. W. Orthogonal self-assembly in folding block copolymers. *J. Am. Chem. Soc.* **2013**, *135* (1), 501-510. DOI: <https://doi.org/10.1021/ja310422w>
- (112) Dirlam, P. T.; Kim, H. J.; Arrington, K. J.; Chung, W. J.; Sahoo, R.; Hill, L. J.; Costanzo, P. J.; Theato, P.; Char, K.; Pyun, J. Single chain polymer nanoparticles via sequential ATRP and oxidative polymerization. *Polym. Chem.* **2013**, *4* (13), 3765-3773. DOI: <https://doi.org/10.1039/c3py00321c>
- (113) Appel, E. A.; Dyson, J.; del Barrio, J.; Walsh, Z.; Scherman, O. A. Formation of single-chain polymer nanoparticles in water through host-guest interactions. *Angew. Chem. Int. Ed.* **2012**, *51* (17), 4185-4189. DOI: <https://doi.org/10.1002/anie.201108659>
- (114) Harth, E.; Van Horn, B.; Lee, V. Y.; Germack, D. S.; Gonzales, C. P.; Miller, R. D.; Hawker, C. J. A facile approach to architecturally defined nanoparticles via intramolecular chain collapse. *J. Am. Chem. Soc.* **2002**, *124* (29), 8653-8660. DOI: <https://doi.org/10.1021/ja026208x>
- (115) Willenbacher, J.; Wuest, K. N. R.; Mueller, J. O.; Kaupp, M.; Wagenknecht, H. A.; Barner-Kowollik, C. Photochemical Design of Functional Fluorescent Single-Chain Nanoparticles. *ACS Macro Lett.* **2014**, *3* (6), 574-579. DOI: <https://doi.org/10.1021/mz500292e>
- (116) Gillhuber, S.; Holloway, J. O.; Frisch, H.; Feist, F.; Weigend, F.; Barner-Kowollik, C.; Roesky, P. W. Ferrocene-driven single-chain polymer compaction. *Chem. Commun.* **2023**, *59* (31), 4672-4675. DOI: <https://doi.org/10.1039/d3cc00736g>
- (117) Murray, B. S.; Fulton, D. A. Dynamic Covalent Single-Chain Polymer Nanoparticles. *Macromolecules* **2011**, *44* (18), 7242-7252. DOI: <https://doi.org/10.1021/ma201331f>
- (118) Claus, T. K.; Zhang, J.; Martin, L.; Hartlieb, M.; Mutlu, H.; Perrier, S.; Delaittre, G.; Barner-Kowollik, C. Stepwise Light-Induced Dual Compaction of Single-Chain Nanoparticles. *Macromol. Rapid Commun.* **2017**, *38* (16). DOI: <https://doi.org/10.1002/marc.201700264>
- (119) Wijker, S.; Monnik, R.; Rijnders, L.; Deng, L.; Palmans, A. R. A. Simultaneously controlling conformational and operational stability of single-chain polymeric nanoparticles in complex media. *Chem. Commun.* **2023**, *59* (36), 5407-5410. DOI: <https://doi.org/10.1039/d3cc00763d>
- (120) Terashima, T.; Sugita, T.; Fukae, K.; Sawamoto, M. Synthesis and Single-Chain Folding of Amphiphilic Random Copolymers in Water. *Macromolecules* **2014**, *47* (2), 589-600. DOI: <https://doi.org/10.1021/ma402355v>

- (121) Shao, Y.; Wang, Y. L.; Tang, Z.; Wen, Z.; Chang, C.; Wang, C.; Sun, D.; Ye, Y.; Qiu, D.; Ke, Y.; Liu, F.; Yang, Z. Scalable Synthesis of Photoluminescent Single-Chain Nanoparticles by Electrostatic-Mediated Intramolecular Crosslinking. *Angew. Chem. Int. Ed.* **2022**, *61* (27), e202205183. DOI: <https://doi.org/10.1002/anie.202205183>
- (122) Watanabe, K.; Tanaka, R.; Takada, K.; Kim, M. J.; Lee, J. S.; Tajima, K.; Isono, T.; Satoh, T. Intramolecular olefin metathesis as a robust tool to synthesize single-chain nanoparticles in a size-controlled manner. *Polym. Chem.* **2016**, *7* (29), 4782-4792. DOI: <https://doi.org/10.1039/c6py00795c>
- (123) Lu, Z.; Zhang, J.; Yin, W.; Guo, C.; Lang, M. Preparation of AIE Functional Single-Chain Polymer Nanoparticles and Their Application in H<sub>2</sub> O<sub>2</sub> Detection through Intermolecular Heavy-Atom Effect. *Macromol. Rapid Commun.* **2022**, *43* (17), e2200156. DOI: <https://doi.org/10.1002/marc.202200156>
- (124) Rubio-Cervilla, J.; Barroso-Bujans, F.; Pomposo, J. A. Merging of Zwitterionic ROP and Photoactivated Thiol–Yne Coupling for the Synthesis of Polyether Single-Chain Nanoparticles. *Macromolecules* **2015**, *49* (1), 90-97. DOI: <https://doi.org/10.1021/acs.macromol.5b02369>
- (125) Arbe, A.; Rubio-Cervilla, J.; Alegría, A.; Moreno, A. J.; Pomposo, J. A.; Robles-Hernández, B.; de Molina, P. M.; Fouquet, P.; Juranyi, F.; Colmenero, J. Mesoscale Dynamics in Melts of Single-Chain Polymeric Nanoparticles. *Macromolecules* **2019**, *52* (18), 6935-6942. DOI: <https://doi.org/10.1021/acs.macromol.9b01264>
- (126) Rubio-Cervilla, J.; Malo de Molina, P.; Robles-Hernandez, B.; Arbe, A.; Moreno, A. J.; Alegria, A.; Colmenero, J.; Pomposo, J. A. Facile Access to Completely Deuterated Single-Chain Nanoparticles Enabled by Intramolecular Azide Photodecomposition. *Macromol. Rapid Commun.* **2019**, *40* (9), e1900046. DOI: <https://doi.org/10.1002/marc.201900046>
- (127) Foster, E. J.; Berda, E. B.; Meijer, E. W. Tuning the Size of Supramolecular Single-Chain Polymer Nanoparticles. *J Polym Sci Pol Chem* **2011**, *49* (1), 118-126. DOI: <https://doi.org/10.1002/pola.24426>
- (128) Gillissen, M. A. J.; Voets, I. K.; Meijer, E. W.; Palmans, A. R. A. Single chain polymeric nanoparticles as compartmentalised sensors for metal ions. *Polym. Chem.* **2012**, *3* (11), 3166-3174. DOI: <https://doi.org/10.1039/c2py20350b>
- (129) Tuten, B. T.; Chao, D. M.; Lyon, C. K.; Berda, E. B. Single-chain polymer nanoparticles reversible disulfide bridges. *Polym. Chem.* **2012**, *3* (11), 3068-3071. DOI: <https://doi.org/10.1039/c2py20308a>
- (130) Chen, J.; Wang, J.; Bai, Y.; Li, K.; Garcia, E. S.; Ferguson, A. L.; Zimmerman, S. C. Enzyme-like Click Catalysis by a Copper-Containing Single-Chain Nanoparticle. *J. Am. Chem. Soc.* **2018**, *140* (42), 13695-13702. DOI: <https://doi.org/10.1021/jacs.8b06875>
- (131) Bai, Y.; Feng, X.; Xing, H.; Xu, Y.; Kim, B. K.; Baig, N.; Zhou, T.; Gewirth, A. A.; Lu, Y.; Oldfield, E.; Zimmerman, S. C. A Highly Efficient Single-Chain Metal-Organic Nanoparticle Catalyst for Alkyne-Azide "Click" Reactions in Water and in Cells. *J. Am. Chem. Soc.* **2016**, *138* (35), 11077-11080. DOI: <https://doi.org/10.1021/jacs.6b04477>
- (132) Liu, C. H.; Dugas, L. D.; Bowman, J. I.; Chidanguro, T.; Storey, R. F.; Simon, Y. C. Forcing single-chain nanoparticle collapse through hydrophobic solvent interactions in comb copolymers. *Polym. Chem.* **2020**, *11* (2), 292-297. DOI: <https://doi.org/10.1039/c9py01235d>

- (133) Liu, J.; Feng, G.; Liu, R.; Tomczak, N.; Ma, L.; Gurzadyan, G. G.; Liu, B. Bright quantum-dot-sized single-chain conjugated polyelectrolyte nanoparticles: synthesis, characterization and application for specific extracellular labeling and imaging. *Small* **2014**, *10* (15), 3110-3118. DOI: <https://doi.org/10.1002/sml.201303505>
- (134) Berkovich, I.; Mavila, S.; Iliashevsky, O.; Kozuch, S.; Lemcoff, N. G. Single-chain polybutadiene organometallic nanoparticles: an experimental and theoretical study. *Chem. Sci.* **2016**, *7* (3), 1773-1778. DOI: <https://doi.org/10.1039/c5sc04535e>
- (135) Blazquez-Martin, A.; Verde-Sesto, E.; Arbe, A.; Pomposo, J. A. Metamorphosis of a Commodity Plastic like PVC to Efficient Catalytic Single-Chain Nanoparticles. *Angew. Chem. Int. Ed.* **2023**, e202313502. DOI: <https://doi.org/10.1002/anie.202313502>
- (136) Gracia, R.; Marradi, M.; Cossio, U.; Benito, A.; Perez-San Vicente, A.; Gomez-Vallejo, V.; Grande, H. J.; Llop, J.; Loinaz, I. Synthesis and functionalization of dextran-based single-chain nanoparticles in aqueous media. *J. Mater. Chem. B* **2017**, *5* (6), 1143-1147. DOI: <https://doi.org/10.1039/c6tb02773c>
- (137) Gracia, R.; Marradi, M.; Salerno, G.; Perez-Nicado, R.; Perez-San Vicente, A.; Dupin, D.; Rodriguez, J.; Loinaz, I.; Chiodo, F.; Nativi, C. Biocompatible single-chain polymer nanoparticles loaded with an antigen mimetic as potential anticancer vaccine. *ACS Macro Lett.* **2018**, *7* (2), 196-200. DOI: <https://doi.org/10.1021/acsmacrolett.8b00052>
- (138) Blanco-Cabra, N.; Movellan, J.; Marradi, M.; Gracia, R.; Salvador, C.; Dupin, D.; Loinaz, I.; Torrents, E. Neutralization of ionic interactions by dextran-based single-chain nanoparticles improves tobramycin diffusion into a mature biofilm. *NPJ Biofilms Microbiomes* **2022**, *8* (1), 52. DOI: <https://doi.org/10.1038/s41522-022-00317-9>
- (139) Hebel, M.; Gacanin, J.; Luckerath, T.; Ng, D. Y. W.; Weil, T. Controlling Polymer Morphologies by Intramolecular and Intermolecular Dynamic Covalent Iron(III)/Catechol Complexation-From Polypeptide Single Chain Nanoparticles to Hydrogels. *Macromol. Rapid Commun.* **2022**, *43* (12), e2100413. DOI: <https://doi.org/10.1002/marc.202100413>
- (140) Malo de Molina, P.; Le, T. P.; Iturraspe, A.; Gasser, U.; Arbe, A.; Colmenero, J.; Pomposo, J. A. Neat Protein Single-Chain Nanoparticles from Partially Denatured BSA. *ACS Omega* **2022**, *7* (46), 42163-42169. DOI: <https://doi.org/10.1021/acsomega.2c04805>
- (141) Tian, X.; Xue, R.; Yang, F.; Yin, L.; Luan, S.; Tang, H. Single-Chain Nanoparticle-Based Coatings with Improved Bactericidal Activity and Antifouling Properties. *Biomacromolecules* **2021**, *22* (10), 4306-4315. DOI: <https://doi.org/10.1021/acs.biomac.1c00865>
- (142) Fan, W.; Tong, X.; Yan, Q.; Fu, S.; Zhao, Y. Photodegradable and size-tunable single-chain nanoparticles prepared from a single main-chain coumarin-containing polymer precursor. *Chem. Commun.* **2014**, *50* (88), 13492-13494. DOI: <https://doi.org/10.1039/c4cc06629d>
- (143) Radu, J. É. F.; Novak, L.; Hartmann, J. F.; Beheshti, N.; Kjøniksen, A.-L.; Nyström, B.; Borbély, J. Structural and dynamical characterization of poly-gamma-glutamic acid-based cross-linked nanoparticles. *Colloid Polym. Sci.* **2007**, *286* (4), 365-376. DOI: <https://doi.org/10.1007/s00396-007-1776-8>

- (144) Nitti, A.; Carfora, R.; Assanelli, G.; Notari, M.; Pasini, D. Single-Chain Polymer Nanoparticles for Addressing Morphologies and Functions at the Nanoscale: A Review. *Acs Appl. Nano Mater.* **2022**, *5* (10), 13985-13997. DOI: <https://doi.org/10.1021/acsanm.2c02313>
- (145) Aiertza, M. K.; Odriozola, I.; Cabanero, G.; Grande, H. J.; Loinaz, I. Single-chain polymer nanoparticles. *Cell. Mol. Life. Sci.* **2012**, *69* (3), 337-346. DOI: <https://doi.org/10.1007/s00018-011-0852-x>
- (146) Sanchez-Sanchez, A.; Perez-Baena, I.; Pomposo, J. A. Advances in click chemistry for single-chain nanoparticle construction. *Molecules* **2013**, *18* (3), 3339-3355. DOI: <https://doi.org/10.3390/molecules18033339>
- (147) Hanlon, A. M.; Chen, R. W.; Rodriguez, K. J.; Willis, C.; Dickinson, J. G.; Cashman, M.; Berda, E. B. Scalable Synthesis of Single-Chain Nanoparticles under Mild Conditions. *Macromolecules* **2017**, *50* (7), 2996-3003. DOI: <https://doi.org/10.1021/acs.macromol.7b00497>
- (148) Galant, O.; Donmez, H. B.; Barner-Kowollik, C.; Diesendruck, C. E. Flow Photochemistry for Single-Chain Polymer Nanoparticle Synthesis. *Angew. Chem. Int. Ed.* **2021**, *60* (4), 2042-2046. DOI: <https://doi.org/10.1002/anie.202010429>
- (149) Liu, R.; Lindsey, J. S. Single-Polymer-Single-Cargo Strategy Packages Hydrophobic Fluorophores in Aqueous Solution with Retention of Inherent Brightness. *ACS Macro Lett.* **2019**, *8* (1), 79-83. DOI: <https://doi.org/10.1021/acsmacrolett.8b00907>
- (150) Liu, R.; Liu, S. J.; Hu, G. F.; Lindsey, J. S. Aqueous solubilization of hydrophobic tetrapyrrole macrocycles by attachment to an amphiphilic single-chain nanoparticle (SCNP). *New J. Chem.* **2020**, *44* (48), 21293-21308. DOI: <https://doi.org/10.1039/d0nj04413j>
- (151) Liu, S. J.; Rong, J.; Liu, R.; Lindsey, J. S. Single-Fluorophore Single-Chain Nanoparticle Undergoes Fluorophore-Driven Assembly with Fluorescence Features Retained in Physiological Milieu. *ACS Appl. Polym. Mater.* **2021**, *3* (4), 1767-1776. DOI: <https://doi.org/10.1021/acsapm.0c01313>
- (152) Guazzelli, E.; Masotti, E.; Kriechbaum, M.; Uhlig, F.; Galli, G.; Martinelli, E. Thermoresponsive Reversible Unimer Micelles of Amphiphilic Fluorinated Copolymers. *Macromol. Chem. Phys.* **2023**, *224* (3). DOI: <https://doi.org/10.1002/macp.202200360>
- (153) Calosi, M.; Guazzelli, E.; Braccini, S.; Lessi, M.; Bellina, F.; Galli, G.; Martinelli, E. Self-Assembled Amphiphilic Fluorinated Random Copolymers for the Encapsulation and Release of the Hydrophobic Combretastatin A-4 Drug. *Polymers* **2022**, *14* (4). DOI: <https://doi.org/10.3390/polym14040774>
- (154) Nguyen, T. K.; Lam, S. J.; Ho, K. K.; Kumar, N.; Qiao, G. G.; Egan, S.; Boyer, C.; Wong, E. H. Rational Design of Single-Chain Polymeric Nanoparticles That Kill Planktonic and Biofilm Bacteria. *ACS Infect. Dis.* **2017**, *3* (3), 237-248. DOI: <https://doi.org/10.1021/acsinfecdis.6b00203>
- (155) Zhang, Y.; Yi, C. L.; Dong, W. H.; Zheng, D.; Yang, Y. Q.; Li, W.; Duan, X. Z.; Yang, D.; Nie, Z. H. Single Copolymer Chain-Templated Synthesis of Ultrasmall Symmetric and Asymmetric Silica-Based Nanoparticles. *Adv Funct Mater* **2022**, *32* (20). DOI: <https://doi.org/10.1002/adfm.202112742>

- (156) Xiong, T. M.; Garcia, E. S.; Chen, J.; Zhu, L.; Alzona, A. J.; Zimmerman, S. C. Enzyme-like catalysis by single chain nanoparticles that use transition metal cofactors. *Chem. Commun.* **2022**, *58* (7), 985-988. DOI: <https://doi.org/10.1039/d1cc05578j>
- (157) Stals, P. J. M.; Gillissen, M. A. J.; Nicolaÿ, R.; Palmans, A. R. A.; Meijer, E. W. The balance between intramolecular hydrogen bonding, polymer solubility and rigidity in single-chain polymeric nanoparticles. *Polym. Chem.* **2013**, *4* (8), 2584-2597. DOI: <https://doi.org/10.1039/c3py00094j>
- (158) Cheng, C. C.; Chang, F. C.; Yen, H. C.; Lee, D. J.; Chiu, C. W.; Xin, Z. Supramolecular Assembly Mediates the Formation of Single-Chain Polymeric Nanoparticles. *ACS Macro Lett.* **2015**, *4* (10), 1184-1188. DOI: <https://doi.org/10.1021/acsmacrolett.5b00556>
- (159) Fischer, T. S.; Schulze-Sunninghausen, D.; Luy, B.; Altintas, O.; Barner-Kowollik, C. Stepwise Unfolding of Single-Chain Nanoparticles by Chemically Triggered Gates. *Angew. Chem. Int. Ed.* **2016**, *55* (37), 11276-11280. DOI: <https://doi.org/10.1002/anie.201602894>
- (160) Zhang, J. L.; Gody, G.; Hartlieb, M.; Catrouillet, S.; Moffat, J.; Perrier, S. Synthesis of Sequence-Controlled Multiblock Single Chain Nanoparticles by a Stepwise Folding-Chain Extension-Folding Process. *Macromolecules* **2016**, *49* (23), 8933-8942. DOI: <https://doi.org/10.1021/acs.macromol.6b01962>
- (161) van Roekel, H. W.; Stals, P. J.; Gillissen, M. A.; Hilbers, P. A.; Markvoort, A. J.; de Greef, T. F. Evaporative self-assembly of single-chain, polymeric nanoparticles. *Chem. Commun.* **2013**, *49* (30), 3122-3124. DOI: <https://doi.org/10.1039/c3cc40931g>
- (162) Cheng, C. C.; Lee, D. J.; Liao, Z. S.; Huang, J. J. Stimuli-responsive single-chain polymeric nanoparticles towards the development of efficient drug delivery systems. *Polym. Chem.* **2016**, *7* (40), 6164-6169. DOI: <https://doi.org/10.1039/c6py01623e>
- (163) Mes, T.; van der Weegen, R.; Palmans, A. R.; Meijer, E. W. Single-chain polymeric nanoparticles by stepwise folding. *Angew. Chem. Int. Ed.* **2011**, *50* (22), 5085-5089. DOI: <https://doi.org/10.1002/anie.201100104>
- (164) Artar, M.; Terashima, T.; Sawamoto, M.; Meijer, E. W.; Palmans, A. R. A. Understanding the Catalytic Activity of Single-Chain Polymeric Nanoparticles in Water. *J Polym Sci Pol Chem* **2014**, *52* (1), 12-20. DOI: <https://doi.org/10.1002/pola.26970>
- (165) Hosono, N.; Palmans, A. R.; Meijer, E. W. "Soldier-Sergeant-Soldier" triblock copolymers: revealing the folded structure of single-chain polymeric nanoparticles. *Chem. Commun.* **2014**, *50* (59), 7990-7993. DOI: <https://doi.org/10.1039/c4cc02789b>
- (166) Liu, Y.; Pauloehrl, T.; Presolski, S. I.; Albertazzi, L.; Palmans, A. R.; Meijer, E. W. Modular Synthetic Platform for the Construction of Functional Single-Chain Polymeric Nanoparticles: From Aqueous Catalysis to Photosensitization. *J. Am. Chem. Soc.* **2015**, *137* (40), 13096-13105. DOI: <https://doi.org/10.1021/jacs.5b08299>
- (167) Stals, P. J. M.; Cheng, C. Y.; van Beek, L.; Wauters, A. C.; Palmans, A. R. A.; Han, S.; Meijer, E. W. Surface water retardation around single-chain polymeric nanoparticles: critical for catalytic function? *Chem. Sci.* **2016**, *7* (3), 2011-2015. DOI: <https://doi.org/10.1039/c5sc02319j>

- (168) Stals, P. J. M.; Gillissen, M. A. J.; Paffen, T. F. E.; Greef, T. F. A.; Lindner, P.; Meijer, E. W.; Palmans, A. R. A.; Voets, I. K. Folding Polymers with Pendant Hydrogen Bonding Motifs in Water: The Effect of Polymer Length and Concentration on the Shape and Size of Single-Chain Polymeric Nanoparticles. *Macromolecules* **2014**, *47* (9), 2947-2954. DOI: <https://doi.org/10.1021/ma500273g>
- (169) Archontakis, E.; Deng, L.; Zijlstra, P.; Palmans, A. R. A.; Albertazzi, L. Spectrally PAINTing a Single Chain Polymeric Nanoparticle at Super-Resolution. *J. Am. Chem. Soc.* **2022**, *144* (51), 23698-23707. DOI: <https://doi.org/10.1021/jacs.2c11940>
- (170) Deng, L.; Albertazzi, L.; Palmans, A. R. A. Elucidating the Stability of Single-Chain Polymeric Nanoparticles in Biological Media and Living Cells. *Biomacromolecules* **2022**, *23* (1), 326-338. DOI: <https://doi.org/10.1021/acs.biomac.1c01291>
- (171) Lu, J.; Ten Brummelhuis, N.; Weck, M. Intramolecular folding of triblock copolymers via quadrupole interactions between poly(styrene) and poly(pentafluorostyrene) blocks. *Chem. Commun.* **2014**, *50* (47), 6225-6227. DOI: <https://doi.org/10.1039/c4cc01840k>
- (172) Zhu, Z.; Xu, N.; Yu, Q.; Guo, L.; Cao, H.; Lu, X.; Cai, Y. Construction and Self-Assembly of Single-Chain Polymer Nanoparticles via Coordination Association and Electrostatic Repulsion in Water. *Macromol. Rapid Commun.* **2015**, *36* (16), 1521-1527. DOI: <https://doi.org/10.1002/marc.201500281>
- (173) Wang, F.; Pu, H.; Jin, M.; Wan, D. Supramolecular Nanoparticles via Single-Chain Folding Driven by Ferrous Ions. *Macromol. Rapid Commun.* **2016**, *37* (4), 330-336. DOI: <https://doi.org/10.1002/marc.201500616>
- (174) Neumann, L. N.; Urban, D. A.; Lemal, P.; Ramani, S.; Petri-Fink, A.; Balog, S.; Weder, C.; Schrettl, S. Preparation of metallosupramolecular single-chain polymeric nanoparticles and their characterization by Taylor dispersion. *Polym. Chem.* **2020**, *11* (2), 586-592. DOI: <https://doi.org/10.1039/c9py01264h>
- (175) Xiang, D.; Jiang, B. Y.; Liang, F. X.; Yan, L. T.; Yang, Z. Z. Single-Chain Janus Nanoparticle by Metallic Complexation. *Macromolecules* **2020**, *53* (3), 1063-1069. DOI: <https://doi.org/10.1021/acs.macromol.9b02388>
- (176) Willenbacher, J.; Altintas, O.; Trouillet, V.; Knöfel, N.; Monteiro, M. J.; Roesky, P. W.; Barner-Kowollik, C. Pd-complex driven formation of single-chain nanoparticles. *Polym. Chem.* **2015**, *6* (24), 4358-4365. DOI: <https://doi.org/10.1039/c5py00389j>
- (177) Thanneeru, S.; Duay, S. S.; Jin, L.; Fu, Y.; Angeles-Boza, A. M.; He, J. Single Chain Polymeric Nanoparticles to Promote Selective Hydroxylation Reactions of Phenol Catalyzed by Copper. *ACS Macro Lett.* **2017**, *6* (7), 652-656. DOI: <https://doi.org/10.1021/acsmacrolett.7b00300>
- (178) Garmendia, S.; Lawrenson, S. B.; Arno, M. C.; O'Reilly, R. K.; Taton, D.; Dove, A. P. Catalytically Active N-Heterocyclic Carbene Release from Single-Chain Nanoparticles Following a Thermolysis-Driven Unfolding Strategy. *Macromol. Rapid Commun.* **2019**, *40* (15), e1900071. DOI: <https://doi.org/10.1002/marc.201900071>
- (179) Cheng, L.; Wu, R.-J.; Li, Y.-M.; Ren, H.; Ji, C.-Y.; Li, W.-J. Single-chain polymer nanoparticles-encapsulated chiral bifunctional metal-organic frameworks for asymmetric sequential reactions. *Inorg. Chem. Commun.* **2022**, *141*. DOI: <https://doi.org/10.1016/j.inoche.2022.109577>

- (180) Sanchez-Sanchez, A.; Arbe, A.; Colmenero, J.; Pomposo, J. A. Metallo-Folded Single-Chain Nanoparticles with Catalytic Selectivity. *ACS Macro Lett.* **2014**, *3* (5), 439-443. DOI: <https://doi.org/10.1021/mz5001477>
- (181) Rothfuss, H.; Knofel, N. D.; Roesky, P. W.; Barner-Kowollik, C. Single-Chain Nanoparticles as Catalytic Nanoreactors. *J. Am. Chem. Soc.* **2018**, *140* (18), 5875-5881. DOI: <https://doi.org/10.1021/jacs.8b02135>
- (182) Izuagbe, A. E.; Truong, V. X.; Tuten, B. T.; Roesky, P. W.; Barner-Kowollik, C. Visible Light Switchable Single-Chain Nanoparticles. *Macromolecules* **2022**. DOI: <https://doi.org/10.1021/acs.macromol.2c01467>
- (183) Sanchez-Sanchez, A.; Pomposo, J. A. Efficient Synthesis of Single-Chain Polymer Nanoparticles via Amide Formation. *Journal of Nanomaterials* **2015**, *2015*, 1-7. DOI: <https://doi.org/10.1155/2015/723492>.
- (184) Liang, J.; Struckhoff, J. J.; Hamilton, P. D.; Ravi, N. Preparation and Characterization of Biomimetic beta-Lens Crystallins Using Single-Chain Polymeric Nanoparticles. *Langmuir* **2017**, *33* (31), 7660-7668. DOI: <https://doi.org/10.1021/acs.langmuir.7b01290>
- (185) Mohamed Irshadeen, I.; Truong, V. X.; Frisch, H.; Barner-Kowollik, C. Red light induced folding of single polymer chains. *Chem. Commun.* **2022**, *58* (93), 12975-12978. DOI: <https://doi.org/10.1039/d2cc05415a>
- (186) Gao, Y.; Bohmer, V. I.; Zhou, D.; Zhao, T.; Wang, W.; Paulusse, J. M. Main-chain degradable single-chain cyclized polymers as gene delivery vectors. *J. Control. Release* **2016**, *244* (Pt B), 375-383. DOI: <https://doi.org/10.1016/j.jconrel.2016.07.046>
- (187) Wong, E. H. H.; Lam, S. J.; Nam, E.; Qiao, G. G. Biocompatible Single-Chain Polymeric Nanoparticles via Organo-Catalyzed Ring-Opening Polymerization. *ACS Macro Lett.* **2014**, *3* (6), 524-528. DOI: <https://doi.org/10.1021/mz500225p>
- (188) Wong, E. H. H.; Qiao, G. G. Factors Influencing the Formation of Single-Chain Polymeric Nanoparticles Prepared via Ring-Opening Polymerization. *Macromolecules* **2015**, *48* (5), 1371-1379. DOI: <https://doi.org/10.1021/ma502526c>
- (189) de Luzuriaga, A. R.; Ormategui, N.; Grande, H. J.; Odriozola, I.; Pomposo, J. A.; Loinaz, I. Intramolecular Click Cycloaddition: An Efficient Room-Temperature Route towards Bioconjugable Polymeric Nanoparticles. *Macromol. Rapid Commun.* **2008**, *29* (12-13), 1156-1160. DOI: <https://doi.org/10.1002/marc.200700877>
- (190) de Luzuriaga, A. R.; Perez-Baena, I.; Montes, S.; Loinaz, I.; Odriozola, I.; García, I.; Pomposo, J. A. New Route to Polymeric Nanoparticles by Click Chemistry Using Bifunctional Cross-Linkers. *Macromol. Symp.* **2010**, *296* (1), 303-310. DOI: <https://doi.org/10.1002/masy.201051042>
- (191) Oria, L.; Aguado, R.; Pomposo, J. A.; Colmenero, J. A versatile "click" chemistry precursor of functional polystyrene nanoparticles. *Adv. Mater.* **2010**, *22* (28), 3038-3041. DOI: <https://doi.org/10.1002/adma.201000243>
- (192) Ormategui, N.; García, I.; Padro, D.; Cabañero, G.; Grande, H. J.; Loinaz, I. Synthesis of single chain thermoresponsive polymernanoparticles. *Soft Matter* **2012**, *8* (3), 734-740. DOI: <https://doi.org/10.1039/c1sm06310c>

- (193) Rubio-Cervilla, J.; Frisch, H.; Barner-Kowollik, C.; Pomposo, J. A. Synthesis of Single-Ring Nanoparticles Mimicking Natural Cyclotides by a Stepwise Folding-Activation-Collapse Process. *Macromol. Rapid Commun.* **2019**, *40* (1), e1800491. DOI: <https://doi.org/10.1002/marc.201800491>
- (194) Chen, J.; Li, K.; Shon, J. S. L.; Zimmerman, S. C. Single-Chain Nanoparticle Delivers a Partner Enzyme for Concurrent and Tandem Catalysis in Cells. *J. Am. Chem. Soc.* **2020**, *142* (10), 4565-4569. DOI: <https://doi.org/10.1021/jacs.9b13997>
- (195) Perez-Baena, I.; Loinaz, I.; Padro, D.; García, I.; Grande, H. J.; Odriozola, I. Single-chain polyacrylic nanoparticles with multiple Gd(III) centres as potential MRI contrast agents. *J. Mater. Chem.* **2010**, *20* (33), 6916-6922. DOI: <https://doi.org/10.1039/c0jm01025a>
- (196) Meldal, M.; Diness, F. Recent Fascinating Aspects of the CuAAC Click Reaction. *Trends in Chemistry* **2020**, *2* (6), 569-584. DOI: <https://doi.org/10.1016/j.trechm.2020.03.007>
- (197) Kolb, H. C.; Finn, M. G.; Sharpless, K. B. Click Chemistry: Diverse Chemical Function from a Few Good Reactions. *Angew. Chem. Int. Ed.* **2001**, *40* (11), 2004-2021. DOI: [https://doi.org/10.1002/1521-3773\(20010601\)40:11<2004::AID-ANIE2004>3.0.CO;2-5](https://doi.org/10.1002/1521-3773(20010601)40:11<2004::AID-ANIE2004>3.0.CO;2-5)
- (198) González-Burgos, M.; Alegría, A.; Arbe, A.; Colmenero, J.; Pomposo, J. A. An unexpected route to aldehyde-decorated single-chain nanoparticles from azides. *Polym. Chem.* **2016**, *7* (43), 6570-6574. DOI: <https://doi.org/10.1039/c6py01602b>
- (199) Zhu, B. C.; Sun, S. Y.; Wang, Y. F.; Deng, S.; Qian, G. N.; Wang, M.; Hu, A. G. Preparation of carbon nanodots from single chain polymeric nanoparticles and theoretical investigation of the photoluminescence mechanism. *J. Mater. Chem. C* **2013**, *1* (3), 580-586. DOI: <https://doi.org/10.1039/c2tc00140c>
- (200) De-La-Cuesta, J.; Verde-Sesto, E.; Arbe, A.; Pomposo, J. A. Self-Reporting of Folding and Aggregation by Orthogonal Hantzsch Luminophores Within a Single Polymer Chain. *Angew. Chem. Int. Ed.* **2021**, *60* (7), 3534-3539. DOI: <https://doi.org/10.1002/anie.202013932>
- (201) Kröger, A. P. P.; Boonen, R. J. E. A.; Paulusse, J. M. J. Well-defined single-chain polymer nanoparticles via thiol-Michael addition. *Polymer* **2017**, *120*, 119-128. DOI: <https://doi.org/10.1016/j.polymer.2017.05.040>
- (202) Sanchez-Sanchez, A.; Akbari, S.; Etxeberria, A.; Arbe, A.; Gasser, U.; Moreno, A. J.; Colmenero, J.; Pomposo, J. A. "Michael" Nanocarriers Mimicking Transient-Binding Disordered Proteins. *ACS Macro Lett.* **2013**, *2* (6), 491-495. DOI: <https://doi.org/10.1021/mz400173c>
- (203) Sanchez-Sanchez, A.; Asenjo-Sanz, I.; Buruaga, L.; Pomposo, J. A. Naked and self-clickable propargylic-decorated single-chain nanoparticle precursors via redox-initiated RAFT polymerization. *Macromol. Rapid Commun.* **2012**, *33* (15), 1262-1267. DOI: <https://doi.org/10.1002/marc.201200180>
- (204) He, J.; Tremblay, L.; Lacelle, S.; Zhao, Y. Preparation of polymer single chain nanoparticles using intramolecular photodimerization of coumarin. *Soft Matter* **2011**, *7* (6), 2380-2386. DOI: <https://doi.org/10.1039/c0sm01383h>

- (205) Frank, P. G.; Tuten, B. T.; Prasher, A.; Chao, D.; Berda, E. B. Intra-chain photodimerization of pendant anthracene units as an efficient route to single-chain nanoparticle fabrication. *Macromol. Rapid Commun.* **2014**, *35* (2), 249-253. DOI: <https://doi.org/10.1002/marc.201300677>
- (206) Tooley, C. A.; Pazicni, S.; Berda, E. B. Toward a tunable synthetic [FeFe] hydrogenase mimic: single-chain nanoparticles functionalized with a single diiron cluster. *Polym. Chem.* **2015**, *6* (44), 7646-7651. DOI: <https://doi.org/10.1039/c5py01196e>
- (207) Fan, W. Z.; Tong, X.; Farnia, F.; Yu, B.; Zhao, Y. CO<sub>2</sub>-Responsive Polymer Single-Chain Nanoparticles and Self-Assembly for Gas-Tunable Nanoreactors. *Chem Mater* **2017**, *29* (13), 5693-5701. DOI: <https://doi.org/10.1021/acs.chemmater.7b01656>
- (208) Fan, W. Z.; Tong, X.; Li, G.; Zhao, Y. Photoresponsive liquid crystalline polymer single-chain nanoparticles. *Polym. Chem.* **2017**, *8* (22), 3523-3529. DOI: <https://doi.org/10.1039/c7py00668c>
- (209) Frisch, H.; Menzel, J. P.; Bloesser, F. R.; Marschner, D. E.; Mundsinger, K.; Barner-Kowollik, C. Photochemistry in Confined Environments for Single-Chain Nanoparticle Design. *J. Am. Chem. Soc.* **2018**, *140* (30), 9551-9557. DOI: <https://doi.org/10.1021/jacs.8b04531>
- (210) Frisch, H.; Bloesser, F. R.; Barner-Kowollik, C. Controlling Chain Coupling and Single-Chain Ligation by Two Colours of Visible Light. *Angew. Chem. Int. Ed.* **2019**, *58* (11), 3604-3609. DOI: <https://doi.org/10.1002/anie.201811541>
- (211) Frisch, H.; Kodura, D.; Bloesser, F. R.; Michalek, L.; Barner-Kowollik, C. Wavelength-Selective Folding of Single Polymer Chains with Different Colors of Visible Light. *Macromol. Rapid Commun.* **2020**, *41* (1), e1900414. DOI: <https://doi.org/10.1002/marc.201900414>
- (212) Song, C. F.; Li, L. Y.; Dai, L. Z.; Thayumanavan, S. Responsive single-chain polymer nanoparticles with host-guest features. *Polym. Chem.* **2015**, *6* (26), 4828-4834. DOI: <https://doi.org/10.1039/c5py00600g>
- (213) Altintas, O.; Willenbacher, J.; Wuest, K. N. R.; Oehlschlaeger, K. K.; Krolla-Sidenstein, P.; Gliemann, H.; Barner-Kowollik, C. A Mild and Efficient Approach to Functional Single-Chain Polymeric Nanoparticles via Photoinduced Diels-Alder Ligation. *Macromolecules* **2013**, *46* (20), 8092-8101. DOI: <https://doi.org/10.1021/ma4015033>
- (214) Maag, P. H.; Feist, F.; Frisch, H.; Roesky, P. W.; Barner-Kowollik, C. Fluorescent and Catalytically Active Single Chain Nanoparticles. *Macromolecules* **2022**, *55*, 9918-9924. DOI: <https://doi.org/10.1021/acs.macromol.2c01894>
- (215) Whitaker, D. E.; Mahon, C. S.; Fulton, D. A. Thermoresponsive dynamic covalent single-chain polymer nanoparticles reversibly transform into a hydrogel. *Angew. Chem. Int. Ed.* **2013**, *52* (3), 956-959. DOI: <https://doi.org/10.1002/anie.201207953>
- (216) Mahon, C. S.; McGurk, C. J.; Watson, S. M. D.; Fascione, M. A.; Sakonsinsiri, C.; Turnbull, W. B.; Fulton, D. A. Molecular Recognition-Mediated Transformation of Single-Chain Polymer Nanoparticles into Crosslinked Polymer Films. *Angew. Chem. Int. Ed.* **2017**, *56* (42), 12913-12918. DOI: <https://doi.org/10.1002/anie.201706379>

- (217) Sanchez-Sanchez, A.; Fulton, D. A.; Pomposo, J. A. pH-responsive single-chain polymer nanoparticles utilising dynamic covalent enamine bonds. *Chem. Commun.* **2014**, *50* (15), 1871-1874. DOI: <https://doi.org/10.1039/c3cc48733d>
- (218) Liu, Y. L.; Turunen, P.; de Waal, B. F. M.; Blank, K. G.; Rowan, A. E.; Palmans, A. R. A.; Meijer, E. W. Catalytic single-chain polymeric nanoparticles at work: from ensemble towards single-particle kinetics. *Mol Syst Des Eng* **2018**, *3* (4), 609-618. DOI: <https://doi.org/10.1039/c8me00017d>
- (219) Mundsinger, K.; Tuten, B. T.; Wang, L.; Neubauer, K.; Kropf, C.; O'Mara, M. L.; Barner-Kowollik, C. Visible-Light-Reactive Single-Chain Nanoparticles. *Angew. Chem. Int. Ed.* **2023**, *62* (23), e202302995. DOI: <https://doi.org/10.1002/anie.202302995>
- (220) Sanchez-Sanchez, A.; Akbari, S.; Moreno, A. J.; Verso, F. L.; Arbe, A.; Colmenero, J.; Pomposo, J. A. Design and preparation of single-chain nanocarriers mimicking disordered proteins for combined delivery of dermal bioactive cargos. *Macromol. Rapid Commun.* **2013**, *34* (21), 1681-1686. DOI: <https://doi.org/10.1002/marc.201300562>
- (221) Benito, A. B.; Aiertza, M. K.; Marradi, M.; Gil-Iceta, L.; Shekhter Zahavi, T.; Szczupak, B.; Jimenez-Gonzalez, M.; Reese, T.; Scanziani, E.; Passoni, L.; Matteoli, M.; De Maglie, M.; Orenstein, A.; Oron-Herman, M.; Kostenich, G.; Buzhansky, L.; Gazit, E.; Grande, H. J.; Gomez-Vallejo, V.; Llop, J.; Loinaz, I. Functional Single-Chain Polymer Nanoparticles: Targeting and Imaging Pancreatic Tumors in Vivo. *Biomacromolecules* **2016**, *17* (10), 3213-3221. DOI: <https://doi.org/10.1021/acs.biomac.6b00941>
- (222) Huggins, M. L. Solutions of Long Chain Compounds. *J. Chem. Phys.* **1941**, *9* (5), 440-440. DOI: <https://doi.org/10.1063/1.1750930>
- (223) Flory, P. J. Thermodynamics of High Polymer Solutions. *J. Chem. Phys.* **1942**, *10* (1), 51-61. DOI: <https://doi.org/10.1063/1.1723621>
- (224) Hansen, C. M. *Hansen Solubility Parameters*; Taylor & Francis Group, LLC, **2007**. ISBN: 9780429127526. DOI: <https://doi.org/10.1201/9781420006834>
- (225) Walton, D. G.; Kellogg, G. J.; Mayes, A. M.; Lambooy, P.; Russell, T. P. A Free-Energy Model for Confined Diblock Copolymers. *Macromolecules* **1994**, *27* (21), 6225-6228. DOI: <https://doi.org/10.1021/ma00099a045>
- (226) Huang, E.; Rockford, L.; Russell, T. P.; Hawker, C. J. Nanodomain control in copolymer thin films. *Nature* **1998**, *395* (6704), 757-758. DOI: <https://doi.org/10.1038/27358>
- (227) Wang, Q.; Nealey, P. F.; de Pablo, J. J. Monte Carlo simulations of asymmetric diblock copolymer thin films confined between two homogeneous surfaces. *Macromolecules* **2001**, *34* (10), 3458-3470. DOI: <https://doi.org/10.1021/ma0018751>
- (228) Park, S. M.; Craig, G. S. W.; La, Y. H.; Nealey, P. F. Morphological Reconstruction and Ordering in Films of Sphere-Forming Block Copolymers on Striped Chemically Patterned Surfaces. *Macromolecules* **2008**, *41* (23), 9124-9129. DOI: <https://doi.org/10.1021/ma801039v>
- (229) Stuen, K. O.; Detcherry, F. A.; Craig, G. S.; Thomas, C. S.; Farrell, R. A.; Morris, M. A.; de Pablo, J. J.; Nealey, P. F. Graphoepitaxial assembly of asymmetric ternary blends of block copolymers and homopolymers. *Nanotechnology* **2010**, *21* (49), 495301. DOI: <https://doi.org/10.1088/0957-4484/21/49/495301>

- (230) Pomposo, J. A. *Single-Chain Polymer Nanoparticles: Synthesis, Characterization, Simulations, and Applications*; Wiley-VCH, **2017**. ISBN: 978-3-527-34242-6
- (231) Verde-Sesto, E.; Arbe, A.; Moreno, A. J.; Cangialosi, D.; Alegría, A.; Colmenero, J.; Pomposo, J. A. Single-chain nanoparticles: opportunities provided by internal and external confinement. *Materials Horizons* **2020**, *7* (9), 2292-2313. DOI: <https://doi.org/10.1039/d0mh00846j>
- (232) Basasoro, S.; Gonzalez-Burgos, M.; Moreno, A. J.; Verso, F. L.; Arbe, A.; Colmenero, J.; Pomposo, J. A. A Solvent-Based Strategy for Tuning the Internal Structure of Metallo-Folded Single-Chain Nanoparticles. *Macromol. Rapid Commun.* **2016**, *37* (13), 1060-1065. DOI: <https://doi.org/10.1002/marc.201600139>
- (233) Zhang, H.; Zhang, L.; You, J. C.; Zhang, N. B. Q.; Yu, L. X. Z.; Zhao, H. Y.; Qian, H. J.; Lu, Z. Y. Controlling the Chain Folding for the Synthesis of Single-Chain Polymer Nanoparticles Using Thermoresponsive Polymers. *CCS Chemistry* **2021**, *3* (8), 2143-2154. DOI: <https://doi.org/10.31635/ccschem.020.202000190>
- (234) Wen, W.; Huang, T. Y.; Guan, S.; Zhao, Y. B.; Chen, A. H. Self-Assembly of Single Chain Janus Nanoparticles with Tunable Liquid Crystalline Properties from Stilbene-Containing Block Copolymers. *Macromolecules* **2019**, *52* (8), 2956-2964. DOI: <https://doi.org/10.1021/acs.macromol.9b00154>
- (235) Gillissen, M. A. J.; Terashima, T.; Meijer, E. W.; Palmans, A. R. A.; Voets, I. K. Sticky Supramolecular Grafts Stretch Single Polymer Chains. *Macromolecules* **2013**, *46* (10), 4120-4125. DOI: <https://doi.org/10.1021/ma4006846>
- (236) Terashima, T.; Mes, T.; De Greef, T. F.; Gillissen, M. A.; Besenius, P.; Palmans, A. R.; Meijer, E. W. Single-chain folding of polymers for catalytic systems in water. *J. Am. Chem. Soc.* **2011**, *133* (13), 4742-4745. DOI: <https://doi.org/10.1021/ja2004494>
- (237) Huerta, E.; Stals, P. J.; Meijer, E. W.; Palmans, A. R. Consequences of folding a water-soluble polymer around an organocatalyst. *Angew. Chem. Int. Ed.* **2013**, *52* (10), 2906-2910. DOI: <https://doi.org/10.1002/anie.201207123>
- (238) Artar, M.; Souren, E. R. J.; Terashima, T.; Meijer, E. W.; Palmans, A. R. A. Single Chain Polymeric Nanoparticles as Selective Hydrophobic Reaction Spaces in Water. *ACS Macro Lett.* **2015**, *4* (10), 1099-1103. DOI: <https://doi.org/10.1021/acsmacrolett.5b00652>
- (239) Huerta, E.; van Genabeek, B.; Stals, P. J.; Meijer, E. W.; Palmans, A. R. A modular approach to introduce function into single-chain polymeric nanoparticles. *Macromol. Rapid Commun.* **2014**, *35* (15), 1320-1325. DOI: <https://doi.org/10.1002/marc.201400213>
- (240) Liu, Y.; Pujals, S.; Stals, P. J. M.; Paulohrl, T.; Presolski, S. I.; Meijer, E. W.; Albertazzi, L.; Palmans, A. R. A. Catalytically Active Single-Chain Polymeric Nanoparticles: Exploring Their Functions in Complex Biological Media. *J. Am. Chem. Soc.* **2018**, *140* (9), 3423-3433. DOI: <https://doi.org/10.1021/jacs.8b00122>
- (241) Engelke, J.; Brandt, J.; Barner-Kowollik, C.; Lederer, A. Strengths and limitations of size exclusion chromatography for investigating single chain folding - current status and future perspectives. *Polym. Chem.* **2019**, *10* (25), 3410-3425. DOI: <https://doi.org/10.1039/c9py00336c>

- (242) Perez-Baena, I.; Asenjo-Sanz, I.; Arbe, A.; Moreno, A. J.; Lo Verso, F.; Colmenero, J.; Pomposo, J. A. Efficient Route to Compact Single-Chain Nanoparticles: Photoactivated Synthesis via Thiol-Yne Coupling Reaction. *Macromolecules* **2014**, *47* (23), 8270-8280. DOI: <https://doi.org/10.1021/ma5017133>
- (243) Wijker, S.; Palmans, A. R. A. Protein-Inspired Control over Synthetic Polymer Folding for Structured Functional Nanoparticles in Water. *ChemPlusChem* **2023**, *88* (7), e202300260. DOI: <https://doi.org/10.1002/cplu.202300260>
- (244) Blasco, E.; Tuten, B. T.; Frisch, H.; Lederer, A.; Barner-Kowollik, C. Characterizing single chain nanoparticles (SCNPs): a critical survey. *Polym. Chem.* **2017**, *8* (38), 5845-5851. DOI: <https://doi.org/10.1039/c7py01278k>
- (245) Liao, S. Y.; Wei, L. X.; Abriata, L. A.; Stellacci, F. Control and Characterization of the Compactness of Single-Chain Nanoparticles. *Macromolecules* **2021**, *54* (24), 11459-11467. DOI: <https://doi.org/10.1021/acs.macromol.1c02071>
- (246) Pomposo, J. A.; Moreno, A. J.; Arbe, A.; Colmenero, J. Local Domain Size in Single-Chain Polymer Nanoparticles. *ACS Omega* **2018**, *3* (8), 8648-8654. DOI: <https://doi.org/10.1021/acsomega.8b01331>
- (247) Hu, J.; Whittaker, M. R.; Duong, H.; Li, Y.; Boyer, C.; Davis, T. P. Biomimetic polymers responsive to a biological signaling molecule: nitric oxide triggered reversible self-assembly of single macromolecular chains into nanoparticles. *Angew. Chem. Int. Ed.* **2014**, *53* (30), 7779-7784. DOI: <https://doi.org/10.1002/anie.201403147>
- (248) Wiester, M. J.; Ulmann, P. A.; Mirkin, C. A. Enzymnachbildungen auf der Basis supramolekularer Koordinationschemie. *Angewandte Chemie* **2010**, *123* (1), 118-142. DOI: <https://doi.org/10.1002/ange.201000380>
- (249) Perez-Baena, I.; Barroso-Bujans, F.; Gasser, U.; Arbe, A.; Moreno, A. J.; Colmenero, J.; Pomposo, J. A. Endowing Single-Chain Polymer Nanoparticles with Enzyme-Mimetic Activity. *ACS Macro Lett.* **2013**, *2* (9), 775-779. DOI: <https://doi.org/10.1021/mz4003744>
- (250) Lambert, R.; Wirotius, A. L.; Garmendia, S.; Berto, P.; Vignolle, J.; Taton, D. Pd(ii)-NHC coordination-driven formation of water-soluble catalytically active single chain nanoparticles. *Polym. Chem.* **2018**, *9* (23), 3199-3204. DOI: <https://doi.org/10.1039/c8py00326b>
- (251) Liu, S.; Tang, M. Q.; Pang, J.; Hu, J. T.; Chen, W. J.; Cheng, J.; Liu, Z. W.; Zhao, H. H.; Tan, R. CO<sub>2</sub>-Switchable Single-Chain Polymeric Nanoparticles Enable Gas-Controllable Reaction Separation for Asymmetric Catalysis in Water. *Acs Sustain Chem Eng* **2022**, *10* (36), 11760-11772. DOI: <https://doi.org/10.1021/acssuschemeng.2c02045>
- (252) Knofel, N. D.; Rothfuss, H.; Willenbacher, J.; Barner-Kowollik, C.; Roesky, P. W. Platinum(II)-Crosslinked Single-Chain Nanoparticles: An Approach towards Recyclable Homogeneous Catalysts. *Angew. Chem. Int. Ed.* **2017**, *56* (18), 4950-4954. DOI: <https://doi.org/10.1002/anie.201700718>
- (253) Adkins, C. T.; Dobish, J. N.; Brown, S.; Harth, E. Water-soluble Semiconducting Nanoparticles for Imaging. *ACS Macro Lett.* **2013**, *2* (8), 710-714. DOI: <https://doi.org/10.1021/mz400370f>

- (254) Kroger, A. P. P.; Hamelmann, N. M.; Juan, A.; Lindhoud, S.; Paulusse, J. M. J. Biocompatible Single-Chain Polymer Nanoparticles for Drug Delivery-A Dual Approach. *ACS Appl. Mater. Interfaces* **2018**, *10* (37), 30946-30951. DOI: <https://doi.org/10.1021/acsami.8b07450>
- (255) Hamelmann, N. M.; Paats, J. D.; Paulusse, J. M. J. Cytosolic Delivery of Single-Chain Polymer Nanoparticles. *ACS Macro Lett.* **2021**, *10* (11), 1443-1449. DOI: <https://doi.org/10.1021/acsmacrolett.1c00558>
- (256) Hamelmann, N. M.; Uijtewaal, S.; Hujaya, S. D.; Paulusse, J. M. J. Enhancing Cellular Internalization of Single-Chain Polymer Nanoparticles via Polyplex Formation. *Biomacromolecules* **2022**, *23* (12), 5036-5042. DOI: <https://doi.org/10.1021/acs.biomac.2c00858>
- (257) Hamelmann, N. M.; Paats, J. D.; Avalos-Padilla, Y.; Lantero, E.; Spanos, L.; Sidenkiamos, I.; Fernandez-Busquets, X.; Paulusse, J. M. J. Single-Chain Polymer Nanoparticles Targeting the Ookinete Stage of Malaria Parasites. *ACS Infect. Dis.* **2023**, *9* (1), 56-64. DOI: <https://doi.org/10.1021/acsinfecdis.2c00336>
- (258) Kröger, A. P. P.; Komil, M. I.; Hamelmann, N. M.; Juan, A.; Stenzel, M. H.; Paulusse, J. M. J. Glucose Single-Chain Polymer Nanoparticles for Cellular Targeting. *ACS Macro Lett.* **2019**, *8* (1), 95-101. DOI: <https://doi.org/10.1021/acsmacrolett.8b00812>
- (259) Jeong, J.; Lee, Y. J.; Kim, B.; Kim, B.; Jung, K. S.; Paik, H. J. Colored single-chain polymeric nanoparticles intramolecular copper phthalocyanine formation. *Polym. Chem.* **2015**, *6* (18), 3392-3397. DOI: <https://doi.org/10.1039/c4py01559b>
- (260) Maag, P. H.; Feist, F.; Truong, V. X.; Frisch, H.; Roesky, P. W.; Barner-Kowollik, C. Visible-Light-Induced Control over Reversible Single-Chain Nanoparticle Folding. *Angew. Chem. Int. Ed.* **2023**, *62* (37), e202309259. DOI: <https://doi.org/10.1002/anie.202309259>
- (261) Offenloch, J. T.; Willenbacher, J.; Tzvetkova, P.; Heiler, C.; Mutlu, H.; Barner-Kowollik, C. Degradable fluorescent single-chain nanoparticles based on metathesis polymers. *Chem. Commun.* **2017**, *53* (4), 775-778. DOI: <https://doi.org/10.1039/c6cc08554g>
- (262) Wedler-Jasinski, N.; Lueckerath, T.; Mutlu, H.; Goldmann, A. S.; Walther, A.; Stenzel, M. H.; Barner-Kowollik, C. Dynamic covalent single chain nanoparticles based on hetero Diels-Alder chemistry. *Chem. Commun.* **2016**, *53* (1), 157-160. DOI: <https://doi.org/10.1039/c6cc07427h>
- (263) Wang, F.; Pu, H.; Che, X. Voltage-responsive single-chain polymer nanoparticles via host-guest interaction. *Chem. Commun.* **2016**, *52* (17), 3516-3519. DOI: <https://doi.org/10.1039/c5cc09984f>
- (264) Xu, M. H.; Wang, L. H. V. Photoacoustic imaging in biomedicine. *Rev. Sci. Instrum.* **2006**, *77* (4). DOI: <https://doi.org/10.1063/1.2195024>
- (265) Upputuri, P. K.; Pramanik, M. Photoacoustic imaging in the second near-infrared window: a review. *J. Biomed. Opt.* **2019**, *24* (4), 1-20. DOI: <https://doi.org/10.1117/1.JBO.24.4.040901>
- (266) Mark, J.; Schmitt, F. J.; Theiss, C.; Dortay, H.; Friedrich, T.; Laufer, J. Photoacoustic imaging of fluorophores using pump-probe excitation. *Biomed. Opt. Express* **2015**, *6* (7), 2522-2535. DOI: <https://doi.org/10.1364/BOE.6.002522>

- (267) Märk, J.; Schmitt, F.-J.; Laufer, J. Photoacoustic imaging of the excited state lifetime of fluorophores. *J. Opt.* **2016**, *18* (5). DOI: <https://doi.org/10.1088/2040-8978/18/5/054009>
- (268) Mark, J.; Wagener, A.; Zhang, E.; Laufer, J. Photoacoustic pump-probe tomography of fluorophores in vivo using interleaved image acquisition for motion suppression. *Sci. Rep.* **2017**, *7*, 40496. DOI: <https://doi.org/10.1038/srep40496>
- (269) Hoffmann, J. F.; Roos, A. H.; Schmitt, F. J.; Hinderberger, D.; Binder, W. H. Fluorescent and Water Dispersible Single-Chain Nanoparticles: Core-Shell Structured Compartmentation. *Angew. Chem. Int. Ed.* **2021**, *60* (14), 7820-7827. DOI: <https://doi.org/10.1002/anie.202015179>
- (270) Thümmeler, J. F.; Maragani, R.; Schmitt, F. J.; Tang, G.; Rahmanlou, S. M.; Laufer, J.; Lucas, H.; Mäder, K.; Binder, W. H. Thermoresponsive swelling of photoacoustic single-chain nanoparticles. *Chem. Commun.* **2023**, *59* (76), 11373-11376. DOI: <https://doi.org/10.1039/d3cc03851c>
- (271) Guo, Z.; Park, S.; Yoon, J.; Shin, I. Recent progress in the development of near-infrared fluorescent probes for bioimaging applications. *Chem. Soc. Rev.* **2014**, *43* (1), 16-29. DOI: <https://doi.org/10.1039/c3cs60271k>
- (272) Thümmeler, J. F.; Roos, A. H.; Krüger, J.; Hinderberger, D.; Schmitt, F. J.; Tang, G.; Golmohamadi, F. G.; Laufer, J.; Binder, W. H. Tuning the Internal Compartmentation of Single-Chain Nanoparticles as Fluorescent Contrast Agents. *Macromol. Rapid Commun.* **2023**, *44* (2), e2200618. DOI: <https://doi.org/10.1002/marc.202200618>
- (273) Ali, M. M. S., Harald D. H. Well-Defined Amphiphilic Thermosensitive Copolymers Based on Poly(ethylene glycol monomethacrylate) and Methyl Methacrylate Prepared by Atom Transfer Radical Polymerization. *Macromolecules* **2004**, *37*, 5219-5227. DOI: <https://doi.org/10.1021/ma030485m>
- (274) Kurzbach, D.; Junk, M. J.; Hinderberger, D. Nanoscale inhomogeneities in thermoresponsive polymers. *Macromol. Rapid Commun.* **2013**, *34* (2), 119-134. DOI: <https://doi.org/10.1002/marc.201200617>
- (275) Hunold, J.; Wolf, T.; Wurm, F. R.; Hinderberger, D. Nanoscopic hydrophilic/hydrophilic phase-separation well below the LCST of polyphosphoesters. *Chem. Commun.* **2019**, *55* (23), 3414-3417. DOI: <https://doi.org/10.1039/c8cc09788g>
- (276) Junk, M. J. N.; Li, W.; Schlüter, A. D.; Wegner, G.; Spiess, H. W.; Zhang, A.; Hinderberger, D. EPR Spectroscopy Provides a Molecular View on Thermoresponsive Dendronized Polymers Below the Critical Temperature. *Macromol. Chem. Phys.* **2011**, *212* (12), 1229-1235. DOI: <https://doi.org/10.1002/macp.201100022>

# Curriculum Vitae

Vor- und Zuname: Justus Friedrich Thümmeler (geb. Hoffmann), M.Sc.

Geburtstag: 18.01.1994

Geburtsort: Halle (Saale)

Staatsangehörigkeit: deutsch

## Schulbildung

09/2000 - 08/2004 Grundschule Schönhausen (Elbe)

09/2004 - 12/2008 Diesterweg-Gymnasium Tangermünde

01/2009 - 07/2012 Elisabeth-Gymnasium Halle: Abitur

## Freiwilliges soziales Jahr

09/2012 - 08/2013 reha FLEX Saline Rehabilitationsklinik (Träger des FSJ: DRK Halle)

## Studium

10/2013 - 09/2016 Chemie Bachelor, Martin-Luther-Universität Halle

Bachelorarbeit: „Quantifizierung von primären Aminen an modifizierten superparamagnetischen Eisenoxidnanopartikeloberflächen“

Note Bachelorarbeit: 1,6 (gut)

Abschlussnote Bachelor: 2,0 (gut)

10/2016 - 10/2018 Chemie Master, Martin-Luther-Universität Halle, Vertiefung: Physikalische Chemie

Masterarbeit (Fraunhofer IMWS): „Voltammetrische und mikroanalytische Untersuchungen zur Inhibierung der Korrosion an Kupfer und Kupferlegierungen durch elektrochemisch abgeschiedene Polymerschichten“

Note Masterarbeit: 1,3 (sehr gut)

Abschlussnote Master: 1,4 (sehr gut)

12/2018 - heute      Promotion zum Thema „*Near-Infrared Fluorescent Single-Chain Nanoparticles as Contrast Agents for Photoacoustic Imaging*“

Martin-Luther-Universität Halle Wittenberg, Naturwissenschaftliche Fakultät II, Institut für Chemie, Makromolekulare Chemie

### Stipendium

2018                      Deutschlandstipendium, Förderer: IDT Biologica

### Kenntnisse und Fähigkeiten

- Synthese und Modifizierung magnetischer Nanopartikel
- elektrochemische Synthese leitfähiger Polymere
- organische Synthese
- Polymersynthese (u.a. lebende Polymerisationen, v.a. RAFT)
- Chemische Charakterisierung
  - Magnetresonanz-Spektroskopie (NMR: 1D, 2D, DOSY, Heterokerne; EPR)
  - Optische Spektroskopie (IR, UV/VIS, Fluoreszenz)
  - Chromatographie (DC, LC, GPC)
- Mikroanalytische Methoden
  - DLS
  - Mikroskopie (TEM, REM, AFM)
- Elektrochemische Charakterisierung
  - Cyclovoltammetrie
  - Impedanzspektroskopie

### Wissenschaftliche Veröffentlichung

*Als Erstautor:*

Hoffmann, J. F.; Pulst, M.; Kreßler, J., Enhanced ion conductivity of poly(ethylene oxide)-based single ion conductors with lithium 1,2,3-triazolate end groups *J. Appl. Polym. Sci.* **2019**, 46949 – 46949, DOI: <https://doi.org/10.1002/app.46949>

Hoffmann, J. F.; Roos, A. H.; Schmitt, F.-J.; Hinderberger, D.; Binder, W. H. Fluorescent and Water Dispersible Single-Chain Nanoparticles: Core-Shell Structured Compartmentation, *Angew. Chem. Int. Ed.* **2021**, 60, 7820 – 7827, DOI: <https://doi.org/10.1002/anie.202015179>

Thümmeler, J. F.; Roos, A. H.; Krüger, J.; Hinderberger, D.; Schmitt, F.-J.; Tang, G.; Golmohamadi, F. G.; Laufer, J.; Binder, W. H. Tuning the Internal Compartmentation of Single-Chain Nanoparticles as Fluorescent Contrast Agents, *Macromol. Rapid Commun.* **2023**, *44*, 2200618, DOI: <https://doi.org/10.1002/marc.202200618>

Thümmeler, J. F.; Maragani, R.; Schmitt, F.-J.; Tang, G.; Rahmanlou, S. M.; Laufer, J.; Lucas, H.; Mäder, K.; Binder, W. H. Thermoresponsive swelling of photoacoustic single-chain nanoparticles, *Chem. Commun.* **2023**, DOI: <https://doi.org/10.1039/s3cc03851c>

*Als Coautor:*

Roos, A. H.; Hoffmann, J. F.; Binder, W. H.; Hinderberger, D. Nanoscale structure and dynamics of thermoresponsive single-chain nanoparticles investigated by EPR spectroscopy, *Soft Matter* **2021**, *17*, 7032 – 7037, DOI: <https://doi.org/10.1039/d1sm00582k>

Hilgeroth, P. S.; Thümmeler, J. F.; Binder, W. H. 3D Printing of Triamcinolone Acetonide in Triblock Copolymers of Styrene–Isobutylene–Styrene as a Slow-Release System, *Polymers* **2022**, *14*, 3742, DOI: <https://doi.org/10.3390/polym14183742>

*Konferenzbeiträge:*

Thümmeler, J. F.; Roos, A. H.; Hinderberger, D.; Schmitt, F.-J.; Tang, G.; Golmohamadi, F. G.; Laufer, J.; Binder, W. H., Labeling Single-Chain Nanoparticles: Formation and Benefits of Nanosized Compartments, *Bordeaux Polymer Conference 2022*, Poster

Thümmeler, J. F.; Schmitt, F.-J.; Tang, G.; Rahmanlou, S. M.; Laufer, J.; Binder, W. H., Tuning Photophysical Properties of Fluorescent Single-Chain Nanoparticles with Thermoresponsive Swelling, *Advanced Polymers via Macromolecular Engineering 2023*, Oral Contribution

---

Justus Friedrich Thümmeler

## Eigenständigkeitserklärung

Hiermit erkläre ich an Eides statt, dass ich die vorliegende Arbeit selbstständig und ohne fremde Hilfe verfasst habe. Andere als die angegebenen Quellen und Hilfsmittel wurden nicht benutzt und die den benutzten Werken wörtlich oder inhaltlich entnommenen Stellen wurden als solche kenntlich gemacht.

Außerdem erkläre ich, die vorliegende Dissertation an keiner anderen wissenschaftlichen Einrichtung zur Erlangung eines akademischen Grades eingereicht zu haben.

Halle (Saale), den

---

Justus Friedrich Thümmeler

## Appendix

Supporting Information to: Fluorescent and Water Dispersible Single-Chain Nanoparticles: Core-Shell Structured Compartmentation, *Angew. Chem. Int. Ed.* **2021**, *60*, 7820 - 7827, DOI: <https://doi.org/10.1002/anie.202015179>

Supporting Information to: Tuning the Internal Compartmentation of Single-Chain Nanoparticles as Fluorescent Contrast Agents, *Macromol. Rapid Commun.* **2023**, *44*, 2200618, DOI: <https://doi.org/10.1002/marc.202200618>

Supporting Information to: Thermoresponsive swelling of photoacoustic single-chain nanoparticles, *Chem. Commun.* **2023**, *59*, 11373 - 11376 DOI: <https://doi.org/10.1039/s3cc03851c>

## Supporting Information

### **Fluorescent and Water Dispersible Single-Chain Nanoparticles: Core–Shell Structured Compartmentation**

*Justus F. Hoffmann, Andreas H. Roos, Franz-Josef Schmitt, Dariush Hinderberger, and  
Wolfgang H. Binder\**

anie\_202015179\_sm\_miscellaneous\_information.pdf

SUPPORTING INFORMATION

---

**Table of Contents**

Experimental Procedures.....	3
Chemicals .....	3
Instrumentation and analysis .....	3
Synthesis and sample preparation .....	5
Supporting Figures.....	11
References.....	18

## SUPPORTING INFORMATION

**Experimental Procedures****Chemicals**

All chemicals were purchased from Sigma Aldrich except triethylamine (TCI), 3-chloro-1-propanol (TCI), boron trifluoride diethyl etherate (TCI), *p*-hydroxychalcone (TCI), diazabicyclo[5.4.0]undec-7-ene (Fluka), diethylamine (Fluka), propargyltosylate (Fluka), trimethylsilyl propargyl alcohol (abcr),  $\text{KH}_2\text{PO}_4$  (Roanal),  $\text{K}_2\text{HPO}_4$  (Th. Geyer), nitromethane (Alfa Aesar) and  $\text{CuSO}_4 \times 5 \text{H}_2\text{O}$  (VEB Laborchemikalien). Before use, azobisisobutyronitrile (AIBN) was freshly recrystallized from methanol and poly(ethylene glycol) methyl ether methacrylate ( $M_n=300$ ) was passed through a basic  $\text{AlO}_x$ -column to remove the stabilizer.

**Instrumentation and analysis**

*NMR spectra* were measured on an Agilent Technologies 400 MHz VNMRS and 500 MHz DD2 at 27°C. Chemical shifts ( $\delta$ ) are reported in ppm and referred to the solvent residual signal (CDCl<sub>3</sub> 7.26 ppm for <sup>1</sup>H and 77.0 ppm for <sup>13</sup>C, methanol-d<sub>4</sub> 3.31 ppm for <sup>1</sup>H and 49.0 ppm for <sup>13</sup>C, D<sub>2</sub>O 4.66 ppm for <sup>1</sup>H).

*DOSY measurements* were done on an Agilent VNMR DD2 500 MHz (sfrq = 499.727 MHz). The experiment was performed under OpenVnmrJ 1.1 and equipped with a 5 mm PFG One NMR probe, z-gradient and temperature unit (27 °C). Diffusion ordered NMR data were acquired by means of the Agilent pulse program DgcsteSL\_cc using a stimulated echo with self-compensating gradient schemes and conventional compensation. The length of the gradient pulse was set to 3.0 ms for <sup>1</sup>H in combination with a diffusion period of 300 ms (D<sub>2</sub>O). Data were systematically accumulated by linearly varying the diffusion encoding gradients over a range from 2% to 95% for 64 gradient increment values.

*DLS measurements* were performed on a DLS 802 by Viscotek in 1.5 mL semi-micro cuvettes (PMMA). The laser wavelength was 825 – 832 nm so no interaction between the laser and the dyes can be expected.

AFM measurements were performed on a Multimode AFM (Veeco Instruments Inc., Plainview, NY, USA) equipped with Tapping Mode cantilevers Tap150Al-G (BudgetSensors, Sofia, Bulgaria) with a force constant of 5 N m<sup>-1</sup>, a nominal resonance frequency of 150 kHz, and a radius of <10 nm. The software for the measurement was NanoScope (Veeco Instruments Inc., Plainview, NY, USA) and Gwyddion 2.55 (freeware, <http://gwyddion.net/>) for interpretation.

*ATR-IR spectra* were measured on a Bruker Tensor Vertex 70 equipped with a Golden Gate Heated Diamond ATR Top-plate.

*THF-based SEC measurements* were performed at 30 °C on a Viscotek GPCmax VE 2001 from Viscotek™ applying a CLM3008 precolumn and a CLM3008 main column. As solvent THF was used and the sample concentration was adjusted to 3 mg·mL<sup>-1</sup> while applying a flow rate of 1 mL·min<sup>-1</sup>. For determination of the molecular weights the refractive index of the investigated sample was detected with a VE 3580 RI detector of Viscotek™. External calibration was done using poly(styrene) (PS) standards (purchased from PSS) with a molecular weight range from 1050 to 115000 g mol<sup>-1</sup>.

*Water-based SEC measurements* were performed at 25 °C on a Viscotek GPCmax VE 2001 from Viscotek™ applying a PSS SUPREMA 5 μm precolumn and a PSS SUPREMA analytical Linear M 5 μm main column. As solvent water (0.05 % NaN<sub>3</sub>, 0.1 M NaCl) was used while applying a flow rate of 1 mL·min<sup>-1</sup>. The sample was detected with a VE 3580 RI detector of Viscotek™ and a UV Detector Knauer Azura UVD 2.19 .

## SUPPORTING INFORMATION

*EPR measurements* were done with the Miniscope MS 5000 and the MS 5000 temperature controller (magnettech GmbH, Berlin, Germany). By using the Freiberg Instruments software the spectra are measured with a sweep width of 10 mT, a modulation amplitude of 0.02 mT, a digital RC filter with a time constant of 0.2 s and a microwave attenuation of 20 dB. Each spectrum represents an accumulation of 3 scans. The samples were prepared in Rotilabo® sample vials and convicted for measuring in Blaubrandts Micropipettes. For the TEMPO probe experiments TEMPO concentrations of 100  $\mu\text{M}$  were used. The spectra were analysed with the EasySpin package version 5.2.27 for MatLab (Mathworks, Inc.)

*UV/VIS/NIR-absorption measurements* were performed on a Perkin Elmer LAMBDA 365 UV/Vis Spectrophotometer using Helma analytics quartz glass cuvettes (d = 10 mm).

*Fluorescence spectra* were measured on a Cary Eclipse fluorescence spectrometer of Agilent using Helma analytics quartz glass cuvettes (d = 10 mm).

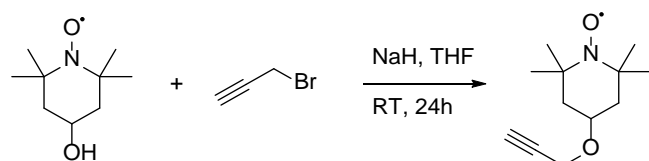
*Turbidimetry measurements* were performed using a MP80 Melting Point System by Mettler Toledo. The heating rate was 1 K/min. The polymer concentration was 1 mg/mL.

*Decay associated spectra* were recorded employing a Hamamatsu R5900 16-channel multi-anode photomultiplier tube (PMT) with 16 separate output (anode) elements and a common cathode and dynode system (PML-16C, Becker&Hickl, Berlin, Germany) as described in Schmitt et al. 2020. A 632 nm pulsed laser diode (PDL-600, Becker&Hickl, Berlin) delivering 80 ps FWHM pulses at a repetition rate of 20 MHz was used for excitation. The fluorescence was observed via a 633 nm longpass filter (F76-631, AHF Analysentechnik, Tübingen, Germany). The determination of the DAS is described in detail in Schmitt et al. 2019.

## SUPPORTING INFORMATION

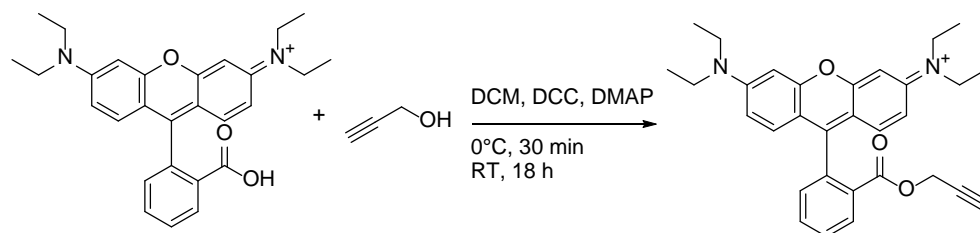
## Synthesis and sample preparation

## Synthesis of TEMPO-alkyne



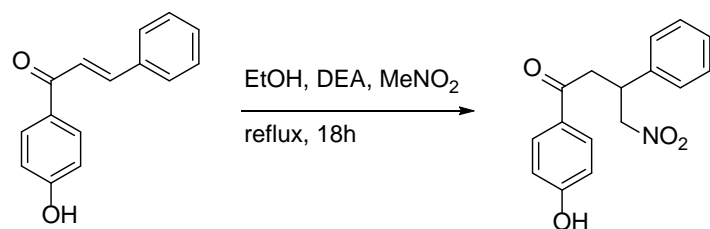
Sodium hydride (60% suspension in mineral oil, 10 mmol, 400 mg) was placed in a Schlenk flask under nitrogen atmosphere and 20 mL of dry THF were added. A solution of *p*-hydroxy-TEMPO (8.71 mmol, 1.5 g) in 5 mL of dry THF was added slowly to the stirring suspension at 0°C. After stirring for 30 min at 0°C propargyl bromide (80% solution in toluene, 11 mmol, 1.0 mL) was added dropwise. The solution was stirred at room temperature for one day and then poured into 150 mL of ice water. The product was extracted with ethyl acetate. The combined organic phases were again washed with water and brine, dried over Na<sub>2</sub>SO<sub>4</sub>, filtered and evaporated under vacuum. The residue was purified by column chromatography (ethyl acetate: hexane 1:2, R<sub>f</sub> = 0.45) to get the product as an orange powder. Yield: 71%. <sup>1</sup>H-NMR (CDCl<sub>3</sub>, 400 MHz, δ in ppm): 4.11 (s, 2H, OCH<sub>2</sub>), 2.46 (s, 1H, ≡CH) (due to paramagnetic broadening of the nitroxide radical not all signals were observable).

## Synthesis of Rhodamine B propargyl ester (RhoB-alkyne)



Rhodamine B (1 mmol, 146 mg), dicyclohexylcarbodiimide (1.1 mmol, 226.96 mg) and propargyl alcohol (1.1 mmol, 61.67 mg, 63.5 μL) were dissolved in dry DCM (5 mL) in a Schlenk tube under nitrogen atmosphere. The tube was wrapped in aluminium foil and put into an ice bath. 4-(Dimethylamino)-pyridine (0.2 mmol, 24.43 mg) was added. The reaction mixture was stirred at 0°C for 30 min and at room temperature over night. The colourless precipitate was removed by filtration and washed with DCM. The DCM was removed in vacuum. The crude product was dissolved in ACN, filtered and dried under vacuum. The product was purified by column chromatography (methanol:chloroform 1:5, R<sub>f</sub> = 0.4) to get the product as a golden powder. Yield: 40%. <sup>1</sup>H-NMR (CDCl<sub>3</sub>, 500 MHz, δ in ppm): 8.31 (1H, m, H<sub>Ar</sub>), 7.84 (1H, m, H<sub>Ar</sub>), 7.75 (1H, m, H<sub>Ar</sub>), 7.35 (1H, m, H<sub>Ar</sub>), 7.06 (2H, m, H<sub>Ar</sub>), 6.91 (2H, m, H<sub>Ar</sub>), 6.86 (2H, m, H<sub>Ar</sub>), 4.61 (2H, d, J = 2.4 Hz, OCH<sub>2</sub>), 3.63 (8H, q, J = 7.2 Hz, N-CH<sub>2</sub>CH<sub>3</sub>), 2.45 (1H, t, J = 2.4 Hz, ≡CH), 1.33 (12H, t, J = 7.2 Hz, CH<sub>3</sub>).

## Synthesis of 1-(4-Hydroxyphenyl)-4-nitro-3-phenylbutan-1-one (aBOD1)

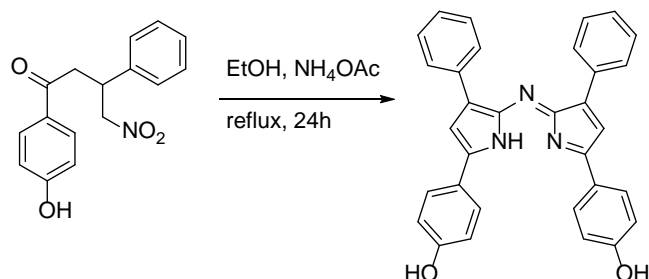


Dimethylamine (45 mmol, 3.02 g, 4.6 mL) and nitromethane (90 mmol, 5.5 g, 4.8 mL) were added to a solution of 4'-hydroxychalcone (9 mmol, 2.02 g) in 15 mL ethanol. The mixture was stirred under reflux for 18 h. The solution was cooled and acidified with 0.1 M HCl. The product was extracted with ethyl acetate and washed with 0.1 M HCl. The organic layer was dried and evaporated under vacuum. The product was purified by column chromatography (DCM:methanol 20:1, R<sub>f</sub> = 0.42) to get the

## SUPPORTING INFORMATION

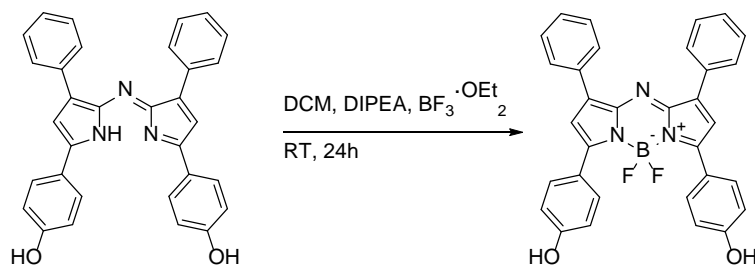
product as colourless solid. Yield: 92%.  $^1\text{H-NMR}$  ( $\text{CDCl}_3$ , 500 MHz,  $\delta$  in ppm): 7.86 (2H, m,  $H_{Ar}$ ), 7.33 (2H, m,  $H_{Ar}$ ), 7.27 (3H, m,  $H_{Ar}$ ), 6.86 (2H, m,  $H_{Ar}$ ), 5.48 (1H, s (broad), OH), 4.92-4.60 (2H, m,  $\text{NO}_2\text{-CH}_2$ ), 4.21 (1H, m, Ph-CH), 3.39 (2H, m,  $\text{O=C-CH}_2$ ).

Synthesis of 5-(4-Hydroxyphenyl)-3-phenyl-1H-pyrrol-2-yl]-[5-(4-hydroxyphenyl)-3-phenylpyrrol-2-ylidene]amine (aBOD2)



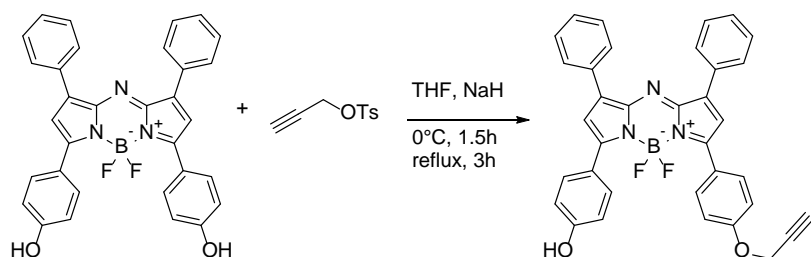
Ammonium acetate (140 mmol, 10.8 g) and aBOD1 (4.2 mmol, 1.2 g) were solved in ethanol (40 mL) and stirred under reflux for 24 h. After cooling to room temperature water (50 mL) was added and the ethanol removed under reduced pressure. The precipitate was filtered and solved in ethyl acetate. The aqueous filtrate was extracted with ethyl acetate. The combined organic layers were dried with  $\text{Na}_2\text{SO}_4$  and the solvent removed under reduced pressure. The product was purified by column chromatography (chloroform:methanol 10:1,  $R_f = 0.44$ ) to get the product as dark blue solid. Yield: 33%.  $^1\text{H-NMR}$  (methanol- $d_4$ , 500 MHz,  $\delta$  in ppm): 8.05 (4H, m,  $H_{Ar}$ ), 7.88 (4H, m,  $H_{Ar}$ ), 7.39 (4H, m,  $H_{Ar}$ ), 7.32 (2H, m,  $H_{Ar}$ ), 7.26 (2H, s,  $H_{Ar}$ ), 6.97 (4H, m,  $H_{Ar}$ ).

Synthesis of  $\text{BF}_2$  Chelate of [5-(4-hydroxyphenyl)-3-phenyl-1H-pyrrol-2-yl]-[5-(4-hydroxyphenyl)-3-phenylpyrrol-2-ylidene]amine (aBOD3)



A solution of aBOD2 (0.7 mmol, 340 mg) in dry DCM (25 mL) was treated with DIPEA (7 mmol, 0.9 g, 1.2 mL) and placed in an ice bath.  $\text{BF}_3\cdot\text{OEt}_2$  (10.5 mmol, 1.49 g, 1.3 mL) was added slowly, the ice bath was removed, and the resulting reaction mixture was stirred at room temperature for 24 h. The solution was diluted with ethyl acetate, washed with water and brine, dried with  $\text{Na}_2\text{SO}_4$  and the solvent was evaporated under vacuum. The product was purified by column chromatography (ethyl acetate:hexane 1:1,  $R_f = 0.36$ ) to get the product as dark red solid. Yield: 65%.  $^1\text{H-NMR}$  (methanol- $d_4$ , 500 MHz,  $\delta$  in ppm): 8.15-8.07 (8H, m,  $H_{Ar}$ ), 7.49-7.39 (6H, m,  $H_{Ar}$ ), 7.28 (1H, s,  $H_{Ar}$ ), 6.92 (4H, m,  $H_{Ar}$ ).

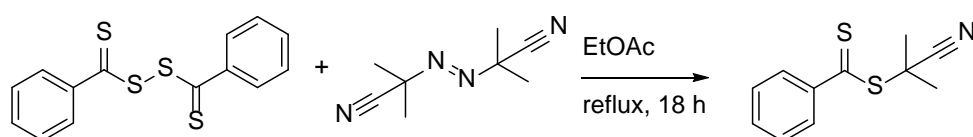
Synthesis of  $\text{BF}_2$  Chelate of 4-{4-phenyl-5-[3-phenyl-5-(4-prop-2-ynoxyphenyl)-pyrrol-2-ylideneamino]-1H-pyrrol-2-yl}phenol (aBOD)



## SUPPORTING INFORMATION

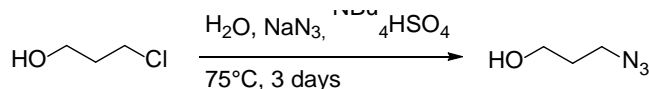
Sodium hydride (60% suspension in mineral oil, 1.125 mmol, 45 mg) and aBOD3 (0.45 mmol, 240 mg) were placed in a flask and dry THF (10 mL) was added. The stirring suspension was placed in an ice bath and propargyl tosylate (0.99 mmol, 208.15 mg, 168.95  $\mu$ L) in THF (5 mL) was added. After 1.5 h the ice bath was removed, and the reaction mixture was stirred under reflux for 3 hours. The reaction was quenched with H<sub>2</sub>O and the product extracted with ethyl acetate. The product solution was dried with Na<sub>2</sub>SO<sub>4</sub> and the solvent evaporated under vacuum. The product was purified by column chromatography (ethyl acetate:hexane 2:1, R<sub>f</sub> = 0.65) to get the product as dark red solid. Yield: 23%. <sup>1</sup>H-NMR (CDCl<sub>3</sub>, 500 MHz,  $\delta$  in ppm): 8.12-8.03 (8H, m, *H<sub>Ar</sub>*), 7.50-7.40 (6H, m, *H<sub>Ar</sub>*), 7.11 (2H, m, *H<sub>Ar</sub>*), 7.05 (2H, s, *H<sub>Ar</sub>*), 6.96 (2H, m, *H<sub>Ar</sub>*), 5.26 (1H, s (broad), OH), 4.79 (2H, d, J = 2.4 Hz, O-CH<sub>2</sub>), 2.58 (1H, t, J = 2.4 Hz,  $\equiv$ CH).

#### Synthesis of Cyanoisopropyl dithiobenzoate (CPDB)



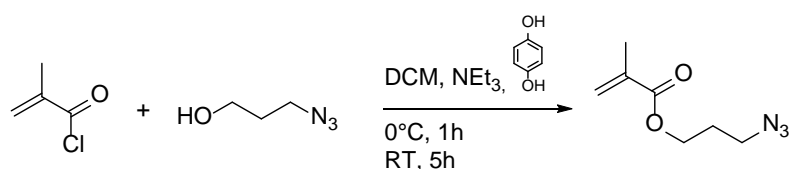
Bis(thiobenzoyl) disulfide (0.8 mmol, 245.2 mg) and AIBN (1.2 mmol, 197.1 mg) were solved in 10 mL ethyl acetate. The solution was degassed by five freeze-pump-thaw cycles and stirred under reflux for 18 h. The crude product was dried under vacuum and purified by column chromatography (hexane:ethyl acetate 10:1, R<sub>f</sub> = 0.27) to get the product as a red oil. Yield: 56%. <sup>1</sup>H-NMR (CDCl<sub>3</sub>, 400 MHz,  $\delta$  in ppm): 7.92 (2H, m, *o-H<sub>Ar</sub>*), 7.56 (1H, m, *p-H<sub>Ar</sub>*), 7.39 (2H, m, *m-H<sub>Ar</sub>*), 1.94 (6H, s, CH<sub>3</sub>).

#### Synthesis of 3-Azido-1-propanol (APOH)



3-Chloro-1-propanol (23.5 mmol, 2.2 g, 2 mL) was added dropwise to a solution of sodium azide (48 mmol, 3.13 g) and tetrabutylammonium hydrogen sulphate (0.2 mmol, 70 mg) in 50 mL water at room temperature. The resulting solution was heated to 75°C. After stirring for three days the product was extracted with DCM. The combined organic phases were dried with Na<sub>2</sub>SO<sub>4</sub> and the solvent evaporated under vacuum to get the product as a colourless liquid. Yield: 85%. <sup>1</sup>H-NMR (CDCl<sub>3</sub>, 400 MHz,  $\delta$  in ppm): 3.71 (2H, t, J = 6.0 Hz, HO-CH<sub>2</sub>), 3.42 (2H, t, J = 6.6 Hz, CH<sub>2</sub>-N<sub>3</sub>), 2.21 (1H, s, OH), 1.80 (2H, tt, J = 6.6, 6.0 Hz, CH<sub>2</sub>CH<sub>2</sub>CH<sub>2</sub>).

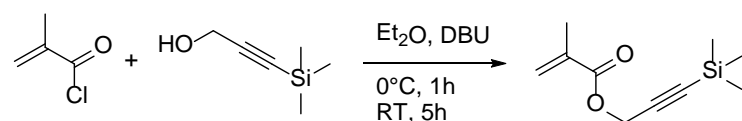
#### Synthesis of 3-Azidopropyl methacrylate (APMA)



APOH (19.3 mmol, 1.95 g, 1.8 mL), triethylamine (28.7 mmol, 2.9 g, 4 mL) and hydroquinone (10  $\mu$ mol, 1 mg) were solved in 25 mL of dry DCM and placed in an ice bath. Methacryloyl chloride (28.7 mmol, 3 g, 2.8 mL) in 5 mL of dry DCM was added dropwise. The resulting solution was stirred at 0°C for 1 h and at room temperature for additional 5 h. The white precipitate was removed by filtration and the product solution washed with water, saturated sodium bicarbonate solution and brine. The organic phase was dried with Na<sub>2</sub>SO<sub>4</sub> and the solvent was removed under vacuum. The product was purified by column chromatography (hexane:diethyl ether 2:1, R<sub>f</sub> = 0.46) to get the product as a pale-yellow liquid. The product was stored with hydroquinone as stabilizer. Yield: 25%. <sup>1</sup>H-NMR (CDCl<sub>3</sub>, 500 MHz,  $\delta$  in ppm): 6.11 (1H, dq, J = 2.0, 1.0, =CH), 5.58 (1H, dq, J = 2.0, 1.6 Hz, =CH), 4.24 (2H, t, J = 6.2 Hz, COO-CH<sub>2</sub>), 3.42 (2H, t, J = 6.7 Hz, CH<sub>2</sub>-N<sub>3</sub>), 1.96 (2H, tt, J = 6.7, 6.2 Hz, CH<sub>2</sub>CH<sub>2</sub>CH<sub>2</sub>), 1.95 (3H, dd, J = 1.6, 1.0 Hz, CH<sub>3</sub>).

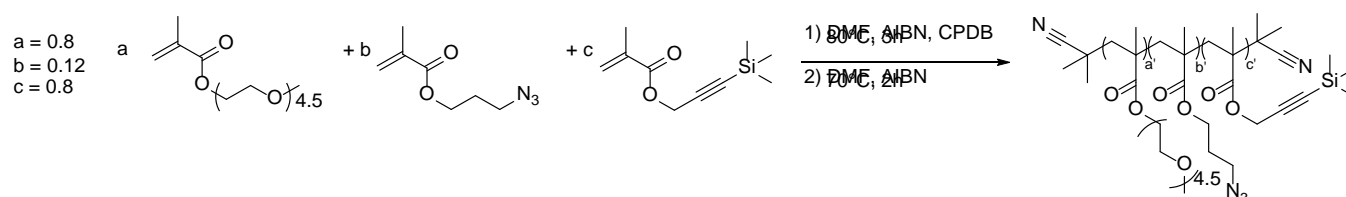
## SUPPORTING INFORMATION

## Synthesis of 3-(Trimethylsilyl)propargyl methacrylate (TMSPMA)



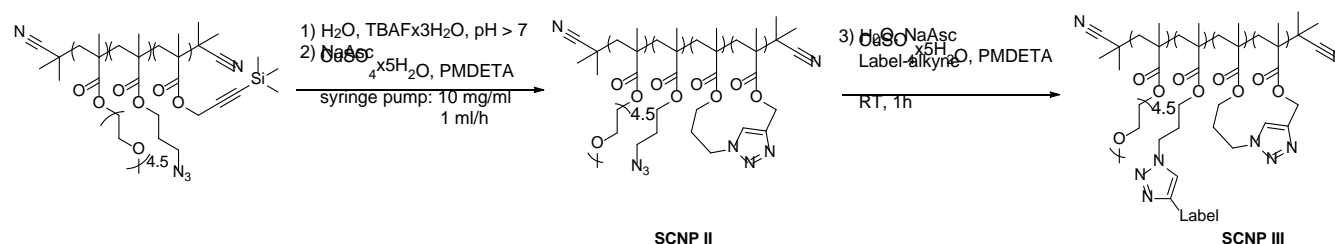
3-(Trimethylsilyl)propargyl alcohol (15.58 mmol, 2.0 g, 2.15 mL) and 1,8-diazabicyclo[5.4.0]undec-7-ene (18.7 mmol, 1.42 g, 1.4 mL) were solved in 20 mL of dry diethyl ether and cooled to 0°C. Methacryloyl chloride (18.7 mmol, 1.95 g, 1.8 mL) in 10 mL of dry diethyl ether was added dropwise. The resulting solution was stirred at 0°C for 1 h and at room temperature for additional 5 h. The yellow precipitate was removed by filtration and the product solution washed with water and brine. The organic phase was dried with Na<sub>2</sub>SO<sub>4</sub> and the solvent was removed under vacuum. The product was purified by column chromatography (hexane:diethyl ether 20:1, R<sub>f</sub> = 0.19) to get the product as colourless liquid. Yield: 30%. <sup>1</sup>H-NMR (CDCl<sub>3</sub>, 400 MHz, δ in ppm): 6.17 (1H, dq, J = 1.0, 2.2 Hz, =CH), 5.61 (1H, dq, J = 1.6, 2.2 Hz, =CH), 4.76 (2H, s, OCH<sub>2</sub>), 1.96 (3H, dd, J = 1.6, 1.0 Hz, CH<sub>3</sub>), 0.18 (9H, s, Si(CH<sub>3</sub>)<sub>3</sub>).

## Synthesis of Poly[(poly(ethylene glycol) methyl ether methacrylate)-co-(3-azidopropyl methacrylate)-co-(3-(trimethylsilyl)propargyl methacrylate)] (Polymer I)



Poly(ethylene glycol) methyl ether methacrylate (M<sub>n</sub>=300) (4.8 mmol, 1.44 g), APMA (0.72 mmol, 121.8 mg, 113.8 μL) and TMSPMA (0.48 mmol, 94.2 mg, 101.3 μL) were solved in 1 mL dry DMF in a Schlenk tube. 1 mL of a stock solution of CPDB (20 mM) and AIBN (4 mM) was added to the solution. The resulting mixture was degassed by five freeze-pump-thaw cycles and stirred at 80°C for 3 h. The product was precipitated in cold hexane:diethyl ether (2:1) as a pink polymer. To remove the RAFT-endgroup, the polymer was solved in DMF, 10 mg of AIBN were added and the solution degassed by bubbling with N<sub>2</sub>. The solution was stirred at 70°C for 2 h. The product was again precipitated in cold hexane:diethyl ether (2:1). The resulting yellow polymer was purified by dialysis in THF. The highly viscous product was stored in DCM at 5°C to prevent auto crosslinking. Yield: 52%. GPC (THF): M<sub>n</sub> = 36.1 kDa, M<sub>n</sub>/M<sub>w</sub> = 1.7. <sup>1</sup>H-NMR (CDCl<sub>3</sub>, 500 MHz, δ in ppm): 4.66-4.55 (CH<sub>2</sub>-≡-Si(CH<sub>3</sub>)<sub>3</sub>), 4.25-3.90 (COOCH<sub>2</sub>), 3.82-3.49 (OCH<sub>2</sub>CH<sub>2</sub>O), 3.48-3.43 (N<sub>3</sub>CH<sub>2</sub>), 3.39 (OCH<sub>3</sub>), 2.07-1.72 (CH<sub>2</sub>), 1.12-0.77 (CH<sub>3</sub>), 0.20 (Si(CH<sub>3</sub>)<sub>3</sub>). IR (KBr): 2178 cm<sup>-1</sup> (ν<sub>alkyne</sub>), 2100 cm<sup>-1</sup> (ν<sub>N3</sub>). Because of peak overlapping, the found values for a', b' and c' were approximated by peak integraion to be 0.83, 0.1 and 0.07 (see Figure S1c)

## Synthesis of unlabelled single-chain nanoparticles (SCNP II) and labelled single chain nanoparticles (SCNP III)

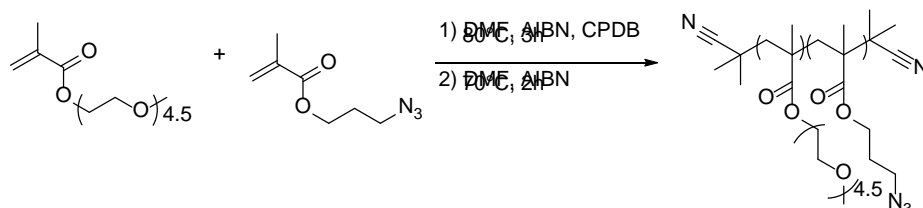


Polymer I (200 mg) and sodium ascorbate (300 mg, 1.5 mmol) were solved in 19 mL degassed H<sub>2</sub>O. A solution of TBAF x 3 H<sub>2</sub>O (116 μmol, 36.57 mg) and PMDETA (48 μmol, 8.3 mg, 10 μL) in 1 mL degassed H<sub>2</sub>O was added. The resulting solution was put into a syringe pump (1 mL/h) and added to a solution of sodium ascorbate (2.76 mmol, 574.22 mg), CuSO<sub>4</sub> x 5 H<sub>2</sub>O

## SUPPORTING INFORMATION

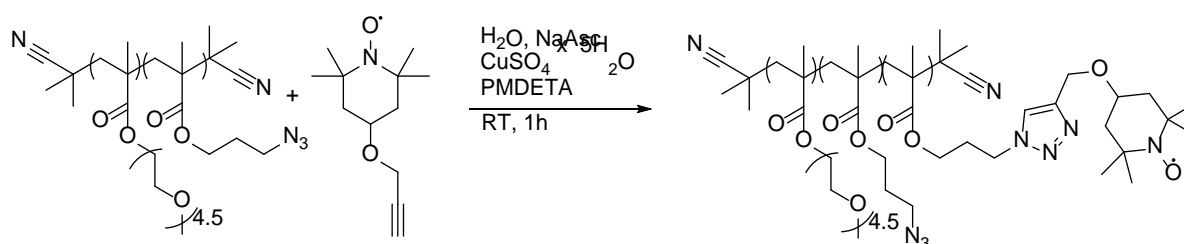
(0.29 mmol, 72.37 mg) and PMDETA (0.58 mmol, 100 mg, 121  $\mu$ L) in 100 mL degassed H<sub>2</sub>O. After 20 h the solution was stirred for one additional hour. To label the resulting SCNPs a solution of sodium ascorbate (0.5 mmol, 100 mg) in 5 mL degassed H<sub>2</sub>O was added to the reaction mixture. After 10 min a solution of 15-20 mg label in 5 mL THF was added and the reaction mixture was stirred for 2 h. The product was extracted with DCM. The DCM was evaporated under vacuum and the solid product was washed multiple times first with THF/PMDETA then with THF and dried under vacuum. Yield: 54%. <sup>1</sup>H-NMR (D<sub>2</sub>O, 500 MHz,  $\delta$  in ppm): 4.32-3.90 (COOCH<sub>2</sub>), 3.82-3.38 (OCH<sub>2</sub>CH<sub>2</sub>O), 3.30 (OCH<sub>3</sub>), 2.07-1.66 (CH<sub>2</sub>), 1.14-0.58 (CH<sub>3</sub>).

*Synthesis of Poly[(poly(ethylene glycol) methyl ether methacrylate)-co-(3-azidopropyl methacrylate)] (Polymer I')*



Poly(ethylene glycol) methyl ether methacrylate (M<sub>n</sub>=300) (3.33 mmol, 1 g) and APMA (0.55 mmol, 107 mg, 100  $\mu$ L) were solved in 1 mL dry DMF in a Schlenk tube. 1 mL of a stock solution of CPDB (20 mM) and AIBN (4 mM) was added to the solution. The resulting mixture was degassed by five freeze-pump-thaw cycles and stirred at 80°C for 3 h. The product was precipitated in cold hexane:diethyl ether (2:1) as a pink polymer. To remove the RAFT-endgroup, the polymer was solved in DMF, 10 mg of AIBN were added and the solution degassed by bubbling with N<sub>2</sub>. The solution was stirred at 70°C for 2 h. The product was again precipitated in cold hexane:diethyl ether (2:1). The resulting yellow, highly viscous polymer was purified by dialysis in THF. Yield: 51%. GPC (THF): M<sub>n</sub> = 18.2 kDa, M<sub>n</sub>/M<sub>w</sub> = 1.4. <sup>1</sup>H-NMR (CDCl<sub>3</sub>, 500 MHz,  $\delta$  in ppm): 4.25-3.90 (COOCH<sub>2</sub>), 3.82-3.47 (OCH<sub>2</sub>CH<sub>2</sub>O), 3.48-3.40 (N<sub>3</sub>CH<sub>2</sub>), 3.37 (OCH<sub>3</sub>), 2.07-1.67 (CH<sub>2</sub>), 1.09-0.77 (CH<sub>3</sub>).

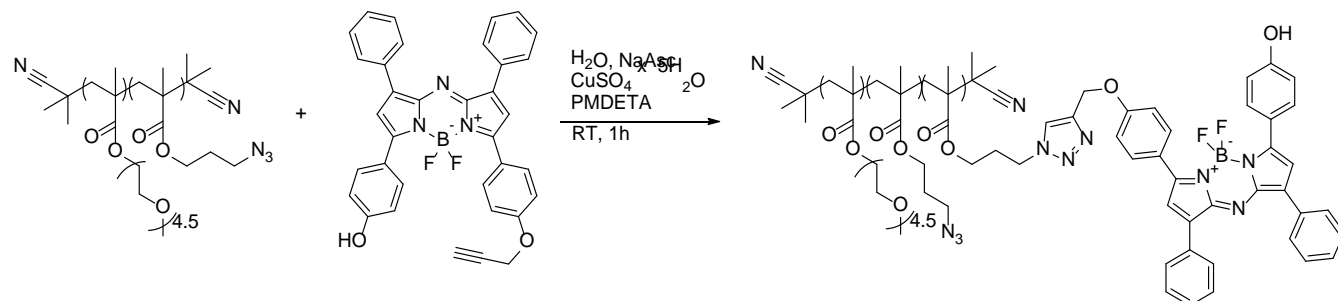
*Synthesis of Poly[(poly(ethylene glycol) methyl ether methacrylate)-co-(3-azidopropyl methacrylate)-co-(TEMPO-labelled methacrylate)] (Polymer I'a)*



Polymer I' (50 mg, 25  $\mu$ mol of N<sub>3</sub>), TEMPO-alkyne (12.5  $\mu$ mol, 2.62 mg) and sodium ascorbate (37.5  $\mu$ mol, 7.4 mg) were solved in a mixture of 10 mL THF and 20 mL degassed H<sub>2</sub>O. A solution of CuSO<sub>4</sub> x 5 H<sub>2</sub>O (7.5  $\mu$ mol, 1.9 mg) and PMDETA (15  $\mu$ mol, 2.6 mg, 3.13  $\mu$ L) in 5 mL degassed H<sub>2</sub>O was added and the resulting mixture was stirred at room temperature. After 1 h the product was extracted with DCM, dried with Na<sub>2</sub>SO<sub>4</sub> and the solvent removed under vacuum. The product was cleaned by dialysis in THF to get an orange polymer. Yield: 80%. <sup>1</sup>H-NMR (CDCl<sub>3</sub>, 500 MHz,  $\delta$  in ppm): 5.10 (triazole-CH), 4.25-3.90 (COOCH<sub>2</sub>), 3.82-3.47 (OCH<sub>2</sub>CH<sub>2</sub>O), 3.48-3.40 (N<sub>3</sub>CH<sub>2</sub>), 3.37 (OCH<sub>3</sub>), 2.07-1.67 (CH<sub>2</sub>), 1.09-0.77 (CH<sub>3</sub>).

## SUPPORTING INFORMATION

Synthesis of Poly[(poly(ethylene glycol) methyl ether methacrylate)-co-(3-azidopropyl methacrylate)-co-(aBOD-labelled methacrylate)] (Polymer I'c)



Polymer I' (50 mg, 25  $\mu\text{mol}$  of  $\text{N}_3$ ), aBOD (12.5  $\mu\text{mol}$ , 7.09 mg) and sodium ascorbate (37.5  $\mu\text{mol}$ , 7.4 mg) were solved in a mixture of 10 mL THF and 10 mL degassed  $\text{H}_2\text{O}$ . A solution of  $\text{CuSO}_4 \cdot 5\text{H}_2\text{O}$  (7.5  $\mu\text{mol}$ , 1.9 mg) and PMDETA (15  $\mu\text{mol}$ , 2.6 mg, 3.13  $\mu\text{L}$ ) in 5 mL degassed  $\text{H}_2\text{O}$  was added and the resulting mixture was stirred at room temperature. After 1 h the product was extracted with DCM, dried with  $\text{Na}_2\text{SO}_4$  and the solvent removed under vacuum. The product was cleaned by dialysis in THF to get a green polymer. Yield: 64%.  $^1\text{H-NMR}$  ( $\text{CDCl}_3$ , 500 MHz,  $\delta$  in ppm): 8.03 ( $H_{Ar}$ ), 7.41 ( $H_{Ar}$ ), 7.05 ( $H_{Ar}$ ), 6.95 ( $H_{Ar}$ ), 5.26 (triazole-CH), 4.49 (triazole- $\text{CH}_2\text{-O}$ ), 4.25-3.90 ( $\text{COOCH}_2$ ), 3.87-3.47 ( $\text{OCH}_2\text{CH}_2\text{O}$ ), 3.47-3.41 ( $\text{N}_3\text{CH}_2$ ), 3.38 ( $\text{OCH}_3$ ), 2.11-1.59 ( $\text{CH}_2$ ), 1.14-0.67 ( $\text{CH}_3$ ).

#### Solving aBOD in water

aBOD (10  $\mu\text{mol}$ , 5.67 mg) was solved in dry THF (2 mL) and Kolliphor EL (0.2 mL) was added. The resulting solution was ultrasonicated for 1 h. The THF was removed under vacuum and the residue was solved in 25 mL water to get a dark green solution.

#### Dispersing of SCNPs in water

The solid (agglomerated) SCNP were placed in a vial and water was added. The suspension was stirred for 18 h until a milky dispersion was formed. The resulting dispersion was ultrasonicated for several hours until it was clear. It is important for the temperature not to rise higher than  $50^\circ\text{C}$ . The SCNPs show LCST-behaviour in water and will not solubilize then.

#### Absorption and fluorescence measurements of aBOD

Since aBOD is a pH-responding dye, the absorption and fluorescence measurements were made in phosphate buffered water. As buffer potassium dihydrogen phosphate and potassium hydrogenphosphate were dissolved in water in a ratio that a 2 M solution of the wanted pH-value was achieved. For the measurements, 20  $\mu\text{L}$  of a dye solution was mixed with 1980  $\mu\text{L}$  of the aqueous buffer.

## SUPPORTING INFORMATION

## Supporting Figures

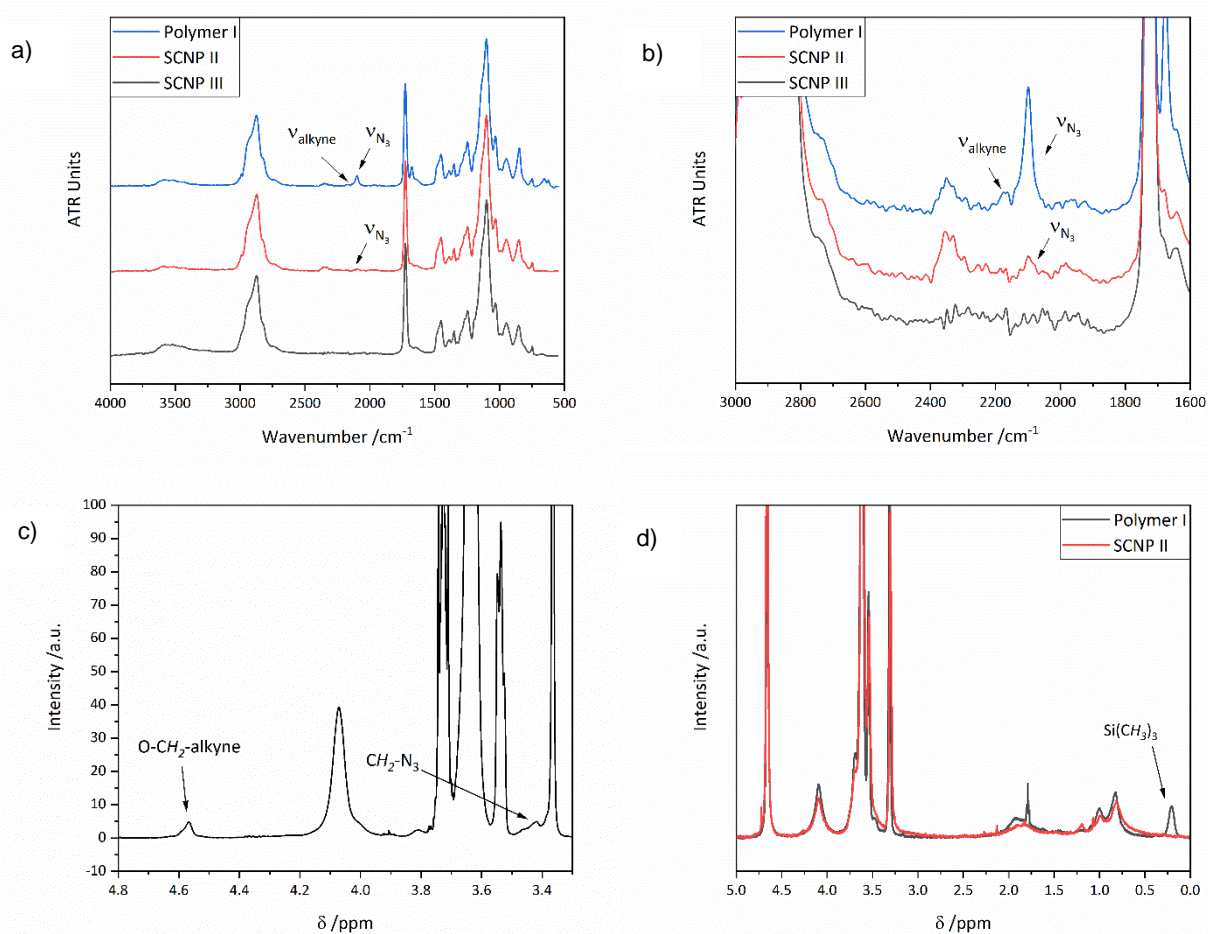


**Figure S1.** Proof of crosslink reaction. Comparison of ATR-IR-spectra of **Polymer I**, **SCNP II**, and **SCNP III** a) complete spectra, b) bands of the reactive groups. c)  $^1\text{H-NMR}$  of **Polymer I** in  $\text{CDCl}_3$ . d) Comparison of  $^1\text{H-NMR}$ -spectra of **Polymer I** and **SCNP II** in  $\text{D}_2\text{O}$ .

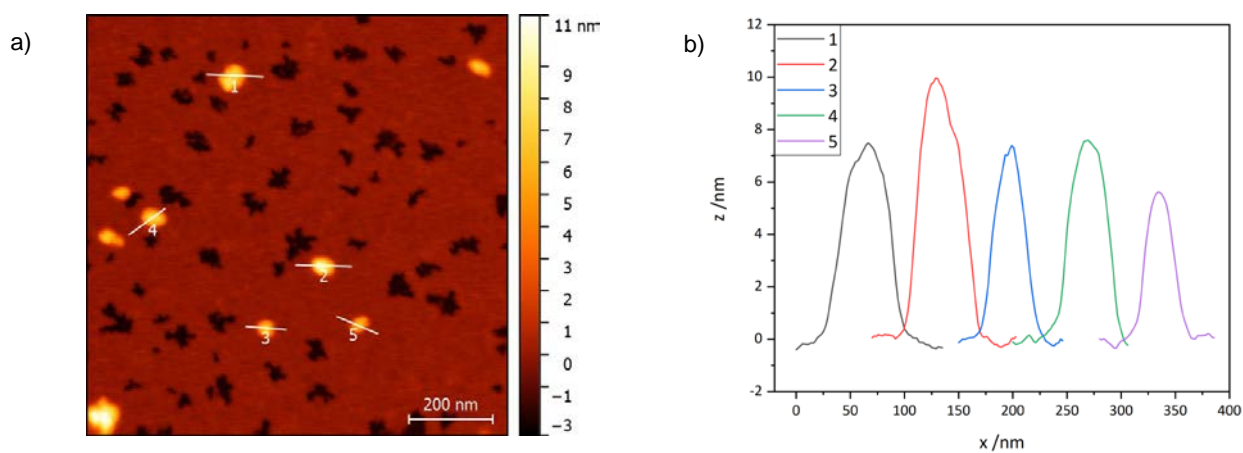


**Figure S2.** a) 2D AFM topography image of **SCNP IIIb** (1 x 1  $\mu\text{m}$ ). b) Height profile of the highlighted particles.

## SUPPORTING INFORMATION

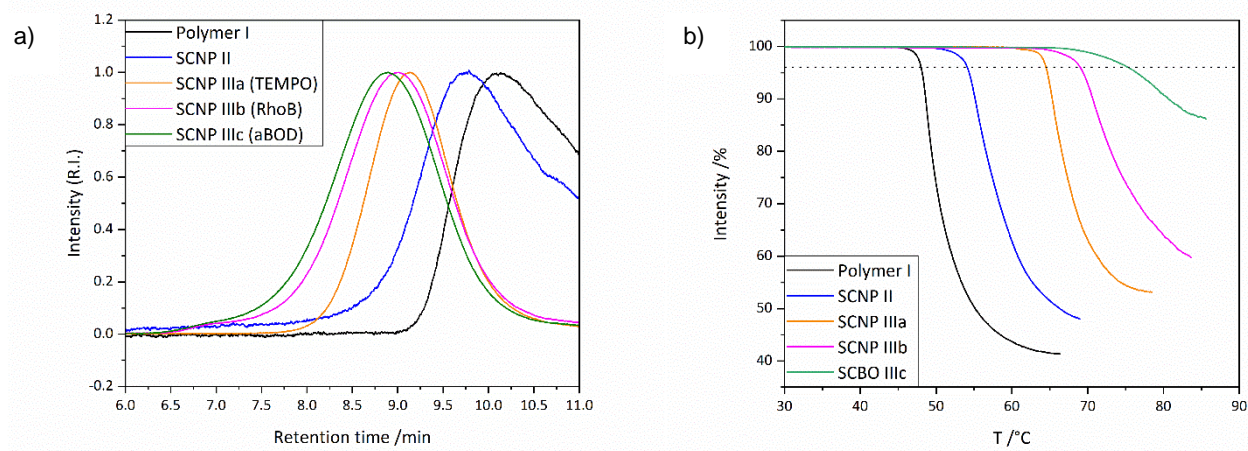


**Figure S3.** a) Water based SEC traces (R.I. detector) of **polymer I**, the unlabelled **SCNP II** and labelled **SCNP IIIa-c**. The peaks were normalized to the peak maxima. The complete and non-normalized chromatograms are depicted in Figure S4. b) Turbimetry measurements of **polymer I**, the unlabelled **SCNP II** and labelled **SCNP IIIa-c** in water. The polymer and nanoparticle concentrations were 1 mg/mL.  $T_{cp}$  was set as the temperature at which the light intensity was decreased to 96%.

## SUPPORTING INFORMATION

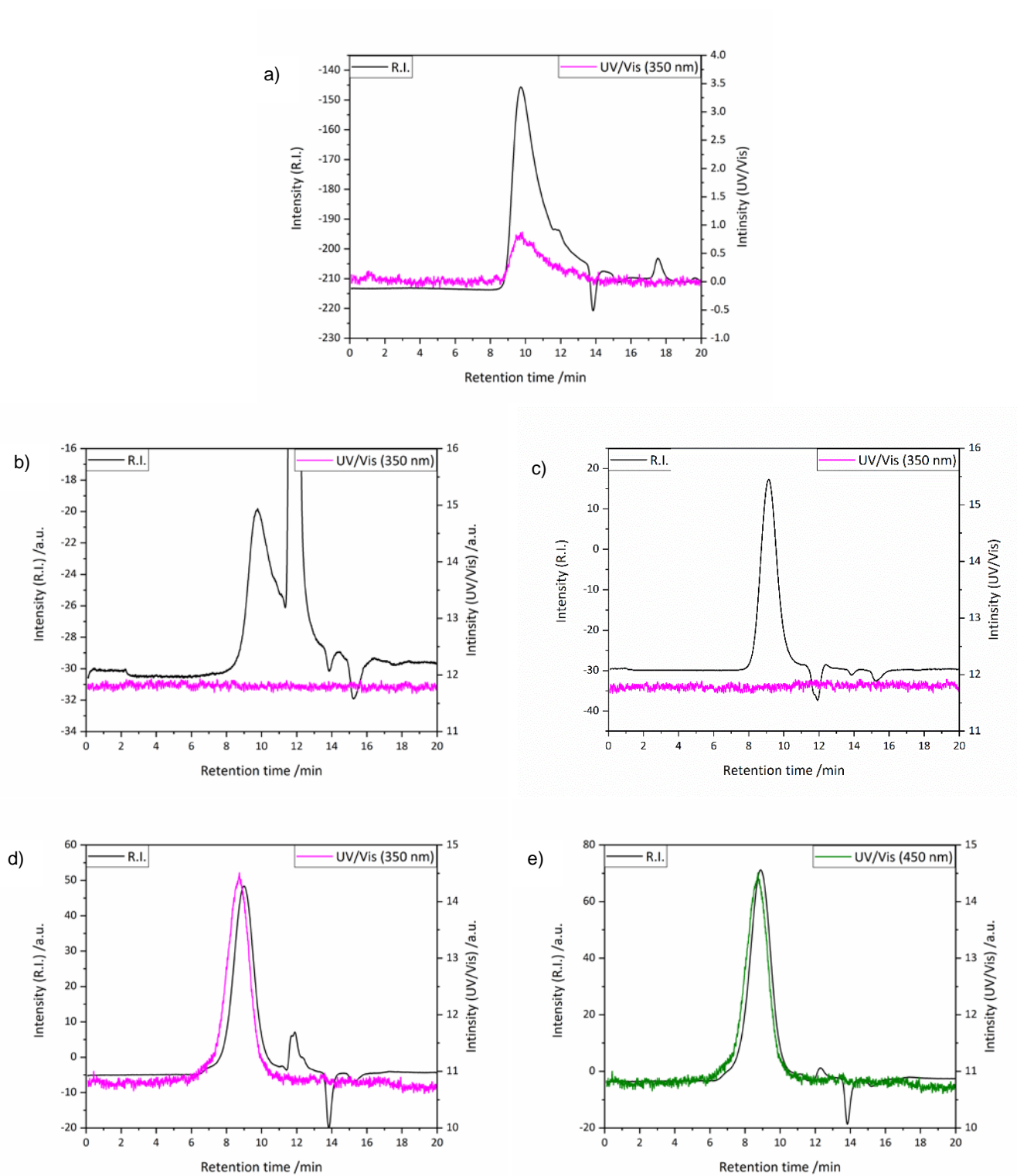


**Figure S4.** R.I. and UV/Vis traces of the GPC measurements in water of a) polymer I, b) the unlabelled SCNP II, c) the TEMPO labelled SCNP IIIa, d) the RhoB-labelled SCNP IIIb, and e) the aBOD-labelled SCNP IIIc. The system peaks start at 11.2 min.



## SUPPORTING INFORMATION

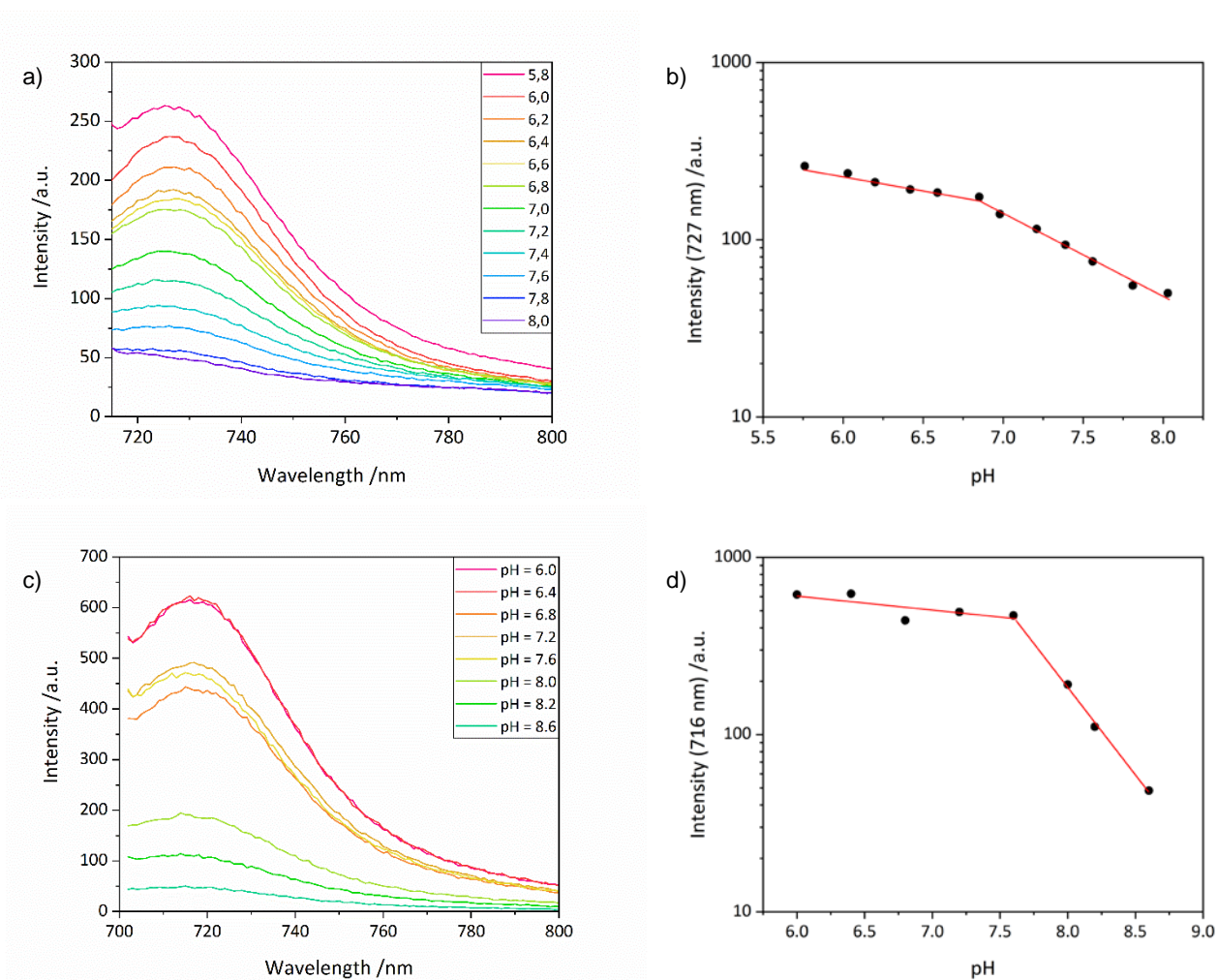


**Figure S7.** a) Fluorescence spectra of aBOD in aqueous phosphate buffers at different pH values ( $c = 10^{-6}$  M,  $\lambda_{Ex} = 680$  nm, slit = 20 nm,  $V_{detector} = 600$  V). b) pH-plot of the fluorescence maxima of aBOD in aqueous phosphate buffers. c) Fluorescence spectra of **SCNP IIIc** in aqueous phosphate buffers at different pH values ( $c = 0.5$  mg/mL,  $\lambda_{Ex} = 694$  nm, slit = 5 nm,  $V_{detector} = 600$  V). d) pH-plot of the fluorescence maxima of **SCNP IIIc** in aqueous phosphate buffers.

## SUPPORTING INFORMATION

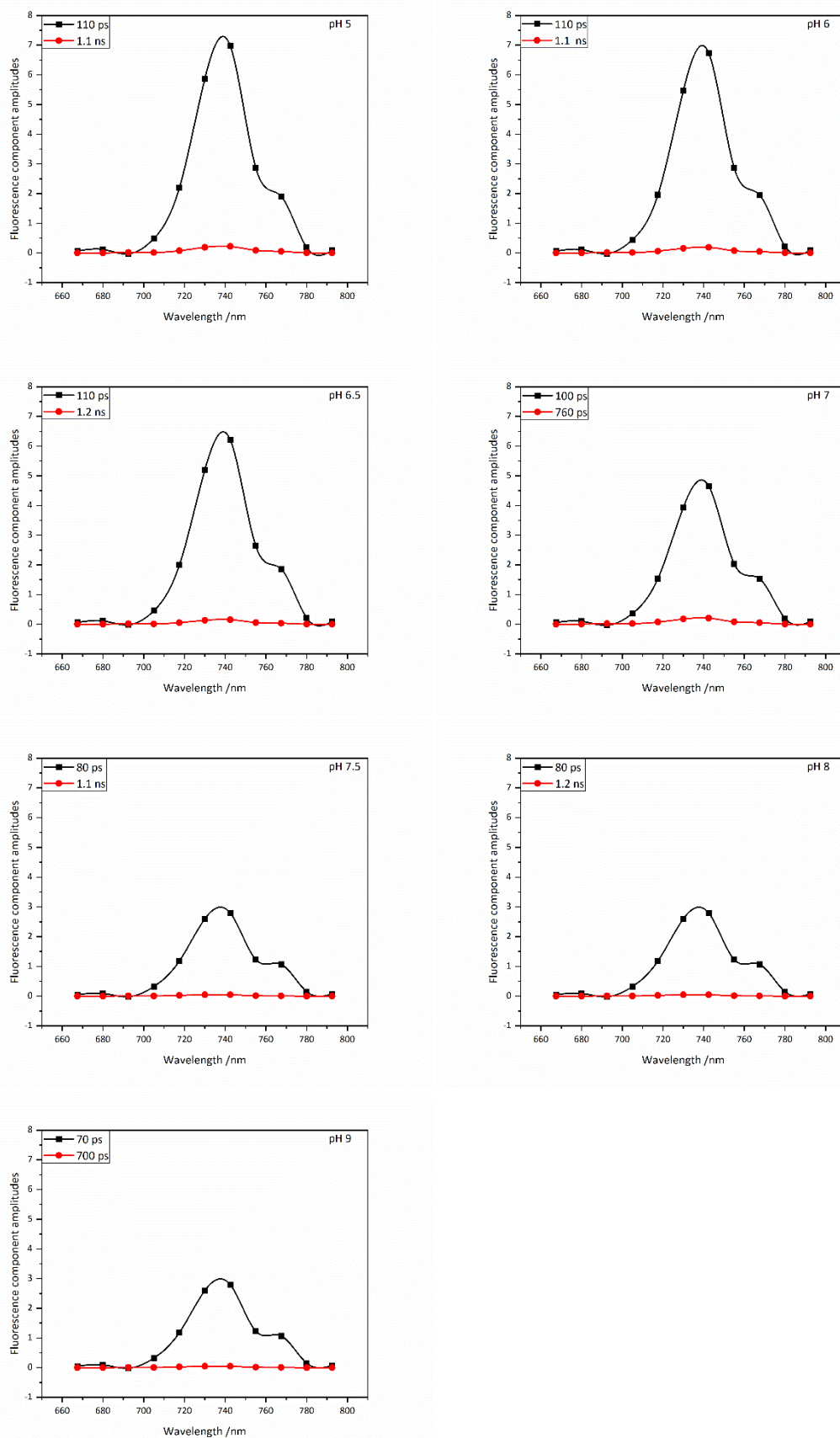


**Figure S8.** Decay associated spectra measured on aBOD in phosphate buffers at different pH values with 3 exponential functions.

## SUPPORTING INFORMATION

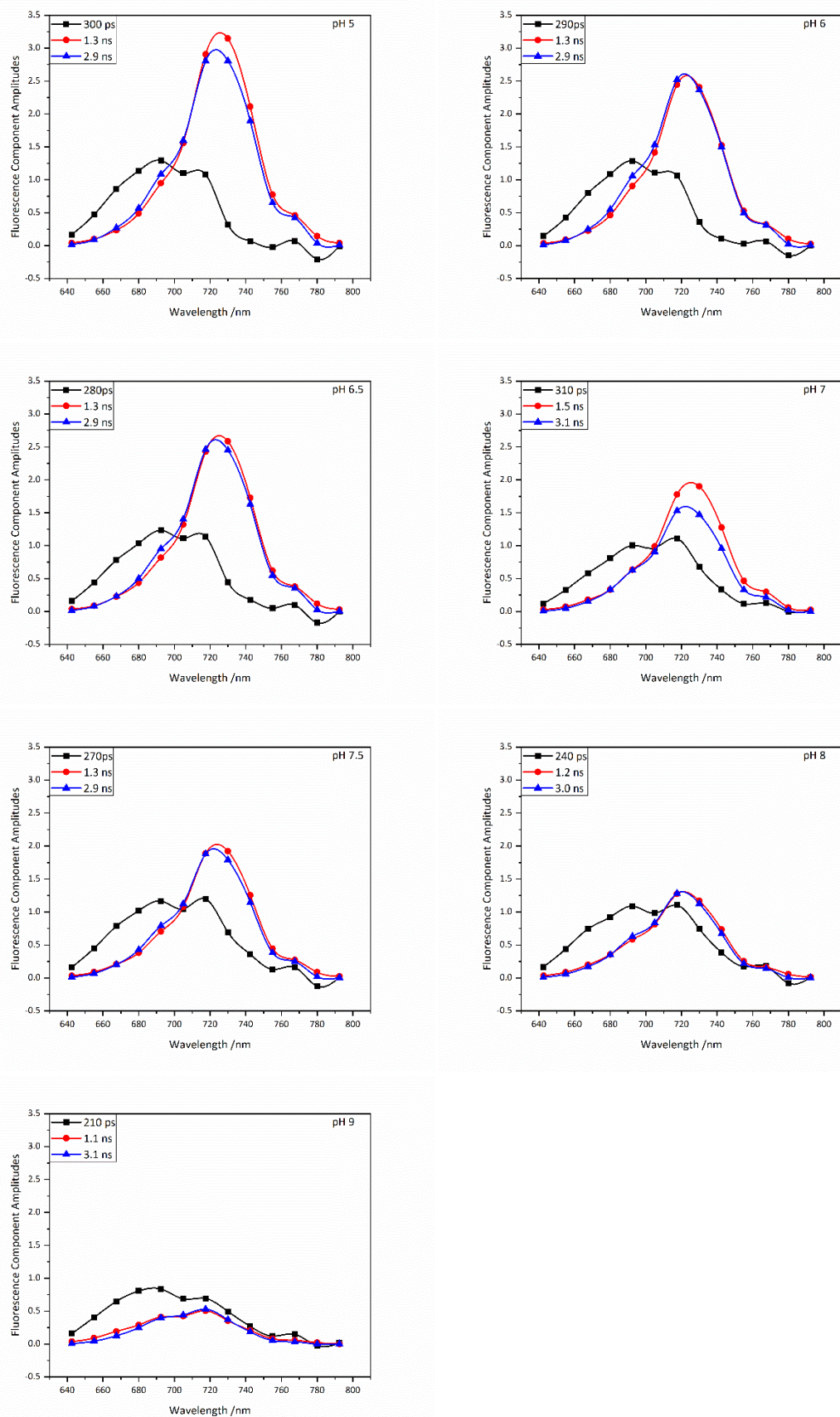
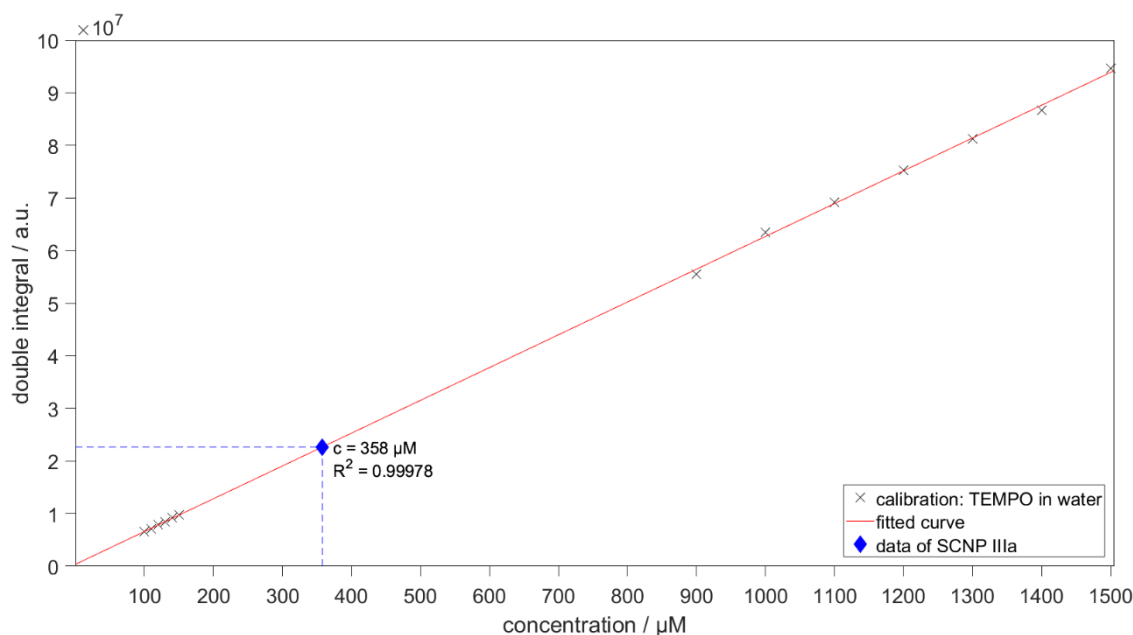


Figure S9. Decay associated spectra measured on SCNP IIIc in phosphate buffers at different pH values with 3 exponential functions.

## SUPPORTING INFORMATION



**Figure S10.** Calibration curve of TEMPO spin probes in water for estimation of the concentration of spin-labels in **SCNP IIIa**.

A concentration series of TEMPO spin probes in water has been used for calibration and approximate quantification of the amount of spin labels in **SCNP IIIa**. The best signal to noise ratio is given for the sample of 10 mg/ml **SCNP IIIa** (see Figure 3a) with a calculated particle concentration of 277  $\mu\text{M}$ . The concentration ratio of labelled TEMPO to **SCNP IIIa** is larger than one (358  $\mu\text{M}$  at a nominal particle concentration of 277  $\mu\text{M}$ ) so that it can be concluded that statistically 1.3 active spin labels are distributed onto the SCNP. Considering the spin-exchange frequency of  $\sim 6$  MHz, one can safely assume that most of the spin-labeled samples that are detected bear one or two active spin labels, the former leading to the general shape of the spectra and the latter adding the moderate spin-exchange frequency due to close contact in the openly solvated or collapsed SCNP.

## References

- [1] F.-J. Schmitt, Z. Y. Campbell, M. Moldenhauer, T. Friedrich, *Journal of Photochemistry and Photobiology A: Chemistry* **2020**, *403*, 112838
- [2] F.-J. Schmitt, Z. Y. Campbell, M. V. Bui, A. Hüls, T. Tomo, M. Chen, E. G. Maksimiv, S. I. Allakhverdiev, T. Friedrich, *Photosynth. Res.* **2019**, *139*, 185-201

**[M]acromolecular**  
**Rapid Communications**

Supporting Information

for *Macromol. Rapid Commun.*, DOI 10.1002/marc.202200618

Tuning the Internal Compartmentation of Single-Chain Nanoparticles as Fluorescent Contrast Agents

*Justus F. Thümmeler, Andreas H. Roos, Jana Krüger, Dariush Hinderberger, Franz-Josef Schmitt, Guo Tang, Farzin Ghane Golmohamadi, Jan Laufer and Wolfgang H. Binder\**

# Tuning the internal compartmentation of single-chain nanoparticles as fluorescent contrasting agents

Justus F. Thümmeler, Andreas H. Roos, Jana Krüger, Dariush Hinderberger, Franz-Josef Schmitt, Guo Tang, Farzin Ghane Golmohamadi, Jan Laufer, Wolfgang H. Binder\*

**Abstract:** Controlling the internal structures of single-chain nanoparticles (SCNPs) is an important factor for their targeted chemical design and synthesis, especially in view of nanosized compartments presenting different local environments as a main feature to embed functionality. We have designed SCNPs bearing near-infrared fluorescent dyes embedded in hydrophobic compartments for use as contrast agents in pump-probe photoacoustic (PA) imaging, displaying improved properties by influencing the location of the dye in the hydrophobic particle core. Compartment formation is controlled via single-chain collapse and subsequent crosslinking of an amphiphilic polymer using external crosslinkers in reaction media of adjustable polarity. Different SCNPs with hydrodynamic diameters of 6-12 nm bearing adjustable label densities were synthesized. We find that the specific conditions for single-chain collapse have a major impact on the formation of the desired core-shell structure, in turn controlling the internal nanocompartments together with the formation of excitonic dye couples, which significantly increase their fluorescence lifetime and PA signal generation. SCNPs in which the dye molecules accumulated at the core also showed a nonlinear PA response as a function of pulse energy – a property that can be exploited as a contrast mechanism in molecular PA tomography.

## **Table of Contents**

Experimental Procedures.....	3
Chemicals.....	3
Instrumentation and Analysis .....	3
Synthesis and Sample Preparation.....	5
Supporting Tables and Figures.....	10

# Experimental Procedures

## Chemicals

All chemicals were purchased from Sigma Aldrich except tetrabutylammonium bromide (TCI), sodium hydroxide (Grüssing), propargyl alcohol (abcr), triethylamine (TCI), 3-chloro-1-propanol (TCI), *p*-hydroxychalcone (TCI), diethylamine (Fluka), propargyltosylate (Fluka), KH<sub>2</sub>PO<sub>4</sub> (Roanal), nitromethane (Alfa Aesar) and CuSO<sub>4</sub> x 5 H<sub>2</sub>O (VEB Laborchemikalien). Before use, azobisisobutyronitrile (AIBN) was freshly recrystallized from methanol and poly(ethylene glycol) methyl ether methacrylate (M<sub>n</sub>=300) was passed through a basic AlO<sub>x</sub>-column to remove the stabilizer.

## Instrumentation and Analysis

*NMR spectra* were measured on an Agilent Technologies 400 MHz VNMRs and 500 MHz DD2 at 27°C. Chemical shifts ( $\delta$ ) are reported in ppm and referred to the solvent residual signal (CDCl<sub>3</sub> 7.26 ppm for <sup>1</sup>H and 77.0 ppm for <sup>13</sup>C, methanol-d<sub>4</sub> 3.31 ppm for <sup>1</sup>H and 49.0 ppm for <sup>13</sup>C, D<sub>2</sub>O 4.66 ppm for <sup>1</sup>H).

*ESI-TOF-MS* measurements were performed on a Bruker Daltonics microTOF via direct injection at a flow rate of 180  $\mu$ L h<sup>-1</sup> in positive mode with an acceleration voltage of 4.5 kV. Samples were prepared by dissolving in a mixture of LC-MS grade methanol and LC-MS grade tetrahydrofuran in a ratio of 1 to 8. The instrument was calibrated using the ESI-L low concentration tuning mix from Agilent Technologies (product no. G1969-85000). The software Data Analysis (version 4.0) was used for data evaluation.

*DOSY measurements* were done on an Agilent VNMR DD2 500 MHz (sfrq = 499.727 MHz). The experiment was performed under OpenVnmrJ 1.1 and equipped with a 5 mm PFG One NMR probe, z-gradient and temperature unit (27 °C). Diffusion ordered NMR data were acquired by means of the Agilent pulse program DgcsteSL\_cc using a stimulated echo with self-compensating gradient schemes and conventional compensation. The length of the gradient pulse was set to 3.0 ms for <sup>1</sup>H in combination with a diffusion period of 300 ms (D<sub>2</sub>O). Data were systematically accumulated by linearly varying the diffusion encoding gradients over a range from 2% to 95% for 64 gradient increment values.

*DLS measurements* were performed on a Litesizer 500 from Anton Paar using 1.5 ml semi-micro cuvettes (PMMA). The irradiation wavelength was 658 nm. The detection angle was maintained at 90° (side scattering) or 175° (back scattering). The temperature was set to 25°C. The sample concentration was 1 mg/mL in water.

*AFM measurements* were performed using a nanosurf CoreAFM with Tap190AI-G Cantilevers in the Phase-contrast mode. The samples were dissolved in molipore water at concentrations of 50  $\mu$ g/mL. The solution was dropped on the mica surface, incubated for 30 seconds and removed with a soft tissue before measurements. Data analysis was done using Gwyddion 2.53 (freeware, <http://gwyddion.net/>).

*ATR-IR spectra* were measured on a Bruker Tensor Vertex 70 equipped with a Golden Gate Heated Diamond ATR Top-plate.

*THF-based SEC measurements* were performed at 30 °C on a Viscotek GPCmax VE 2001 from Viscotek<sup>TM</sup> applying a CLM3008 precolumn and a CLM3008 main column. As solvent THF was used and the sample concentration was adjusted to 3 mg·ml<sup>-1</sup> while applying a flow rate of 1 ml·min<sup>-1</sup>. For determination of the molecular weights the refractive index of the investigated sample was detected with a VE 3580 RI detector of Viscotek<sup>TM</sup>. External calibration was done using poly(styrene) (PS) standards (purchased from PSS) with a molecular weight range from 1050 to 115000 g mol<sup>-1</sup>.

*Water-based SEC measurements* were performed at 25 °C on a Viscotek GPCmax VE 2001 from Viscotek™ applying a PSS SUPREMA 5 µm precolumn and a PSS SUPREMA analytical Linear M 5 µm main column. As solvent water (0.05 % NaN<sub>3</sub>) was used while applying a flow rate of 1 ml·min<sup>-1</sup>. The sample was detected with a VE 3580 RI detector of Viscotek™ and a UV Detector Knauer Azura UVD 2.19 .

*EPR measurements* were done with the Miniscope MS 5000 and the MS 5000 temperature controller (magnettech GmbH, Berlin, Germany) at 20 °C. By using the Freiberg Instruments software the spectra are measured with a sweep width of 10 mT, a modulation amplitude of 0.02 mT, a digital RC filter with a time constant of 0.2 s and a microwave attenuation of 20 dB. Each spectrum represents an accumulation of 10 scans. The samples were prepared in Rotilabo® sample vials and convicted for measuring in Blaubrandts Micropipettes. The spectra were analyzed with the EasySpin package version 5.2.27 for MatLab (Mathworks, Inc.)

*UV/VIS/NIR-absorption measurements* were performed on a Perkin Elmer LAMBDA 365 UV/Vis Spectrophotometer using Helma analytics quartz glass cuvettes (d = 10 mm).

*Fluorescence spectra* were measured on a Cary Eclipse fluorescence spectrometer of Agilent using Helma analytics quartz glass cuvettes (d = 10 mm).

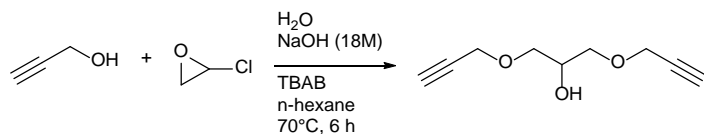
*Turbidimetry measurements* were performed on a JASCO J-1500 with a PTC-510 cell holder. The samples were measured in a Helma analytics quartz glass cuvettes (d = 10 mm) at concentrations of 1 mg/mL in water. The samples were heated from 30 °C to 90°C with a heating rate of 1 K/min. The transmittance was measured at a wavelength of 500 nm. The temperature at 50% of the normalized transmittance was taken as cloud point temperature  $T_{cp}$ .

*Decay associated spectra* were recorded employing a Hamamatsu R5900 16-channel multi-anode photomultiplier tube (PMT) with 16 separate output (anode) elements and a common cathode and dynode system (PML-16C, Becker&Hickl, Berlin, Germany) as described in Schmitt et al. 2020. A 632 nm pulsed laser diode (PDL-600, Becker&Hickl, Berlin) delivering 80 ps FWHM pulses at a repetition rate of 20 MHz was used for excitation. The fluorescence was observed via a 633 nm longpass filter (F76-631, AHF Analysentechnik, Tübingen, Germany). The determination of the DAS is described in detail in Schmitt et al. 2019.

*Photoacoustic pump-probe spectroscopy:* A tunable dual-OPO laser system (SpitLight EVO III Dual OPO, Innolas Laser GmbH, Germany) provided pump and probe excitation pulses of 5 ns duration at a repetition frequency of 100 Hz. The outputs of the OPO laser system were coupled into a bifurcated fiber bundle (8 mm core diameter) (Laser Components GmbH, Germany) for the measurement. A custom-made cuvette (path length: 6 mm, volume: 1 mL) was placed in a water bath filled in with distilled water and illuminated with the output of the fiber bundle (10 mm beam diameter at the cuvette). Beam shutters (Lasermat Ltd., UK) and ND filters placed in front of the focus lens were used to control the optical fluence. The PA signal was detected using a polyvinylidene fluoride (PVDF) transducer (PA1483, Precision Acoustics Ltd., UK), amplified with a 20 dB voltage preamplifier (HVA-200M-40-F, FEMTO Messtechnik GmbH, Germany) and recorded using a digitizer card (National Instruments, USA). The efficiency of the PA signal generation in fluorophores was varied by exploiting the effects of stimulated emission, i.e., the SCNP suspensions were illuminated with a pump pulse that coincides with the absorption spectrum while the probe pulse coincided with the maximum of the fluorescence spectrum. The time-course of the PA signal amplitude was modulated by introducing a variable time delay,  $\Delta t$ , ranging from 0 to 10 ns between pump and probe pulses.

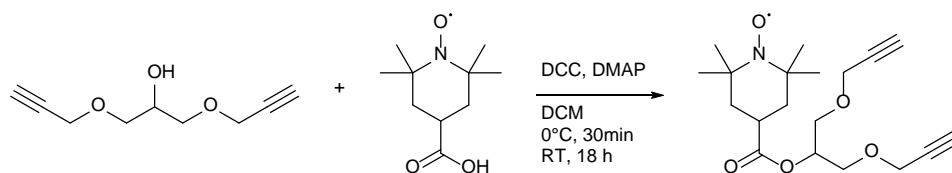
## Synthesis and Sample Preparation

### Synthesis of 1,3-bis(2-propyn-1-yloxy)-2-propanol **1**



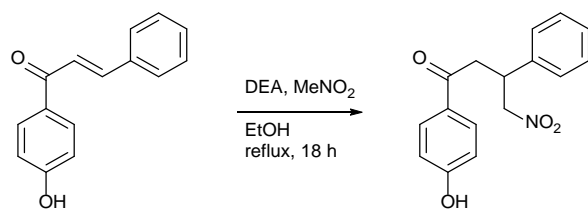
Tetrabutylammonium bromide (0.4 mmol, 128.85 mg) was given to an 18 M solution of NaOH in water (5 mL). *n*-Hexane (5 mL) were added and the resulting biphasic mixture heated to  $70^\circ\text{C}$  under vigorous stirring. Propargyl alcohol (20 mmol, 1.12 g, 1.18 mL) was added. After 10 minutes epichlorohydrin (8 mmol, 740 mg, 630  $\mu\text{L}$ ) was added and the reaction solution was stirred for 6 h at  $70^\circ\text{C}$ . The resulting solution was poured into 100 mL cold water and neutralized with HCl. The product was extracted with ethyl acetate. The combined organic phases were dried with  $\text{Na}_2\text{SO}_4$  and evaporated under vacuum. The product was purified by column chromatography (ethyl acetate:hexane 1:1,  $R_f = 0.45$ ). Yield: 53%.  $^1\text{H-NMR}$  ( $\text{CDCl}_3$ , 400 MHz,  $\delta$  in ppm): 4.19 (4H, m,  $\equiv\text{C-CH}_2$ ), 4.00 (1H, m, HO-CH), 3.59 (4H, m, O-CH $_2$ =CH)

### Synthesis of 1,3-bis(prop-2-yn-1-yloxy)propan-2-yl 1-hydroxy-2,2,6,6-tetramethylpiperidinyloxy-4-carboxylate **2** (TEMPO)



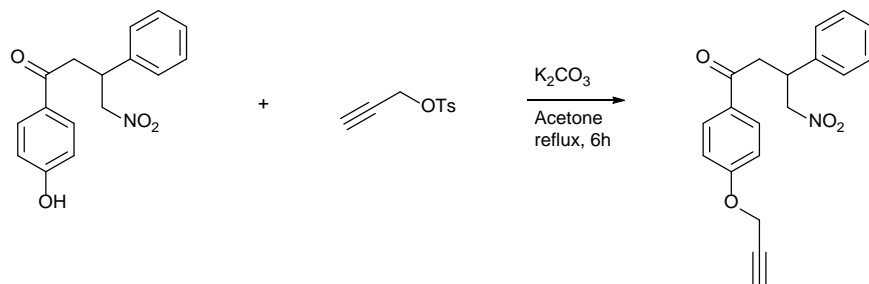
Under  $\text{N}_2$ -atmosphere carboxy-TEMPO (1 mmol, 200.26 mg), *N,N'*-dicyclohexylcarbodiimide (DCC, 1.1 mmol, 227 mg) and **1** (1.1 mmol, 185 mg, 174.7  $\mu\text{L}$ ) were dissolved in DCM (10 mL) and placed in an ice bath. 4-dimethylaminopyridine (DMAP, 0.2 mmol, 24.4 mg) was added and stirred for 30 min at  $0^\circ\text{C}$ . The reaction solution was stirred for further 18 h at room temperature. The precipitate was filtered and the DCM removed under reduced pressure. The crude product was purified by column chromatography (DMC:methanol 100:1,  $R_f = 0.65$ ). Yield: 56%.  $^1\text{H-NMR}$  ( $\text{CDCl}_3$ , 500 MHz,  $\delta$  in ppm, because of the nitroxyl radical some peaks do not appear in the spectrum and all other peaks are broadened): 5.32 (1H, COOCH), 4.26 (4H,  $\equiv\text{C-CH}_2$ ), 3.80 (4H, O-CH $_2$ ), 2.49 (2H,  $\equiv\text{CH}$ ). ESI-TOF:  $m/z$  calculated for  $\text{C}_{18}\text{H}_{26}\text{NO}_5^- + \text{Na}^+ [\text{M} + \text{H}^+] = 373.1860$ , found 373.1857.

### Synthesis of 1-(4-hydroxyphenyl)-4-nitro-3-phenylbutan-1-one **3**



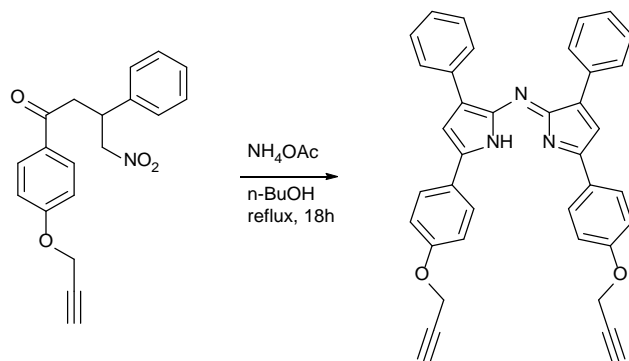
*p*-Hydroxychalcone (8.9 mmol, 2g) was dissolved in ethanol (15 mL). The solution was heated to reflux ( $90^\circ\text{C}$  oil bath temperature). Diethylamine (44.5 mmol, 3.25 g, 4.6 mL) and nitromethane (89 mmol, 5.43 g, 4.8 mL) were added dropwise and the reaction solution was stirred under reflux for 18 h. The solution was poured in 100 mL water and the product extracted with DCM. The crude product was purified by column chromatography (methanol:DCM 1:10,  $R_f = 0.47$ ).  $^1\text{H-NMR}$  ( $\text{CDCl}_3$ , 400 MHz,  $\delta$  in ppm): 7.85 (2H, m,  $H_{Ar}$ ), 7.33 (2H, m,  $H_{Ar}$ ), 7.27 (3H, m,  $H_{Ar}$ ), 6.86 (2H, m,  $H_{Ar}$ ), 5.74 (1H, s (broad), OH), 4.88-4.64 (2H, m,  $\text{NO}_2\text{-CH}_2$ ), 4.21 (1H, m, Ph-CH), 3.39 (2H, m, O=C-CH $_2$ ).

Synthesis of 4-nitro-3-phenyl-1-(4-(prop-2-yn-1-yloxy)phenyl)butan-1-one **4**



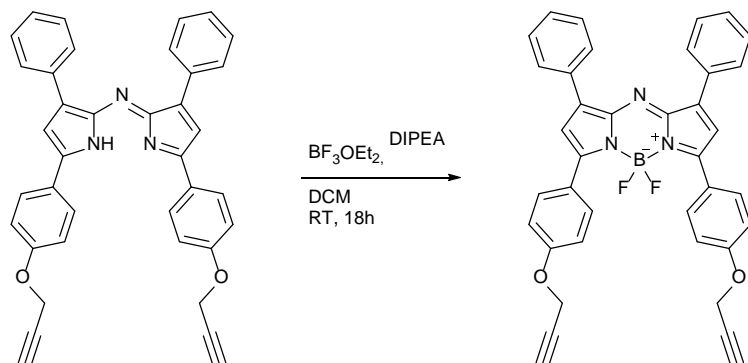
**3** (3.5 mmol, 1g) was dissolved in acetone (20 mL).  $K_2CO_3$  (11 mmol, 1.52 g) was added and the dispersion was heated to  $70^\circ C$  (reflux). Propargyl tosylate (5.25 mmol, 1.1 g, 895  $\mu L$ ) was dissolved in 3 mL acetone, added to the reaction mixture. After 6 h it was cooled to room temperature, filtrated and the acetone was removed under reduced pressure. The crude product was dissolved in ethyl acetate and washed with water. The organic phase was dried with  $Na_2SO_4$  and reduced under reduced pressure. The product was purified by column chromatography (ethyl acetate:hexane 1:3,  $R_f = 0.25$ ). Yield: 55%.  $^1H$ -NMR ( $CDCl_3$ , 400 MHz,  $\delta$  in ppm): 7.91 (2H, m,  $H_{ar}$ ), 7.33 (2H, m,  $H_{ar}$ ), 7.27 (3H, m,  $H_{ar}$ ), 7.01 (2H, m,  $H_{ar}$ ), 5.74 (1H, s (broad), OH), 4.86-4.65 (2H, m,  $NO_2-CH_2$ ), 4.75 (2H, d,  $J = 2.4$  Hz,  $\equiv C-CH_2$ ), 4.21 (1H, m, Ph-CH), 3.40 (2H, m, O=C- $CH_2$ ), 2.55 (1H, t,  $J = 2.4$  Hz,  $\equiv CH$ ).

Synthesis of [5-(4-prop-2-yn-1-yloxyphenyl)-3-phenyl-1H-pyrrol-2-yl]-[5-(4-prop-2-yn-1-yloxyphenyl)-3-phenylpyrrol-2-ylidene]amine **5**



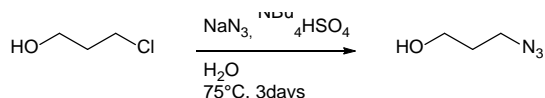
**4** (2.23 mmol, 722 mg) and ammonium acetate (78.1 mmol, 6 g) in *n*-BuOH (25 mL) were heated under reflux ( $130^\circ C$  oil bath) for 20 h. The reaction was cooled to room temperature and filtrated. The isolated solid was washed with cold *n*-BuOH and dried under vacuum. The product was used with no further purification. Yield: 51%.  $^1H$ -NMR ( $CDCl_3$ , 500 MHz,  $\delta$  in ppm): 8.06 (4H, m,  $H_{Ar}$ ), 7.92 (4H, m,  $H_{Ar}$ ), 7.42 (2H, m,  $H_{Ar}$ ), 7.35 (2H, m,  $H_{Ar}$ ), 7.14 (6H, m,  $H_{Ar}$ ), 5.36 (1H, s (broad), NH), 4.81 (2H, d,  $J = 2.3$  Hz,  $\equiv C-CH_2$ ), 2.59 (1H, t,  $J = 2.3$  Hz,  $\equiv CH$ ).

Synthesis of  $BF_2$ -chelate of [5-(4-prop-2-yn-1-yloxyphenyl)-3-phenyl-1H-pyrrol-2-yl]-[5-(4-prop-2-yn-1-yloxyphenyl)-3-phenylpyrrol-2-ylidene]amine **6** (aza-BODIPY)



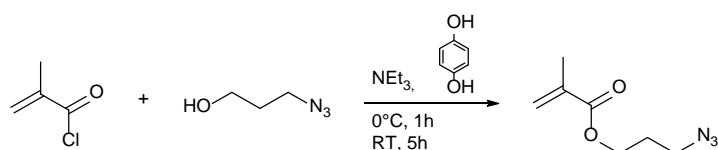
**5** (0.2 mmol, 113.5 mg) was dissolved in dry DCM (50 mL). DIPEA (2.4 mmol, 310.2 mg, 408  $\mu$ L) was added. The solution was stirred for 10 min at room temperature before being cooled to 0°C.  $\text{BF}_3\text{OEt}_2$  (3.6 mmol, 510.9 mg, 44  $\mu$ L) was added. The resulting solution was stirred at 0 °C for 30 min and then at room temperature for 18 h. The product solution was washed with  $\text{NH}_4\text{Cl}$ -solution, brine, and water, dried with  $\text{Na}_2\text{SO}_4$  and the solvent removed under reduced pressure. The crude product was purified by column chromatography (DCM:hexane 3:1,  $R_f = 0.54$ ) to get the product as a red solid. Yield: 77%.  $^1\text{H-NMR}$  ( $\text{CDCl}_3$ , 500 MHz,  $\delta$  in ppm): 8.09 (4H, m,  $H_{Ar}$ ), 8.06 (4H, m,  $H_{Ar}$ ), 7.49-7.38 (6H, m,  $H_{Ar}$ ), 7.09 (4H, m,  $H_{Ar}$ ), 7.03 (2H, m,  $H_{Ar}$ ), 4.76 (2H, d,  $J = 2.4$  Hz,  $\equiv\text{C-CH}_2$ ), 2.57 (1H, t,  $J = 2.4$  Hz,  $\equiv\text{CH}$ ).

#### Synthesis of 3-Azido-1-propanol **7**



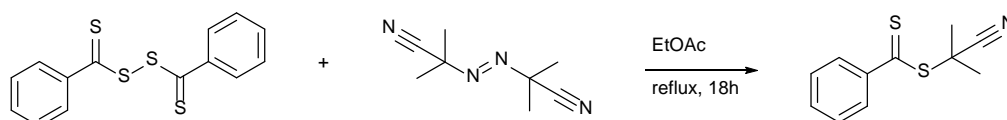
3-Chloro-1-propanol (23.5 mmol, 2.2 g, 2 ml) was added dropwise to a solution of sodium azide (48 mmol, 3.13 g) and tetrabutylammonium hydrogen sulphate (0.2 mmol, 70 mg) in 50 ml water at room temperature. The resulting solution was heated to 75°C. After stirring for three days the product was extracted with DCM. The combined organic phases were dried with  $\text{Na}_2\text{SO}_4$  and the solvent evaporated under vacuum to get the product as a colorless liquid. Yield: 85%.  $^1\text{H-NMR}$  ( $\text{CDCl}_3$ , 400 MHz,  $\delta$  in ppm): 3.71 (2H, t,  $J = 6.0$  Hz,  $\text{HO-CH}_2$ ), 3.42 (2H, t,  $J = 6.6$  Hz,  $\text{CH}_2\text{-N}_3$ ), 2.21 (1H, s,  $\text{OH}$ ), 1.80 (2H, tt,  $J = 6.6, 6.0$  Hz,  $\text{CH}_2\text{CH}_2\text{CH}_2$ ).

#### Synthesis of 3-Azidopropyl methacrylate **8**



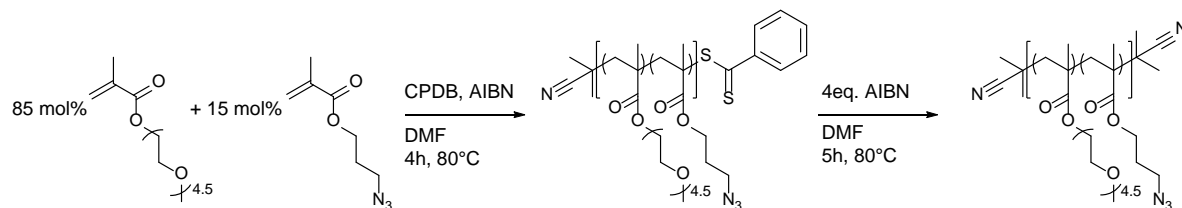
**7** (19.3 mmol, 1.95 g, 1.8 ml), triethylamine (28.7 mmol, 2.9 g, 4 ml) and hydroquinone (10  $\mu$ mol, 1 mg) were dissolved in 25 ml of dry DCM and placed in an ice bath. Methacryloyl chloride (28.7 mmol, 3 g, 2.8 ml) in 5 ml of dry DCM was added dropwise. The resulting solution was stirred at 0°C for 1 h and at room temperature for additional 5 h. The white precipitate was removed by filtration and the product solution washed with water, saturated sodium bicarbonate solution and brine. The organic phase was dried with  $\text{Na}_2\text{SO}_4$  and the solvent was removed under vacuum. The product was purified by column chromatography (hexane:diethyl ether 2:1,  $R_f = 0.46$ ) to get the product as a pale-yellow liquid. The product was stored with hydroquinone as stabilizer. Yield: 25%.  $^1\text{H-NMR}$  ( $\text{CDCl}_3$ , 500 MHz,  $\delta$  in ppm): 6.11 (1H, dq,  $J = 2.0, 1.0$ ,  $=\text{CH}$ ), 5.58 (1H, dq,  $J = 2.0, 1.6$  Hz,  $=\text{CH}$ ), 4.24 (2H, t,  $J = 6.2$  Hz,  $\text{COO-CH}_2$ ), 3.42 (2H, t,  $J = 6.7$  Hz,  $\text{CH}_2\text{-N}_3$ ), 1.96 (2H, tt,  $J = 6.7, 6.2$  Hz,  $\text{CH}_2\text{CH}_2\text{CH}_2$ ), 1.95 (3H, dd,  $J = 1.6, 1.0$  Hz,  $\text{CH}_3$ ).

#### Synthesis of Cyanoisopropyl dithiobenzoate **9 (CPDB)**



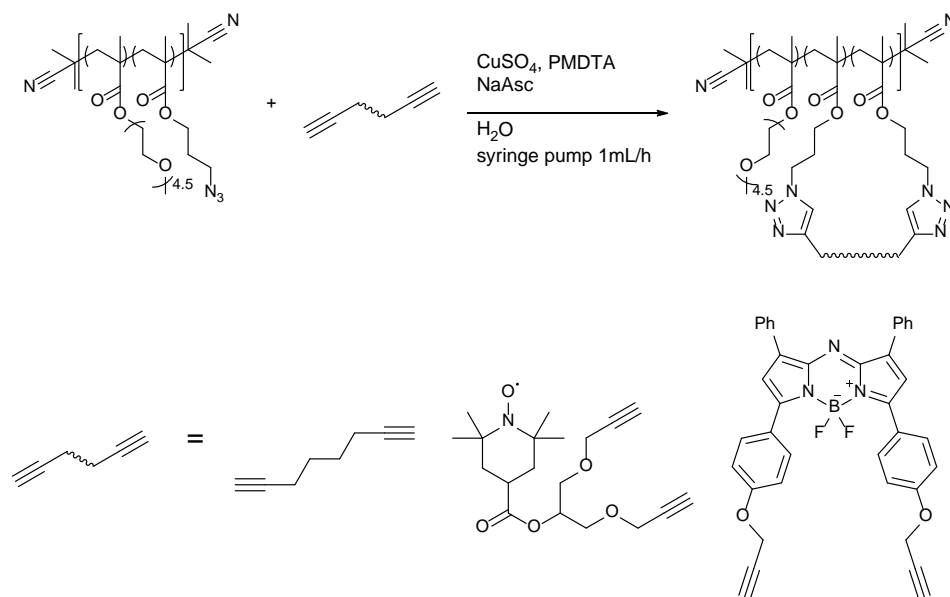
Bis(thiobenzoyl) disulfide (0.8 mmol, 245.2 mg) and AIBN (1.2 mmol, 197.1 mg) were dissolved in 10 ml ethyl acetate. The solution was degassed by five freeze-pump-thaw cycles and stirred under reflux for 18 h. The crude product was dried under vacuum and purified by column chromatography (hexane:ethyl acetate 10:1,  $R_f = 0.27$ ) to get the product as a red oil. Yield: 56%.  $^1\text{H-NMR}$  ( $\text{CDCl}_3$ , 400 MHz,  $\delta$  in ppm): 7.92 (2H, m,  $o\text{-H}_{Ar}$ ), 7.56 (1H, m,  $p\text{-H}_{Ar}$ ), 7.39 (2H, m,  $m\text{-H}_{Ar}$ ), 1.94 (6H, s,  $\text{CH}_3$ ).

Synthesis of Poly[(poly(ethylene glycol) methyl ether methacrylate)-co-(3-azidopropyl methacrylate)] (PEAMA)



Poly(ethylene glycol) methyl ether methacrylate ( $M_n=300$ ) (12.243 mmol, 3.672 g) and **8** (2.16 mmol, 365.4 mg, 341.52  $\mu\text{L}$ ) were dissolved in 2 ml dry DMF in a Schlenk tube. 2 ml of a stock solution of CPDB (24 mM, 48  $\mu\text{mol}$ ) and AIBN (4.8 mM, 9.6  $\mu\text{mol}$ ) was added to the solution. The resulting mixture was degassed by five freeze-pump-thaw cycles and stirred at 80°C for 4 h. The product was precipitated in cold hexane:diethyl ether (2:1) as a pink polymer. To remove the RAFT-endgroup, the polymer was dissolved in DMF (15 mL), AIBN (4eq) was added and the solution degassed by bubbling with  $\text{N}_2$ . The solution was stirred at 80°C for 5 h. The product was again precipitated in cold hexane:diethyl ether (2:1). The resulting yellow, highly viscous polymer was purified by dialysis in THF. Yield: 72%. GPC (THF):  $M_n = 34.6$  kDa,  $M_w/M_n = 1.4$ , DP = 123.  $^1\text{H-NMR}$  ( $\text{CDCl}_3$ , 500 MHz,  $\delta$  in ppm): 4.25-3.90 ( $\text{COOCH}_2$ ), 3.82-3.47 ( $\text{OCH}_2\text{CH}_2\text{O}$ ), 3.48-3.40 ( $\text{N}_3\text{CH}_2$ ), 3.37 ( $\text{OCH}_3$ ), 2.07-1.67 ( $\text{CH}_2$ ), 1.09-0.77 ( $\text{CH}_3$ ).

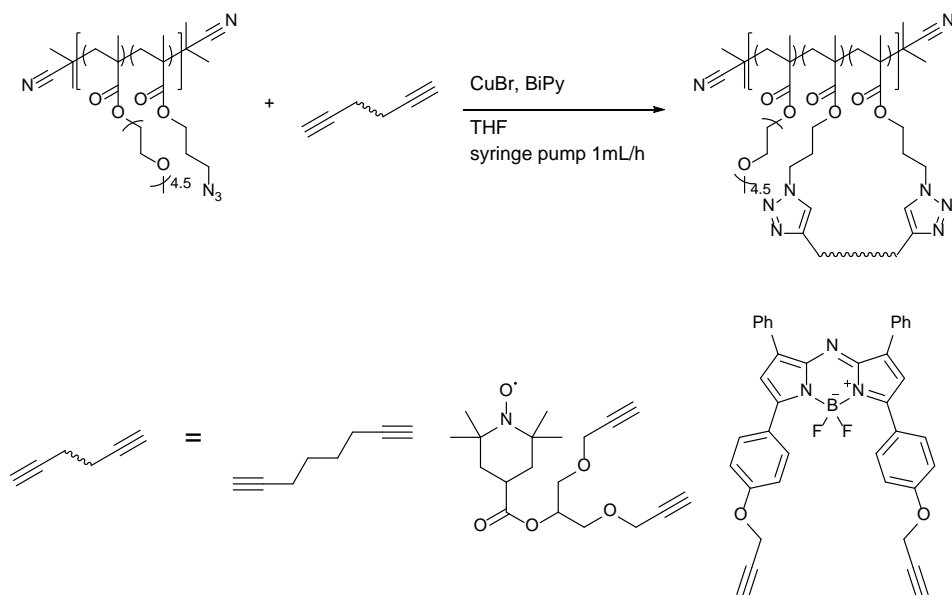
General procedure for the single chain collapse in water (SCNP<sub>water</sub>)



PEAMA (200 mg,  $1.07 \times 10^{-4}$  mol  $\text{N}_3$ ) and crosslinker (octadiyne, TEMPO, aza-BODIPY, or mixtures of octadiyne and TEMPO/aza-BODIPY, 0.5 eq. to  $\text{N}_3$ ,  $\Sigma 5.35 \times 10^{-5}$  mol) were dissolved in 20 ml THF. The solution was put into a syringe pump (1 ml/h) and added to a solution of sodium ascorbate (7.5 mol, 1.5 g),  $\text{CuSO}_4 \times 5 \text{H}_2\text{O}$  (0.5 mmol, 125 mg) and PMDTA (1 mmol, 173 mg, 209  $\mu\text{l}$ ) in 120 ml degassed  $\text{H}_2\text{O}$ . After 20 h the solution was stirred for one additional hour. For the purification it is important to keep the product wet since the redissolution of dried samples is difficult. The product (and THF) was extracted with DCM. The DCM was reduced under vacuum to get a solution in THF. This solution was passed over a silica column to remove remaining copper impurities. The resulting solution was purified by dialysis going from THF with 1 mL PMDTA to a mixture of water/THF (1:1) and in the end to pure THF. The product was dried under vacuum. Yield: 50%.

Since TEMPO gets deactivated by sodium ascorbate, it needed to be reactivated. Therefore after the finished addition of the polymer/crosslinker solution, first sodium ascorbate ( $2.5 \times 10^{-4}$  mol, 50 mg) in 5 mL water and then  $\text{H}_2\text{O}_2$  (30wt% in  $\text{H}_2\text{O}$ , 5  $\mu\text{L}$ ) in 5 mL water were added. The remaining procedure was followed as described above.

### General procedure for the single chain collapse in THF (SCNP<sub>THF</sub>)



PEAMA (200 mg,  $1.07 \times 10^{-4}$  mol  $N_3$ ) and crosslinker (octadiyne, TEMPO, aza-BODIPY, or mixtures of octadiyne and TEMPO/ aza-BODIPY, 0.5 eq. to  $N_3$ ,  $\Sigma$   $5.35 \times 10^{-5}$  mol) were dissolved in 20 ml THF. The solution was put into a syringe pump (1 ml/h) and added to a solution of CuBr (0.5 mmol, 71.1 mg) and 2,2' bipyridine (1 mmol, 173 mg, 209  $\mu$ l) in 100 ml THF. After 20 h the solution was stirred for one additional hour. 50 mL water were added and the solution was stirred for 30 minutes. For the purification it is important to keep the product wet since the redissolution of dried samples is difficult. THF was removed under reduced pressure to get an aqueous solution. The product was extracted with DCM. THF was added and the DCM was reduced under vacuum to get a solution in THF. This solution was passed over a silica column to remove remaining copper impurities. The resulting solution was purified by dialysis going from THF with 1 mL PMDTA to a mixture of water/THF (1:1) and in the end to pure THF. The product was dried under vacuum. Yield: 60%.

### Dispersing of SCNPs in water

The solid (agglomerated) SCNP were placed in a vial and water was added. The suspension was stirred for 18 h until a milky dispersion was formed. The resulting dispersion was ultrasonicated for several hours until it was clear. It is important for the temperature not to rise higher than 50°C. The SCNPs show LCST-behavior in water and will not solubilize then.

### Solving aza-BODIPY in water ( $c = 5 \times 10^{-5}$ M)

aza-BODIPY (5  $\mu$ mol, 3.03 mg) was dissolved in dry THF (2 ml) and Kolliphor EL (Kolel, 0.2 ml) was added. The resulting solution was ultrasonicated for 30 minutes. The THF was removed under vacuum and the residue was dissolved in 100 ml water to get a dark green solution.

## Supporting Tables and Figures

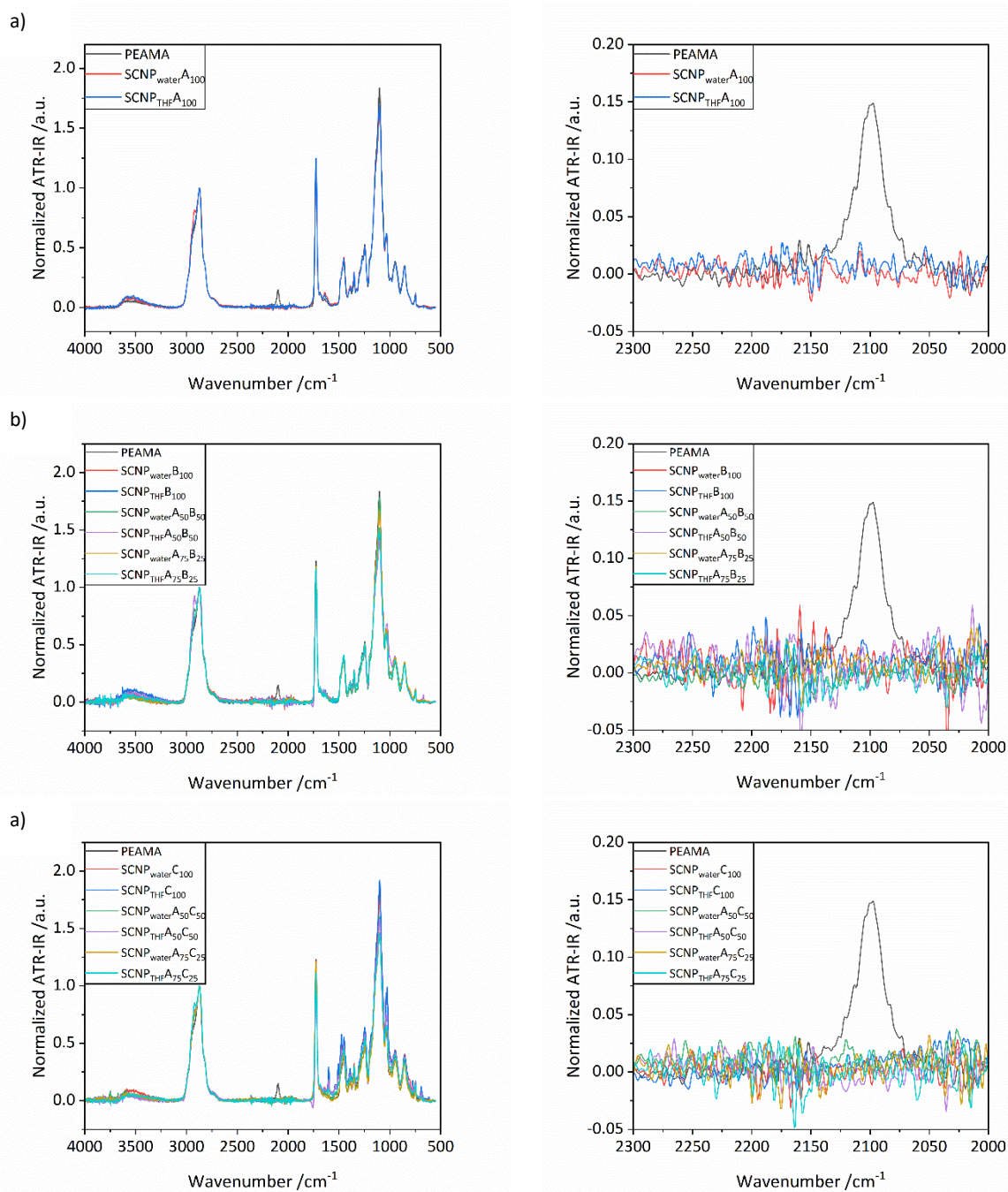


**Figure S1.** Normalized ATR-IR spectra of PEAMA and the labeled SCNPs with a) octadiyne (A), b) TEMPO (B), and c) aza-BODIPY (C) as crosslinkers. Left side: full spectra, right side: zoom to the azide band.

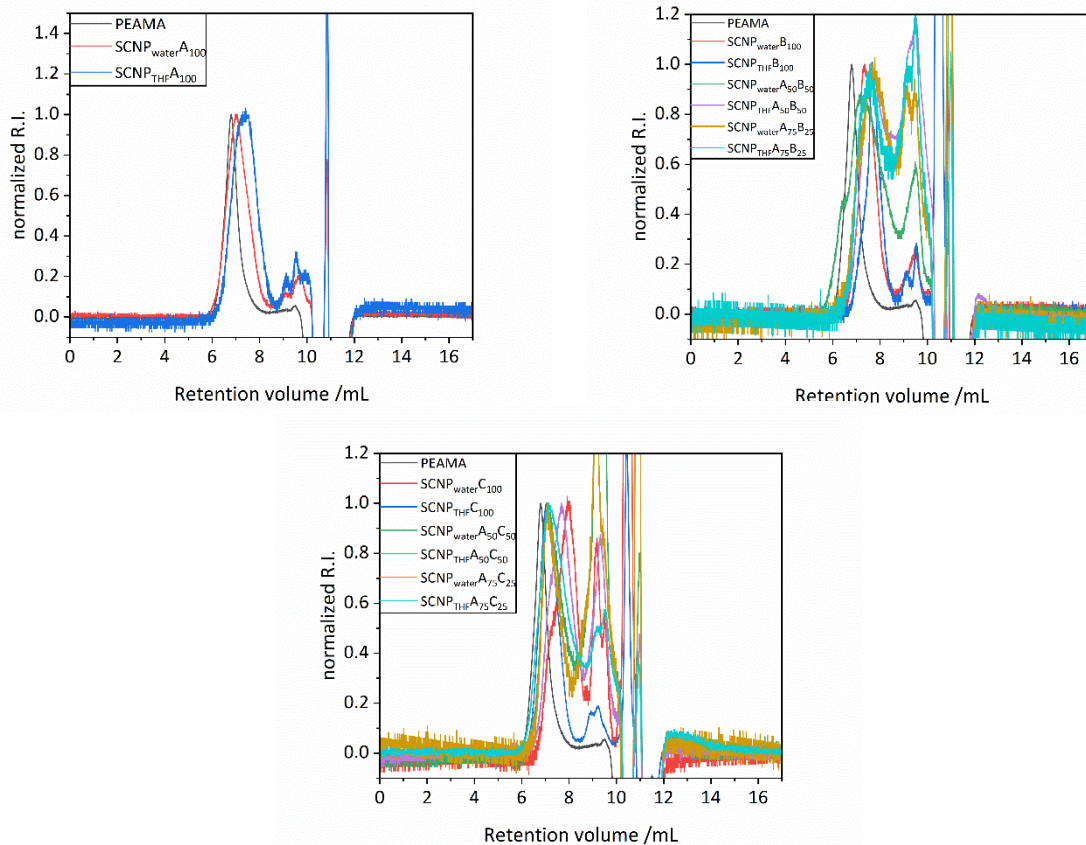


**Figure S2.** THF based SEC R.I. traces of PEAMA, and the SCNPs a) octadiyne (**A**), b) TEMPO (**B**), and c) aza-BODIPY (**C**) as crosslinkers.

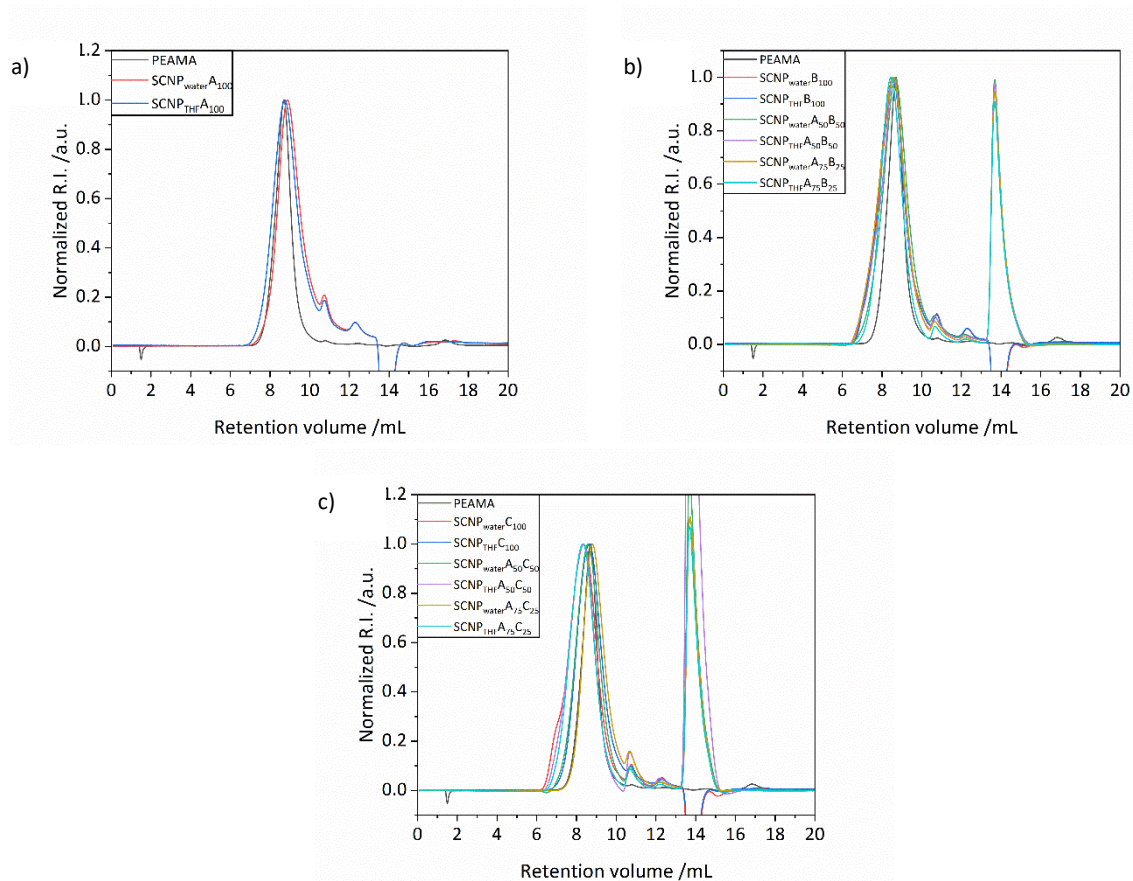


**Figure S3.** Water based SEC R.I. traces of PEAMA, and the SCNPs with a) octadiyne (A), b) TEMPO (B), and c) aza-BODIPY (C) as crosslinkers.

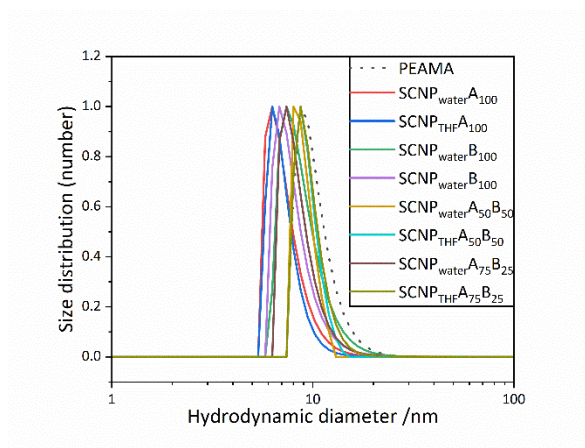


**Figure S4.** Number weighted size distribution of the precursor polymer PEAMA and the SCNPs with octadiyne and B as crosslinkers as determined by DLS at concentrations of 1 mg/mL in water.

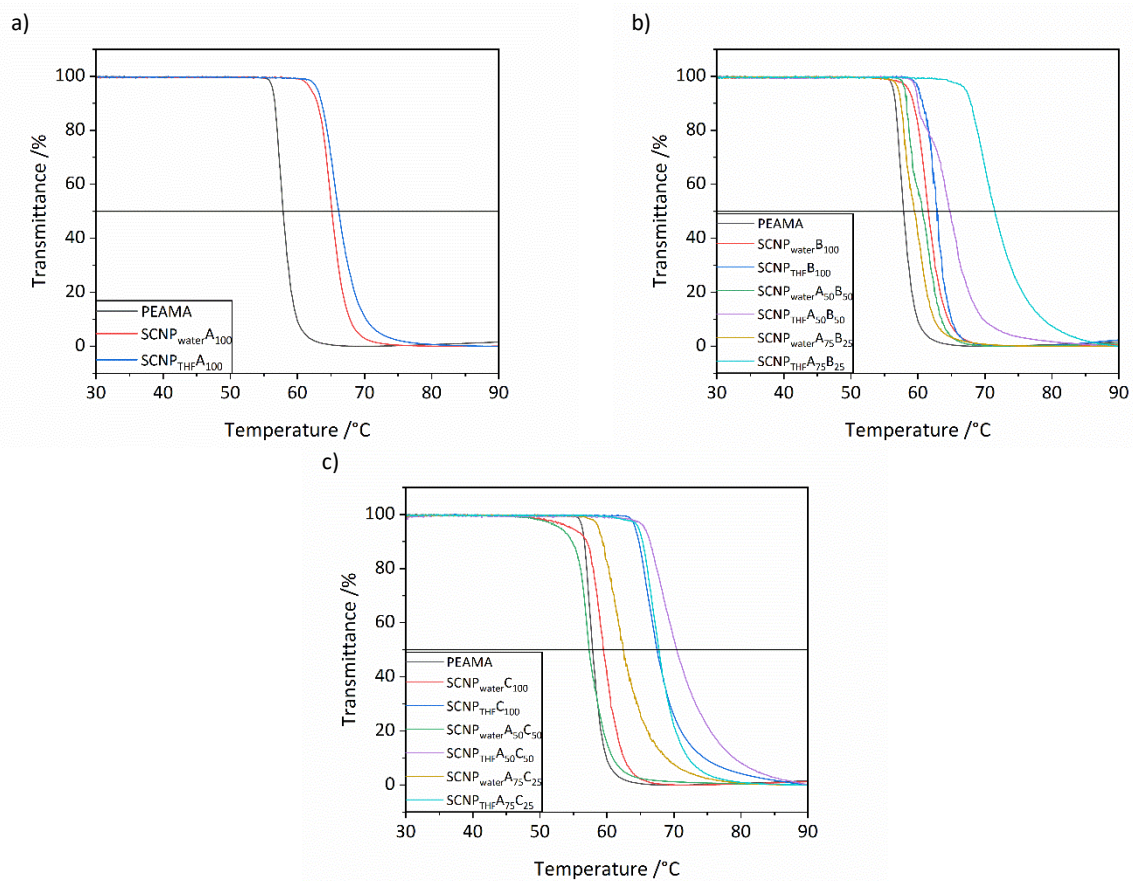


**Figure S5.** Turbidimetry measurements of PEAMA and all SCNPs with a) octadiyne (**A**), b) TEMPO (**B**), and c) aza-BODIPY (**C**) as crosslinkers.

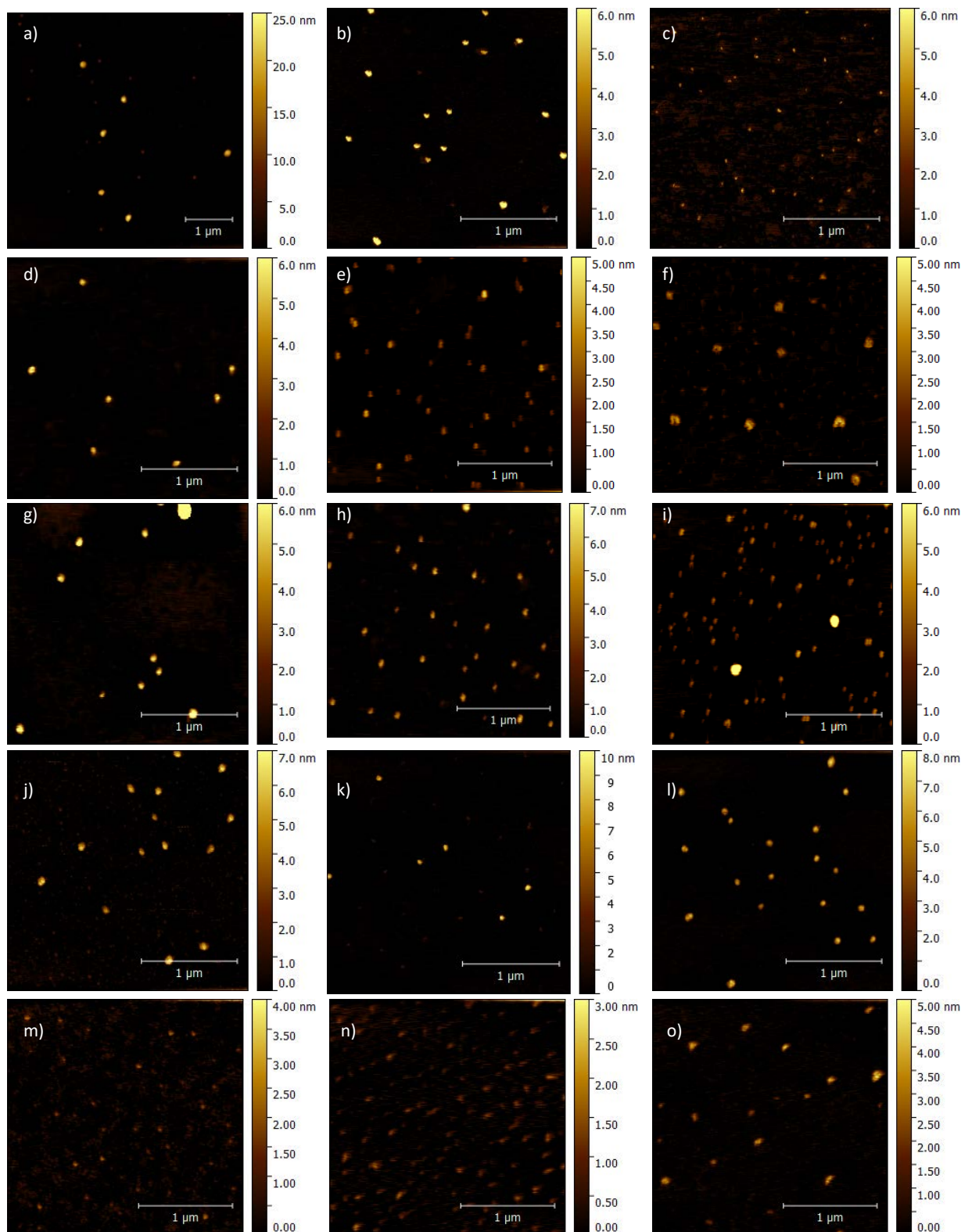


**Figure S6.** AFM topographies of a) PEAMA, b) SCNP<sub>water</sub>A<sub>100</sub>, c) SCNP<sub>THFA</sub>A<sub>100</sub>, d) SCNP<sub>water</sub>C<sub>100</sub>, e) SCNP<sub>water</sub>A<sub>50</sub>C<sub>50</sub>, f) SCNP<sub>water</sub>A<sub>75</sub>C<sub>25</sub>, g) SCNP<sub>THF</sub>C<sub>100</sub>, h) SCNP<sub>THFA</sub>A<sub>50</sub>C<sub>50</sub>, i) SCNP<sub>THFA</sub>A<sub>75</sub>C<sub>25</sub>, j) SCNP<sub>water</sub>B<sub>100</sub>, k) SCNP<sub>water</sub>A<sub>50</sub>B<sub>50</sub>, l) SCNP<sub>water</sub>A<sub>75</sub>B<sub>25</sub>, m) SCNP<sub>THF</sub>B<sub>100</sub>, n) SCNP<sub>THFA</sub>A<sub>50</sub>B<sub>50</sub>, o) SCNP<sub>THFA</sub>A<sub>75</sub>B<sub>25</sub>.

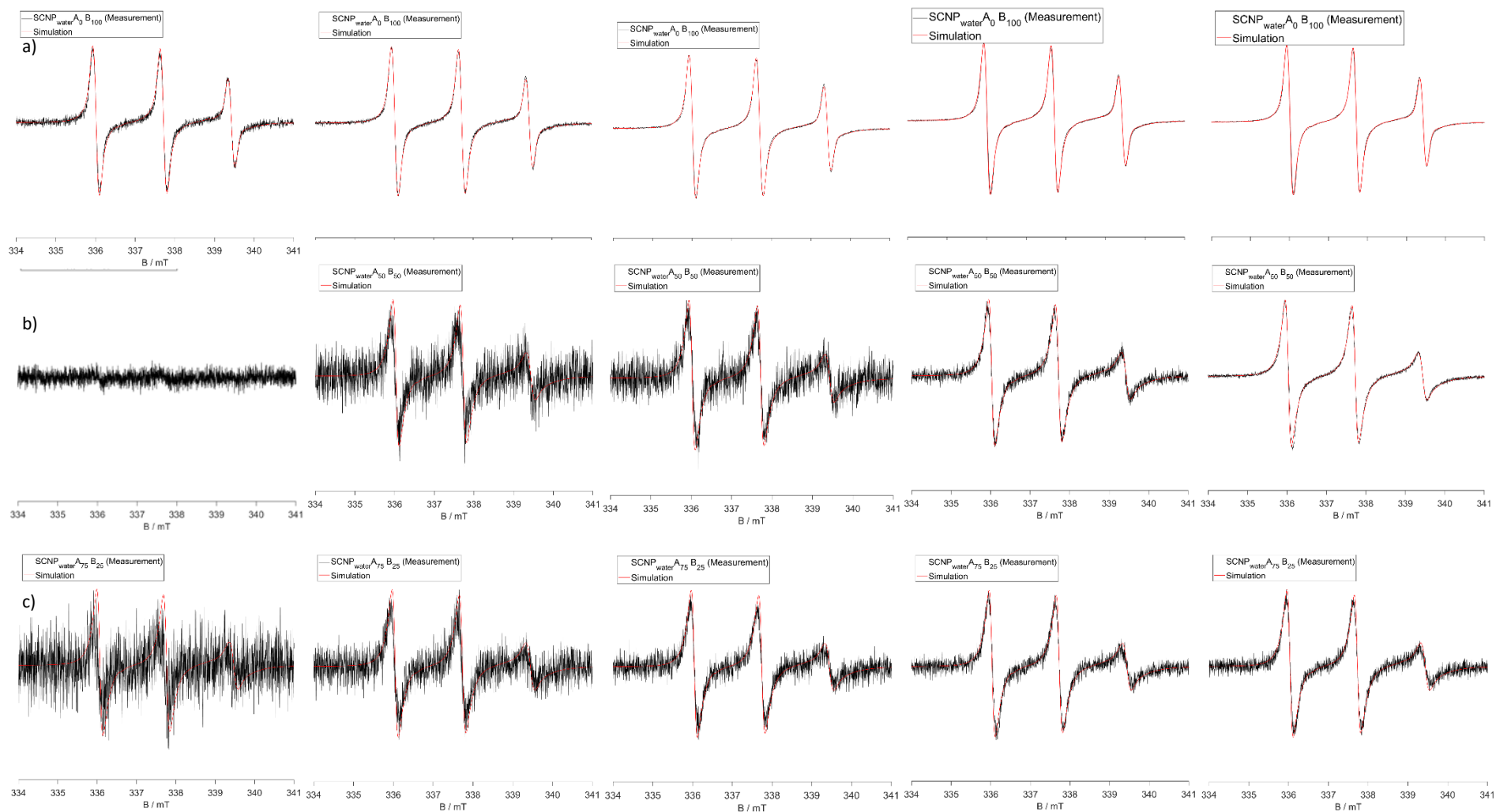


**Figure S7.** EPR spectra with simulated spectra of the water collapsed and TEMPO labeled SCNPs measured in water. a)  $\text{SCNP}_{\text{water}}\text{A}_0\text{B}_{100}$ , b)  $\text{SCNP}_{\text{water}}\text{A}_{50}\text{B}_{50}$ , c)  $\text{SCNP}_{\text{water}}\text{A}_{75}\text{B}_{25}$ . From left to right:  $1 \text{ mg mL}^{-1}$ ,  $2.5 \text{ mg mL}^{-1}$ ,  $5 \text{ mg mL}^{-1}$ ,  $7.5 \text{ mg mL}^{-1}$ ,  $10 \text{ mg mL}^{-1}$ .

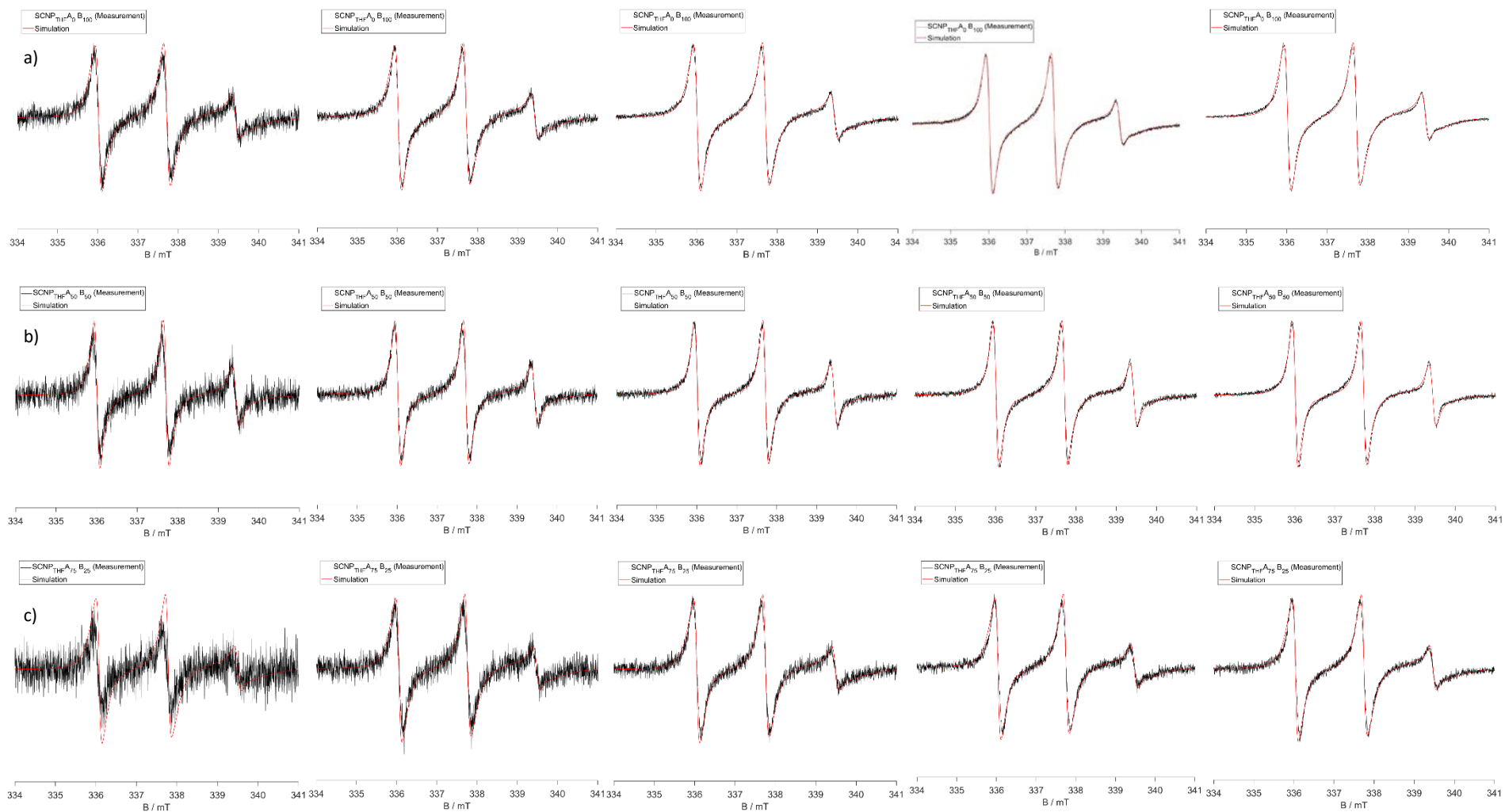


**Figure S8.** EPR spectra with simulated spectra of the THF collapsed and TEMPO labeled SCNPs measured in water. a)  $\text{SCNP}_{\text{THFA}0\text{B}100}$ , b)  $\text{SCNP}_{\text{THFA}50\text{B}50}$ , c)  $\text{SCNP}_{\text{THFA}25\text{B}75}$ . From left to right: 1 mg mL<sup>-1</sup>, 2.5 mg mL<sup>-1</sup>, 5 mg mL<sup>-1</sup>, 7.5 mg mL<sup>-1</sup>, 10 mg mL<sup>-1</sup>.

**Table S1.** Calculated amounts of different label components, and their respective values for  $a_{iso}$ ,  $\tau$ , and exchange coupling, as measured by EPR spectroscopy. The signal for SCNP<sub>water</sub>A<sub>50</sub>B<sub>50</sub> at 1 mg mL<sup>-1</sup> was too weak to be simulated.

Sample	Concentration mg/mL	$a_{iso, total}$	Species 1			Species 2			Species 3		
			Amount /%	$\tau$ x10 <sup>-10</sup>	Exchange coupling /MHz	Amount /%	$\tau$ x10 <sup>-10</sup>	Exchange coupling /MHz	Amount /%	$\tau$ x10 <sup>-10</sup>	Exchange coupling /MHz
SCNP <sub>water</sub> B <sub>100</sub>	10	1.69	0.20	7.28	3.0	0.65	21.3	3.0	0.15	0.19	0.0
	7.5	1.69	0.20	7.28	3.0	0.65	21.3	3.0	0.15	0.19	0.0
	5	1.69	0.20	7.28	3.0	0.65	21.3	3.0	0.15	0.19	0.0
	2.5	1.69	0.20	7.28	3.0	0.65	21.3	3.0	0.15	0.19	0.0
	1	1.69	0.20	7.28	3.0	0.65	21.3	3.0	0.15	0.19	0.0
SCNP <sub>water</sub> A <sub>50</sub> B <sub>50</sub>	10	1.69	0.35	7.28	3.0	0.65	21.3	3.0	-	-	-
	7.5	1.69	0.35	7.28	3.0	0.65	21.3	3.0	-	-	-
	5	1.69	0.35	7.28	3.0	0.65	21.3	3.0	-	-	-
	2.5	1.69	0.35	7.28	3.0	0.65	21.3	3.0	-	-	-
	1	-	-	-	-	-	-	-	-	-	-
SCNP <sub>water</sub> A <sub>75</sub> B <sub>25</sub>	10	1.69	0.35	7.28	3.0	0.65	21.3	3.0	-	-	-
	7.5	1.69	0.35	7.28	3.0	0.65	21.3	3.0	-	-	-
	5	1.69	0.35	7.28	3.0	0.65	21.3	3.0	-	-	-
	2.5	1.69	0.35	7.28	3.0	0.65	21.3	3.0	-	-	-
	1	1.69	0.35	7.28	3.0	0.65	21.3	3.0	-	-	-
SCNP <sub>THF</sub> B <sub>100</sub>	10	1.69	0.15	5.10	2.8	0.85	21.3	2.8	-	-	-
	7.5	1.69	0.15	5.10	2.8	0.85	21.3	2.8	-	-	-
	5	1.69	0.15	5.10	2.8	0.85	21.3	2.8	-	-	-
	2.5	1.69	0.15	5.10	2.8	0.85	21.3	2.8	-	-	-
	1	1.69	0.15	5.10	2.8	0.85	21.3	2.8	-	-	-
SCNP <sub>THF</sub> A <sub>50</sub> B <sub>50</sub>	10	1.71	0.35	5.10	3.0	0.65	21.3	3.0	-	-	-
	7.5	1.71	0.35	5.10	3.0	0.65	21.3	3.0	-	-	-
	5	1.71	0.35	5.10	3.0	0.65	21.3	3.0	-	-	-
	2.5	1.71	0.35	5.10	3.0	0.65	21.3	3.0	-	-	-
	1	1.71	0.35	5.10	3.0	0.65	21.3	3.0	-	-	-
SCNP <sub>THF</sub> A <sub>75</sub> B <sub>25</sub>	10	1.71	0.15	5.10	2.5	0.85	21.3	2.5	-	-	-
	7.5	1.71	0.15	5.10	2.5	0.85	21.3	2.5	-	-	-
	5	1.71	0.15	5.10	2.5	0.85	21.3	2.5	-	-	-
	2.5	1.71	0.15	5.10	2.5	0.85	21.3	2.5	-	-	-
	1	1.71	0.15	5.10	2.5	0.85	21.3	2.5	-	-	-

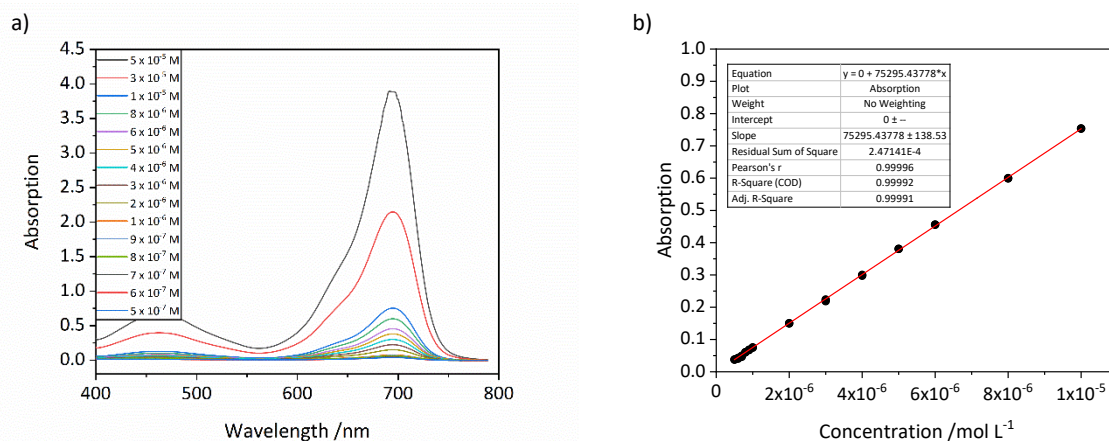


**Figure S9.** a) Absorption spectra of aza-BODIPY in water with KolEl as surfactant at concentrations from  $5 \times 10^{-7}$  M to  $5 \times 10^{-5}$  M. b) Concentration dependent absorption of aza-BODIPY in water at 695 nm with linear fit.

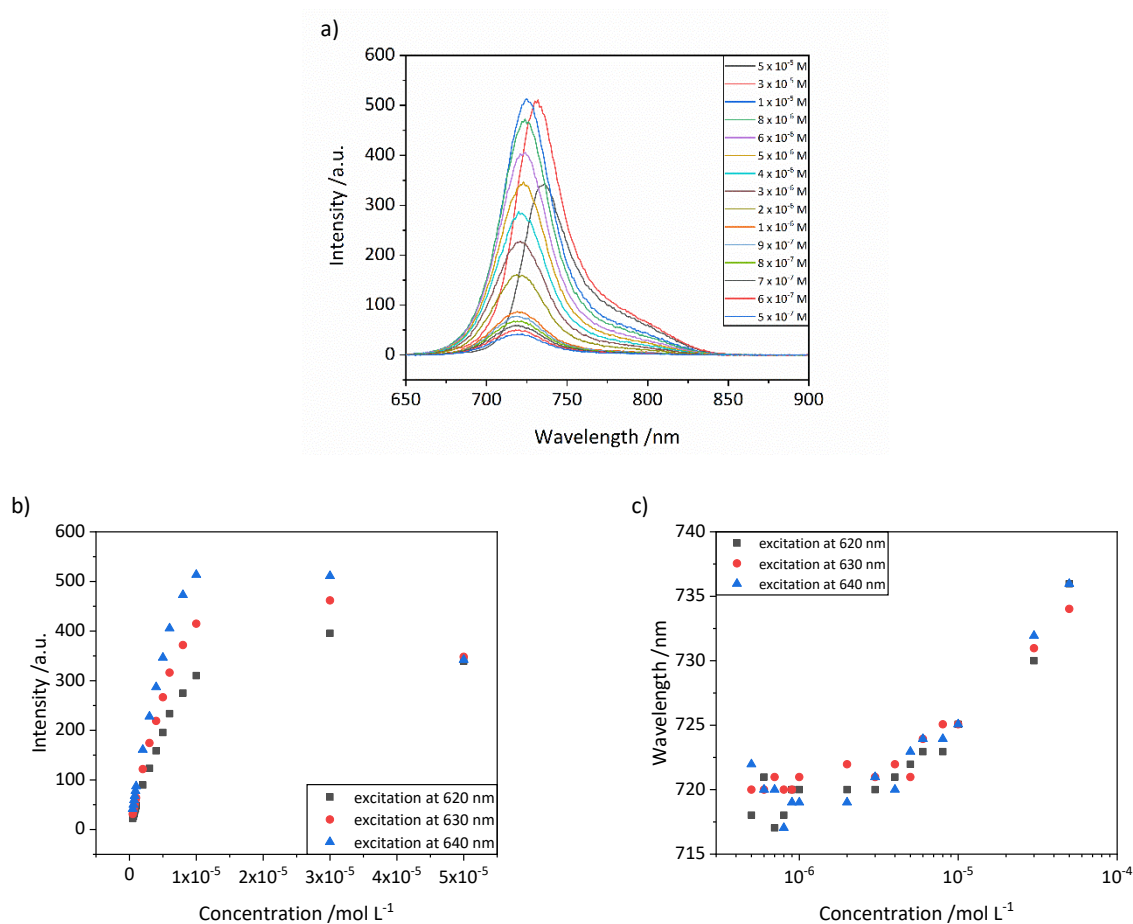


**Figure S10.** a) Fluorescence spectra of aza-BODIPY in water with KolEl as surfactant at concentrations from  $5 \times 10^{-7}$  M to  $5 \times 10^{-5}$  M,  $\lambda_{\text{exc}} = 640$  nm, slit = 5 nm,  $V_{\text{detector}} = 600$  V. Concentration dependence of b) intensity, and c) maximum wavelength of aza-BODIPY in water with KolEl as surfactant.

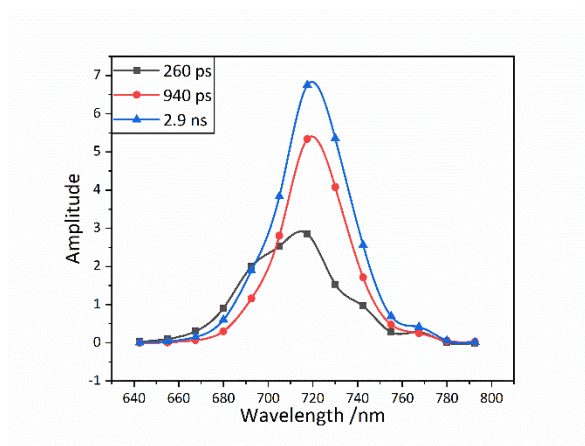


**Figure S11.** Decay associated spectrum of aza-BODIPY in water with Kolliphor EL as surfactant at a concentration of  $5 \times 10^{-5}$  M.

# Thermoresponsive Swelling of Fluorescent Single-Chain Nanoparticles

Justus F. Thümmeler, Ramesh Maragani, Franz-Josef Schmitt, Guo Tang, Samira Mahmoudi  
Rahmanlou, Jan Laufer, Henrike Lucas, Karsten Mäder, Wolfgang H. Binder\*

## Table of Contents

Experimental Procedures .....	2
Chemicals .....	2
Instrumentation and Analysis.....	2
Synthesis and Sample Preparation .....	5
Supporting Tables and Figures .....	13

# Experimental Procedures

## Chemicals

All chemicals were purchased from Sigma Aldrich except tetrabutylammonium bromide (TCI), sodium hydroxide (Grüssing), triethylamine (TCI), 3-chloro-1-propanol (TCI), *p*-hydroxycalcone (TCI), diethylamine (Fluka), propargyltosylate (Fluka), nitromethane (Alfa Aesar) and CuSO<sub>4</sub> x 5 H<sub>2</sub>O (VEB Laborchemikalien). Before use, azobisisobutyronitrile (AIBN) was freshly recrystallized from methanol. Oligo(ethylene glycol) methyl ether methacrylate (M<sub>n</sub>=300) was passed through a basic AlO<sub>x</sub>-column to remove the stabilizer.

## Instrumentation and Analysis

*ESI-TOF-MS* measurements were performed on a Bruker Daltonics microTOF via direct injection at a flow rate of 180 μL h<sup>-1</sup> in positive mode with an acceleration voltage of 4.5 kV. Samples were prepared by dissolving in a mixture of LC-MS grade methanol and LC-MS grade tetrahydrofuran in a ratio of 1 to 8. The instrument was calibrated using the ESI-L low concentration tuning mix from Agilent Technologies (product no. G1969-85000). The software Data Analysis (version 4.0) was used for data evaluation.

*NMR spectra* were measured on an Agilent Technologies 400 MHz VNMRs and 500 MHz DD2 at 27°C. Chemical shifts (δ) are reported in ppm and referred to the solvent residual signal (CDCl<sub>3</sub> 7.26 ppm for <sup>1</sup>H and 77.0 ppm for <sup>13</sup>C, methanol-d<sub>4</sub> 3.31 ppm for <sup>1</sup>H and 49.0 ppm for <sup>13</sup>C, D<sub>2</sub>O 4.66 ppm for <sup>1</sup>H).

*DOSY-NMR measurements* were done on an Agilent VNMR DD2 500 MHz (sfrq = 499.727 MHz). The experiment was performed under OpenVnmrJ 1.1 and equipped with a 5 mm PFG One NMR probe, z-gradient and temperature unit. Diffusion ordered NMR data were acquired by means of the Agilent pulse program DgcsteSL\_cc using a stimulated echo with self-compensating gradient schemes and conventional compensation. The length of the gradient pulse was set to 3.0 ms for <sup>1</sup>H in combination with a diffusion period of 300 ms (D<sub>2</sub>O). Data were systematically accumulated by linearly varying the diffusion encoding gradients over a range from 2% to 95% for 64 gradient increment values.

The hydrodynamic diameter *D<sub>h</sub>* were calculated using the Stokes-Einstein equation

$$D_h = \frac{k_B \cdot T}{3 \cdot \pi \cdot \eta_{D2O}(T) \cdot D} \quad (S1)$$

with the Boltzmann constant *k<sub>B</sub>*, temperature *T*, diffusion coefficient *D*, and the temperature dependent viscosity of the solvent  $\eta_{D2O}(T)$ . The viscosity  $\eta_{D2O}$  was calculated with

$$\eta_{D2O} [mPa \cdot s] = 0.313 + 38112,5 * e^{-0,036 * T [K]} \quad (S2)$$

plotting data were taken from Millero et al. (1971).<sup>1</sup>

*ATR-IR spectra* were measured on a Bruker Tensor Vertex 70 equipped with a Golden Gate Heated Diamond ATR Top-plate.

*THF-based SEC measurements* were performed at 30 °C on a Viscotek GPCmax VE 2001 from Viscotek™ applying a CLM3008 precolumn and a CLM3008 main column. As solvent THF was used and the sample concentration was adjusted to 3 mg·mL<sup>-1</sup> while applying a flow rate of 1 ml·min<sup>-1</sup>. For determination of the molecular weights the refractive index of the investigated sample was detected with a VE 3580 RI detector of Viscotek™. External calibration was done using poly(styrene) (PS) standards (purchased from PSS) with a molecular weight range from 1050 to 115000 g mol<sup>-1</sup>.

*Cell toxicity* of the SCNP formulations was tested using a Resazurin reduction 96 well assay on NHDF cells. Two time points were analyzed. NHDF were cultured in DMEM (high glucose) + 10% FCS + 1% penicillin-streptomycin @ 37 °C under 5% CO<sub>2</sub> in a standard cell culture incubator. For 24 h 20,000 cells/100 µL were seeded per 96 well, for 96 h 5,000 cells/100 µL were used. On the 2nd day after seeding, SCNP formulations were added in increasing concentrations from 0.00001 mg/ml to 0.5 mg/mL. Pure cell culture medium served as negative control (= 100% viability) and 0.025% Triton X100 was used as positive control (= 0% viability). All varying concentrations of the assay were performed as octuplicates (n = 8). After incubating for 24 or 96 h, resp., 20 µL Resazurin stock solution (440 µM in PBS, f.c. 44 µM) was added to each well and the mixture was incubated for 2 h @ 37 °C under 5% CO<sub>2</sub>. Then, fluorescence intensity was determined with the Cytation<sup>TM</sup> 5 imaging reader (BioTek Instruments) using for excitation the BP 531(20) and for emission BP 593(20). Cell viability was expressed as a percentage of the negative controls (untreated cells) after subtraction of the blank. The assay was performed three times and then, mean and S.D. were calculated and plotted for data evaluation (n = 3).

*Turbidimetry measurements* were performed on a JASCO J-1500 with a PTC-510 cell holder. The samples were measured in Helma analytics quartz glass cuvettes (d = 1 mm) at concentrations of 1 mg/mL in water. The samples were heated from 30 °C to 90°C with a heating rate of 1 K/min. The transmittance was measured at a wavelength of 500 nm. The temperature at 50% of the normalized transmittance was taken as cloud point temperature  $T_{cp}$ .

*UV/VIS/NIR-absorption measurements* were performed on a Perkin Elmer LAMBDA 365 UV/Vis Spectrophotometer using Helma analytics quartz glass cuvettes (d = 10 mm). Temperature control was achieved using the Perkin Elmer Peltier System L365. The measurements were each repeated three times.

*Fluorescence spectra* were measured on a Cary Eclipse fluorescence spectrometer of Agilent using Helma analytics quartz glass cuvettes (d = 10 mm). Temperature control was achieved using the Agilent Cary Single Cell Peltier Accessory Type SPVF-1x0. The measurements were each repeated three times.

*Decay associated spectra* were recorded employing a Hamamatsu R5900 16-channel multi-anode photomultiplier tube (PMT) with 16 separate output (anode) elements and a common cathode and dynode system (PML-16C, Becker&Hickl, Berlin, Germany) as described in Schmitt et al. 2020. A 632 nm pulsed laser diode (PDL-600, Becker&Hickl, Berlin) delivering 80 ps FWHM pulses at a repetition rate of 20 MHz was used for excitation. The fluorescence was observed via a 633 nm longpass filter (F76-631, AHF Analysentechnik, Tübingen, Germany). The determination of the DAS is described in detail in Schmitt et al. 2019.

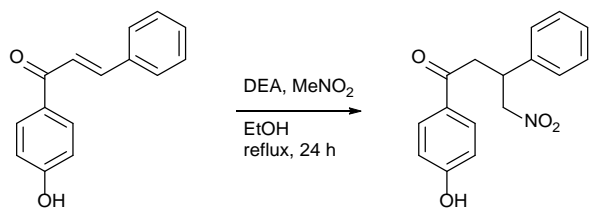
The sample was placed in a standard 1x1 cm Quartz cuvette and cuvette holder (CHV100, Thorlabs, Newton, USA). The temperature was adjusted by a Peltier element at the surface of the cuvette holder with the warm side attached with thermally conductive paste. Temperature was then monitored with a standard thermoelement with an accuracy of about +/- 1°C. The measurements were each repeated three times.

*Photoacoustic (PA) pump-probe spectroscopy*: A wavelength tuneable dual-OPO laser system (SpitLight EVO III Dual OPO, Innolas Laser GmbH, Germany) provided pump and probe excitation pulses of 5 ns duration at a repetition frequency of 100 Hz. The outputs of the OPO laser system were coupled into a bifurcated fiber bundle (8 mm core diameter) (Laser Components GmbH, Germany) for the measurement. A custom-made cuvette (path length = 6 mm, volume = 2 mL) was placed in a water bath filled in with distilled water and illuminated with the output of the fiber bundle (10 mm beam diameter at the cuvette). Neutral density filters were used to control the optical fluence. The PA signal was detected using a polyvinylidene fluoride

transducer (PA1483, Precision Acoustics Ltd., UK), amplified with a 20 dB voltage preamplifier (HVA-200M-40-F, FEMTO Messtechnik GmbH, Germany) and recorded using a digitizer card (National Instruments, USA). The efficiency of the PA signal generation in fluorophores was varied by exploiting the effects of stimulated emission, i.e., the SCNP solutions were illuminated with a pump pulse that coincides with the absorption spectrum while the probe pulse coincided with the maximum of the fluorescence spectrum. The time-course of the PA signal amplitude was generated using simultaneous pump-probe excitation. PA signals were measured at room temperature in aqueous SCNP solutions with a concentration of  $1 \text{ mgmL}^{-1}$  and in pure aBOD dye solutions with a concentration of  $10^{-4} \text{ M}$  using pump and probe wavelengths that coincided with the wavelengths of their peak absorption and fluorescence ( $\lambda_{\text{pump}} = 704 \text{ nm}$  and  $\lambda_{\text{probe}} = 720 \text{ nm}$  for SCNP solutions,  $\lambda_{\text{pump}} = 700 \text{ nm}$  and  $\lambda_{\text{probe}} = 720 \text{ nm}$  for pure dye solutions).

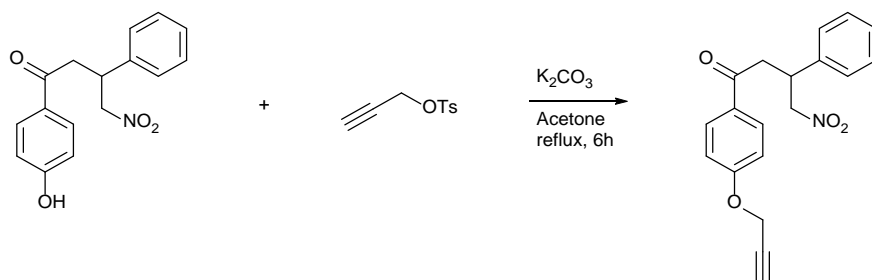
## Synthesis and Sample Preparation

### Synthesis of 1-(4-hydroxyphenyl)-4-nitro-3-phenylbutan-1-one **1**



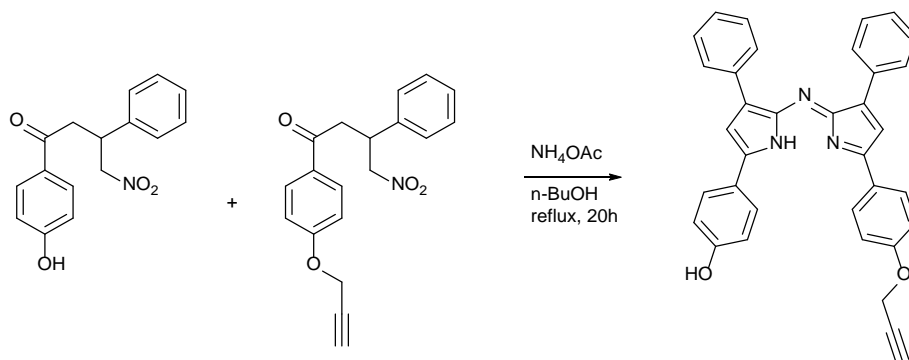
*p*-Hydroxychalcone (14.7 mmol, 3g) was dissolved in ethanol (20 mL). The solution was heated to reflux (90°C oil bath temperature). Diethylamine (66.75 mmol, 4.88 g, 6.9 mL) and nitromethane (147 mmol, 8.15 g, 7.2 mL) were added dropwise and the reaction solution was stirred under reflux for 18 h. The solution was poured in 100 mL 1 M HCl and the product extracted with ethyl acetate. The crude product was purified by column chromatography (methanol:DCM 1:10,  $R_f = 0.47$ ).  $^1\text{H-NMR}$  ( $\text{CDCl}_3$ , 400 MHz,  $\delta$  in ppm): 7.85 (2H, m,  $H_{Ar}$ ), 7.33 (2H, m, edge://settings/profiles  $H_{Ar}$ ), 7.27 (3H, m,  $H_{Ar}$ ), 6.86 (2H, m,  $H_{Ar}$ ), 5.74 (1H, s (broad), OH), 4.88-4.64 (2H, m,  $\text{NO}_2\text{-CH}_2$ ), 4.21 (1H, m, Ph-CH), 3.39 (2H, m, O=C- $\text{CH}_2$ ).

### Synthesis of 4-nitro-3-phenyl-1-(4-(prop-2-yn-1-yloxy)phenyl)butan-1-one **2**



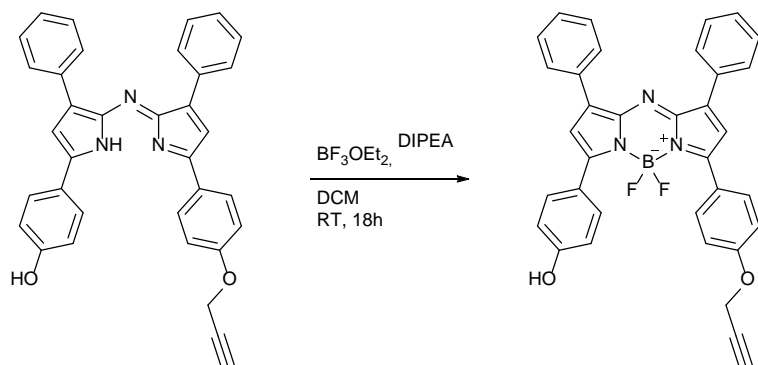
**1** (5 mmol, 1.43g) was dissolved in acetone (30 mL).  $\text{K}_2\text{CO}_3$  (15 mmol, 2.07 g) was added and the dispersion was heated to 70°C (reflux). After 1 h propargyl tosylate (7.5 mmol, 1.58 g, 1.28 mL) was dissolved in 5 mL acetone and added to the reaction mixture. After 6 h it was cooled to room temperature, filtrated and the acetone was removed under reduced pressure. The crude product was dissolved in ethyl acetate and washed with water. The organic phase was dried with  $\text{Na}_2\text{SO}_4$  and removed under reduced pressure. The product was purified by column chromatography (ethyl acetate:hexane 1:3,  $R_f = 0.25$ ). Yield: 55%.  $^1\text{H-NMR}$  ( $\text{CDCl}_3$ , 400 MHz,  $\delta$  in ppm): 7.91 (2H, m,  $H_{Ar}$ ), 7.33 (2H, m,  $H_{Ar}$ ), 7.27 (3H, m,  $H_{Ar}$ ), 7.01 (2H, m,  $H_{Ar}$ ), 5.74 (1H, s (broad), OH), 4.86-4.65 (2H, m,  $\text{NO}_2\text{-CH}_2$ ), 4.75 (2H, d,  $J = 2.4$  Hz,  $\equiv\text{C-CH}_2$ ), 4.21 (1H, m, Ph-CH), 3.40 (2H, m, O=C- $\text{CH}_2$ ), 2.55 (1H, t,  $J = 2.4$  Hz,  $\equiv\text{CH}$ ).

### Synthesis of [5-(4-Hydroxyphenyl)-3-phenyl-1H-pyrrol-2-yl]-[4-prop-2-yn-1-yloxyphenyl]-3-phenylpyrrol-2-ylidene]amine **3**



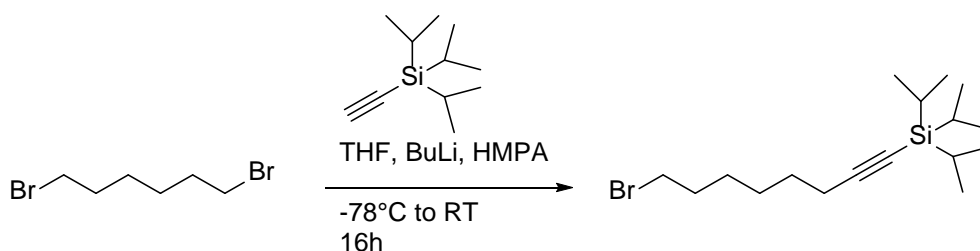
**1** (2.16 mmol, 618 mg), **2** (2.16 mmol, 700 mg) and ammonium acetate (150 mmol, 11.6 g) in *n*-BuOH (50 mL) were heated under reflux (130°C oil bath) for 20 h. The reaction mixture was cooled in an ice bath and filtrated. The isolated solid was washed with cold *n*-BuOH and dried under vacuum. The product was purified by column chromatography (CHCl<sub>3</sub>:methanol 20:1, *R<sub>f</sub>* = 0.51). Yield: 7%. <sup>1</sup>H-NMR (CDCl<sub>3</sub>, 500 MHz, δ in ppm): 8.05 (4H, m, *H<sub>Ar</sub>*), 7.93 – 7.82 (4H, m, *H<sub>Ar</sub>*), 7.42 (4H, m, *H<sub>Ar</sub>*), 7.35 (2H, m, *H<sub>Ar</sub>*), 7.13 (4H, m, *H<sub>Ar</sub>*), 6.99 (2, m, *H<sub>Ar</sub>*), 4.80 (2H, d, *J* = 2.3 Hz, ≡C-CH<sub>2</sub>), 2.59 (1H, t, *J* = 2.3 Hz, ≡CH).

*Synthesis of BF<sub>2</sub>-chelate of [5-(4-Hydroxyphenyl)-3-phenyl-1H-pyrrol-2-yl]-[4-prop-2-yn-1-yloxyphenyl]-3-phenylpyrrol-2-ylidene]amine 4 (αBOD)*



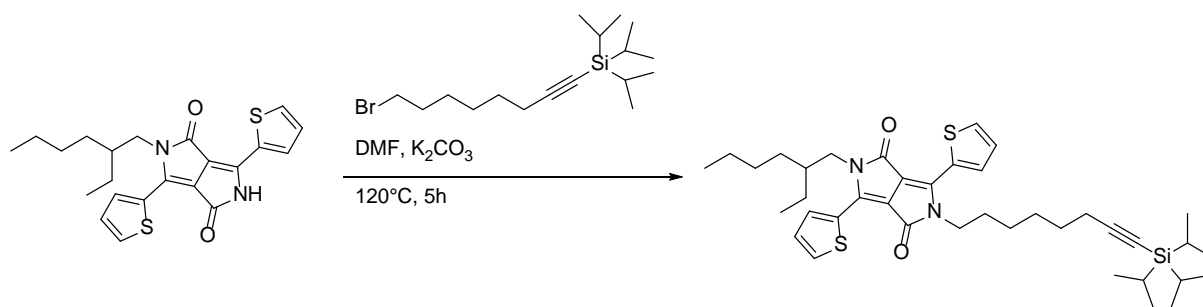
**3** (0.15 mmol, 80 mg) was dissolved in dry DCM (20 mL). DIPEA (1.8 mmol, 233 mg, 306 μL) was added. The solution was stirred for 10 min at room temperature before being cooled to 0°C. BF<sub>3</sub>OEt<sub>2</sub> (2.7 mmol, 383 mg, 333 μL) was added. The resulting solution was stirred at 0 °C for 30 min and then at room temperature for 18 h. The product solution was diluted with ethyl acetate, washed with NH<sub>4</sub>Cl-solution, brine, and water, dried with Na<sub>2</sub>SO<sub>4</sub>, and the solvent removed under reduced pressure. The crude product was purified by column chromatography (ethyl acetate:hexane 1:1, *R<sub>f</sub>* = 0.38) to get the product as a red solid. Yield: 91%. <sup>1</sup>H-NMR (CDCl<sub>3</sub>, 500 MHz, δ in ppm): 8.13 - 8.02 (8H, m, *H<sub>Ar</sub>*), 7.50 – 7.40 (6H, m, *H<sub>Ar</sub>*), 7.13 – 7.06 (2H, m, *H<sub>Ar</sub>*), 7.04 (2H, m, *H<sub>Ar</sub>*), 6.96 - 6.92 (2H, m, *H<sub>Ar</sub>*), 4.78 (2H, d, *J* = 2.4 Hz, ≡C-CH<sub>2</sub>), 2.58 (1H, t, *J* = 2.4 Hz, ≡CH).

*Synthesis of (8-bromooct-1-yn-1-yl)triisopropylsilane 5*



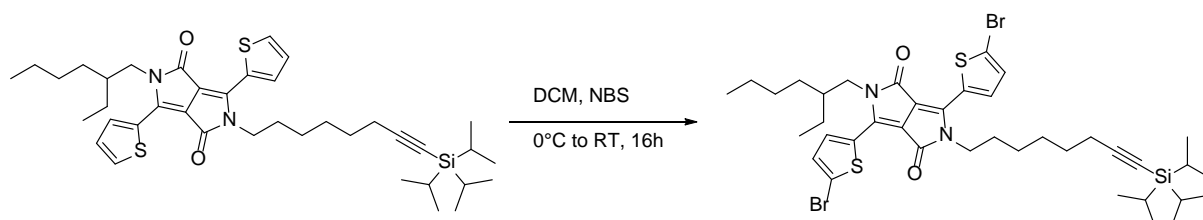
A flame dried flask flushed with argon was cooled to –78 °C and charged with a solution of ethynyltriisopropylsilane (2.0 g, 10.98 mmol) in dry THF (15 mL). After stirring the mixture at –78°C for 5 min, *n*-BuLi was added dropwise (2.5 M in hexane, 4.39 ml, 10.98 mmol). After stirring at –78°C for 1 h, HMPA (5.43 ml, 31.22 mmol) was added. To this resulting solution a solution of 1,5-dibromohexane (3.20 g, 13.11 mmol) in THF (5 mL) was added dropwise. The mixture was stirred at –78°C for 5 min and then at room temperature for 16 h. The reaction was quenched with a saturated aqueous solution of NH<sub>4</sub>Cl (10 mL) and volatiles were removed under reduced pressure. The aqueous phase was extracted with DCM (3 × 20 mL) and the combined organic layers were dried over Na<sub>2</sub>SO<sub>4</sub>, filtered, and the solvent removed under reduced pressure. The crude product was purified using column chromatography (hexane) to get **5** as a colourless oil. Yield: 88%. <sup>1</sup>H-NMR (CDCl<sub>3</sub>, 400 MHz, δ in ppm): 3.41 (m, 2H), 2.26 (t, 2H), 1.56 (q, 3H), 1.46 (m, 4H), 1.27 (m, 3H), 1.05 (m, 16H), 0.80 (m, 3H); <sup>13</sup>C-NMR (CDCl<sub>3</sub>, 100 MHz, δ in ppm): 108.79, 80.24, 77.31, 76.99, 76.87, 34.65, 33.57, 33.42, 32.69, 32.51, 31.58, 29.05, 28.72, 28.56, 27.74, 27.61, 27.29, 26.90, 22.64, 22.57, 20.65, 19.60, 18.59, 18.50, 14.06, 11.37, 11.29, 11.14.

*Synthesis of 2-(2-ethylhexyl)-3,6-di(thiophen-2-yl)-5-(8-(triisopropylsilyl)oct-7-yn-1-yl)-2,5-dihydropyrrolo[3,4-c]pyrrole-1,4-dione **6***



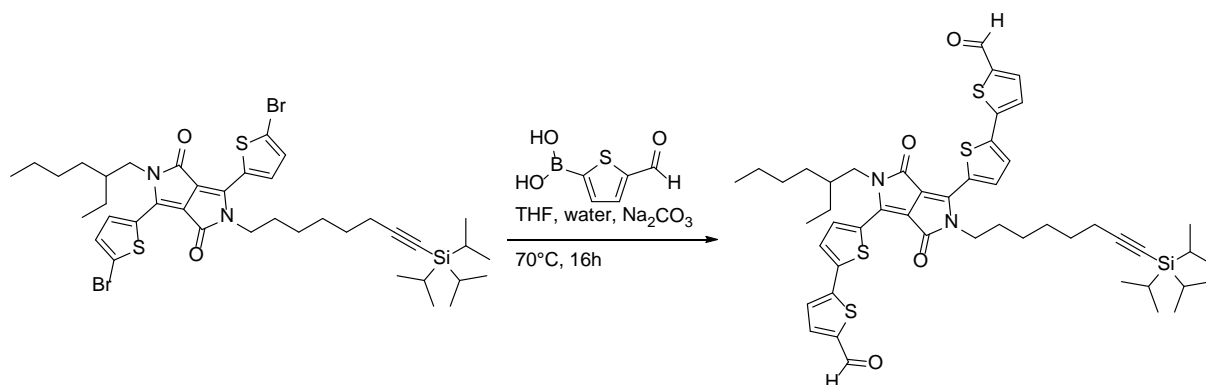
In 50 ml anhydrous dimethylformamide 2-(2-methylheptyl)-3,6-di(thiophen-2-yl)-2,5-dihydropyrrolo[3,4-c]pyrrole-1,4-dione (1.0 g, 2.42 mmol) and 18-crown-6 (0.032 g, 0.12 mmol) were dissolved at 120°C. Anhydrous  $K_2CO_3$  (0.502 g, 3.63 mmol) was added. After 1 h **5** (1.08 g, 3.13 mmol) was added dropwise over 1 h and stirring was maintained for 20 h. The cooled reaction mixture was diluted with 20 ml water and 15 ml ethyl acetate, concentrated under reduced pressure, dissolved in ethyl acetate, washed with water and dried using  $MgSO_4$ . After removing solvents under reduced pressure, the residue was precipitated from chloroform into methanol and the collected precipitates were further purified via column chromatography using 0 - 10 % diethyl ether in hexane (best separation effect at 5 %) to get **6** as a dark red solid. Yield: 73%.  $^1H$ -NMR ( $CDCl_3$ , 400 MHz,  $\delta$  in ppm): 8.93 (d,  $J = 2$ Hz, 2H) 7.63 (d, 2H), 7.26 (t, 2H), 4.07 (t, 4H), 2.24 (t, 2H), 1.75 (m, 4 H), 1.52 (m, 10 H), 1.04 (m, 30H);  $^{13}C$ -NMR ( $CDCl_3$ , 100 MHz,  $\delta$  in ppm): 161.72, 161.32, 140.36, 139.95, 135.34, 135.25, 133.42, 132.26, 130.62, 129.71, 128.59, 128.36, 108.96, 107.68, 80.17, 52.11, 45.83, 42.09, 39.07, 30.21, 29.88, 28.27, 26.36, 23.51, 23.05, 19.72, 18.63, 14.00, 11.56, 11.26, 10.48 ppm; MALDI-TOF:  $m/z$  calculated for  $C_{39}H_{56}N_2O_2S_2Si$ , 676. 355 [M] found 676.304.

*Synthesis of 3,6-bis(5-bromothiophen-2-yl)-2-(2-ethylhexyl)-5-(8-(triisopropylsilyl)oct-7-yn-1-yl)-2,5-dihydropyrrolo[3,4-c]pyrrole-1,4-dione **7***

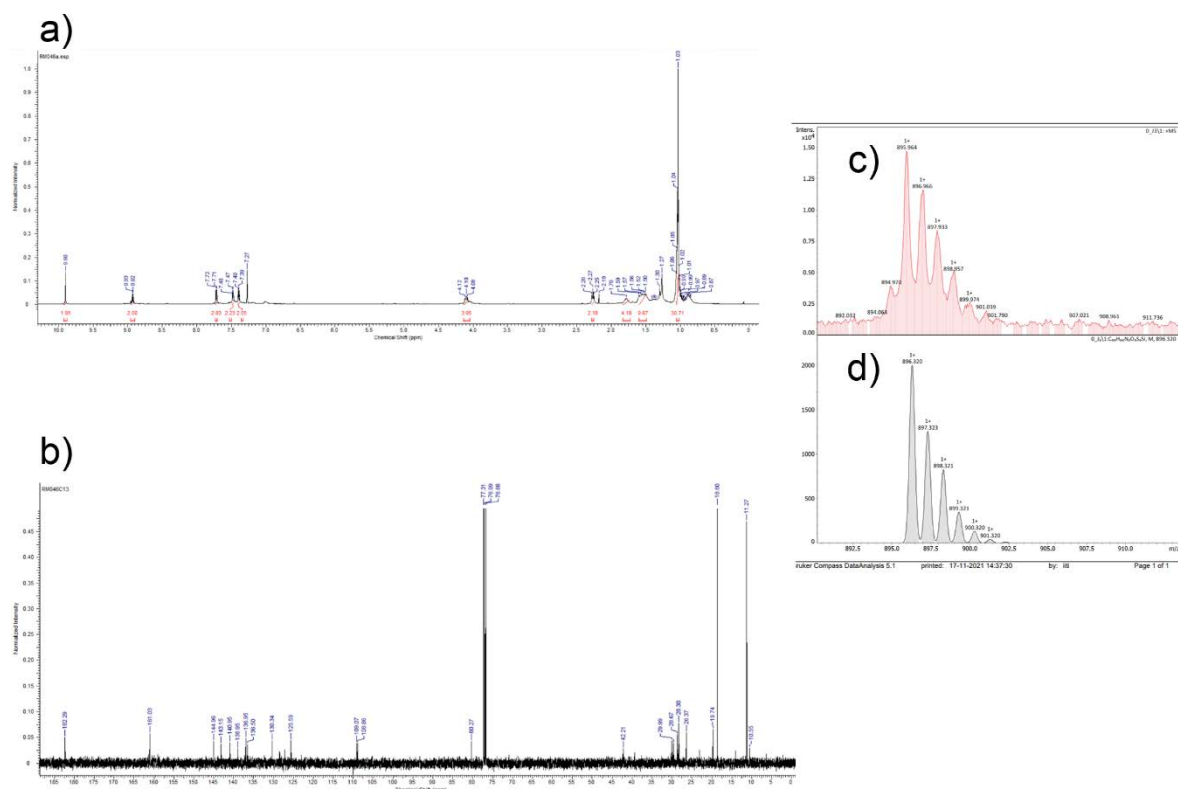


To a solution of compound **6** (1.0 g, 1.47 mmol) in 35 mL chloroform at 0 °C N-bromosuccinimide (0.579 g, 3.25 mmol) was added in portions. After stirring for 16 h protected from light the reaction solution was washed with water and brine, and dried over  $MgSO_4$ . Upon removing solvents under reduced pressure, the target material was isolated by column chromatography, using 8 - 10 % diethyl ether in hexane to get **7** as purple solid. Yield: 48%.  $^1H$ -NMR ( $CDCl_3$ , 400 MHz,  $\delta$  in ppm): 8.69 (d,  $J = 2$ Hz, 2H) 7.26 (d, 2H), 4.00 (t, 4H), 2.26 (t, 2H), 1.75 (m, 4 H), 1.35 (m, 10 H), 1.04 (m, 30H);  $^{13}C$ -NMR ( $CDCl_3$ , 100 MHz,  $\delta$  in ppm): 160.96, 135.35, 131.64, 131.03, 108.90, 42.15, 29.94, 28.65, 28.26, 28.33, 23.02, 19.72, 18.62, 11.26, 10.45 ppm; MALDI-TOF:  $m/z$  calculated for  $C_{39}H_{54}Br_2N_2O_2S_2Si$ , 832. 176 [M] found 832.056.

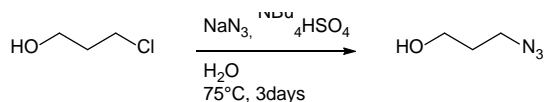
Synthesis of 5',5'''-(2-(2-ethylhexyl)-3,6-dioxo-5-(8-(triisopropylsilyl)oct-7-yn-1-yl)-2,3,5,6-tetrahydropyrrolo[3,4-c]pyrrole-1,4-diyl)bis([(2,2'-bithiophene)-5-carbaldehyde]) **8** (DPP)



**7** (0.2 g, 0.24 mmol), Pd(PPh<sub>3</sub>)<sub>4</sub> (0.013 g, 0.01 mmol), and Na<sub>2</sub>CO<sub>3</sub> (0.254 g, 2.39 mmol) were dissolved in degassed THF (19 mL) and degassed water (5 mL) under argon atmosphere. The mixture was heated to 45°C and stirred for 30 min. A solution of 5-formylthiophen-2-yl boronic acid (0.082 g, 0.52 mmol) in degassed THF (25 mL) was added slowly, and the mixture was refluxed for 12 h until a blue coloration was observed. After cooling to room temperature, the mixture was extracted with DCM and dried over Na<sub>2</sub>SO<sub>4</sub>. Upon removing solvents under reduced pressure, the crude product was purified by column chromatography using 28% DCM in hexane to get **8** as a dark purple solid. Yield: 46%. <sup>1</sup>H-NMR (CDCl<sub>3</sub>, 400 MHz, δ in ppm): 9.90 (s, 2H), 8.93 (d, J = 2 Hz, 2H), 7.72 (d, 2H), 4.30 (t, 4H), 2.26 (t, 2H), 1.75 (m, 4 H), 1.35 (m, 10 H), 1.03 (m, 30H); <sup>13</sup>C-NMR (CDCl<sub>3</sub>, 100 MHz, δ in ppm): 182.29, 161.03, 144.96, 143.15, 140.95, 138.95, 136.95, 136.50, 130.34, 131.64, 125.59, 109.07, 108.86, 80.27, 42.21, 29.99, 29.67, 28.30, 26.37, 19.74, 18.60, 11.27, 10.55 ppm; ESI-TOF: m/z calculated for C<sub>49</sub>H<sub>60</sub>N<sub>2</sub>O<sub>4</sub>S<sub>4</sub>Si, 896. 320 [M] found 895.964.

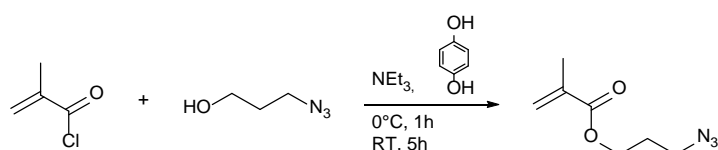


### Synthesis of 3-Azido-1-propanol **9**



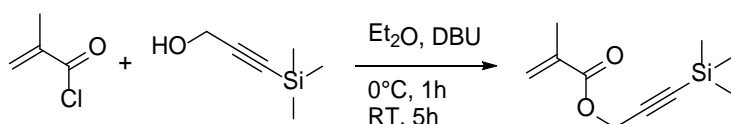
3-Chloro-1-propanol (23.5 mmol, 2.2 g, 2 ml) was added dropwise to a solution of sodium azide (48 mmol, 3.13 g) and tetrabutylammonium hydrogen sulphate (0.2 mmol, 70 mg) in 50 ml water at room temperature. The resulting solution was heated to 75°C. After stirring for three days the product was extracted with DCM. The combined organic phases were dried with Na<sub>2</sub>SO<sub>4</sub> and the solvent evaporated under vacuum to get the product as a colorless liquid. Yield: 85%. <sup>1</sup>H-NMR (CDCl<sub>3</sub>, 400 MHz, δ in ppm): 3.71 (2H, t, *J* = 6.0 Hz, HO-CH<sub>2</sub>), 3.42 (2H, t, *J* = 6.6 Hz, CH<sub>2</sub>-N<sub>3</sub>), 2.21 (1H, s, OH), 1.80 (2H, tt, *J* = 6.6, 6.0 Hz, CH<sub>2</sub>CH<sub>2</sub>CH<sub>2</sub>).

### Synthesis of 3-Azidopropyl methacrylate **10 (APMA)**



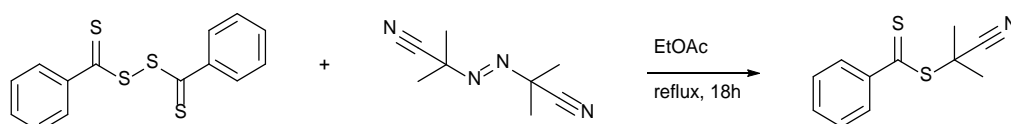
**9** (19.3 mmol, 1.95 g, 1.8 ml), triethylamine (28.7 mmol, 2.9 g, 4 ml) and hydroquinone (10 μmol, 1 mg) were dissolved in 25 ml of dry DCM and placed in an ice bath. Methacryloyl chloride (28.7 mmol, 3 g, 2.8 ml) in 5 ml of dry DCM was added dropwise. The resulting solution was stirred at 0°C for 1 h and at room temperature for additional 5 h. The white precipitate was removed by filtration and the product solution washed with water, saturated sodium bicarbonate solution and brine. The organic phase was dried with Na<sub>2</sub>SO<sub>4</sub> and the solvent was removed under vacuum. The product was purified by column chromatography (hexane:diethyl ether 2:1, R<sub>f</sub> = 0.46) to get the product as a pale-yellow liquid. The product was stored with hydroquinone as stabilizer. Yield: 25%. <sup>1</sup>H-NMR (CDCl<sub>3</sub>, 500 MHz, δ in ppm): 6.11 (1H, dq, *J* = 2.0, 1.0, =CH), 5.58 (1H, dq, *J* = 2.0, 1.6 Hz, =CH), 4.24 (2H, t, *J* = 6.2 Hz, COO-CH<sub>2</sub>), 3.42 (2H, t, *J* = 6.7 Hz, CH<sub>2</sub>-N<sub>3</sub>), 1.96 (2H, tt, *J* = 6.7, 6.2 Hz, CH<sub>2</sub>CH<sub>2</sub>CH<sub>2</sub>), 1.95 (3H, dd, *J* = 1.6, 1.0 Hz, CH<sub>3</sub>).

### Synthesis of 3-(Trimethylsilyl)propargyl methacrylate **11 (TMSPMA)**



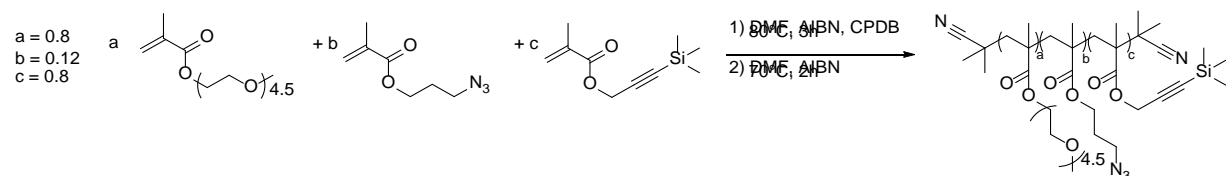
3-(Trimethylsilyl)propargyl alcohol (15.58 mmol, 2.0 g, 2.15 ml) and 1,8-diazabicyclo[5.4.0]undec-7-ene (18.7 mmol, 1.42 g, 1.4 ml) were solved in 20 ml of dry diethyl ether and cooled to 0°C. Methacryloyl chloride (18.7 mmol, 1.95 g, 1.8 ml) in 10 ml of dry diethyl ether was added dropwise. The resulting solution was stirred at 0°C for 1 h and at room temperature for additional 5 h. The yellow precipitate was removed by filtration and the product solution washed with water and brine. The organic phase was dried with Na<sub>2</sub>SO<sub>4</sub> and the solvent was removed under vacuum. The product was purified by column chromatography (hexane:diethyl ether 20:1, R<sub>f</sub> = 0.19) to get the product as colourless liquid. Yield: 30%. <sup>1</sup>H-NMR (CDCl<sub>3</sub>, 400 MHz, δ in ppm): 6.17 (1H, dq, *J* = 1.0, 2.2 Hz, =CH), 5.61 (1H, dq, *J* = 1.6, 2.2 Hz, =CH), 4.76 (2H, s, OCH<sub>2</sub>), 1.96 (3H, dd, *J* = 1.6, 1.0 Hz, CH<sub>3</sub>), 0.18 (9H, s, Si(CH<sub>3</sub>)<sub>3</sub>).

### Synthesis of Cyanoisopropyl dithiobenzoate **12 (CPDB)**



Bis(thiobenzoyl) disulfide (0.8 mmol, 245.2 mg) and AIBN (1.2 mmol, 197.1 mg) were dissolved in 10 ml ethyl acetate. The solution was degassed by five freeze-pump-thaw cycles and stirred under reflux for 18 h. The crude product was dried under vacuum and purified by column chromatography (hexane:ethyl acetate 10:1,  $R_f = 0.27$ ) to get the product as a red oil. Yield: 56%.  $^1\text{H-NMR}$  ( $\text{CDCl}_3$ , 400 MHz,  $\delta$  in ppm): 7.92 (2H, m, *o*- $H_{Ar}$ ), 7.56 (1H, m, *p*- $H_{Ar}$ ), 7.39 (2H, m, *m*- $H_{Ar}$ ), 1.94 (6H, s,  $\text{CH}_3$ ).

*Synthesis of Poly[(oligo(ethylene glycol) methyl ether methacrylate)-co-(3-azidopropyl methacrylate)-co-(3-(trimethylsilyl)propargyl methacrylate)] (PEATMA)*



Oligo(ethylene glycol) methyl ether methacrylate ( $M_n=300$ ) (11.52 mmol, 3.46 g), APMA (1.73 mmol, 292 mg, 273  $\mu\text{L}$ ) and TMSPMA (1.15 mmol, 226 mg, 243  $\mu\text{L}$ ) were dissolved in 2.8 ml dry DMF in a Schlenk tube. 2 mL of a stock solution of AIBN (4.8 mM, 9.6  $\mu\text{mol}$ ) and CPDB (24 mM, 48  $\mu\text{mol}$ ). The resulting mixture was degassed by five freeze-pump-thaw cycles and stirred at 80°C for 3 h. The product was precipitated in cold hexane:diethyl ether (2:1) as a pink polymer. To remove the CTA-endgroup, the polymer was dissolved in 20 mL DMF, AIBN (152  $\mu\text{mol}$ , 25 mg) was added and the solution degassed by bubbling with  $\text{N}_2$ . The solution was stirred at 70°C for 18 h. The solvent was removed under reduced pressure. The resulting yellow polymer was purified by dialysis in THF. The highly viscous product was stored in THF at 5°C to prevent auto-crosslinking. Yield: 54%. GPC (THF):  $M_n = 33.6$  kDa,  $D = 1.9$ .  $^1\text{H-NMR}$  ( $\text{CDCl}_3$ , 500 MHz,  $\delta$  in ppm): 4.66-4.55 ( $\text{CH}_2\text{-Si}(\text{CH}_3)_3$ ), 4.25-3.90 ( $\text{COOCH}_2$ ), 3.82-3.49 ( $\text{OCH}_2\text{CH}_2\text{O}$ ), 3.48-3.43 ( $\text{N}_3\text{CH}_2$ ), 3.39 ( $\text{OCH}_3$ ), 2.07-1.72 ( $\text{CH}_2$ ), 1.12-0.77 ( $\text{CH}_3$ ), 0.20 ( $\text{Si}(\text{CH}_3)_3$ ). IR (KBr): 2178  $\text{cm}^{-1}$  ( $\nu_{\text{alkyne}}$ ), 2100  $\text{cm}^{-1}$  ( $\nu_{\text{N}_3}$ ).

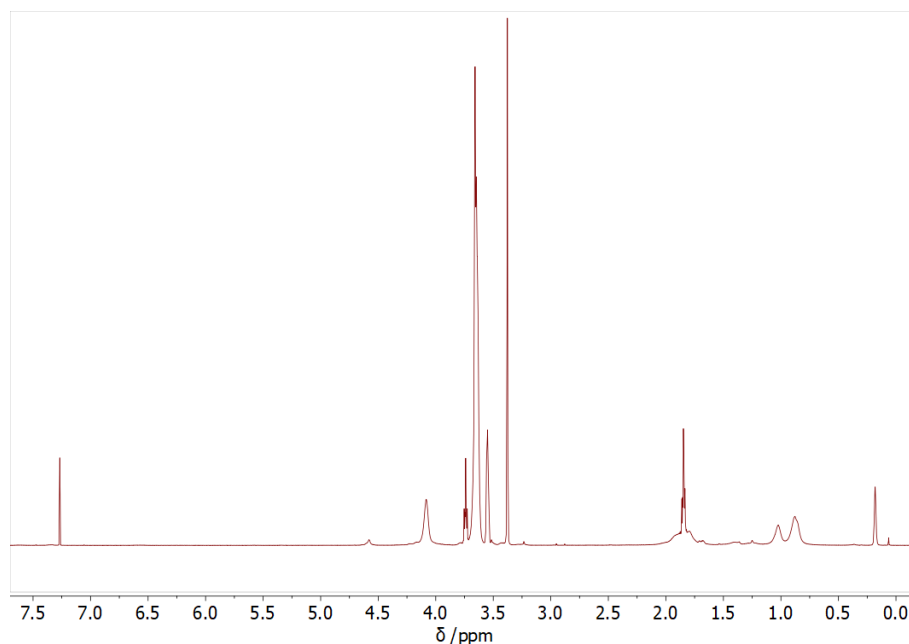
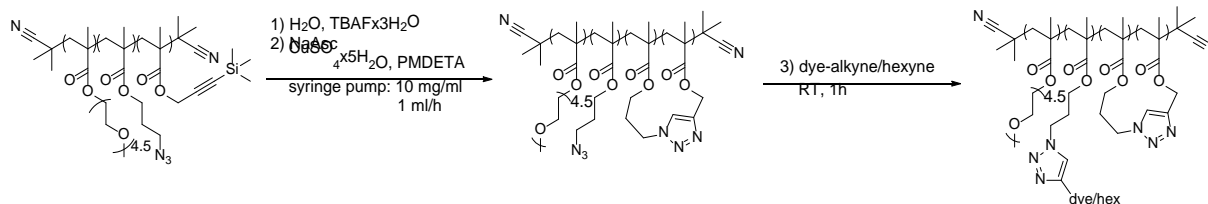


**Figure S2.** NMR spectrum of the precursor polymer PEATMA in  $\text{CDCl}_3$  (residual THF signals at 3.74 ppm and 1.85 ppm).

**General procedure for the single chain collapse (SCNP\_[dye]\_[dye content per SCNP])**



PEATMA (100 mg,  $4.35 \times 10^{-5}$  mol N<sub>3</sub>,  $2.90 \times 10^{-5}$  mol alkyne) was dissolved in 9 ml deionized water. A solution of TBAF x 3H<sub>2</sub>O (1.2 eq.  $3.48 \times 10^{-5}$  mol 11 mg) in 1 mL deionized water was added. The solution was put into a syringe pump (0.5 mL/h) and added to a solution of sodium ascorbate (7.5 mmol, 1.5 g), CuSO<sub>4</sub> x 5 H<sub>2</sub>O (0.5 mmol, 125 mg) and PMDTA (1 mmol, 173 mg, 209  $\mu$ l) in 100 ml degassed water. After 20 h the solution was stirred for one additional hour. For labelling, a solution of the corresponding, deprotected (for DPP) dye in 5 mL THF followed by a solution of hexyne in 5 mL THF were added, with 30 min stirring after each addition. For exact amounts of dye and hexyne for each synthesis see Table S1 below. For the purification it is important to keep the product wet since the redissolution of dried samples is difficult. The product (and THF) was extracted with DCM. The DCM was reduced under vacuum to get a solution in THF. This solution was passed over a silica column to remove remaining copper impurities. The resulting solution was purified by dialysis going from THF with 1 mL PMDTA to a mixture of water/THF (1:1) and in the end to pure THF. The product was dried under vacuum. Yield: 50%.

**Table S1.** Amount of the corresponding dyes and hexyne, that were used for the labelling reaction.

Sample name	dye	dye molecules per SCNP	amount of	
			dye (n / 10 <sup>-5</sup> mol; m / mg)	hexyne (n / 10 <sup>-5</sup> mol; m / mg)
SCNP_Hex	-	(hexyne only)	-	1.74; 1.44
SCNP_aBOD_1	aBOD	1	0.29; 1.65	1.74; 1.44
SCNP_aBOD_5	aBOD	5 (aBOD only)	1.74; 9.90	-
SCNP_DPP_1	DPP	1	0.29; 2.60	1.74; 1.44
SCNP_DPP_5	DPP	5 (DPP only)	1.74; 15.60	-

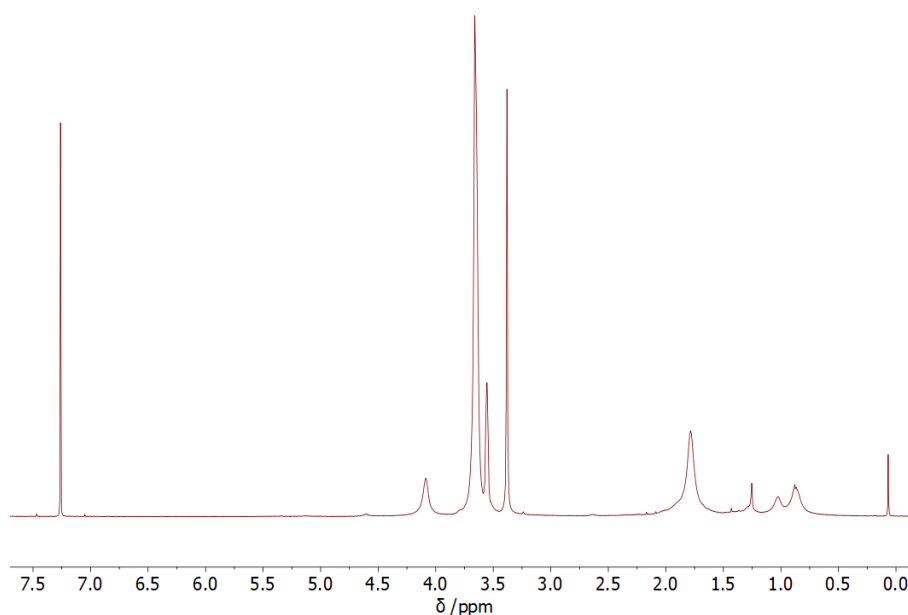


**Figure S3.** Exemplary NMR spectrum of the SCNP\_Hex in CDCl<sub>3</sub>, showing the complete consumption of the TMS-protected alkyne (removal of TMS at 0.20 ppm).

#### *Dispersing of SCNPs in water*

The solid (agglomerated) SCNP were placed in a vial and water was added. The suspension was stirred for 18 h until a milky dispersion was formed. The resulting dispersion was sonicated for several hours until it was clear. It is important for the temperature not to rise higher than 50°C. The SCNPs show LCST-behaviour in water and will not solubilize then.

#### *Solving aza-BODIPY in water ( $c = 5 \times 10^{-5} M$ )*

aza-BODIPY (5  $\mu\text{mol}$ , 3.03 mg) was dissolved in dry THF (2 ml) and Kolliphor EL (Kolel, 0.2 ml) was added. The resulting solution was sonicated for 30 minutes. The THF was removed under vacuum and the residue was dissolved in 100 ml water to get a dark green solution.

#### *Preparation of mixtures with complex biological media*

A dispersion of SCNP\_aBOD\_1 at a concentration of 1 mg/mL was prepared as described above. 200  $\mu\text{L}$  of this dispersion were added to 1.8 mL water, phosphate buffered saline (PBS), Dulbecco's Modified Eagle's Medium (DMEM), or DMEM with 10% bovine serum albumin (BSA) to reach concentrations of 0.1 mg/mL. The mixtures were vortexed and equilibrated for 24 h.

## Supporting Figures

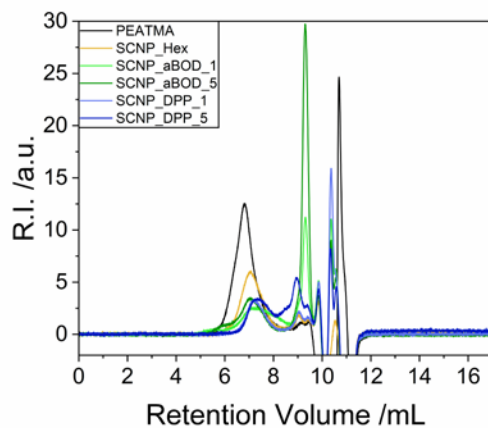


**Figure S4.** Baseline corrected R.I. traces of THF-based GPC measurements of PEATMA and the SCNPs. System peaks occur starting from ~8.5 mL.

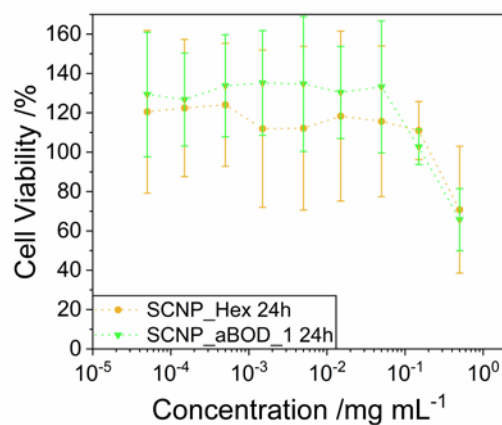


**Figure S5.** 24h Cell viability assay on NHDF cells of SCNP\_Hex and SCNP\_aBOD\_1.



**Figure S6.** DOSY-NMR spectra of SCNP\_Hex in D<sub>2</sub>O, measured at 27°C (green) and 45°C (red), showing a reduction in hydrodynamic diameter at high temperatures.

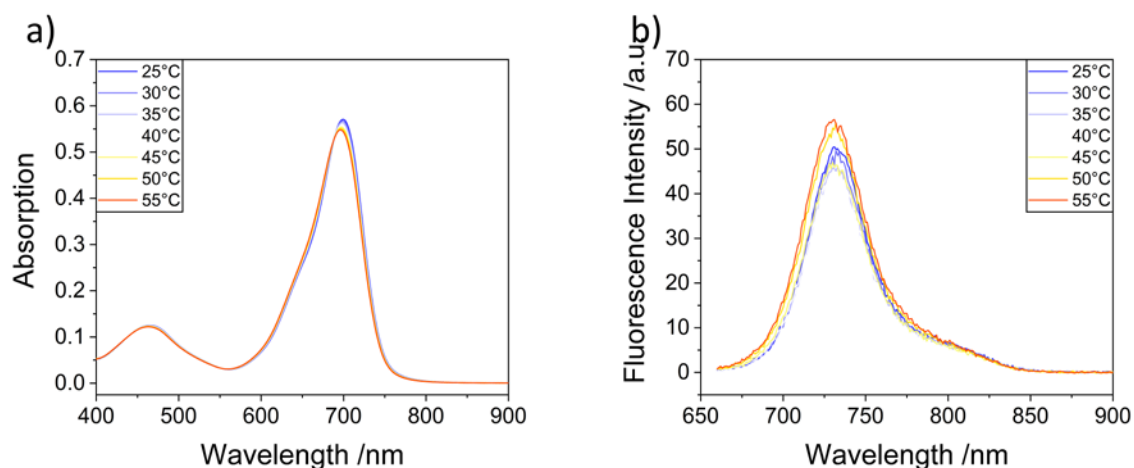


**Figure S7.** Temperature dependent a) Absorption and b) fluorescence spectra of aBOD in water (Kolel) at concentrations of  $1 \times 10^{-5}$  M,  $\lambda_{\text{ex}} = 650$  nm.

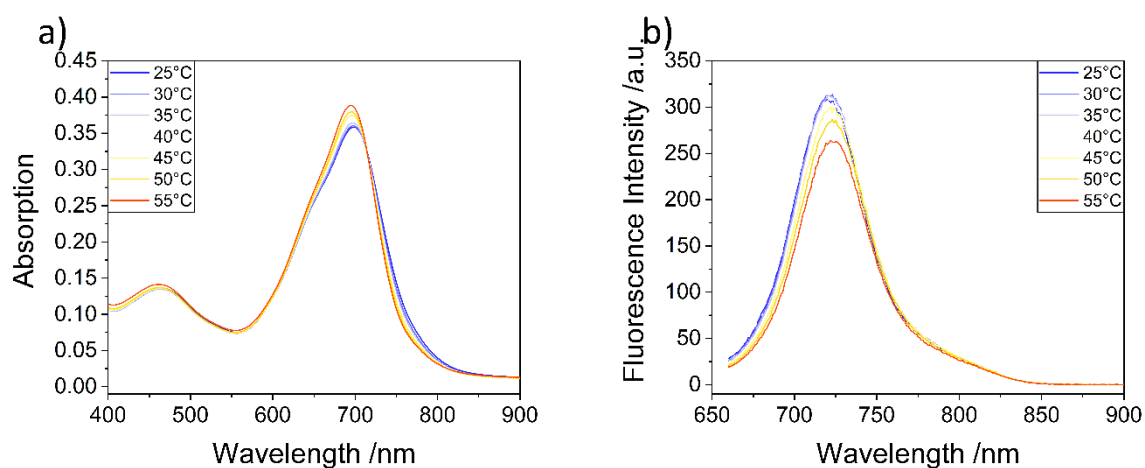


**Figure S8.** Temperature dependent a) absorption and b) fluorescence spectra of SCNP\_aBOD\_1 in water at a dye concentration of  $5 \times 10^{-5}$  M,  $\lambda_{\text{ex}} = 650$  nm.

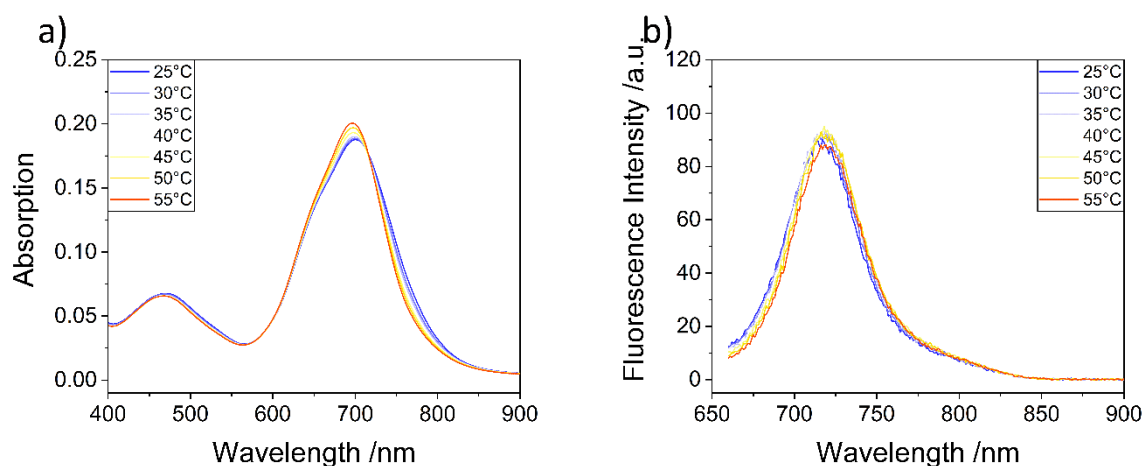


**Figure S9.** Temperature dependent a) absorption and b) fluorescence spectra of SCNP\_aBOD\_5 in water at a dye concentration of  $5 \times 10^{-5}$  M,  $\lambda_{\text{ex}} = 650$  nm.

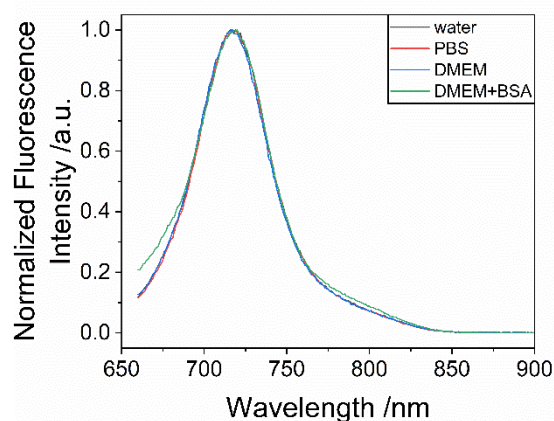


**Figure S10.** Fluorescence spectra of SCNPs\_aBOD\_1 in water, phosphate buffered saline (PBS), Dulbecco's Modified Eagle's Medium (DMEM), and DMEM with 10% bovine serum albumin (BSA) at concentrations of 0.1 mg/mL,  $\lambda_{ex} = 650$  nm. The spectra were normalized due to differences in the pH values of the solutions which are close to the  $pK_a$  value of the aBOD labeled SCNPs and trigger major differences in fluorescence intensities.<sup>2</sup>

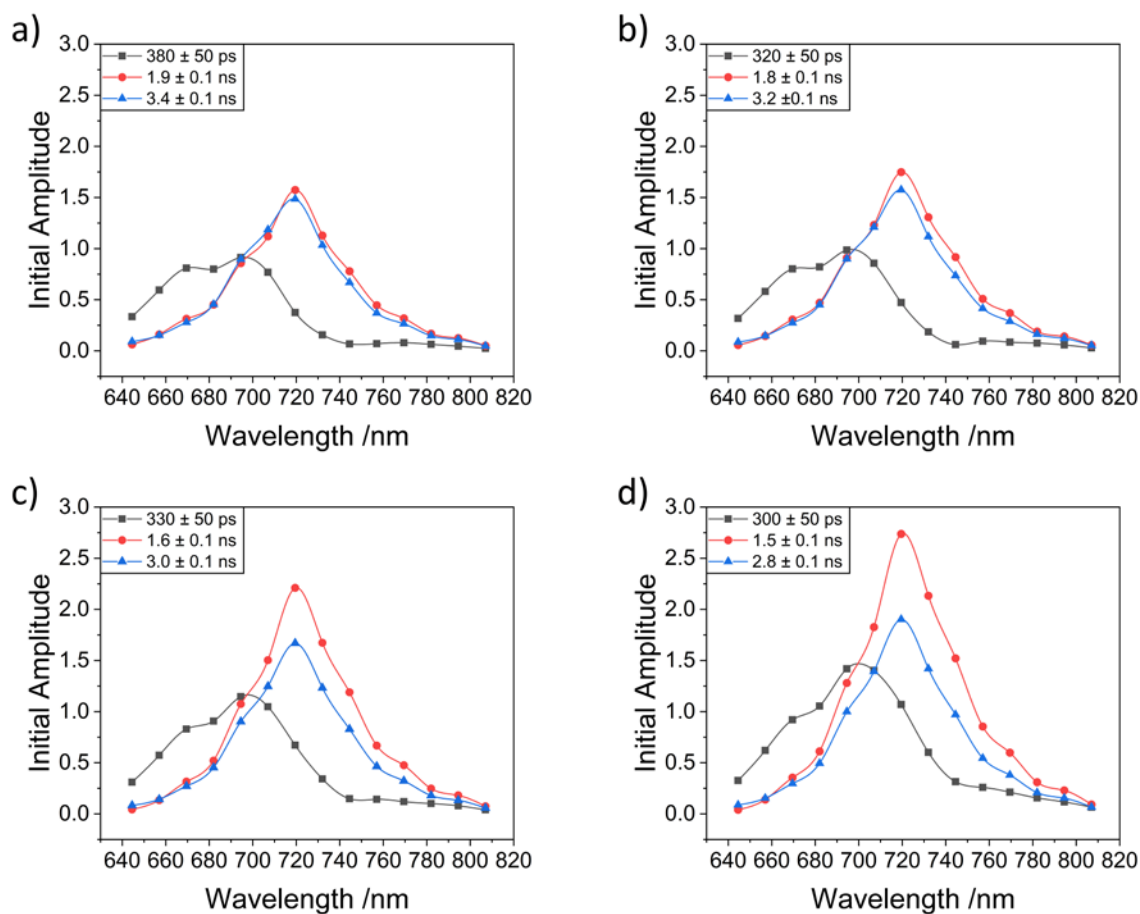


**Figure S11.** Decay associated spectra of SCNPs\_aBOD\_1 at a) 20 °C, b) 30 °C, c) 40 °C, and d) 50 °C.

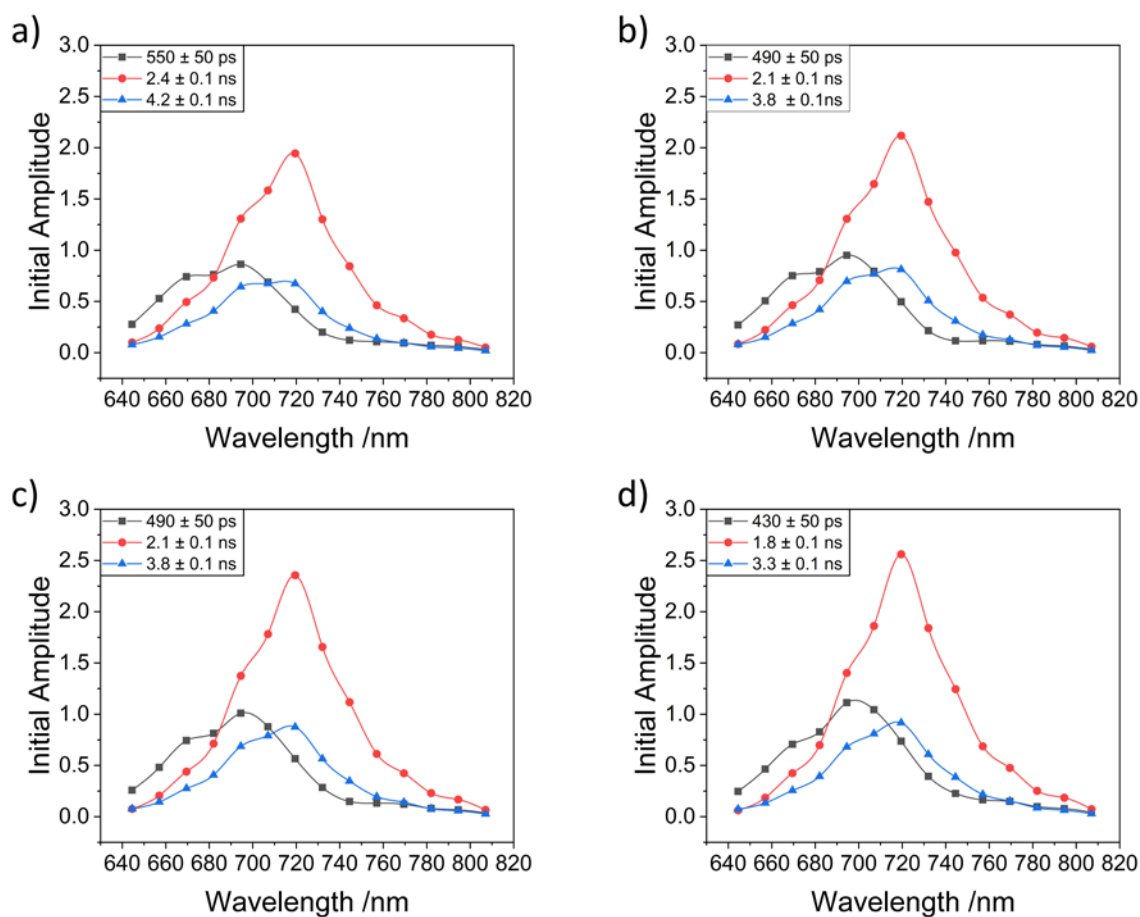


**Figure S12.** Decay associated spectra of SCNPs at a) 20 °C, b) 30 °C, c) 40 °C, and d) 50 °C.

- 1 F. J. Millero, R. Dexter and E. Hoff, *Journal of Chemical Engineering Data*, 1971, **16**, 85-87.
- 2 J. F. Hoffmann, A. H. Roos, F. J. Schmitt, D. Hinderberger and W. H. Binder, *Angew. Chem. Int. Ed.*, 2021, **60**, 7820-7827.